Technische Universität München

Institut für Wasserchemie und Chemische Balneologie

Lehrstuhl für Analytische Chemie und Wasserchemie

Magnetic Nanocomposites for Rapid Biosensing of Staphylococcal Enterotoxin B in Milk

Angelika Maria Nistler

Vollständiger Abdruck der von der Fakultät für Chemie der Technischen Universität München zur Erlangung des akademischen Grades eines

Doktors der Naturwissenschaften

genehmigten Dissertation.

Vorsitzender:	Prof. Dr. Michael Schuster
Prüfer der Dissertation:	1. Priv.-Doz. Dr. Michael Seidel
	2. Prof. Dr. Reinhard Nießner

Die Dissertation wurde am 05.09.2018 bei der Technischen Universität München eingereicht und durch die Fakultät für Chemie am 08.11.2018 angenommen.

Acknowledgements

This thesis was prepared during January 2015 and December 2017 at the Institute of Hydrochemistry, Chair of Analytical Chemistry and Water Chemistry, Technical University of Munich under supervision of PD Dr. Michael Seidel.
This research project was financially supported by the Federal Ministry of Education and Research (LEVERA, No. 13N12613), Deutsche Forschungsgemeinschaft (DFG) and by the TUM International Graduate School of Science and Engineering (MiCSMaP, No. 9.06, BIOMAG No. 10.03).
Further, I want to especially thank PD. Dr. Michael Seidel for his academic supervision, patience, continuous support and faithful guidance throughout my work. Thank you for always taking time for discussion.
I want to address a special thank to Prof. Dr. Reinhard Niessner for the friendly reception at the Institute and scientific disussions and for giving me the trust to accomplish my thesis.
Thanks to Prof. Alan Jasanoff and Dr. Peter Harvey from MIT in Boston (USA) for the possibility to spend several months in their laboratory. I had a wonderful time in your lab and learned not only a lot about Magnetic Resonance Imaging but also about the american way of life. Their input made this work more versatile in an academic and especially personal way.
I would like to warmly thank Dr. Matthias Opel for conducting SQUID magnetometry measurements and for his helpful discussions about the principles of magnetism. Additionally I would like to thank Dr. Berhard Gleich for his help in magnetic calculations and Dr. Christine Rümenapp for her support and help in nanoparticle synthesis and characterization. I would like to thank Prof. Dr. F. Wagner for conducting Mössbauer spectroscopy, Dr. G. Ganskow and C. Sternkopf for conducting SEM measurements, and Dr. M. Hanzlik and M. Götzfried for TEM measurements.

Thanks to my fellow master students Nadine Berger and Jaroslaw Marciniszyn for their high interest in the project and their help in the laboratory. For proof-reading this thesis, I want to thank Carolin Hartmann and Catharina Kober. I thank all my colleagues at the IWC for their constant helpfulness and the warm and friendly atmosphere. A special thanks to my collaborates in the Microarray Group: Jonas Bemetz, Verena Meyer, Sandra Schäfer. I want to express my gratefulness towards my dear collegues Catharina Kober, Anna-Catherine Neumann, Katharina Stutzer and Anika Wunderlich for their good mood, help and support during my time at the Institute.

Special thanks to my dear friend Carolin Hartmann for her support and true friendship during my time at the Institute. Thank you for being such wonderful friend and sharing daily PhD life with me as well as an amazing time in Boston. I was lucky to meet many wonderful people at my time at the IWC. Thank you all for creating a great scientific atmosphere. At last but not at least, I want to thank my family and Leo for their constant belief in me and my skills.

Publication

Parts of this thesis have been published in the following scientific journal:

Angelika Nistler, Carolin Hartmann, Christine Rümenapp, Matthias Opel, Bernhard Gleich, Natalia P. Ivleva, Reinhard Niessner, and Michael Seidel, Production and characterization of long-term stable superparamagnetic iron oxide-shell silica-core nanocomposites, Journal of Magnetic Materials and Magnetism, 442 (2017), pp. 497–503.

Contents

Acknowledgements **iii**

1 Introduction **1**

2 Fundamentals **5**
2.1 Magnetic Nanoparticles 6
2.1.1 Composition 6
2.1.2 Magnetism 6
2.1.3 Synthesis methods of iron oxide nanoparticles 9
2.1.4 Chemistry of iron oxides 13
2.2 Magnetic nanocomposites 14
2.2.1 Basics 14
2.2.2 Types of magnetic nanocomposites and their synthesis 14
Multicomponent, magnetic hybrid nanoparticles 14
Colloidal crystals 16
Matrix-dispersed nanoparticles 16
2.3 Surface functionalization of iron oxide nanoparticles 22
2.3.1 Organic materials 22
Small molecules and surfactants 22
Polymers 24
2.3.2 Inorganic materials 24
2.3.3 Conjugation of antibodies to iron oxide nanoparticles . 25
Antibody structure and modification sites 25
Functionalization chemistry 26
2.4 Analytical characterization of magnetic nanoparticles 31
2.4.1 Characterization of size and morphology 31
2.4.2 Electron microscopy 31
Transmission electron microscopy (TEM) 31
Scanning electron microscopy (SEM) 32
2.4.3 Dynamic Light Scattering (DLS) 34
2.4.4 Magnetic characteristics 36
2.4.5 Characterization of chemical compositon of nanoparticle core 38
Raman microspectroscopy (RM) 38
Mössbauer spectroscopy 39
2.4.6 Characterization of nanoparticle surface 41
Fourier-transform infrared spectroscopy (FT-IR) 41
Zetapotential 42
2.5 Bacterial pathogens and toxins in foodborne illness 43
2.6 Staphylococcal Enterotoxins 45

2.6.1 Source . . . 45
2.6.2 Properties and Structure . . . 45
2.6.3 Staphylococcal enterotoxins in foodborne poisoning associated diarrhea . . . 46
2.6.4 SEB as potential biological warfare agent . . . 47
2.7 Separation and concentration of bacterial pathogens and toxins from food matrices . . . 49
2.7.1 Non-selective target separation and concentration methods . . . 50
Filtration . . . 50
Centrifugation . . . 51
2.7.2 Selective target separation and concentration methods 51
Immunomagnetic separation (IMS) . . . 51
Immunofiltration . . . 54
2.8 Analytical detection methods for SEB . . . 56
2.8.1 Serologic tests . . . 56
2.8.2 Nucleic acid-based detection . . . 56
2.8.3 Chromatographic methods . . . 57
2.8.4 Immunological-based assays . . . 58
Principles of detection . . . 58
Nanoparticle-based detection methods for SEB . . . 62
Commercially available detection methods for SEs . . . 64

3 Materials and Methods **65**
3.1 Materials . . . 65
3.1.1 Instruments . . . 65
3.1.2 Software . . . 66
3.1.3 Materials and Chemicals . . . 67
Material . . . 67
Chemicals and Reagents . . . 68
Antibodies and Antigens . . . 71
Buffers . . . 72
3.2 Methods . . . 74
3.2.1 Synthesis of iron oxide-shell silica-core nanocomposites 74
3.2.2 Functionalization of iron oxide-shell silica-core nanocomposites . . . 76
3.2.3 Synthesis of maghemite and magnetite nanoparticle reference materials . . . 76
3.2.4 Characterization of iron oxide-shell silica-core nanocomposites . . . 76
Characterization of size and morphology . . . 76
Analysis of magnetic properties . . . 77
Determination of iron conent by ICP-MS measurements 77
Raman microspectroscopy (RM) . . . 77
Fouriertransformed infrared spectroscopy (FT-IR) . . . 78
Mössbauer spectroscopy . . . 78
Analysis of zeta potential . . . 78

Ninhydrin colorimetric assay 78
Separation capability of magnetic nanocomposites in milk 79
3.2.5 Biotinylation of anti-SEB antibody S419/5/5/5 79
3.2.6 IMS of SEB for MNC-SMIA I 80
Antibody functionalization of iron oxide-shell silica core nanocomposites 80
IMS step of SEB in 0.6 mL milk 80
3.2.7 IMS of SEB for MNC-SMIA II 81
Antibody functionalization of iron oxide-shell silica core nanocomposites 81
IMS of SEB in 100 mL milk 81
3.2.8 Microarray Chip Production 82
Microarray surface chemistry 82
Immobilization of antibodies 84
Preparation of microarray chips 84
3.2.9 MCR 3 86
3.2.10 Procedure of CL-SMIA on analysis platform MCR 3 . . 86
3.2.11 Procedure of the MNC-SMIA I and II on analysis platform MCR 3 SLT 87
3.2.12 Read out and data analysis 90

4 Results and Discussion **91**
4.1 Iron oxide-shell silica-core nanocomposites 91
4.1.1 Synthesis strategy of bare iron oxide-shell silica-core nanocomposites 91
4.1.2 Characterization of bare iron oxide-shell silica-core nanocomposites 93
Size and morphology 93
Magnetic characteristics 95
Chemical characteristics 98
4.1.3 Influence of synthesis reaction time on characteristics of iron oxide-shell silica-core nanocomposites 104
Influence on size and morphology 104
Influence on composition 106
Influence on magnetic characteristics 107
4.1.4 Functionalization of iron oxide-shell silica-core nanocomposites 109
Functionalization strategy 109
Surface characterization of organosilane-functionalized iron oxide-shell silica-core nanocomposites . 110
Magnetic characteristics of organosilane-functionalized iron oxide-shell silica-core nanocomposites . 113
4.1.5 Long-term stability of iron oxide-shell silica-core nanocomposites 115
4.1.6 Summary 117

4.2 Chemiluminescence sandwich microarray immunoassay (CL-SMIA) for detection of SEB in milk . . . 118
4.2.1 Calibration of CL-SMIA . . . 119
4.2.2 Recovery experiments . . . 120
4.3 Magnetic nanocomposite based chemiluminescence sandwich microarray immunoassay (MNC-SMIA I) . . . 121
4.3.1 Development of MNC-SMIA I . . . 121
4.3.2 Optimization of MNC-SMIA I . . . 124
Selection of antibodies . . . 125
Conditions of microarray chip incubation . . . 126
Influence of blocking buffer on background signal . . . 130
Influence of marker enzyme . . . 133
Influence of exposure time . . . 134
Concentration of capture and detection antibody . . . 136
Titration of magnetic nanocomposite-antibody conjugate 139
Summary . . . 140
4.3.3 Calibration of MNC-SMIA I . . . 141
4.3.4 Recovery experiments . . . 143
4.3.5 Comparison of CL-SMIA and MNC-SMIA I . . . 144
4.4 Development of MNC-SMIA II in large volumes of milk . . . 146
4.4.1 Assay principle MNC-SMIA II in large volumes of milk 146
4.4.2 Separation capability of iron oxide-shell silica-core nanocomposites in milk . . . 147
4.4.3 Optimization of MNC-SMIA II in large volumes of milk 151
Titration of magnetic nanocomposite-antibody conjugate 151
Influence of analyte incubation time . . . 152
4.4.4 Calibration of MNC-SMIA II in 100 mL milk . . . 154
4.4.5 Recovery experiments . . . 156
4.4.6 Comparison of SMIAs for the detection and quantification of SEB in milk . . . 157

5 Summary and Outlook **161**

A MCR 3 SLT **165**
A.1 Fluidic plan of the MCR 3 SLT . . . 165
A.2 MCR 3 Program: MNC-SMIA (front channel) . . . 166

Bibliography **169**

List of Abbreviations

APTES	(3-Aminopropyl)triethoxysilane
CCD	Charge-coupled device
CDC	Centers for Disease Control and Prevention
CL	Chemiluminescence
d	Diameter
DLS	Dynamic Light Scattering
DSC	Disuccinimidyl carbonate
EC_{50}	Half maximal effective concentration
EDC	1-Ethyl-3-(3-dimethylaminopropyl)carbodiimide
ELISA	Enzyme linked immunosorbent assay
Fab	Antigen-binding fragment
FC	Field-cooled
Fe_3O_4	Magnetite
FT-IR	Fourier transform infrared spectroscopy
GOPTS	(3-Glycidyloxypropyl)trimethoxysilane
h	Hour
HER2	Human epidermal growth factor receptor 2
ICP-MS	Inductively coupled plasma mass spectrometry
IgG	Immunoglobuline G
IMS	Immunomagnetic separation
IWC	Institute of Hydrochemistry, TU Munich
LOD	Limit of Detection
LFI	Lateral flow immunoassay
MNC-SMIA	Magnetic nancomposites-based sandwich microarray immunoassay
m	Number of repetitions
M	Molar
MCR 3	Microarray Chip Reader of the 3rd generation
mAb	Moncolonal antibody
Maldi-TOF	Matrix-assisted laser desorption/ionization time of flight
MHC	Major histocompatibility complex
min	Minute
M_S	Magnetic saturation
MWCO	Molecular weight cutoff
MS	Mass spectrometry
n	Number of concentrations
NHS	N-Hydroxysuccinimide
pAb	Polyclonal antibody
PCR	Polymerase chain reaction
PBS	Phosphate buffered saline
PEG	Polyethylene glycol

PVP	Polyvinylpyrrolidone
RM	Raman microspectroscopy
rpm	Rounds per minute
RT	Room temperature
SDS	Sodium dodecyl sulfate
SEA	Staphylococcal enterotoxin A
SEB	Staphylococcal enterotoxin B
SEl	Staphylococcal enterotoxin-like
SEM	Scanning electron microscopy
SEs	Staphylococcal enterotoxins
SMIA	Sandwich microarray immunoassay
SQUID	Scanning electron quantum interference device
$\mathbf{T_B}$	Blocking temperature
TEM	Transmission electron microscopy
TSST-1	Toxic shock syndrome toxin-1
v/v	Ratio of volumes
WHO	World Health Organization
WR	Working range
w/v	Weight per volume
ZFC	Zero field-cooled
γ**-Fe$_2$O$_3$**	Maghemite

Chapter 1

Introduction

Due to recent outbreaks of food poisoning caused by foodborne pathogens, food safety has become a globally expanding issue and thus a leading topic in public health. According to the World Health Organization (WHO) foodborne diseases cause death of about two millions individuals in the world each year [1]. From the farm where the food is produced, to the handling practices of manufacturers, to our own kitchens, food safety involves all stages of food production and consumption [2]. Therefore, quality control with regard to hygiene and food safety is fundamental for public health and consumer confidence. The main goal of food safety authorities is not only to stop foodborne diseases after an outbreak, but also prevent them from occuring. The time from occurence of a microbial danger to the identification of the responsible pathogen or toxin and finally the spreading in the food chain supply is a crucial step. The shorter this time frame, the faster food can be declared as harmless or dangerous and therefore the outbreak risk can be dramatically reduced.

Staphylococcal enterotoxins (SEs) are one of the most common causes of acute food contamination and poisoning, accounting for numerous foodborne-disease outbreaks all over the world. The Center of Disease control (CDC) further stated that the proteotoxins SEs affect approximately 80 million people in the United States, resulting in 325,000 hospitalizations and more than 5,000 deaths each year [1].
Stayphylococcal enterotoxin B (SEB) and Staphylococcal enterotoxin A (SEA) are two of the most common SEs. SEB is a heatstable enterotoxin produced by the ubiquitous appearing Gram-positive bacterium *Staphylococcus aureus* (*S. aureus*). It is not only associated with food poisoning but also regarded as a potential biological warfare agent, which may be used for bioterrorism attacks on the food supply chain [1]. Since the preparation of the proteoxin ricin by terrorist groups as well as ricin findings in the US postal system in 2003, it has become apparent that there is an urgent need for the development of a rapid and sensitive detection method of proteotoxins including SEB. Due to their ease of preparation, availability, high toxicity and their lack of therapeutic options, high molecular-weight proteotoxins could be easily used as food contaminants to affect a large number of people [3].
Only a very low amount of SEB (1 $\mathrm{ng\,g^{-1}}$) is needed to induce food poisoning [3]. The proteotoxin SEB functions as potent gastrointestinal toxin and a superantigen causing typical symptoms such as severe diarrhea, abdominal

pain, nausea and high fever. The disease is usually self-resolving and rarely lethal, however elderly and children are more susceptible [1].

To ensure a fast surveillance and response to foodborne-disease outbreaks, a rapid method is required which enables a sensitive quantification of SEB in complex food matrices. In 2003 the WHO stated that the optimal approach to reduce the number of food poisoning-related disease outbreaks are preventative measures which include stricter food control, hand and environmental hygiene, identification and isolation of carriers, and proper *S. aureus* antibiotic therapy [1].
A rapid and applicable analytical method could not only identify the source of the foodborne disease after an outbreak, but also prevent an outbreak before affecting the population and therefore support official food control agencies.

Since proteotoxins such as SEB are acting in the absence of the producing organism *S. aureus* and its genetic information, their detection cannot be grounded on cultivation methods or nucleic-acid based methods. Consequently, immunological, mass spectrometric or functional assays are required to detect the toxin itself.
An immunoassay based on specific antibodies which bind their target protein with high affinity, is highly advantageous due to its high specificity, selectivity and sensitivity.
On the one hand, a major problem of current analytical methods for the quantification of SEB in food samples ist their lack of sensitivity. On the other hand, various analytical approaches (e.g. biosensor technologies) work well in buffer solutions, but fail when used in complex matrices due to the inference of matrix components with binding reagents or techniqual equipment [3]. Analytical methods such as enzyme linked immunosorbent assays (ELISA) or mass spectrometry (MS) therefore require the prior enrichment and isolation of the target analyte from the complex food matrix, which is labor-intensive and prolongs the assay time in a case of an acute outbreak.

Magnetic nanocomposites offer the major advantage of being easily separated from complex food matrices and are thus perfectly suitable for immunomagnetic enrichment procedures. The ultimate goal of this thesis was the coupling of a facile and efficient immunomagnetic separation (IMS) step based on nanocomposites with specifically tailored magnetic and morphological characteristics to a sensitive microarray analysis on the automated flow-based microarray analysis platform MCR 3. Hereby, the potential of a prior selective pre-enrichment and concentration step by IMS to increase the assay sensitivity and enable the possibility to rapidly analyze larger amounts of food samples was tested.
An important task during the PhD thesis was the synthesis of iron oxide-shell silica core nanocomposites which bear highly beneficial magnetic features for applications in IMS - the simple manipulation by permanent magnets and superparamagnetism for easily switching on and off the magnetic response.

For the first time, the novel iron oxide-shell silica-core nanocomposites should be applied along with antibodies against SEB to establish a highly sensitive magnetic nancomposite-based sandwich microarray immunoassay (MNC-SMIA) on the microarray platform MCR 3 SLT. To realize this immunoassay, iron oxide-shell silica-core nanocomposites functionalized with biotinylated anti-SEB detection antibodies are incubated in milk spiked with SEB. Nanocomposites bind SEB in the milk by an affinity reaction. An IMS step is applied, to selectively enrich and isolate SEB from the initial sample volume of either 0.6 mL or 100 mL.
In order to guarantee a rapid magnetic separation of the nanocomposites, both manual and automatic separation techniques had to be tested with regard to time-effectiveness, effectivity and practicability.

SEB is quantified by MNC-SMIA. The assay readout is performed by chemiluminescence (CL) imaging after enzymatic reaction of horseradish peroxidase with luminol and hydrogen peroxide on each spot of the microarray. A second task during this thesis was the step by step optimization of MNC-SMIA to achieve a rapid, simple and highly sensitive immunoassay for the detection and quantification of SEB in the complex food matrix milk.

Chapter 2

Fundamentals

2.1 Magnetic Nanoparticles

Due to their size, surface-to-volume ratio and their unique magnetic and physiochemical properties magnetic nanoparticles exhibit physical behavior different from the bulk material. In the following the magnetism of nanoparticles, chemical characteristics and their physicochemical properties are introduced.

2.1.1 Composition

Magnetic nanoparticles are consisting of a broad variety of compositions and phases such iron oxides (maghemite and magnetite), pure metals (e.g. Fe, Co), ferromagnets ($MgFe_2O_4$, $MnFe_2O_4$, $CoFe_2O_4$) as well as alloys $CoPt_3$, FePt [4].
One of the most common materials for magnetic nanoparticles are iron oxides, which have been applied as contrast agent for *in vitro* diagnostics for nearly half a century. Iron oxide-based nanoparticles are of increasing scientific interest since they are inexpensive to prepare, exhibit physical and chemical stability, biocompatibility and are environmentally safe [5]. In this section approaches for the synthesis of iron oxide nanoparticles are highlighted.

2.1.2 Magnetism

Magnetic nanoparticles for medical and biological applications can be classified into paramagnetic, ferromagnetic and superparamagnetic particles. In general, the core material and the size and shape of superparamagentic and ferromagnetic particles predominantly define its magnetic characteristics.
Magnetism is strongly dependent on the temperature. The type of the core material at a given temperature decides whether the magnetic nanoparticles is para-, ferro-, or ferrimagnetic. If the temperature is higher than the material specific Curie temperature, ferromagnetism and superparamagnetism disappear, and the material exhibit paramagnetic characteristics [6]. In the next section, a short overview of distinct types of magnetism is given with a focus on the magnetism of iron oxide nanoparticles.

Paramagnetism

Whereas superparamagnetic and ferromagnetic nanoparticles are consisting of a magnetic core and a surface coating, paramagnetic particles are usually chelates of paramagnetic ions with no distinct core and surface coating (e.g. gadolinium, magnesium, lithium, tantalum) [7, 8]. In paramagnetic particles each atom behaves as individual, non-interacting and randomly orientated molecular magnet with a magnetic dipole moment. Without application of an external magnetic field, all dipole moments of paramagnetic materials are orientated randomly. After application of an external magnetic field,

the molecular magnets start to align along with the direction of the magnetic field forming a net magnetic moment. If the magnetic field strength is increased, magnetic saturation (M_S) can be achieved. M_S is the maximum magnetization and arises when all the magnetic dipoles of the particles are aligned with the external field. It only occurs at very low temperatures or at a rather high magnetic field strength. After removal of the magnetic field, the molecular magnets instantaneously orientate randomly due to thermal fluctuations. Thus, in paramagnetic materials no net magnetization or remanence occur [7].

Ferromagnetism

The magnetic moments of ferromagnetic particles are fixed in their direction and organized in so called Weiss domains, which are separated each by a Bloch or a Néel wall [9]. Weiss domains are defined as small magnetized domains in the crystals of the magnetic material.
Depending on the alignment of the magnetic moments in the Weiss domains the magnetic behavior can be classified in ferromagnetism (all moments are aligned in the same direction), antiferromagnetism (the magnetic moments are alternating their direction in each Weiss domain) or ferrimagnetism (the magnetic moments are unequal and alternating their direction) [10]. Without an application of an external magnetic field, the magnetic dipole moments in the distinct Weiss domains are not orientated in the same direction. When the ferromagnetic material is placed in a magnetic field, the domain walls reorganize and both total magnetic moment and magnetisation of the ferromagnetic particle begin to align with the external field. If the external magnetic field is removed, the magnetization of the ferromagnetic particle can be partially or even fully retained. Thus the particle shows a magnetic remanence and act as a permanent magnet [7]. The number of Weiss domains depend on the size of the nanoparticle. If the core size D_c is lower than the cricital size D_{sd}, only one energetic more favourable single domain state consisting of only one Weiss domain occurs instead of the multi domain state (Figure 2.1).

Superparamagnetism

Superparamagnetism occurs if the size of a ferromagnetic single domain particle is further decreased. Consequently the D_c is smaller than a second critical size D_{sp} for superparamagnetic nanoparticles (Figure 2.1). In nanoparticles, which are smaller than the critical size D_{sp}, thermal fluctuations outcompete the dipole-dipole interactions. This results in a random flip of the magnetization in absence of an external magnetic field. Thus, superparamagnetic nanoparticles do not show any remanent magnetization without applied external magnetic field [7, 11]. The required external field strength to saturate superparamagnetic particles is comparable to the field strength for ferromagnetic particles. Various critical sizes D_{sd} for ferromagnetic single

domain particles and D_{sp} for superparamagnetic particles of different materials are shown in Figure 2.1. Above a particular temperature, the so called blocking temperature T_B, both ferromagnetic and ferrimagnetic nanoparticles, exhibit superparamagnetic characteristics [8]. In general, T_B indicates the transition between superparamagnetic behavior and blocked state.

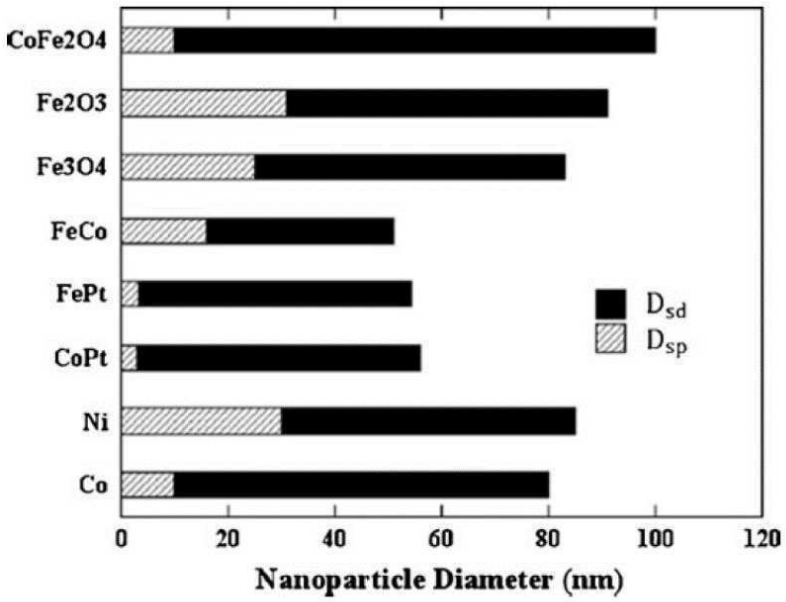

FIGURE 2.1: The critical sizes for the observation of superparamagnetism and single-domain behaviour, D_{sp} and D_{sd}, respectively, in a variety of common ferromagnetic fine particles are shown. For core diameters $D_c < D_{sp}$, they exhibit superparamagnetism; for $D_c > D_{sd}$, they split into multiple domains to minimize their overall energy and between $D_{sp} < D_c > D_{sd}$, they are ferromagnetic and exhibit a single domain [7].

The magnetic moment μ of a magnetic dipole in a magnetic field B follows a Langevin function, given by Equation 2.1 [7]

$$\mu = \mu_{sat} \cdot L(B) \tag{2.1}$$

with the saturation of the magnetic moment μ_{sat} and the Langevin term given by Equation 2.2 [12] with the Boltzmann constant κ_B and the measuring temperature T = 300 K.

$$L(B) = \coth(\frac{\mu_{sat} B}{\kappa_B T}) - \frac{\kappa_B T}{\mu_{sat} B} \tag{2.2}$$

2.1.3 Synthesis methods of iron oxide nanoparticles

Up to now, various distinct synthetic methods including co-precipitation, thermal decomposition, hydrothermal and solvothermal syntheses, sol-gel synthesis, ultrasound irradiation and biological synthesis have been applied to synthesize magnetic iron oxide nanoparticles. All those methods can be classified into aqueous and non-aqueous synthesis routes. Magnetic nanostructures with different morphologies have been prepared including particles, wires, and rods [5]. In the following the main synthetic routes for the preparation of iron oxide nanoparticles are listed.

Co-precipitation

The most convential synthetic strategy to produce iron oxide nanoparticles is the co-precipitation of Fe^{3+} and Fe^{2+} salts in aqueous solutions. In general, ferric and ferrous ions are mixed in a 1:2 molar ratio in a very basic aqueous solution at room temperature (RT) or elevated temperature under inert gas atmosphere. Although the co-precipitation has the significant advantage of easily producing a large amount of iron oxide nanoparticles, the fast particle formation rate also induces some severe drawbacks such as the broad particle size distribution, low control over particle size and morphology as well as the utilization of a strong base in the synthesis protocol [5]. To achieve a narrow size distribution and monodispersity of iron oxide nanoparticles, the optimum parameters for the concentration and type of precursors, pH, ionic strength, stirring speed, temperature, base and reaction time have to be optimized.

High-temperature thermal decomposition

Another important approach is the thermal decomposition of organometallic or coordinated iron precursors in organic solvents at high temperature (Figure 2.2). During the thermal decomposition the precursor is either injected in a hot reaction mixture or the reaction mixture is prepared at RT and heated in a closed or open reaction vessel. Typical synthesis precursors are ferric salts such as $Fe(CO)_3$, iron(III) actetylacetonate, iron oleate, iron(III) N-nitrosophenylhydroxylamine, Prussian blue, Fe-urea complex or ferrocene. Usually tensids such as oleic acid or hexadecylamine are added as stabilizer in order to slow down the nucleation process and inhibit the growth of the iron oxide nanoparticles and therefore favor the formation of small iron oxide nanoparticles [4].
In thermal decomposition nucleation process can be separated from growth and therefore complex hydrolysis reactions, which typically occur during

co-precipitation method, can be avoided. Whereas co-precipitation is carried out at RT resulting in low crystalline nanoparticles, the thermal decomposition method commonly produces highly monodisperse and crystalline nanoparticles with a narrow size distribution. Nevertheless, the thermal decomposition method has the disadvantage that only low amounts of nanoparticles are produced. Additionally, since the nanoparticles are synthesized in organic solvents, they have to be further functionalized to be applicable in aqueous environments.
In general, thermal decomposition at high temperature results in the production of spherical nanoparticles below 30 nm. Additionally, the thermal decomposition method offers the advantage to tailor the shape and size of iron oxide nanoparticles by the use of different precursors, additives and solvents during the thermal decomposition process [5].

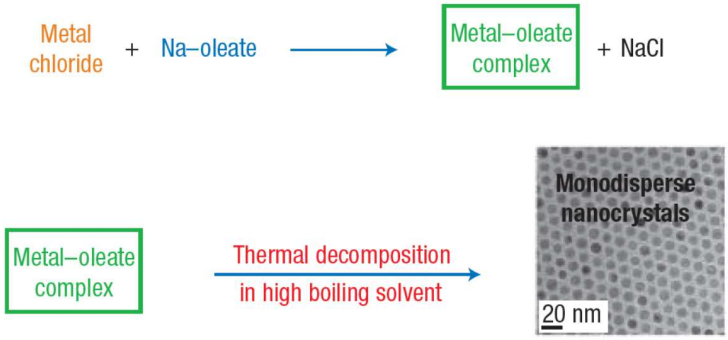

FIGURE 2.2: The overall scheme for the synthesis of monodisperse nanocrystals [13]. Metal–oleate precursors were prepared from the reaction of metal chlorides and sodium oleate. The thermal decomposition of the metal–oleate precursors in high boiling solvent produced monodisperse nanocrystals.

Microemulsion

A microemulsion is defined as a clear, thermodynamically stable isotropic dispersion of two immiscible liquids (oil and water). The surfactants are forming a monolayer at the interface between the oil and water. Hereby, the hydrophobic tails of the surfactant moleculs are dissolved in the oil phase and the hydrophilic head groups are dissolved in the aqueous phase. The microemulsion method can be divided in two types of microemulsions: oil dispersed in water (O/W) and water dispersed in oil (W/O). The latter is also called reverse microemulsion. In water-in-oil emulsions, the aqueous phase is dispersed in microdroples at around 1-50 nm surrounded by a monolayer of surfactant molecules in the hydrocarbon phase. After incorporation of a soluble metal salt, it will reside in the aqueous microdroplets surrounded by oil. Subsequently, the microdroplets will collide, coalesce and break forming a precipitate inside the micelles [14]. By addition of an organic solvent such as acetone or ethanol, the precipitate containing the nanoparticles can be extracted by centrifugation or filtration [4]. Widely used surfactants for the preparation of magnetic iron oxide nanoparticles include bis(2-ethylhexyl) sulfosuccinate, sodium dodecyl sulfate (SDS), cetyltrimethylammonium bromide, and polyvinylpyrrolidone (PVP).
However, due to aggregation of the prepared iron oxide nanoparticles, several washing processes and further stabilization treatments are required. Additionally, the microemulsion technique results in low yields and requires a high consumption of solvents [4].

Sol-gel and polyol reactions

The sol-gel process is a typical wet-chemical synthesis route for the preparation of nanostructured metal oxides. The method is based on the hydrolysis and condensation of precursors in solution forming a sol. A sol is defined as a stable dispersion of colloidal particles or polymers in a solvent. Typical precursors for the synthesis of iron oxide nanoparticles are iron alkoxides and iron salts which undergo various forms of hydrolysis and polycondensation reactions [5]. Additional condensation and polymerization is resulting in a three-dimensional metal oxide network, the so called wet gel [15].
All reactions are performed at RT. Thus, to obtain the crystalline particles, a following drying and thermal decomposition step of the gel is performed by heating at elevated temperature.
Typical solvents of sol-gel reactions are polyols such as diethylene glycol. Whereas sol-gel methods use an oxidation reaction, the methods involving polyols employ a reduction reaction and are therefore called the inversed sol-gel method. Hereby, the polyols are not only solvents but also act as reducing agent and stabilizer to control particle growth and interparticle aggregation [5].

The polyol reactions offer the advantages of producing a large amount of iron oxide nanoparticles and good control over size distribution. Nevertheless, similar to the co-precipitation method all parameters such as solvent, temperature, pH, concentration and nature of precursors have to be precisely adjusted.

Hydrothermal method

The hydrothermal method also called the solvothermal method is performed in aqueous enviroment in a sealed container (e.g. autoclave) under a pressure higher than 138 bar and temperature in the range of 130 - 250 °C. These reactions involve either the hydrolysis and subsequent oxidation or the neutralization of mixed metal hydroxides. By using the hydrothermal method nanoparticles with a narrow size distribution and monodispersity can be obtained [4]. One major drawback of the conventional hydrothermal method is the slow reaction kinetics at any given temperature. Therefore, microwave heating can be applied to improve the kinetics of crystallization of the particles during the hydrothermal method [15].
A summary of the advantages and drawbacks of the mentioned synthetic routes are listed in Table 2.1

TABLE 2.1: Summarized comparison of main synthesis routes for the preparation of iron oxide nanoparticles [4].

Method	**T**	**Time**	**Solvent**	**Size distribution**	**Yield**
Co-precipitation	RT	20 - 30 min	water	broad	high
Thermal decomposition	200 - 320 °C	hours/ days	organic	high	high
Microemulsion	20 - 50 °C	hours	organic	narrow	low
Hydrothermal method	130 - 250 °C	hours/ days	water/ ethanol	very narrow	medium

2.1.4 Chemistry of iron oxides

Among the eight known iron oxides, the most important ones for the synthesis of magnetic nanoparticles are magnetite (Fe_3O_4) and maghemite (γ-Fe_2O_3). Fe_3O_4, magnetite, is a mixed Fe(II)-Fe(III) oxide. The magnetite crystals appear black [5]. Magnetite shows a cubic inverse spinel structure. It consists of a close packed cubic array of oxide ions. The Fe (II) ions are arranged on half of the octrahedral sites, whereas the Fe (III) ions are split evently across the remaining octahedral sites and the tetrahedral sites [5]. (Figure 2.3a).
As shown in Figure 2.3 b), maghemite exhibits a cubical organisation of its oxide ions in which the Fe (III) ions are randomly located in the octahedral or tetrahedral cavities. The Fe (III) oxides are reddish brown.
Maghemite (γ-Fe_2O_3) is formed by the gentle oxidation of magnetite, or the heating of lepidocrocite (γ-FeO(OH)). Due to the high electron mobility in the cubic spinel structure of the magnetite, magnetite nanoparticles are subjected to an interfacial transfer of ions and / or electrons. Thus, magnetite shows a high sensitivity to oxidation and therefore transformation into maghemite. Consequently, to obtain magnetite nanoparticle not only pH, temperature and ionic strength are crucial for the synthesis but also strictly anaerobic conditions.

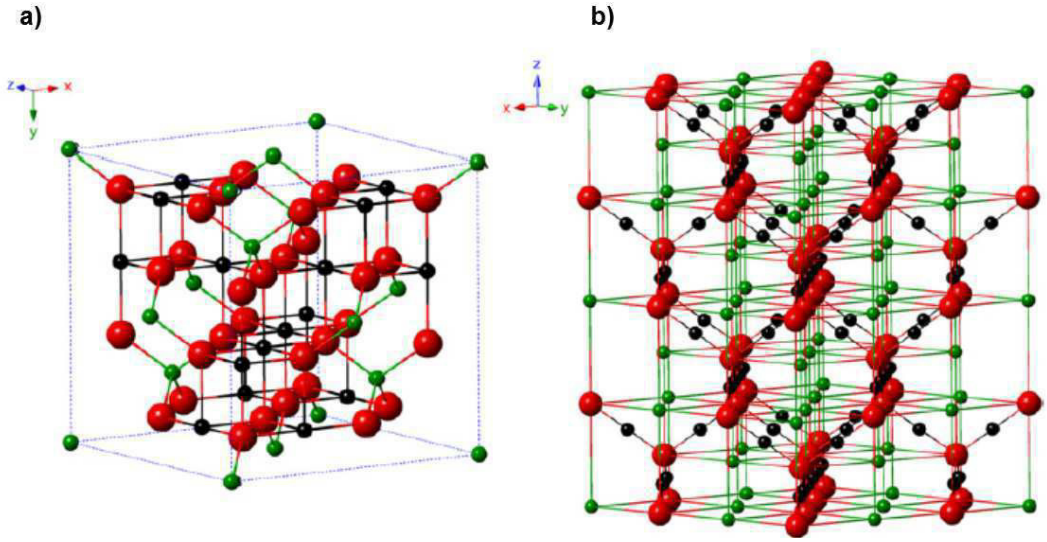

FIGURE 2.3: Crystal structure of: a) magnetite and b) maghemite [5].

Magnetite is oxidized to maghemite in the presence of oxygen:
$Fe_3O_4 + 4.5\,H_2O + 0.25\,O_2 \longrightarrow 3\,Fe(OH)_3 \rightleftharpoons Fe_2O_3 \cdot nH_2O$

Magnetite is transformed into maghemite in acidic environments:
$Fe_3O_4 + 2\,H^+ \longrightarrow \gamma Fe_2O_3 + Fe^{2+} + H_2O$

2.2 Magnetic nanocomposites

2.2.1 Basics

A nanocomposite is a multi-phasic material derived from two or more distinct constituents, in which one of the solid constituents usually exhibit a nanoscale structure of less than 100 nm. In a nanocomposite the properties of the constituents are combined resulting in novel functional materials [16]. Currently, many research groups are focusing on the preparation of magnetic nanocomposites due to the unique possibility of individually tailoring their morphological, chemical, and physical characteristics.
One prominent natural nanocomposite is nacre (mother of pearl), which exhibits a layered structure of calcium carbonate and a small amount of embedded organic biopolymers such as proteins and chitin. Due to its nanocomposite structure, nacre shows superior structural robustness resulting in a thousand-fold increase of toughness, although the ceramic constituent is typically rather brittle [17].

Basically, magnetic nanocomposites are multi-component materials, which contain nanosized magnetic material. In general, nanosized superparamagnetic nanoparticles are prepared and incorporated into or grafted onto the non-magnetic matrix (e.g. organic polymer, silica) in order to generate composite materials with unique and improved material characteristics.

The inclusion of magnetic nanoparticles in a nanocomposite material offers a broad variety of possible applications in biology and medicine. They can be used as novel drug delivery systems, contrast agents for magnetic resonance imaging, carrier for magnetic separation and purification of biochemical products (e.g. nucleic acids, proteins, cells) or applied in the field of catalysis. Magnetic nanoparticles also offer the promising potential for technical applications such as data storage devices [17].
Various morphologies of magnetic hybrid nanocomposites are displayed in Figure 2.4.

2.2.2 Types of magnetic nanocomposites and their synthesis

This section gives a short overview of various types of functional magnetic nanocomposites. Different synthetic approaches for the preparation of magnetic nanocomposites are presented.

Multicomponent, magnetic hybrid nanoparticles

The design of multicomponent magnetic nanoparticles is defined as the combination of two nanosized entities into a single hybrid particle. Hybrid nanoparticles offer highly benificial advantages such as dual imaging capabilities for medical diagnosis (e.g. simultaneous magnetic and optical imaging),

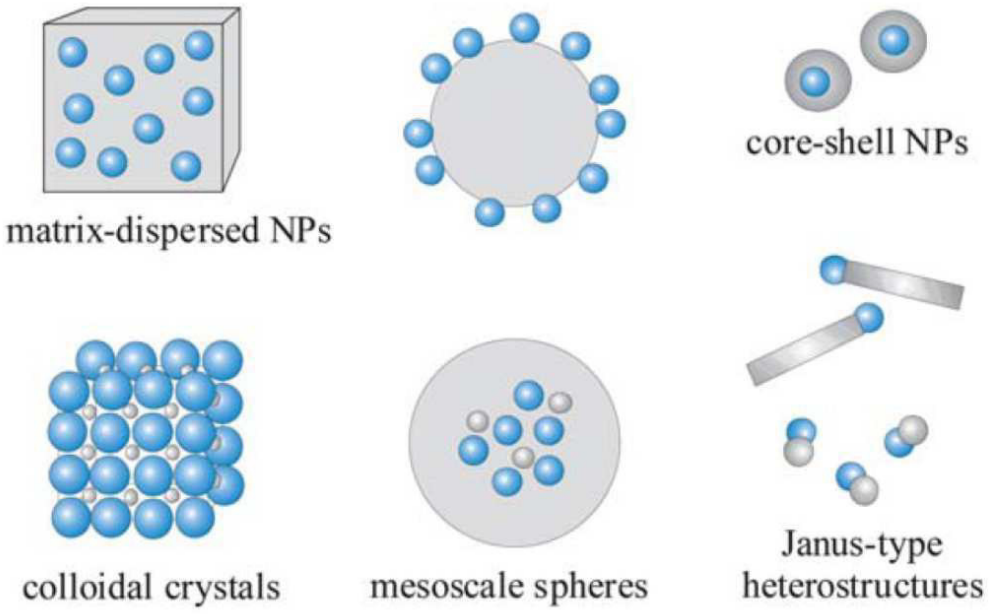

FIGURE 2.4: Typical morphologies of magnetic nanocomposite materials [17].

combination of magnetic imaging and therapy as well as multiplexing sensors [16]. The morphologies of multicomponent, magnetic hybrid nanoparticles can be divided into core-shell type nanoparticles and heterooligomers. Heterooligomers are oligomers which are composed of two or more distinct monomers. In general, nanoparticles are initially prepared of one material and subsequently applied as nucleation seeds to deposit the second material [17].

A typical example for multicomponent hybrids is the gold/magnetite structure, which combines magnetic and high-contrast X-ray materials as dual agent for the simultaneous MRI and X-ray detection. The synthesis of gold nanoparticles embedded in a hollow iron oxide shell has recently been published. Firstly, gold nanoparticles were synthesized. An iron shell around the gold seeds core was deposited by thermolysis of $Fe(CO)_5$. A following air-oxidation of iron was performed in order to generate hollow iron oxide shells. Furthermore, the growth of a magnetite shell on gold nanoparticles was obtained by decomposition of iron(III) acetylacetonate on gold nanoparticles in high-boiling solvents.
Heterostructures for diagnostic and therapeutic applications were generated. Hereby, dumbell-like gold/magnetite nanoparticles were heterofunctionalized with cisplatin and human epidermal growth factor receptor 2 (HER2)-specific monoclonal antibody herceptin. The nanocomposites were able to deliver cisplatin into Her2-positive breast cancer cells for therapeutic effects [17].

Colloidal crystals

Colloidal crystals are defined as assembly of small nanoparticles of distinct materials into an ordered macroscopic superstructure in order to produce composite materials with new material properties. For example, magnetic nanocomposites with semiconductor quantum dots or metal particles were combined to generate a three-dimensionally ordered binary superlattice [17].

Matrix-dispersed nanoparticles

Superparamagnetic nanoparticles can be incorporated or grafted onto the surface of a non-magnetic matrix material. The matrix material is typically an organic polymer or silica (SiO_2). The matrix material protects the superparamagnetic cores partially against oxidation in air and aqueous environments but also against particle aggregation, which may induce ferromagnetism.
Multifunctional nanocomposites which consist of superparamagnetic particles for magnetic manipulation, optical probes (e.g. fluorescent dyes or quantum dots) for tracking, functional groups for selective targeting and bioconjugation and entrapped drugs for therapy are promising candidates in a variety of applications.
In general, there are two basic synthetic strategies for the preparation of these nanocomposites. The magnetic nanoparticles are directly encapsulated within the non-magnetic matrix or deposited on the surface of previously synthesized non-magnetic materials. Hereby, the nanoparticles can be adsorbed from colloidal solutions or produced *in situ*.

Matrix-dispersed nanoparticles can be classified in:

(1) functional magnetic polymers

(2) silica-based magnetic nanocomposites

The polymer in **(1) functional magnetic polymers** offers several advantages such as stabilization of nanoparticles, enhanced mechanical and chemical stability, transparency in the visible range of the electromagnetic spectrum, the possiblity of encapsulating therapeutics and imaging agents as well as multivalency for bioconjugation. Therefore, magnetic polymers are of increasing interest in various biomedical applications such as MRI contrast enhancement, targeted drug delivery, hyperthermia, catalysis, bioseparation, protein immobilization and biosensors [18].
There are different synthetic strategies for the preparation of functional magnetic polymers [18]:
(a) *Direct modification with polymers* such as synthetic polymers (e.g. poly(glycol monoacrylate), poly(acrylic acid) or biopolymers (e.g. dopamine-conjugated hyaluronic acid, polypeptides, dextrans) results in a magnetic single-core surrounded by a polymer shell.

(b) *"Grafting from" method* involves the application of surface-initiated controlled polymerization and leads to a magnetic core with surrounding polymer brushes. Hereby, monodentate polymers with a single anchoring group at the end of polymer chain are used to stabilize superparamagnetic iron oxide nanoparticles.
(c) *Inorganic silica / polymer hybridization* produces multifunctional hybrid nanocomposites. For example silica-functionalized iron oxide nanoparticles were further modified with polymers to obtain multifunctional nanocomposites.
Another synthetic approach for the production of functional magnetic polymers is the (d) *self-assembly* of amphiphilic block copolymer (e.g. poly(ethylene glycol)-block-polylactide methyl ether) and self-association of ionic polymers (e.g. poly(amidoamine) dendrimers, poly(L-lysine).

An important subtype of matrix-dispersed nanoparticles are **(2) silica-based magnetic nanocomposites**. Since in this PhD thesis a new synthetic approach for the synthesis of iron oxide-shell silica-core nanocomposites was developed, the preparation of core-shell-like iron oxide / silica-based nanocomposites will be highlighted.
Silica is a very common and attractive matrix material for coating or embedding of magnetic nanoparticles due to biocompatibility, hydrophilicity and its high stability against degradation. Additionally, the silanol surface groups can be easily modified with a variety of functional groups for further functionalization (e.g. antibodies, proteins, nucleic acids). Furthermore, mesoporous silica nanomaterial can be produced with well-defined pore sizes and large surface areas, which is highly advantageous for application in catalysis and bioseparation [19].

Iron oxide-based silica nanocomposites are especially interesting due to the possibility of individually tailoring their magnetic characteristics to the specific applications. Particularly for applications in bioseparation and catalysis, magnetic properties such as superparamagnetism for easily switching on and off the magnetic response, as well as the simple magnetic manipulation by permanent magnets have shown to be highly beneficial.
Superparamagnetism is only present in very small magnetic nanoparticles (< 30 nm for maghemite) [11]. Very small nanoparticles are usually not separable by permanent magnets. The deposition or inclusion of iron oxide nanoparticles into a silica matrix is a promising approach, because a magnetic cluster domain is formed which allows the simple magnetic separation by permanent magnets and retains an overall superparamagnetic nature. Thus, both relevant magnetic properties can be combined in one nanocomposite.
As shown in Figure 2.5 iron oxide-based silica nanocomposites can be subdivided in the most common and widely used iron oxide-core silica-shell nanocomposites or the inverse iron oxide-shell silica-core nanocomposites.
Numerous procedures are available for the synthesis of particles composed of a magnetic core and a silica shell (Figure 2.5a).

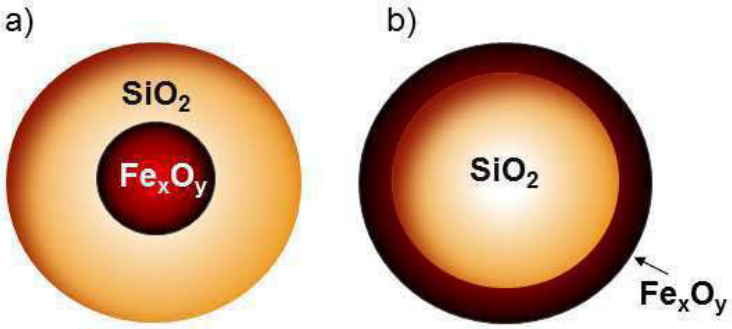

FIGURE 2.5: Distinct morphologies of iron oxide-based silica core-shell nanocomposites. Iron oxides are displayed in red colour and silica in yellow colour.

A typical synthesis approach for the preparation of magnetic-core silica-shell nanocomposites is the aerosol route. Lopez et al. have published a spray-drying route for the preparation of mesoporous maghemite-silica microspheres [20, 21]. Hereby, the initial solution containing all the precursors was evaporated into droplets and a simultaneous micelle formation and silica condensation triggered the self-assembling of microspheres. These aerosol-generated particles were spherical with a size ranging between 100 to 500 nm and a large surface area [20].
Furthermore, silica coated maghemite hollow spheres with tunable magnetic properties were prepared by aerosol pyrolysis of methanol solutions containing iron ammonium citrate and silicon ethoxide [21].
Non-aggregated nanocomposites consisting of a single magnetite nanocrystal core and a mesoporous silica shell with a size of around 45 - 105 nm have successfully been prepared by a sol-gel process. Hereby, cetyltrimethylammonium bromide serves as organic template for the formation of mesopores in the sol-gel reaction [21, 22]. These nanocomposites were successfully applied as magnetic resonance imaging agents in *in vivo* imaging studies and due to their small size allowed a long blood circulation.

Until now, studies on the synthesis of the inverse nanocomposite architecture - a silica core with a magnetic iron oxide shell - are rare (Figure 2.5b).
A short overview of current synthesis approaches for their preparation as well as their characteristics is shown in Table 2.2.
One example is the modification of the surface of both metal and silica nanoparticles with suitable functional groups, which enables iron oxide nanoparticles to be attached to the silica core surface via covalent linkage chemistry [19, 23].

Raspberry-like superparamagnetic nanocomposites were prepared by covalently linking silica core nanoparticles to monodisperse superparamagnetic iron oxide nanoparticles using epoxy-amine coupling chemistry [23].
Griffete et al. have demonstrated that the reaction of amino modified silica particles with tert-butylnitrite provides a diazonium surface functionality, which covalently attaches iron oxide nanoparticles on the silica surface in basic conditions [19].

Another approach is the adsorption of magnetic nanoparticles on the silica surface. Since in this case the nanoparticles are not covalently linked to the silica core, a dense silica or gold layer is often used to enclose them [24, 25]. This coating is essential to retain their physical integrity and resistance to heat or pH changes [26] .
For example, Stoeva et al. have prepared a three-layer nanocomposite consisting of a silica core, magnetic inner layer and a gold surface [25]. Positively charged amino-modified SiO_2 particles were used as templates for the electrostatic assembly of negatively charged superparamagnetic magnetite nanoparticles (diameter (d): 1 nm). In the next step the SiO_2-Fe_3O_4 particles electrostatically attract small gold nanoparticle seeds, which act as nucleation sites for the formation of a continuous gold shell around the SiO_2-Fe_3O_4 particles via upon $HAuCl_4$ reduction.
In a second approach heterocoagulation between positively charged magnetic nanoparticles and negatively charged silica particles were used to prepare nanocomposites with high monodispersity. The nanocomposites were functionalized with sodium silicate and a subsequent fluorescent polymer shell was introduced [24].

Several studies revealed the common problem of inhomogeneous surface coverage of silica spheres with nanoparticles [26–28] .
However, the major drawback of all these mentioned strategies is that magnetic nanoparticles are generally pre-synthesized and then immobilized onto the silica nanomaterial, which involves multiple complex and time-consuming synthesis strategies. Few reports have recently been published about the *in situ* fabrication of magnetic nanoparticles and simultaneous deposition onto silica spheres.
An example for the *in situ* fabrication is the synthesis of maghemite/silica microspheres by formation of monodispersed organic/inorganic hybrid microspheres by urea-formaldehyde polymerization and a subsequent removal of the organic template by calcination at elevated temperatures [29]. The total synthesis approach is rather time-consuming (> 30 hours).

Moreover, spherical iron/silica nanocomposites were *in situ* first synthesized by hydrolysis of iron(III) acetylacetonate solutions containing the silica cores and sodium dodecylsulfate. Subsequently, the core-shell particles were thermally reduced under hydrogen atmosphere to produce magnetic nanocomposites [30]. This multistep synthesis takes around 27 hours [30].
In summary, both synthetic approaches yet lack in shortness of synthesis time and operation steps. Thus, it is still a challenge to develop a rapid, reliable and simple protocol for the fabrication of silica-core/iron oxide-shell nanocomposites, which decreases reaction costs and simplifies the synthesis steps.

TABLE 2.2: Overview of various iron oxide-shell silica-core nanocomposites in literature. The nanocomposite size is displayed as diameter (d) and the magnetic saturation value as M_S.

Composition	Synthesis route	Characteristics	Application
Raspberry-shaped (Fe_3O_4-SiO_2) [23]	Covalent linkage chemistry, epoxy-amine	d: 200 nm, M_S: 2.1 emu g^{-1}	-
Spherical (Fe_3O_4-SiO_2) [30]	Hydrolysis of iron(III) acetylacetonate thermal reduction, *in situ*	d: 600nm, M_S: 2 - 4.2 emu g^{-1}	-
Three-layer, spherical (Fe_3O_4-SiO_2-Au) [25]	Electrostatic adsorption	d: 200 nm	Probes for DNA
Mesoporous microspheres (γ-Fe_2O_3-SiO_2) [29]	Polymerization of urea-formaldehyde calcination	d: 1.72 µm, M_S: 17.2 emu g^{-1},	Magnetic separation of DNA
Fe_3O_4-SiO_2-core, fluorescent polymer shell (pyrene) [24]	Heterocoagulation, electrostatic interaction	d: 583 nm, M_S: 1.26 emu g^{-1}	-
Spherical γ-Fe_2O_3-Au-SiO_2 [31]	Polymer template synthesis, calcination	d: 4.4 µm, M_S: 8 emu g^{-1}	Magnetic recoverable catalysts
Dye doped Fe_3O_4-SiO_2 [32]	Covalent linkage chemistry, adsorption	d: 70 - 130 nm,	Contrast agent in magnetic resonance imaging, fluorescence imaging, drug delivery
Spherical Fe_3O_4-SiO_2 [19]	Covalent linkage chemistry (diazonium salt)	d: 300 nm	-
Raspberry-shaped dye doped or quantum dots doped (Fe_3O_4-SiO_2) [33]	High temperature treatment $Fe(acac)_3$ in polyalcohol, *in situ*	d: 50-900 nm	*In vivo* magnetic resonange imaging, fluorescence imaging

2.3 Surface functionalization of iron oxide nanoparticles

The intrinsic instability of iron oxide nanoparticles over long time periods results in a loss of their dispersibility. Firstly, the small nanoparticles tend to aggregate into larger particle clusters in order to reduce surface energy. Secondly, due to their high surface area and chemical activity bare iron oxide nanoparticles tend to be oxidized easily in air resulting in a loss of their magnetism [34, 35].
Hence, it is essential to form a protective layer around the nanoparticle surface, which increases their colloidal and chemical stability as well as improves their biocompatibility. Depending on the method of preparation e.g. thermal decomposition iron oxide nanoparticles are due to their capping with nonpolar end groups (e.g. oleic acid) initially hydrophobic and therefore not water dispersible. Water dispersibility is crucial for biochemical and biomedical applications. The introduction of functional hydrophilic groups onto the particle surface by specific functionalization further enlarges their possible use from nonpolar to aqueous environments and also provides anchorage for the covalent binding of specific ligands (e.g. drugs, proteins, DNA, antibodies) for their application.
In the following section, various strategies for the surface functionalization of iron oxide nanoparticles by organic and inorganic materials are presented.

2.3.1 Organic materials

Small molecules and surfactants

Silane chemistry is a common and widely used functionalization approach, due to the covalent bond formation, which results in robust and more versatile nanoparticles. The silane agents offer additional advantages such as improved biocompatibility, chemical stability as well as high density of surface functional end groups.
The silane compounds, which contain alkoxygroups, are hydrolyzed in the presence of water. Active silanol molecules are formed. The silanol molecules subsequently react with the OH-groups on the surface of the iron oxide nanoparticle by condensation. A stable Fe-O-Si bond is generated. Following polycondensation leads to a silane network on the surface of nanoparticles [35]. After the functionalization the terminal functional groups of the alkoxysilanes are available for immobilization of specific ligands (e.g. antibodies, proteins, DNA). The reaction mechanism is shown in Figure 2.6.

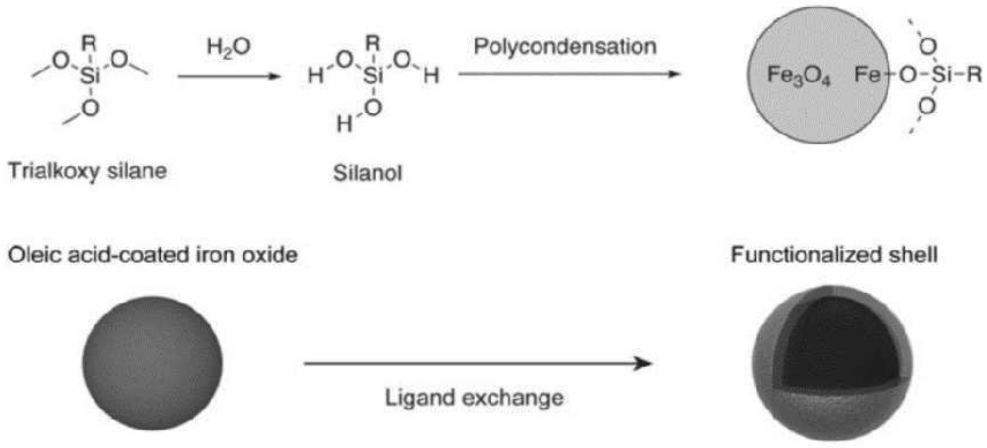

FIGURE 2.6: Reaction mechanism for the condensation of alkoxysilanes on the surface of iron oxide nanoparticles [35].

Currently, numerous alkoxysilanes are available which enable the introduction of a broad variety of terminal functional groups onto the surface of the nanoparticles (e.g. -COOH, -NH_2, -SH, -CHO, -C_2H_4O). The functional terminal groups of the alkoxysilanes can be further modified by the attachment of a variety of bioactive molecules.
The alkoxysilanes 3-aminopropyltriethyloxysilane (APTES), p-aminophenyl trimethoxysilane (APTS), mercaptopropyltriethoxysilane (MPTES) and (3-glycidyloxypropyl)trimethoxysilane (GOPTS) are usually applied for introducing amino, sulfhydryl and epoxy groups, respectively.
The so-called ligand exchange is a well known approach for noble metal nanoparticles, which is widely used for the functionalization via silane chemistry. An excess of the ligand is added to the nanoparticle dispersion resulting in the replacement of the original ligand on the nanoparticle surface. For example, the self-assembly of thiol groups strongly attached to the nanoparticle surface have widely been used for the functionalization of metal nanoparticles [34].
De Palma et al. have developed a ligand exchange method by using hexane as solvent and acetic acid as catalyst to form the reactive silanol molecules [36]. In another study, the solvent toluene, the catalyst water were applied and the base triethylamine was added to generate the reactive silanol groups on the nanoparticle surface [37].
Nevertheless, a serious drawback of those ligand exchange methods is the extensive reaction time of 24 to 72 hours. To overcome this, Bloemen et al. have developed a rapid and simple ligand exchange method by using ultrasonication as an energy source to dramatically accelerate this process. Consequently, water dispersible organosilane functionalized nanoparticles around 10 nm were generated in around five hours [35].

Another approach is to directly add small organic molecules such as citric acid, vitamins, cyclodextrins or aminoacids during the synthesis procedure. For instance, Xia et al. have published a simple method for the preparation of water dispersible magnetite nanoparticles by application of polyethylene glycol nonylphenylether and cyclodextrin in aqueous conditions [38]. In contrast to the silane chemistry, small organic molecules are not covalently bound to the nanoparticle surface which often results in a lack of stability in acidic or basic conditions and therefore an increased agglomeration tendency.

Polymers

Polymer coatings are of increasing interest, since they not only provide multifunctional groups and colloid stability, but also have a positive effect on pharmacokinetics and biodistribution [5]. They can be divided in natural polymers (e.g. dextran, starch, gelatin, chitosan) or synthetic polymers (alginate, poly(ethyleneglycol), poly (vinylalcohol), poly(lactide acid)).
There are several approaches to surround the iron oxide nanoparticles with a hydrophilic polymeric shell including *in situ* and post-synthesis functionalization. In *in situ* approaches, the common routes are sol-gel process and microemulsion polymerization. For instance, Gupta et al. have demonstrated an *in situ* microemulsion polymerization method for the preparation of poly-(ethyleneglycol)-functionalized iron oxide nanoparticles [14]. Nevertheless, this direct method often results in colloidal instability as well as an uncontrollable polymer shell thickness [5].
Consequently, the prevalent synthesis strategy for creating a polymeric shell is post synthesis functionalization. Hereby, the physical adsorption and functional groups anchoring on the surface of iron oxide nanoparticles are the common mechanisms [5]. Furthermore, heterogeneous polymerization (e.g. inverse mini/emulsion polymerization) is also a promising functionalization strategy. A severe drawback is the fact that polymeric shells or copolymer layers may decrease the M_S of the iron oxide nanoparticles.

2.3.2 Inorganic materials

Inorganic materials may offer a variety of unique properties such as high electron density and optical absorption (e.g. gold and silver nanoparticles), fluorescence in form of semiconductor quantum dots (e.g. CdSe or CdTe), phosphorescence (e.g. doped oxide materials: Y_2O_3) and magnetic moments such as manganese or cobalt oxide nanoparticles. Therefore, they can be used for the improvement for semiconductor efficiency, information storage, optoelectronics, catalysis, and optical bioimaging [5].

Another simple approach for protecting nanoparticles is to form a pure single-metal or nonmetal shell (e.g. gold, silver, platinum, palladium, iron, carbon etc.). Whereas gold, silver and carbon functionalization will decrease the saturation magnetization of the nanoparticles, coatings such as cobalt, platinum, copper and palladium have the opposite effect. Metal functionalized

nanoparticles can be prepared by direct reduction of the single-metal ions on the surface of the iron oxide nanoparticles. For example, widely used gold-modified magnetite nanoparticles were prepared by sonolysis of a mixture containing gold ions and amino-coated magnetite nanoparticles in the presence of reducing agent [34]. Furthermore, metal oxides or sulfides are widely used to functionalize iron oxide nanoparticles (e.g. ZnO,TiO_2, SnO_2, CdS, ZnS, PbS). A magnetic material such as Co_3O_4, NiO, Mn_xO_y coated on iron oxide nanoparticles will form a nanocomposite consisting of two magnetic components with advanced magnetic characteristics [5].

2.3.3 Conjugation of antibodies to iron oxide nanoparticles

Numerous biological molecules such as proteins, antibodies, polypeptides, biotin and avidin can be immobilized to the surface of iron oxide nanoparticles by non-covalent or covalent coupling chemistry via functional end groups. These functionalized nanoparticles can be applied e.g. in a specific magnetic separation approach of proteins, DNA, cells or biochemical products.
In this thesis, the iron oxide-based nanocomposites are conjugated to monoclonal antibodies. Therefore, the different coupling strategies for antibodies to iron oxide nanoparticles are highlighted.

Antibody structure and modification sites

In order to choose the best method for conjugation, it is essential to understand the functional groups available on the antibody. In general, common antibody conjugation strategies employ one of these three target groups [39]:

Primary amines (–NH_2): occur primarily on lysine residues and the N-terminus of each polypeptide chain. They are abundant, easy acessible and widely distributed over the entire antibody.

Sulfhydryl groups (–SH): occur on cysteine residues and exist as disulfide bonds which stabilize the whole-molecule structure. Hinge-region disulfides can be selectively reduced to make free sulfhydryls available for further surface modification.

Carboxyls (–COOH): occur at the C-terminus of each polypeptide chain and in the side chains of aspartic acid and glutamic acid. Carboxyls are usually presented on the surface

Carbohydrates (sugars): glycosylation occurs primarily in the F_c region of antibodies. Sugars in the polysaccharide moieties that contain cis-diols can be oxidized to create active aldehydes (–CHO) for modification.

Functionalization chemistry

1. Peptidic bonds

The most common approach for the conjugation of antibodies is the formation of peptidic bonds. This reaction is versatile, since antibodies contain both primary amine groups and terminal carboxylic acids. The typical nanoparticle ligands also display these functional groups (e.g. APTES, citric acid) or can be easily modified such as amino-dextran or carboxy-dextran [40]. The covalent coupling of an amine group to a carboxylic acid forming an amide is carried out in aqueous environments at acidic conditions (pH 4 - 5).

In principle, the carboxylic group has to be activated using a water soluble carbodiimide such as 1-ethyl-3-(3-dimethylaminopropyl)carbodiimide hydrochloride), EDC. EDC is a zero-length crosslinker, which causes direct conjugation of carboxylates (–COOH) to primary amines ($–NH_2$) without becoming part of the final amide-bond crosslinkage between target molecules. EDC reacts with the carboxylic acid group to form an active o-acylisourea active intermediate. The intermediate directly reacts with the amine group in a nucleophilic reaction to form an amide bond. The EDC by-product is released as soluble urea derivative. It has to be noted, that the active o-acylisourea active intermediate is unstable in aqueous conditions resulting in its rapid hydrolysis. The reaction scheme is displayed in Figure 2.7.
N-hydroxysuccinimide ester (NHS) or the water-soluble sulfo-NHS are usually added in EDC coupling reactions to stabilize the o-acylisourea active intermediate. Hereby, EDC couples NHS to carboxylic acids and form a more stable NHS ester [41].
Nevertheless, an important drawback of EDC-chemistry is the random polymerization, since peptide and proteins basically contain numerous carboxyls and amines on their surface. In order to overcome this problem, heterobifunctional crosslinkers are typically applied.

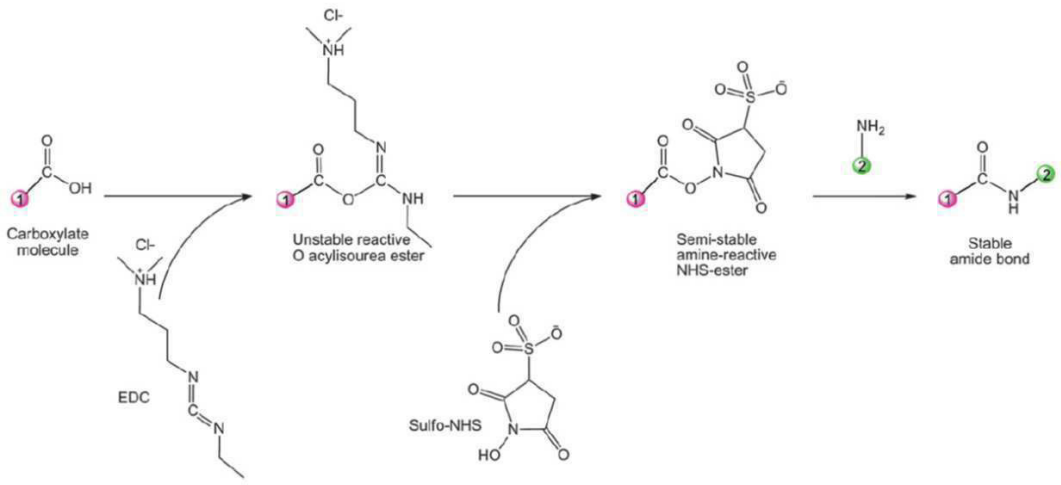

FIGURE 2.7: Reaction scheme of EDC–NHS chemistry [41].

2. Thiol chemistry

Since thiol groups are abundant in proteins but less numerous than primary amines, they are attractive targets for protein conjugation resulting in a more selective and precise crosslinking. Thiol groups also called sulfhydryl groups (-SH) exist either as single groups in the side chains of cysteine or in form of disulfide bonds (-S-S-).
The disulfide bonds connect both heavy and light chains and the antibody halves at the hinge region, and are therefore participating in the tertiary structure of each subunit. Additionally, free sulfhydryl groups can be easily introduced via reaction with primary amines using sulfhydryl-addition agents such as e.g. 2-iminothiolane (Traut's Reagent).

Sulfhydryls are reactive towards e.g. maleimides, haloacetyls and pyridyl disulfides, whereas maleimides are the most common ones.
Maleimides react with thiol groups in the pH range of 6.5 to 7.5, forming a stable, irreversible thioether linkage. The reaction scheme is shown in Figure 2.8.
However, the disulfide bonds have to be reduced to free sulfhydryls to make them available for crosslinking with thiol-reactive compounds. In general, some of the native disulfide bonds are cleaved with reducing agents. Since disulfides in the hinge region are most susceptible to reduction, it is possible to selectively cleave only these disulfides and consequently to split the antibody into monovalent halves without damaging the structure and antigen-binding sites [39].

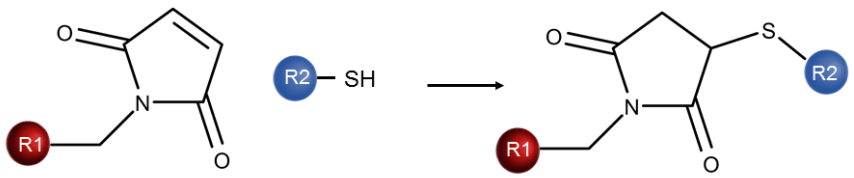

FIGURE 2.8: Maleimide reaction scheme for chemical conjugation to a sulfhydryl, adapted with modification from [41].

Another approach is haloacetyl crosslinker which contains an iodoacetyl or a bromoacetyl group. Haloacetyls react with sulfhydryl groups at physiologic to alkaline conditions (pH 7.2 - 9), resulting in stable thioether linkages. In contrast, pyridyl disulfides react with sulfhydryl groups over a broad pH range to form disulfide bonds. During this reaction, a disulfide exchange occurs between the molecule's –SH group and the reagent's 2-pyridyldithiol group [40].

3. Carbohydrates

An attractive target for the conjugation of antibodies to nanoparticle is carbohydrate moieties. Aldehydes are not existing naturally in proteins but can be created wherever oxidizable sugar groups also called reducing sugars exist. First, the carbohydrates have to be oxidized to create reactive aldehydes. Periodic acid is a common mild agent for effectively oxidizing vicinal diols in carbohydrate sugars in order to form reactive aldehyde groups [39].
Aldehydes (RCHO) contain the reactive carbonyl-oxygen double bond (C=O), which makes the carbon atom electrophilic and therefore reactive to the nucleophile amine. Aldehyde-activated (oxidized) sugars can be reacted directly to secondary amines through reductive amination or to reagents that have been activated with hydrazide groups.
The reaction scheme of the reductive amination can be seen in Figure 2.9. The Schiff base (Figure 2.9) formed with ordinary amines rapidly hydrolyzes in aqueous conditions and has to be be reduced to a secondary amine linkage for stabilization. A mild reducing agent is sodium cyanoborohydride ($NaCNBH_3$) .

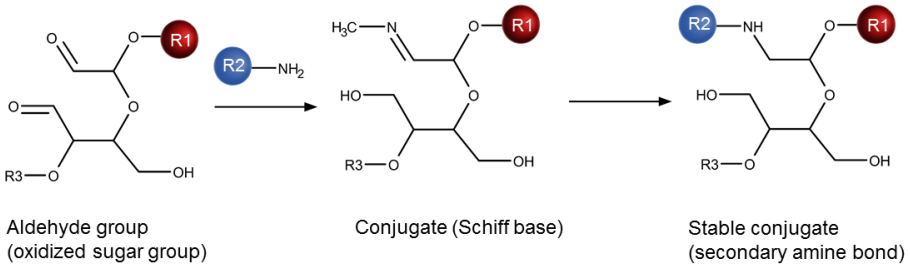

FIGURE 2.9: Reaction scheme of the reductive amination of aldehydes with primary amines.

4. Click chemistry

Another popular bioconjugation approach is click chemistry. The main advantage of click chemistry is its bioorthogonality. The reaction is highly specific and none of the two reactive groups can react with any functional groups in biological systems, which provides high selectivity in complex biological media [40]. In a typical click reaction, an azide group reacts rapidly and highly specific with an alkyne to form a [3+2] cycloaddition product. The reaction mechanism is displayed in Figure 2.10.
Azide or alkyne groups are not naturally present in biomolecules and have to be therefore introduced by application of alkyne-NHS-ester or azide-NHS-ester.

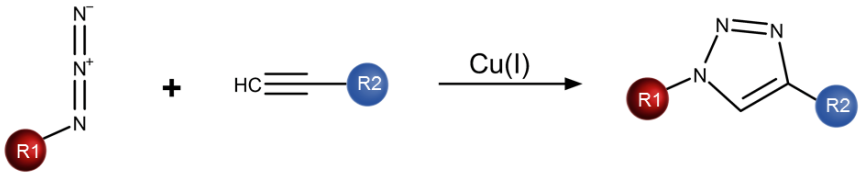

FIGURE 2.10: Reaction scheme of copper-catalyzed azide-alkyne cycloaddition, adapted and modified from [42].

5. Biological interactions

Another widely used but very expensive approach is bio-activated nanoparticle surfaces such as streptavidin, biotin or protein A/G. In contrast to surface functional groups which covalently bind the antibodies, biological interactions bind the antibody in a non-covalent manner. One important example is the biological interaction between biotin and avidin/streptavidin. Hereby, a biotinylated antibody binds its interaction partner avidin or streptavidin with high affinity on the nanoparticle surface (Figure 2.11). Protein A and protein G, for instance, are small proteins originally derived from bacteria, which bind with high affinity and specifity to constant fractions of immunoglobulin G (IgG) antibodies [39].

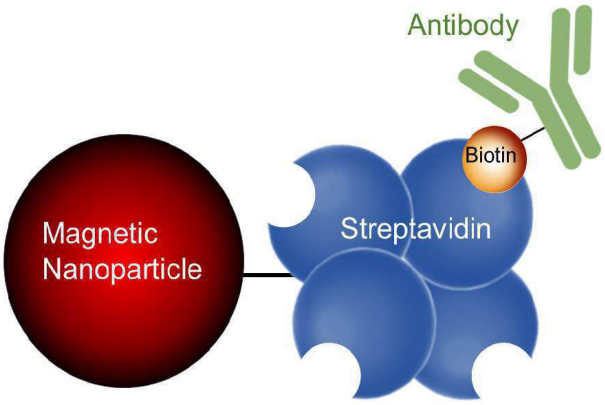

FIGURE 2.11: Schematic illustration of the biological interaction between streptavidin and a biotinylated antibody.

6. Epoxy chemistry

A very promising approach for the conjugation of antibodies to nanoparticles is epoxy chemistry, which was successfully applied in this PhD thesis for the conjugation of biotinylated anti-SEB antibodies onto the nanoparticle surface. The hydrophilic iron oxide-shell silica-core nanocomposites are functionalized by organosilane chemistry with reactive surface epoxy groups.
Surface epoxy groups allow direct covalent binding of antibodies via amine or thiol groups depending on the pH in solution. A slightly basic pH favours the binding to thiol groups. At higher pH conditions, the epoxy group will bind to amino groups. The latter was used for the bioconjugation step in this thesis.
Generally, the epoxide group reacts with the primary amine nucleophiles on the antibody in a ring-opening process at a moderate alkaline buffer environment (pH 9.3). During the coupling process, ring opening forms a β-hydroxy group on the epoxy compound, covalently binding the biotinylated detection antibody to the nanocomposite surface [39]. The synthesis scheme of the antibody-conjugation to the nanocomposites is shown in Figure 2.12. The antibody-functionalized magnetic nanocomposites were subsequently incubated in BSA to block unspecific binding sites.

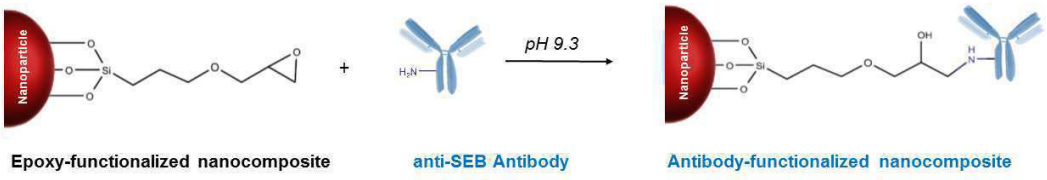

FIGURE 2.12: Schematic scheme for the antibody-functionalization to epoxysilane-coated iron oxide-shell silica-core nanocomposites.

2.4 Analytical characterization of magnetic nanoparticles

Besides to the controlled synthesis of nanoparticles and nanocomposites, another important aspect is their detailed analytical characterization. Hereby, characterization techniques can be classified in analytical methods for the characterization of their magnetic properties, size and morphology as well as the detailed analysis of the nanoparticle core material and surface.

2.4.1 Characterization of size and morphology

Both, core size and the size distribution have a crucial influence on the characteristics of any nanomaterial. Hence, reliable methods to determine these parameters are essential.

2.4.2 Electron microscopy

Transmission electron microscopy (TEM)

TEM is a powerful analytical tool for providing detailed information about size and shape of nanoparticles. The detailed structure of a magnetic nanoparticle can be analyzed to the atomic level.
In principle, TEM is a microscopy technique, in which a beam of accelerated electrons is transmitted through an ultra thin specimen and interacts with the specimen as it passes through it. Consequently, an image is formed from the interaction of the electrons transmitted through the specimen. This image is subsequently magnified and can be detected by a sensor such as a CCD camera or focused onto an imaging device (e.g. fluorescent screen, photographic film).
TEM applies the same basic principles as the light microscope but uses electrons instead of light. The achieveable resolution for TEM images is many orders of magnitude better compared to a conventional light microscope. The resolution of a modern TEM is about 0.2 nm, which is approximately 1000 times higher than of a standard light microscope.
A TEM is composed of several components including a vacuum system in which the electrons travel, an electron emission source for generation of the electron stream, electromagnetic lenses, as well as electrostatic plates (Figure 2.13). The source of electrons (cathode) is typically a heated tungsten filament or a sharply pointed rod of lanthanum hexaboride. The final electrode of the electron gun is the anode, which usually appears in form of a disk with an axial hole. A high energy beam of electrons is produced by the electron gun. This beam of electron is focused into a small, thin, coherent beam by applying electromagnetic lenses. The electron beam then travels through the specimen in the sample holder. After striking the specimen, parts of the electron beam are transmitted. Depending on the density of the material, some electrons are scattered and disappear from the beam. The transmitted

portion is focused by the objective lense into an image of phosphor screen or CCD camera [43, 44].

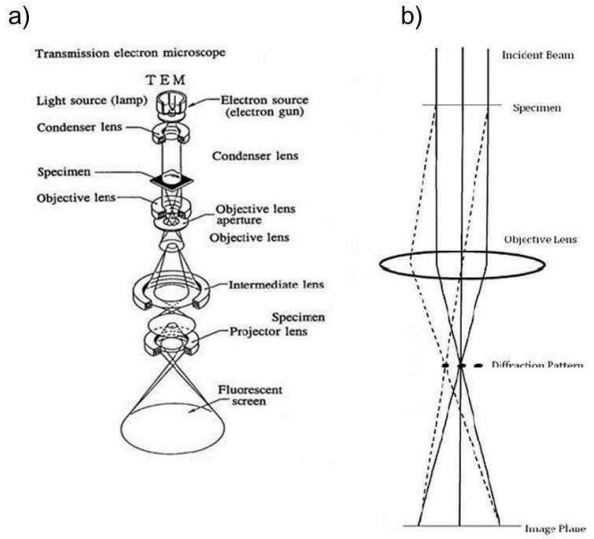

FIGURE 2.13: a) Schematic illustration of the components of a TEM, b) ray diagram for the diffraction mechanism in TEM [44].

Nevertheless, only a small sampling size can be measured by TEM due to the small field of view, which makes it rather difficult to provide a stastical analysis of size and size distribution of a sample [45]. Consequently, the analyzed region may not be representative for the whole sample. The sample preparation for TEM is relatively complex and time-consuming, since the sample is required to be ultra thin for electron transmittance. Another important drawback of TEM is that, the drying process during the sample preparation as well as the electron beam during the measurement may alter the characteristics of the nanoparticles.

Scanning electron microscopy (SEM)

SEM is another electron microscopy technique, desgined for directly analyzing the surface structure. In SEM the surface is scanned in a rectangular raster scan pattern with a focused beam of electrons with relatively low energy (Figure 2.14). The electron source and electromagnetic lenses, which generate and focus the beam are similar to those described for TEM. In contrast to the broad static beam used in TEM, the SEM beam is focused to a fine point and scans over the sample in a raster scan pattern. Since no penetration of the sample is required, the accelerating voltages are lower compared to TEM (5 - 30 kV). Due to the very thin and focused electron beam, SEM micrographs have a large depth of field, which results in a characteristic three-dimensional appearance.
A schematic illustration of the components of a SEM is shown in Figure 2.14. In principle, the electron beam stimulates the emission of high-energy backscattered electrons and low-energy secondary electrons from the surface of the specimen. The backscattered electrons can also result in the emission

of secondary electrons as they pass the sample and exit the sample surface. Whereas secondary electrons are essential to show morphology and topography in a sample, backscattered electrons are relevant for illustration contrasts in compositions e.g. in multiphase sytems such as nanocomposites.
The electron beam also generates X-rays from the sample. These X-rays have energies, which are characteristic for the element that emitted them. By analyzing these X-rays with an energy-dispersive (EDX) analyzer, it is possible to obtain an elemental mapping of the sample surface layer [43, 44]. For a conventional SEM an electrically conductive coating (e.g. gold) is usually applied onto the specimen for analysis in order to overcome charging of the surface by the electron beam. Newer SEM techniques such as Field Emission Scanning Electron Microscopes (FE-SEMs) apply lower-energy electron beams. This avoids the problem of surface charging and, therefore, the application of conductive layer on the specimen is not required [46].
A Field Emission Scanning Electron Microscopy (FE-SEM) allows to obtain information in higher resolution and works in a greater energy range. The most prominent difference between SEM and FE-SEM is the electron generation system. FE-SEM applies a field emission gun which provides focused high and low-energy electron beams and therefore improves spatial resolution. A finely focused electron beam (< 10 nm) is produced by thermionic emission heating also called field emission with an acceleration voltage of approximately 50 - 150 kV [43]. In general, SEM provides a detailed three-dimensional topographical imaging of the sample. SEM is a rather costly and time consuming analytical technique, which provides only limited information about the size distribution and true population average [47]. Morevover, it is limited to solid and small samples, which are able to fit inside the sampling chamber [48].

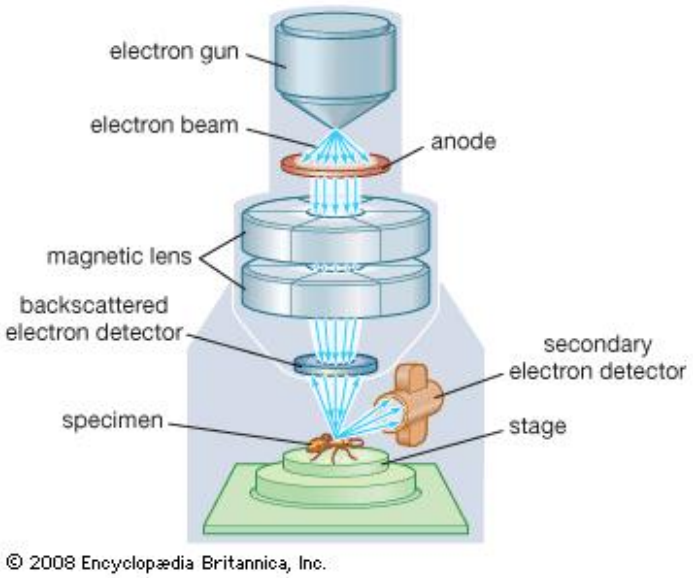

FIGURE 2.14: Schematic illustration of the components of a SEM [46].

2.4.3 Dynamic Light Scattering (DLS)

DLS also known as photon correlation spectroscopy is a viable and useful technique to analyze both the nanoparticle core size and the size distribution. DLS measures the Brownian motion of particles and relates this to their particle size in order to provide information about the size distribution (polydispersity), hydrodynamic diameter d(H), as well as the colloidal stability of the nanoparticle dispersion [49]. Brownian motion is defined as the random movement of particles, which are suspended in a fluid (e.g. liquid, gas), resulting from their collision with moving solvent molecules in the fluid. In general, the smaller the particle, the higher is the Brownian motion.
The principle of a DLS measurument is shown in Figure 2.15. In DLS, the particles in the dispersion are exposed to a light beam. When the light hits a particle, the intensity and the direction of the light beam are altered. Thus, the light scatters in all directions, which is also called Rayleigh scattering. The time-dependent fluctuations in the scattered light intensity are measured by a fast photon detector. This depends on the translational diffusion coefficient of the particle, which undergoes Brownian motion.

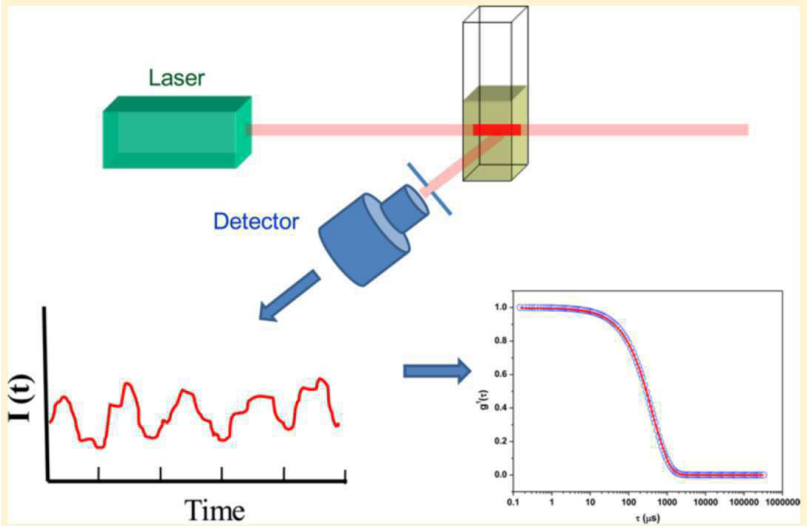

FIGURE 2.15: Schematic illustration of basic work principle of DLS measurements [45].

Small particles rapidly diffuse in the liquid resulting in a high fluctuating intensity signal. Larger particles diffuse more slowly and cause a lower fluctuating intensity signal [50]. For spherical particles, the hydrodynamic diameter of the particle can be calculated from its diffusion coefficient according to the Stokes-Einstein equation Equation 2.3 with D = translational diffusion coefficient, T = temperature, μ = Boltzmann constant and η = viscosity.

$$d(H) = \frac{kT}{3\eta\pi D} \tag{2.3}$$

It is essential to note, that DLS measures the hydrodynamic diameter of a nanoparticle. Since the nanoparticle moves through the liquid, a thin electric

dipole layer also called hydration layer surrounds the particle. This diameter is called hydrodynamic diameter and is typically larger than the core diameter measured by electron microscopy [51–53]. Another important term is polydispersity. The term polydispersity is derived from the polydispersity Index, a parameter calculated from a cumulants analysis of the DLS-measured intensity autocorrelation function. This value is an estimate of the size distribution of the particles in the sample distribution. In general, a polydispersity index value from 0.1 - 0.25 is defined as a narrow size distribution, whereas a polydispersity value > 0.5 is referred to a broad size distribution [45].
Basically, DLS is a simple and less labor intensive analytical tool which only requires a short measuring time of less than a few minutes. The measurements are directly perfomed in the liquid environment of the sample and, therefore, represent a large quantity of particles. Nevertheless, DLS has various sample-specific limitations. For strictly monodisperse nanoparticles, DLS measurements lead to reasonably accurate results. However, this technique is unable to distinguish between nanoparticles with slight differences in diameter or polydisperse samples [54]. This can be attributed to the fact, that DLS measurses the fluctuations in the scattered light intensity, which is proportional to the sixth power of the particle diameter. Additionally, various parameters such as concentration or ionic strength of the analyzed sample can strongly influence the results.

2.4.4 Magnetic characteristics

Superconductingcting Quantum Interference Device (SQUID) Magnetometry is one of the most sensitive analytical methods to analyze magnetic properties, since it allows direct determination of the overall magnetic moment of a sample in absolute units.
A schematic illustration of the SQUID can be seen in Figure 2.16. In a SQUID two parallel Josephson junctions are formed by two superconductors, which are separated by two thin insulating layers. These insulating layers are so thin, that electrons can move across the thin insulating layers. This electron movement is called Josephson tunneling. The flow of current between the superconductors in the absence of an applied voltage is termed Josephson effect [55].
In principle, the sample is located in the center of a superconducting wire, which produces magnetic fields up to 7 Tesla. Hereby, the sample space is filled with helium. To obtain the magnetic signal of the sample, a superconducting pick-up coil with four windings is used. During the measurement the sample is moved up and down and produces an alternating magnetic flux in the pick-up coil. This magnetic flux results in an alternating outpout voltage of the SQUID. This superconducting pick-up coil and the SQUID antenna transfer magnetic flux from the sample to the SQUID. The SQUID is located distantly from the sample in a liquid helium bath. Basically the SQUID acts as magnetic flux-to voltage converter. The voltage is subsequently amplified. Readout is performed by electronics [55].

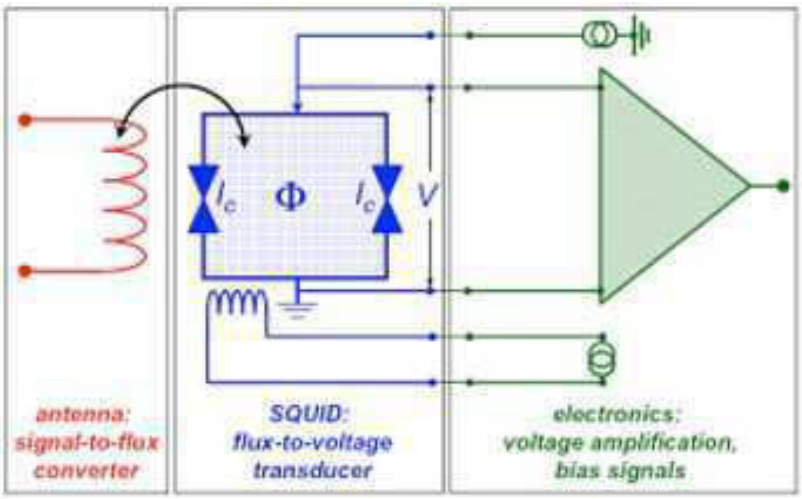

FIGURE 2.16: Schematic illustration of basic work principle of SQUID [55].

In order to analyze the magnetic behaviour of a sample, the magnetization M as a function of the magnetic field H can be measured. Figure 2.17 shows the various magnetic responses for different magnetic materials.
After application of an external magnetic field to superparamagnetic nanoparticles, the magnetic moments in particles align towards the applied magnetic field. In absence of a magnetic field, thermal fluctuations outcompete the dipole-dipole interactions in particles, a random flip of the magnetization is induced. The nanoparticles do not show any remanent magnetization (M_r) at

zero field [11]. Hence, for superparamagnetic particles the magnetization as a function of the applied magnetic field is a reversible sigmoidal (S-shaped) curve at RT [12]. No hysteresis can be seen.
In contrast to the S-shaped curve in the case of superparamagnetic nanoparticles (green loop), ferromagnetic nanoparticles (red loop) show hysteresis. After removal of the external magnetic field, ferromagnetic nanoparticles still exhibit remanent magnetization. The magnetic response of both paramagnetic (blue line) and diamagnetic (black line) nanoparticles is also displayed in the schematic illustration.

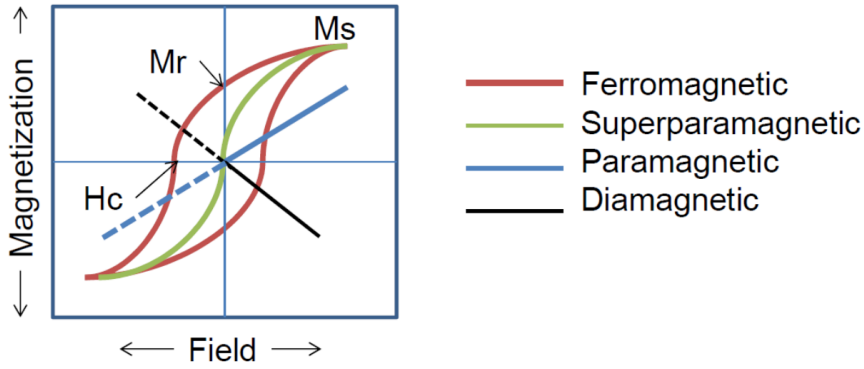

FIGURE 2.17: M(H) curves illustrating M(H) curves for superparmagnetic, diamagnetic, paramagnetic and ferromagnetic materials. The X-axis displays the applied field, and the Y-axis shows the magnetization of the sample as a function of field exposure [56].

2.4.5 Characterization of chemical compositon of nanoparticle core

Raman microspectroscopy (RM)

Raman spectroscopy is together with infared spectroscopy (IR) one of the main vibrational spectroscopy methods. Raman spectroscopy combined with optical microscopy allows an identification and chemical analysis of different substances through characteristic vibrational spectra with a spatial resolution in the µm-range.

After irradation of a sample with monochromatic light, typically in the near infrared or near ultraviolet range, several effects can be observed. Light passes interference-free through the sample (transmission) or is reflected. Part of the light is scattered in all spatial directions with the same frequency as the initial light. This is called elastic scattering or Rayleigh scattering. A small amount of light is scattered in all spatial directions with different frequencies than the initial light. This phenomen is called inelastic scattering or Raman scattering. The difference between the frequencies of the inital and emitted light equals the frequency of the associated vibration (Raman shift). Additionally, the inelastic scattered light can be divided in Stokes and anti-Stokes scattering. In Stokes scattering the energy of the initial light is higher than the energy of the scattered light. In anti-Stokes scattering the opposite effect occurs. If the molecule is in the ground state, Stokes scattering occurs. For anti-Stokes scattering the molecular state of the molecule is an excited vibrational state. Since more electrons are in the ground state, the intensity of the Stokes band is higher than the intensity of anti-Stokes bands [57]. An energy-level diagram, which shows the types of excitation in a Raman spectrum is shown in Figure 2.18.
In principle, a beam of photons, typically with wavelenghts in the visible region, from a pulsed laser is directed through a plasma line filter in order to remove the background. The photons are scattered by molecules in the sample. Raman scattering enters the objective in the reversed direction. By applying an edge filter, Raleigh scattering and anti-Stokes scattering can be filtered. By applying a notch filter, which only filters Rayleigh scattering, Stokes and anti-Stokes scattering can be observed. The single wavelengths are isolated by applying a monochromator and detected with a CCD camera. This results in a spectrum showing the energy losses. These energy losses are characteristic of the molecule with which the photon interacts.

Since vibrational levels of a sample are highly dependent upon the molecular environment, different compounds of the same element show a completely different pattern of signals. Raman spectra are therefore fingerprint spectra, which are highly characterstic for each substance. Additionally RM is a non-destructive spectroscopic method, which only requires very low sample preparation. Since water is only a weak Raman scatterer, RM allows the analysis of wet samples as well as biological samples. Nevertheless, RM also

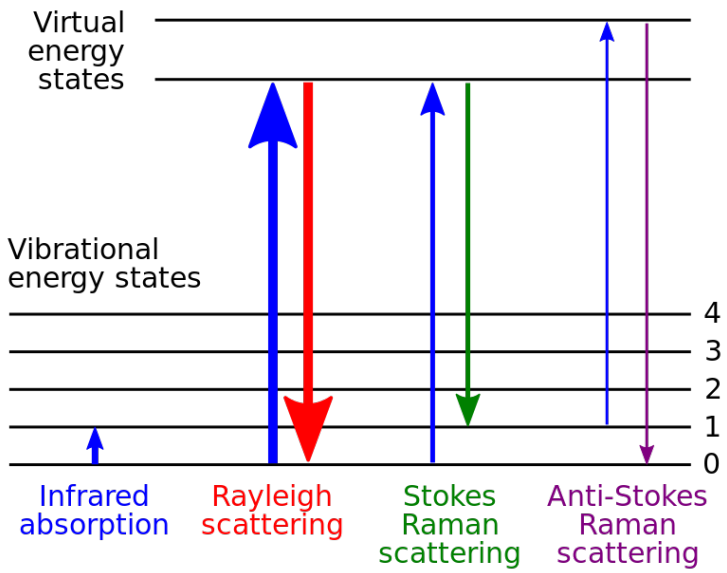

FIGURE 2.18: Energy-level diagram illustrating the various types of excitation in Raman spectra. [57].

exhibit several problems. For Raman spectroscopy only a very weak signal is measured, which requires the application of powerful lasers, filters for Raleigh scattering and sensitive detectors. The excitation by applying a laser may possibly destroy the sample. Thus, laser power is often reduced to overcome this problem. The major drawback of RM is the existence of fluorescence, which can overlap with the Raman lines. Therefore, a laser with higher intensity or photobleaching can be used in order to reduce the fluorescence.

RM is a reliable tool for the analysis of magnetic nanoparticles and the monitoring of their stability, since it allows not only a specific determination of the chemical composition of the nanoparticles, but also the characterization of the crystalline and amorphous structure of iron oxides [58]. RM has already been successfully applied for analysis of different magnetic nanoparticles [59, 60] and various iron oxides [58, 59, 61, 62]. It is a very sensitive and reliable analytical technique to differentiate between the two iron oxides maghemite and magnetite [52, 63].

Mössbauer spectroscopy

Detailed information about the physical, chemical and magnetic properties of nanoparticles can be obtained by Mössbauer spectroscopy. Mössbauer spectroscopy relies on the so called Mössbauer effect. The Mössbauer effect can be described as the recoil-free, resonant absorption and emission of gamma rays of nuclei in atoms, when undergoing varieties of energy level transitions. These changes in the energy levels provide information about the local environment of the atom. These energy levels can be splitted or changed due to the different electric and magnetic environment of the nuclei.

The gamma rays are passing through an absorber containing the resonant isotope and are detected eventually by a proportional counter. Iron is the main nucleus examined by Mössbauer spectroscopy. In nature, iron exists in three valence states: Fe^0, $Fe^{2+}$and Fe^{3+}, as well as in different types of coordination (e.g. tetrahedral, octahedral). Mössbauer spectroscopy is very sensitive to different iron oxides and iron oxide-hydroxides and allows a reliable differentiation between the iron oxides maghemite and magnetite.
In order to detect the different types of iron oxides by Mössbauer spectroscopy a ^{57}Co source is applied which decays to an unstable ^{57}Fe. ^{57}Fe subsequently releases gamma rays. These gamma rays are absorbed by other iron nuclei, if those are present in a crystal lattice of the identical surrounding environment. In case that the emitting and absorbing nuclei are the same, the transition energies and resonance are identical. This effect is isotope specific. Iron nuclei in different environments show resonance when the energy of the emitted gamma ray is slightly varied. Therefore, the source is moved in an oscillating manner in order to record the spectrum in velocity steps. Any difference in the s-electron environment between the source and absorber results in a shift in the resonance energy of the transition. This appears in the Mössbauer spectrum as a chemical shift from zero velocity in a positive or negative manner [64]. Thus, Mössbauer spectroscopy detects slight changes in the energy levels of an atomic nucelus, which depends on its surrounding environment.
In general, there are three types of nuclear interactions: 1) isomer shifts (chemical shifts), 2) quadrupole splitting and 3) magnetic hyperfine splitting. The combination of isomer shift, quadrupole splitting and magnetic hyperfine splitting is typically sufficient to distinguish between iron oxides and iron hydroxides.

The gamma rays detected per second are plotted as a function of the velocity, which results in the typical Mössbauer absorption spectrum. As mentioned above, Mössbauer spectroscopy is very sensitive to different iron oxides and iron oxidehydroxides and allows a distinction between Fe(II) and Fe(III) [52, 63].
In the spinel structure of magnetite (Fe_3O_4) the octahedral sites are occupied by one Fe(II) and one Fe(III), the tetrahedral sites are occupied by one Fe(III). Due to the different isomer shifts of Fe(II) and Fe(III) in the spinel structure of magnetite, the Mössbauer spectrum of magnetite shows two discrete sextets of its magnetic hyperfine splitting. The sextets are slightly shifted from each other [63]. The presence of Fe(II) can be clearly confirmed by a small shoulder peak in one sextet.
In maghemite, only one sextet of its magnetic hyperfine splitting is expected. Additionally, the absence of the Fe(II) peak is prominent [52].

2.4.6 Characterization of nanoparticle surface

Fourier-transform infrared spectroscopy (FT-IR)

FT-IR can be applied to analyze surface characteristics of magnetic nanocomposites due to the vibration and rotation of the molecules under the influence of infrared light [65].
Besides to RM, FT-IR is one of the main vibrational spectroscopy methods. The basic principle of FT-IR is, that molecules absorb light in the infrared region of the electromagnetic spectrum. This absorption, resulting from vibrational frequencies of chemical bonds, corresponds specifically to the bonds, which are present in the molecule. A typical measured frequency ranges from 4000 to 600 cm^{-1}.
In principle, a conventional infrared spectrometer contains a light source (e.g. Nernst lamp, glow bar), which generates continuous electromagnetic radiation. The polychromatic radiation is subsequently separated into two light beams of the same intensity. One light beam passes the sample, whereas the second light beam is the reference beam. The monochromator decomposes the radiation to frequencies. The detector subsequently registers the optical signals and converts them into electric signals. After amplification of the electric signal, a spectrum is generated.
In an IR-spectrum the transmittance (%) is plotted against the wavenumber (cm^{-1}). Since different chemical structures produce different spectral fingerprints, the resulting signal at the detector is a spectrum showing a molecular fingerprint of the sample.
The transmittance T is calculated by the ratio of the intensity of the transmitted light I and the intensity of the inserted light I_0:

$$T = \frac{I}{I_0} \tag{2.4}$$

FT-IR is an advanced technology of the IR. Hereby, the spectrum is not generated by directly measuring the absorbance.
Infrared light from the light source passes through a Michelson interferometer. The basic Milchelson interferometer consists of broad-band light source which emits light in the mid-IR range, a beam splitter and two mirrors (fixed, moving). The light, produced by the light source, is directed to the beam splitter and ideally 50 % of the light is reflected towards the fixed mirror and 50 % of the light is transmitted towards the moving mirror. The moving mirror is typically moving a very short distance away from the beam splitter. Then, light is reflected from the two mirrors back to the beam splitter. The two beams are eventually recombined by the beam splitter. Parts of the initial light pass the sample compartiment. Whereas one beam travels a fixed path length, the other is constantly changing due to the moving mirror. Thus, the two beams at the detector have an optical path difference.

In the Michelson interferometer, the two light beams are recombined and interfere with each other. The intensity of the interference is then recorded in an interferogram. The interferogram can be converted to a spectrum by Fourier transformation. Generally, all frequencies are measured simultaneously, which results in very rapid measurements.

Zetapotential

Another important analytical method to analyze the surface coating of magnetic nanoparticles is the analysis of the zeta potential. The stability of a nanoparticle dispersion in aqueous media can be expressed by zeta potential.
The zeta potential describes the electric potential between the inter-facial double layer of ions surrounding a dispersed particle and the bulk dispersion. Basically, nanoparticles usually exhibit a surface charge in dispersion. When an electric field is applied, nanoparticles are moving in the liquid due to their interaction between the charged particle and the applied field. This phenomen is called electrophoresis. The zeta potential of nanoparticles can be determined by measuring the velocity of their movement towards an electrode. The velocity of this motion is directly proportional to the electrical potential of the particle at the shear plane, also called the zeta potential. The velocity of the particles can be measured by detecting the Doppler shift in the scattered light.
The value of the zeta potential is related to the stability of a colloidal nanoparticle dispersion. If the absolute value is higher than 20 - 25 mV, the nanoparticles are usually electrostatically stable [35]. A value close to zero usually results in a fast aggregation or even precipitation of the nanoparticles [45].

2.5 Bacterial pathogens and toxins in foodborne illness

Foodborne illness is defined as disease of infectious or toxic nature caused by consumption of contaminated food or water. Diseases caused by foodborne pathogens have become a major threat to public health, which affect, according to the World Health Organization (WHO), approximately 600 millions, and causes 420,000 deaths each year. They are classified in intoxication and infection. Intoxication is caused by ingestion of toxin produced by pathogens, whereas infection is caused by ingestion of food containing viable pathogens [42].

Foodborne pathogens include bacteria, viruses, fungi, toxins as well as parasites. In general, there are 31 known pathogens causing foodborne diseases, whereas bacterial pathogens represent the vast majority of cases. The most common bacterial pathogens, which induce foodborne diseases include *Campylobacter spp., Listeria monocytogenes, Salmonella spp., Staphylococcus aureus, Clostridium perfringens, Escherichia coli O157:H7* and other shiga toxin-producing *E. coli* strains (STEC), and *Vibrio spp.*. In some cases, toxins produced by bacteria are the source of foodborne illness such as *Clostridium botulinum, Clostridium perfringens, Staphylococcus aureus* and *Bacillus cereus* [66].

The contamination of food can occur at any stage in the process from food prodution to consumption ("farm to plate") [2]. For instance, food can be exposed to pathogens and toxins from environmental contamination such as pollution of water, soil and air. Due to new nutritional trends involving the consumption of raw and fresh food as well as dry products, the occurence of foodborne disease outbreaks has significantly increased in the last years [67]. Fruits, vegetables, dairy, seafood, meat, poultry and especially ready-to-eat products are mainly involved in foodborne outbreaks.

Symptoms caused by *Salmonella, Campylobacter*, and enterohaemorrhagic *Escherichia coli* include headache, nausea, vomiting, abdominal pain and severe diarrhea. Whereas outbreak sources of salmonellosis are usually eggs and poultry, *Campylobacter* contaminations are mainly caused by raw milk, raw and undercooked poultry and drinking water. Enterohaemorragic *Escherichia coli* is associated with unpasteurized milk, undercooked meat and fresh fruits or vegetables.
Among the most severe foodborne infections is listeriosis caused by *Listeria*. Listeriosis may provoke severe illness (e.g. sepsis, meningitis, encephalitis) and death. In pregnant women it may lead to stillbirth or spontaneous abortion. *Listeria* is usually found in unpasteurized dairy products and ready-to-eat foods and is able to grow at refrigeration temperatures.

SEs are one of the most frequent sources of acute food contamination and poisoning, causing numerous foodborne-disease outbreaks around the world. The intoxication is called staphylococcal food poisoning. Staphylococcal food poisoning is a non-contagious gastrointestinal illness, which is caused by the consumption of food contaminated with preformed SEs [68].
The CDC further stated that the proteotoxins SEs affect approximately 80 million people in the United States, resulting in 325,000 hospitalizations and more than 5,000 deaths each year [1]. Foodborne diseases also have an essential economic impact with estimated anual costs of around 35 billion dollars in the United States. SEs will be discussed in detail in the following thesis section.

2.6 Staphylococcal Enterotoxins

2.6.1 Source

Staphylococcus aureus (S. aureus) is a a non-motile, spherical Gram-positive bacterium (coccus) of approximately 1 µm in diameter, which appears in pairs, short chain, or bunched, grape-like clusters under microscopic examination. It is an ubiquitious bacterium predominantly found in the anterior nares, throat, and skin of around one third of the general population. 50 – 80 % of individuals carrying it at any particular time point [69]. *S. aureus* produces a variety of exoproteins with toxicological effects such as hyaluronidase, staphylokinase, nucleases, lipases, proteases, collagenases, hemolysins, exfoliative toxins, and superantigen proteins including the toxic shock syndrome toxin-1 (TSST-1), staphylococcal enterotoxin-like proteins (SEls) and SEs [70].
The current nomenclature of SEs uses the term “SE” followed by the alphabetical letter in the order in which an SE was discovered [70]. An exception is SEF, which was later renamed TSST-1 and lacks emetic activity. The first five discovered SEs (SEA - SEE) are usually called the "classical SEs". Up to now, more than 23 distinct SEs are known from SEA to SEV.
Furthermore, the enterotoxins can be divided into SEs and staphylococcal enterotoxin-like (SEl) depending on whether or not they evoke emesis.
Only enterotoxins that induce vomiting after oral administration in a primate model will be designated as SEs. Related toxins that lack emetic activity or have not been tested for it, are classifed as staphylococcal enterotoxin-like proteins (SEls) [70]. The induction of emesis is basically tested on primate models [68].

2.6.2 Properties and Structure

Numerous SEs are pyrogenic and induce emesis and gastroenteritis as well as superantigenicity. In contrast to common antigens, superantigens are not processed by antigen-presenting cells before being presented to T- cells. They directly stimulate T- cells by cross-linking the major histocompatibility complex (MHC) class II molecules on the antigen-presenting cells with the variable portion of the T-cell antigen receptor β-chain or the T-cell antigen receptor α-chain for SE. Hence, this ultimately results in an activation of a large number of T-cells followed by proliferation and massive release of chemokines and proinflammatory cytokines that may eventually lead to potentially lethal toxic shock syndrome [71].

A minimum of 20 serologically distinct SEs have been described. Whereas SEA, SED and SEE share 70 - 90% sequence homology, they only share 50 - 60% with SEB, SEC, and TSST-1.
The SE are globular single-chain proteins with an average length of around 220 - 240 amino acids with a molecular weight of approximately 20 - 30 kDa

[71]. The staphylococcal superantigens show a high variability in their amino acid sequence, but have a similar three-dimensional structure during folding, as revealed by crystallographic analyses [1]. In general, SEs consist of α-helices and β-sheet components, which are arranged in two unequal domains forming a compact ellipsoid shape [70]. The β-sheet structure protects the toxin from a rapid degradation by proteases and from denaturation at high temperatures. Additionally the β-sheet structure gives the molecule an almost cylindrical shape and therefore a high contact area, which lend the molecule the characteristics of a superantigen. It usually contains a highly flexible disulfide loop, which has been implicated with emetic activity [68].

Overall, SEs are resistant to environmental conditions such as freezing, drying, heat and low pH values. Therefore mild cooking of contaminated food may not lead to a denaturation of the enterotoxins. Additionally SEs are resistant to inactivation by gastrointestinal proteases including pepsin, trypsin, rennin and papain, which retains their acitvity in the digestive tract after ingestion [1, 71].

2.6.3 Staphylococcal enterotoxins in foodborne poisoning associated diarrhea

The most common SEs are SEA and SEB. Whereas SEA is responsible for around 80 % of the cases of food poisoning outbreaks in the USA, SEB is responsible for 10 % of the cases.
SEB is not only connected to food poisoning but also known as a biological warfare agent, which may be applied for bioterrorism attacks on the food supply chain. The second most common SE associated with food poisoning is SED. The SEs SEE and SEH have been documented to be the source in some cases of food poisoning. SEF is associated with toxic shock syndrome, the SEs SEG and SEI are not intensively studied, but are attributed a minor role in food poisoning [1]. Table 2.3 shows a list of staphylococcal food poisoning.
Only a very low amount of SEB (1 ng g^{-1}) is needed to induce food poisoning [3]. For example, the amount of toxin in an outbreak caused by enterotoxin (SEA)-contaminated chocolate milk was reported to be only 0.5 ng mL^{-1} [1]. Since the enterotoxin is already preformed, staphylococcal food poisoning has a relatively short incubation time from one to 6 hours after gastrointestinal digestion and three to 12 hours after inhalation. Typical symptoms of the disease include nausea, vomiting, abdominal pain, cramps and severe diarrhea. The disease is usually self-limiting and usually resolves after 24 to 48 hours after onset. It is rarely lethal although letal cases have occured among the elderly, infants and severely debilitated persons. Foods which favor growth of *S. aureus* are characterized by high protein content. Thus, frequently contaminated food include meat and poultry, egg products, salads (tuna, chicken), bakery products (e.g. pastries, sandwich fillings) and milk and dairy products [71].

TABLE 2.3: Staphylococcal food poisoning in literature.

Year	Location	Contaminated food	Number of cases	Reference
1984	Scotland	Sheep milk cheese	27	[72]
1985	USA	Chocolate milk	> 1000	[73]
1998	Brazil	Meat, rice, beans	4000	[74]
2000	Japan	Low-fat milk	13420	[75]
2009	France	Raw milk cheese	23	[76]

The high incidence of staphylococcal food poisoning is due to the insufficient pasteurization and decontamination of SE contaminated food as well as its contamination during handling or preparation by individuals who are carriers of *S. aureus*. Consequently, food handlers carrying enterotoxin producing-*S. aureus* are regarded as the main source of food contamination. Nevertheless, *S. aureus* is also present in food animals, and dairy cattle, sheep and goats. Especially, if these animals are suffering from subclinical mastitis, SE contamination in milk and dairy products have occured [68].
Moreover, *S. aureus* grows over a wide range of temperature and pH which makes for example inadequate refrigeration a potential and typical source of outbreaks. Since the preformed SE is heat-stable, heating the contaminated food only kills the bacteria but does not destroy the toxin itself [77]. Besides to food poisoning a major concern to public health is the emergence of multi-drug resistant strains of *S. aureus* as common cause of nosocomial wound infections hospitalized patients in the clinical setting.

2.6.4 SEB as potential biological warfare agent

The proteotoxin SEB is the only known SE that has been examined as a biological warfare weapon. Among the SEs, SEB is the most potent SE, since it requires much lower quantities for toxic effects than synthetic chemicals [78]. Due to its stability to heat, proteolytic digestion and pH as well as its ease of production and easy distribution in an aerolized form, SEB was of particular interest in the Cold War era. Additionally, a series of laboratory accidents in the 1940s to 1960s in the United States led to intensive research of SEB as a biowarfare agent [79]. Whereas only a very low amount of 0.4 ng kg^{-1} SEB is required to induce symptoms, the lethal dose is approximately at 0.02 µg kg^{-1}. Inhalation of SEB results in symptoms such as shortness of breath and chest pain. With heavy exposure, severe symptoms such as high fever, pulmonary edema, possible acute respiratory distress syndrome, or septic shock could occur.

The risk of mortality by SEB exposure as a biowarfare weapon is low, however, even at a low dose it could effectively incapacitate the general population or front line soldiers due to its high emetic potential [1]. Hence, SEB has been classified as an incapacitating agent by the CDC. Although there is several ongoing research about the development of vaccines, there is currently no available antidote or preventive vaccine [79].
In addition to its inhalation, SEB may be used for bioterrorism attacks on the food supply chain or water systems. Due to their ease of preparation, availability, high toxicity and their lack of therapeutic options, high molecular-weight proteotoxins such as SEB could be easily used as food or water contaminants to affect a large number of people [3].

2.7 Separation and concentration of bacterial pathogens and toxins from food matrices

Rapid and simple high-throughput processes for the extraction, concentration and purification of bacterial pathogens and toxins from food are of increasing interest in order to avoid or mitigate foodborne illness outbreak.
Time-extensive enrichment or plating steps in the widely used cultural enrichment method, which takes several days, are not suitable for a rapid concentration and pathogen detection in case of an urgent foodborne disease outbreak. Additionally, cultural methods are not able to detect proteotoxins such as SEB, which may be present in absence of its producing bacterium. Effective concentration and separation methods prior to the detection significantly reduce the time of testing and therefore contribute to an immediate identification of the outbreak sources.
The aim of the concentration and separation method is to rapidly transfer the analytes in a concentration range in which the analysis of choice can be performed and to separate the target analyte from food samples, ideally without affecting the properties of the target analyte. For instance, if the initial sample volume is narrowed down with a concentration factor of 1000, a bacterial contamination of e.g. 100 cells in 1 L (= 0.1 cells/mL) can be detected in a concentrate of 1 mL by polymerase chain reaction (PCR).

The complex food matrix is a heterogeneous mixture of various components such as inorganic particles, biochemical molecules and microflora. Whereas, for instance, fat and other particulates may interfere with antibody-binding, carbohydrates can interfere with nucleic acid-based amplification methods [66]. Thus, to guarantee a low detection limit, the food matrix has to be separated in order to avoid interferences of the matrix with the analysis method.

In this section, the most widely and commonly used methods for concentration and separation in complex food matrices are discussed briefly.
An overview of culture-independent separation and concentration methods and culture-dependent enrichment processes is shown in Figure 2.19. In general, the concentration and separation methods can be divided in selective and non-selective methods.

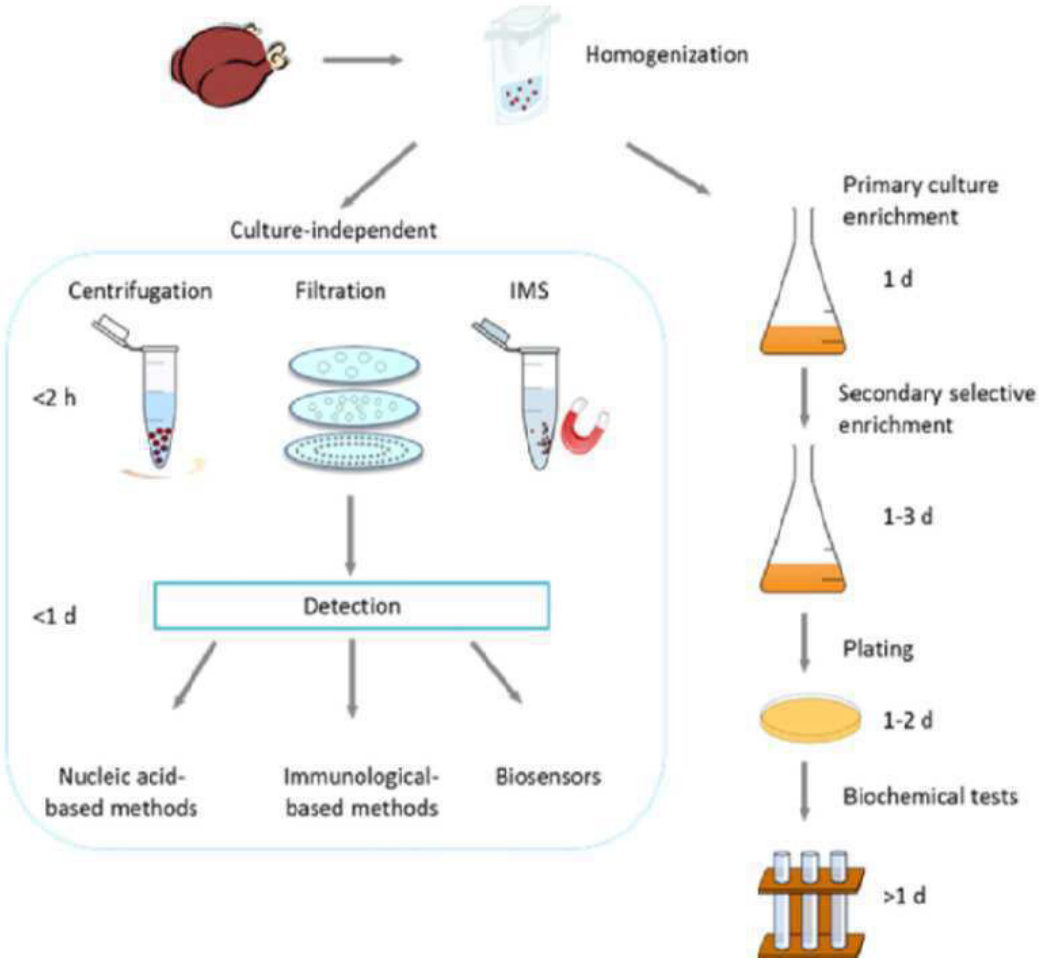

FIGURE 2.19: Comparison of culture-independent detection including pre-processing techniques of centrifugation, filtration, IMS, to conventional culture-based method including enrichment and plating steps [66].

2.7.1 Non-selective target separation and concentration methods

The most commonly used physical separation techniques are filtration and centrifugation due to their simplicity. Although, both methods require multiple separation and washing steps which significantly decrease the recovery of the pathogens.

Filtration

Filtration is a non-selctive approach where particles in liquid solutions or gas mixtures are separated depending on their size. During filtration a food homogenate or food matrix is passed through a filter. The porous filter membrane acts as a barrier which retains larger particles, and allows smaller particles to pass through the membrane into the filtrate. The filtrate of food samples can be discarded. Consequently, the sample is separated in filtrate and retenate. If desired, the pathogens can be released from the filter via principles of elution. Basically, filtration are pressure-driven methods [80]. The

four main methods of pressure-driven filtration are microfiltration, ultrafiltration, nanofiltration, and reverse osmosis, in order of decreasing pore size. Ultrafiltration membranes with a small pore size from 1 - 100 nm are generally used in separating of macromolecules, viruses, proteins and peptides. The molecular weight cutoff (MWCO) is at 5 - 5000 kDa. For the separation of bacteria and viruses an ultrafiltration membrane with a mean pore size of 20 nm is used.

Centrifugation

Centrifugation is usually applied to concentrate bacterial cells in solution. In principle high-speed rotation forms bacterial pellets, the remaining supernatant can be removed, and the bacteria can be resuspended in a smaller volume. In general, centrifugation is a rapid and simple method taking around 5 - 30 min. Nevertheless, there are some disadvantages of this method for the application in complex food matrices. Centrifugation tends to concentrate food debris along with the bacterial cells, which requires multiple and time-consuming washing steps in order to remove the food debris. Consequently, this may result in a reduced bacterial concentration, prolonged time, and also limits the compatibility with automated on-line systems [80].

2.7.2 Selective target separation and concentration methods

A selective target separation and concentration method can be achieved by affinity-based separation techniques involving ligands (e.g. antibodies, lectins or phages), which are covalently bound to particles or immobilized on filter material. The most common separation techniques using target specific antibodies are immunomagnetic separation and immunofiltration.

Immunomagnetic separation (IMS)

IMS is a promising technique for the separation and concentration of pathogens and toxins from food matrix [81]. Besides antibodies, affinity binders such as aptamers, bacteriophage proteins or lectins have been immobilized to magnetic particles.
Originally, IMS was developed for the isolation of blood cells and was later commercialized in the 1990s. Monodisperse superparamagnetic polymer particles also known as Dynabeads are commercially available from Dynal (Oslo, Norway). Dynabeads exhibit an even dispersion of superparamagnetic nanomaterials (magnetite and maghemite) coated with a thin polymer shell.
Another commercially available product for the magnetic separation is the magnetic-activated cell sorting (MACS) system from Miltenyi Biotec GmbH (Bergisch-Gladbach, Germany). The MACS separation system uses smaller particles consisting of iron oxide and aminodextranes. These beads are approximately 50 nm in diameter, and require a strong magnetic field gradient [82].
In principle, antibodies are conjugated to the surface of superparamagnetic nanoparticles, which enable the specific capture and isolation of the targeted

pathogen or toxin from complex matrices. The antibody-conjugated magnetic particles are incubated in the sample and bind the desired target analyte via antigen-antibody interaction with high affinity, forming a complex composed of the magnetic particle and target analyte. A magnetic field (e.g. permanent neodymium magnet or high-gradient magnetic columns) is applied and the magnetic particles with the immobilized antigen are attracted towards the magnetic field and therefore immobilized against the vessel wall or trapped inside the magnetic column. The matrix can be removed. Several washing and resuspension steps by on-off magnetic field cycles allow a specific isolation and separation of the target analyte. The magnetic particles along with the desired analyte can be resuspended in a small volume of buffer, which allows a simple and rapid concentration [83, 84]. A schematic illustration of the IMS can be seen in Figure 2.20.

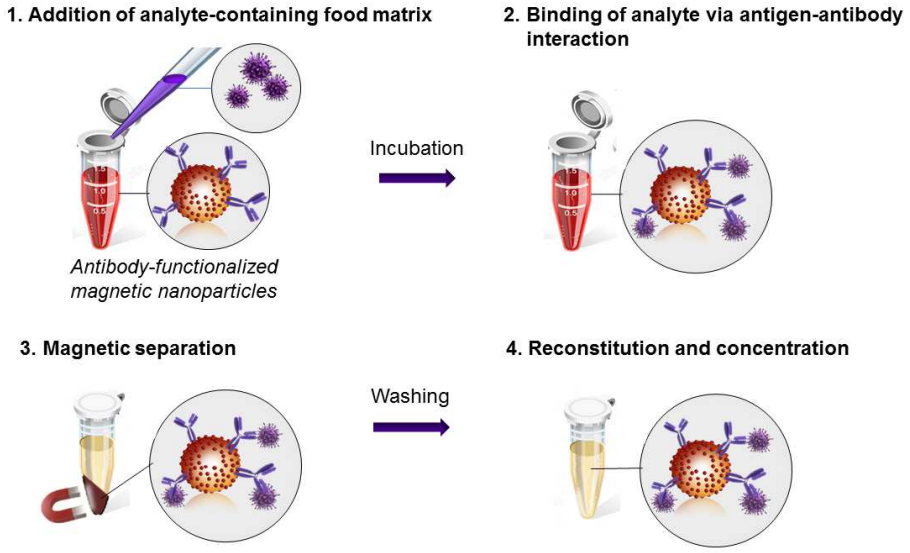

FIGURE 2.20: Principle of IMS in complex matrices.

Magnetic separation technique can be divided in high gradient magnetic separation (HGMS) and low gradient magnetic separation (LGMS), according to the magnitute of the magnetic field gradient applied in the magnetic separation [85].
In HGMS, a column is packed with magnetically susceptible wires surrounded by an electromagnet [86]. When the external magnetic field is applied, the magnetic wires within the column magnetize, dehomogenize the magnetic field and inducing a high gradient magnetic field (> 100 T m^{-1}). The sample passes through the columns and magnetic nanoparticles are captured on the magnetically susceptible wires and are therefore isolated (Figure 2.21a). Another popular approach is the separation by high gradient magnetic columns, which was commercialized by Miltenyi Biotec GmbH (Bergisch-Gladbach, Germany).

In contrast, LGMS involves a rather simple separation of magnetic materials by applying a hand held permanent magnet. This induces a non-homogeneous magnetic field gradient across the magnetic particle dispersion. The magnetic nanoparticles are attracted towards the permanent magnet by magnetophoretic force and therefore isolated from the dispersion (Figure 2.21b). The magnitude of magnetic field gradient in this set-up is generally less than 100 T m^{-1}.

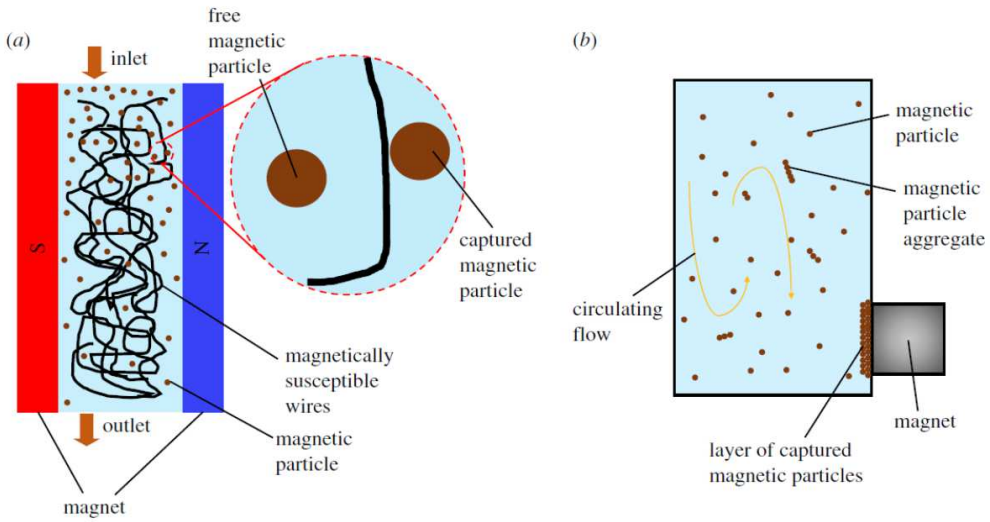

FIGURE 2.21: Illustration of HGMS a) and LGMS b) processes [85].

IMS has been applied for the separation and isolation of food borne pathogens including *L. monocytogenes, Bacillus stearothermophilus, Vibrio parahaemolyticus, E. coli O157:H7, Salmonella spp., Cryptosporidium*, and enteric viruses from mixed cell populations [80].
Pappert et al. applied a nanoparticle-based IMS step coupled to a sandwich chemiluminescence-ELISA for the enrichment and quantification of *E. coli* [87].
Aprodu et al., compared the IMS with a precipitation reaction and a density gradient centrifugation and quantified *S. aureus* via PCR. The comparison revealed that, all three mentioned methods in this study only achieved a concentration factor of maximum 15 and involved multiple separation steps [88].

IMS offers various advantages such as simple and rapid isolation of the target and removal of food components and potential inhibitors of detection methods in the matrix. Furthermore, a reduction of large sample volume to a volume suitable for analysis, and the possibility of automation and scale-up separation can be obtained by IMS [80]. Additionally, the IMS is perfectly suitable for food matrices with high solid contents.
However, in order to achieve a high recovery in large sample volumes, a high amount of antibodies and magnetic nanoparticles is required. Due to the high production costs of specific antibodies, IMS usually only allows the

processing of small volumes [80]. For the application in large food samples, antibodies are required which can be produced both at low-cost and in large volumes. The production of monoclonal antibodies in plant cells, the so called plantibodies, could enable the application of immunologic concentration methods in large sample volumes [89].

Immunofiltration

A very important separation method is the immunofiltration. Hereby, highly specific antibodies are immobilized in the pores of a filter material, which allows the specific enrichment of analytes (e.g. pathogens and toxins). A promising approach is the application of monolithic columns as solid support material. Monolithic columns are continuous supports consisting of porous organic polymers or inorganic material. The highly interconnected macropores of the monolith enable the formation of flow-through channels in the network skeleton [90]. Consequently, the separation process is achieved faster than with conventional columns packed with spherical porous particles.

In principle, specific antibodies are immobilized on the support material of the monolithic columns. The liquid food matrix containing the foodborne pathogen is passed through the monolithic column and the antibody binds the desired analyte with a high affinity [91]. Other sample components are passing through the monolithic column in the filtrate. The analyte can be subsequently eluted from the column. Consequently, the eluate contains the highly concentrated analyte, which is separated from the food matrix. A schematic illustration of the immunofiltration process is displayed in Figure 2.22.
A commercial example for immunofiltration is the antibody immunocolumn for analytical processes (ABICAP), which uses immobilized antibodies on hydrophobic polyethylene frits [92].
At the Institute of Hydrochemistry (IWC), monolithic columns were already functionalized with antibodies as affinity ligands. Ott et al. applied epoxy-based macroporous monolithic columns for the rapid immunofiltration of *Staphylococcus aureus*. The bacteria were quantified by flow cytometry. After immunofiltration the sensitivity was significantly increased and a limit of detection (LOD) of 42 *S. aureus*/mL was obtained [90].
With regard to concentration factors, selectivity and rapidity the monolithic immunofiltration is an effective method for the fast separation and concentration of analytes [90]. An important advantage of the immunofiltration technique is that large volumes of contaminated food liquids can be easily processed in a short time. Liquid samples can be passed through the monolithic column with high flow rates and low backpressure [93].
However, the availability of highly specific and sensitive antibodies for the specific foodborne microorganisms or toxins may limit the broad application of this method. In contrast to IMS, monolithic immunofiltration is not suitable for food samples with a high solid content, since food debris may block the pores of the monolithic columns. Therefore, the food sample has to be

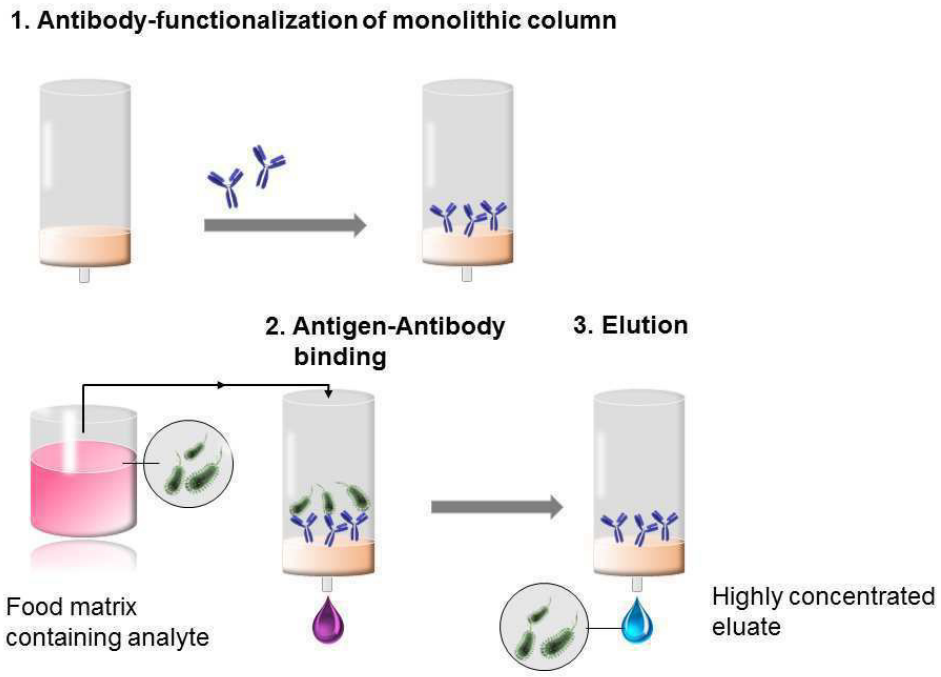

FIGURE 2.22: Principle of monolithic immunofiltration in complex food matrices.

homogenized and pre-treated before applying the monolithic immunofiltration.

In this thesis, **IMS** was applied to obtain an effective concentration and isolation of the target analyte SEB in milk.

2.8 Analytical detection methods for SEB

In order to ensure food safety and public health and minimize the outbreak of foodborne illness, it is highly essential to test food samples for the presence of SEs. In recent years there has been a tremendous progress in detection techniques to achieve rapid, sensitive and selective methods for the detection and quantification of SEs in food matrices.
The detection of *S. aureus* can be achieved by the recovery of the bacterium itself or its preformed toxins. Since SEB may still be present after bacteria are inactivated (e.g. by heat treatment), the detection of the preformed toxins are crucial.
According to the European Food Regulation (EC) No 2073/2005 the stated limit value is the absence of SE in a food sample of 25 g. In general, staphylococcal bacteria are usually detected by microbiological techniques or molecular biology, whereas the detection of SEB is commonly achieved by immunological methods. The following section gives a brief overview of the current analytical detection methods for SEB.

2.8.1 Serologic tests

Serologic tests have been widely applied for the detection of SEs and include gel diffusion tests and agglutination tests. These tests rely on antigen-antibody bindings in the serum. Whereas the gel diffusion test is based on the precipitation produced by antigen-antibody interaction, the agglutination test is based on the agglutination of antibody functionalized cells or particles. For instance, a latex agglutination test for SEB detection was developed using latex particles functionalized with sensitive anti-SEB antibodies. A LOD of 0.2 ng mL^{-1} could be achieved [94].
The reversed passive latex agglutination test (RPLA) for the detection of several SEs (SEA - SEA) was later commercialized. In a standard agglutination test a soluble antibody reacts with a particulate antigen (e.g. bacterial cells). In contrast, in a reversed agglutination test, the antibody, which is immobilized onto particles reacts with the soluble antigen. The cross-linking of the latex particles by antigen-antibody reaction induces the visible latex agglutination reaction [95, 96]. Nevertheless, the serologic tests lack in specificity and sensitivity [66]. Additionally serologic tests are rather time-consuming and labor-intensive and therefore do not meet the requirements for real-time detection.

2.8.2 Nucleic acid-based detection

Nucleic acid-based detection methods can be divided in the amplification of nucleic acids by PCR and hybridization of nucleic acids using probes [66].
PCR is one of the most widely used method to detect SEs in food. Whereas serological or immunological methods rely on the expression and presence

of SEs in food samples, PCR is able to detect enterotoxin-producing bacteria prior to the production of the toxin. PCR-based methods can detect SE genes, since the DNA remains intact after heating even though the bacteria is destroyed [97]. Hence, nucleic acid-based detection methods are designated as indirect methods.
Wilson et al. first reported a detection method of SE genes by PCR [98]. Two primers for the amplification of SEB and SEC genes and the staphylococcal nuclease gene were applied. A LOD of 1 femtogram of purified target DNA in dried skimmed milk was obtained.
Up to now, there are numerous PCR methods for the detection of SE genes such as multiplex PCR, quantitative real-time PCR, reverse-transcriptase PCR (RT-PCR). The most prominent PCR method for the detection of SEB genes in food is the quantitative PCR (qPCR) which monitors the formation and quantity of the amplified DNA products in real-time. In principle, the genetic material is amplified by using selective target primers. The increase of DNA is quantified with the suitable intercalating fluorescent dye or from the breakdown of a dye-labeled probe during amplification of the target sequence. For instance, Sharma et al. reported a multiplex PCR method for the detection of all staphylococcus enterotoxins [99].

In summary, PCR is a very reliable, highly target-specific and fast detection method which only requires a low amount of target DNA, but is aimed at the analysis of DNA not the SEs and is therefore an indirect detection method. Additionally it can be applied in numerous food matrices such as vegetable, milk, cheese and meat products. However, the food matrix can interefere with the PCR by nucleic acid degradation or direct inhibition leading to false negative PCR results. Therefore, a time-consuming pre-treatment of the food sample is crucial.

2.8.3 Chromatographic methods

SEs are proteins which can be enzymatically degraded to peptides and subsequently separated by liquid chromatography (LC). A following analysis by collision-induced dissociation tandem mass spectrometry (MS/MS) can be applied to gain information about the molecular weights and primary amino sequences of amino acids. For the first time, Kientz et al. have developed a liquid chromatography electrospray ionization mass spectrometry (LC-ESI-MS) approach for the detection of SEB with a LOD of 3 pmol mL^{-1} [100]. Since then, various approaches have been published about the quantification of SEs in distinct food matrices by LC-MS/MS [101–103]. The chromatographic methods are very sensitive, but generally requires time-consuming sample pre-treatment steps.

2.8.4 Immunological-based assays

Immunoassays exist in many different formats and variations. In general, immunoassays can be performed as homogeneous and heterogenous immunoassays.
Homogeneous immunoassays do not require any separation and washing steps of the free unbound antigen before measurement.
Hetereogeneous immunoassays require the careful separation of antibody-bound and free antigen. Besides, immunoassays can be further divided into direct competitive, indirect non-competitive and sandwich immunoassays. Sandwich immunoassays tend to be more sensitive and robust. Therefore, sandwich assays are the most commonly used.
In a sandwich immunoassay, the capture antibody is immobilized on a solid surface. The antigen binds to the capture antibody on the solid support with high affinity. The detection antibody is then added, which binds the antigen at a different epitope than the capture antibody. Thus, the antigen forms a so called sandwich between the two antibodies.
For quantification of the analyte, a huge variety of reporters can be used. Reporters (e.g. enzymes, flurophores, biotin) can be directly conjugated to the detection antibody or to a secondary antibody, which binds the detection antibody (e.g. IgG-HRP). The substrate for the enzyme is subsequently added in order to produce a readout as the detection signal. The generated signal is hereby proportional to the amount of antigen present in the sample.

Principles of detection

The applied antibody-linked reporter for measuring the binding event determines the detection mode.
The main detection modes can be classified in colorimetric detection, chemiluminescence, electrochemical detection and fluorescence.

1. Colorimetric detection

Enzyme-linked immunosorbent assay (ELISA) is a common and widely used approach for the detection of SEB. This method relies on a colorimetric detection. ELISA is typically performed on high binding polystyrene microtiter plates.
Quantification is obtained by the cleavage of the chromogenic substrate 3,3,-5,5-tetramethylbenzidine (TMB) catalyzed by the enzyme HRP, which produces a blue metabolite for signal detection. A spectrophotometric plate reader is used for measuring the colorimetric reaction.
Saunders et al. first applied an ELISA for the detection of SEA with a LOD of 0.4 $\mu g\,L^{-1}$ (20 hours detection time) to 3.2 $\mu g\,L^{-1}$ (one - three hours detection time) [104]. Up to now, various ELISA approaches for the detection of SEB have been reported in food samples (e.g. cheese, potatoe salad, ham and milk) [105, 106].
A screening sandwich ELISA for the detection of SEB in cheese with a LOD of 0.5 to 1.0 ng was reported using anti-SEB antibodies [107]. Another ELISA

approach achieved a lower detection limit of 0.05 µg L^{-1} [108]. ELISA is a viable and commonly used technique. However, multiple washing and incubation steps prolong the assay time. Additional, the development of a multiplex assay for several SEs is challenging.

Lateral flow immunoassay (LFI) is a paper-based platform for the detection and quantification of analytes in complex mixtures. A colorimetric reaction can be induced by nanoparticles (gold, silver) or enzymatic reactions [109]. LFIs represent a simple and rapid on-site detection method.
The LFI, based on a double-antibody sandwich format on a nitrocellulose membrane, was successfully applied to detect SEB with a LOD of 1 ng mL^{-1} [110]. Hereby, antibody-functionalized gold nanoparticles were applied.
In general, LFIs offer several advantages such as low-cost production, short detection time (5 - 30 mins), as well as suitability for on-site testing with minimum skill required. Additionally, LFI usually only allow a qualitative detection [66]. Nevertheless, LFI often lead to false positive results and lack in sensitivity which often requires prior time-consuming cultural enrichment steps.

2. Chemiluminescence (CL)

CL reactions after antibody-antigen binding on a solid surface are widely applied as detection method for immunoassays. Basically, CL is defined as the emission of energy in form of light as the result of a chemical reaction.
The antibody sandwich is formed by using a biotin-labeled detection antibody. The enzyme horseradish peroxidase (HRP) is a commonly used enzyme reporter, which catalyzes CL reactions. During the immunoassay, the added streptavidin-HRP binds to the biotinylated detection antibody. The CL reagents (hydrogen peroxide and luminol) are added. Hereby, HRP catalyzes the decomposition of luminol in the presence of hydrogen peroxide to produce an excited state intermediate called 3-aminophthalate that emits light at 425 nm as as it decays to the ground state and induce CL [111].
The mechanism of the CL reaction can be seen in Figure 2.23. The CL signal is recorded by a highly sensitive charge-coupled device (CCD) camera. The end point of the CL reaction after a defined time is achieved by intensive washing steps between the affinity reaction and the CL reagents [112].

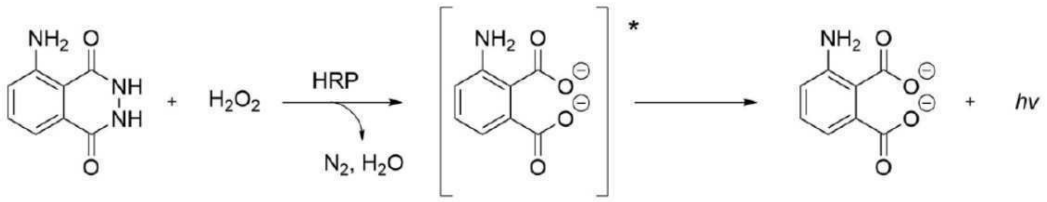

FIGURE 2.23: HRP-catalyzed CL reaction of luminol [113].

A highly versatile and rapid analytical tool for the detection of SEB is a CL-based *sandwich microarray immunoassay (SMIA)*. Microarrays can be defined as a collection of microscopic spots or features of biological capture molecules (e.g. DNA, antibodies) spatially arranged in a predefined order on a solid substrate [114].
The measuring principle relies on the previously described sandwich immunoassay. Whereas the sandwich ELISA is performed on a microtiter plate, a microarray is generated by immobilizing the capture antibody on the microarray surface (e.g. glass slide). Similar to a sandwich ELISA, the capture antibody captures the antigen SEB and immobilizes it on the microarray glass slide. Specific biotin-labeled detection antibodies are added and bind to the captured antigen in order to complete the antibody sandwich. This enables the formation of the sandwich immunoassay on the spots where the antigen is bound to the capture antibody. The CL signal is generated as described above. If the specific antigen is not present, the sandwich of the capture antibody-antigen-detection antibody does not form, and the detection antibody is not available to produce a CL signal. A schematic illustration of a CL-based SMIA can be seen in Figure 2.24.
Multiplex immunoassay technologies are of increasing interest, since the possible simultaneous quantification of various pathogens and toxins reduces time, costs and effort in case of a foodborne outbreak. An appealing analytical approach for multiplex detection (antibody-based and molecular biological) can be performed on microarray analysis platforms. A microarray with integrated instrumentation for a multiplexed analytical application is designated as a flow-through microarray platform. It consists of a fluidic system for introducing the sample, a reagent supply, a flow cell, a microarray on a substrate, and a detection system. The analytical steps are hereby carried out automatically by application of computer-controlled pumps and valves [112].
At the IWC, a rapid and simultaneous detection of ricin, SEB and saxitoxin by CL-based microarray immunoassay was reported. A LOD of 0.1 $\mu g\,L^{-1}$ for SEB was achieved [115]. Besides to CL, the readout of multiplex SMIAS on microarray analysis platforms can be additionally performed by fluorescence [116] or electrochemical reactions [117].
Another published analytical method applying CL is an image-based electrochemiluminescence assay for simultaneous detection of SEB in dairy milk products with a LOD of 10 pg mL^{-1} was developed [118].

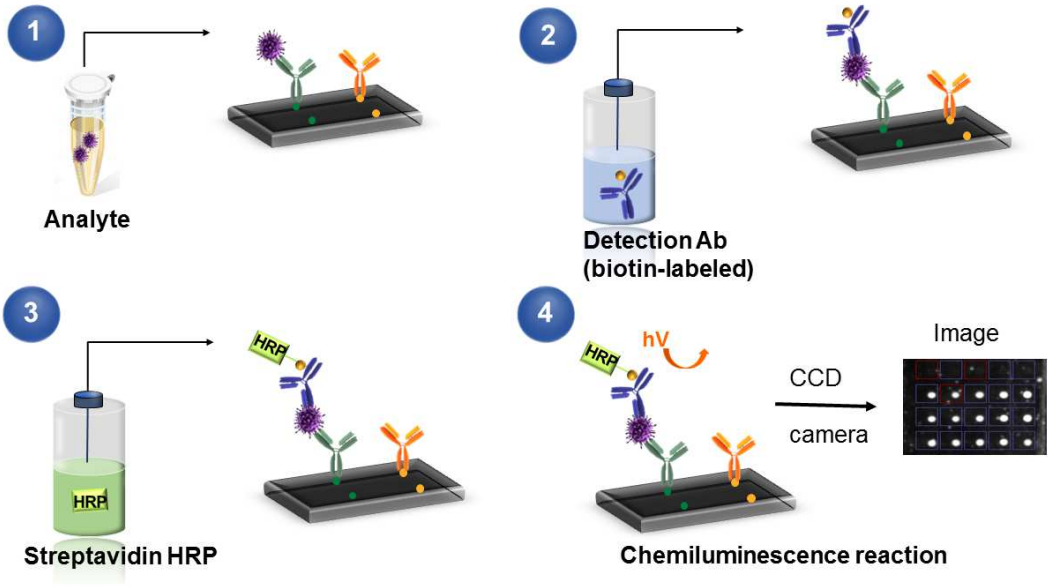

FIGURE 2.24: Principle of CL-SMIA for the detection of SEB in a flow-based CL microarray: 1) Binding of analyte SEB to immobilized capture antibodies, 2) Bindung of the biotin-labeled detection antibody, 3) Binding of HRP-conjugated streptavidin 4) CL reaction.

3. Eletrochemical detection

Other relevant techniques applying electrochemical detection are electrochemical biosensors [119, 120].
The portable Toxin detector, produced by Bruker Detection Corp. (Leipzig, Germany) is a commercially available electrochemical biosensor for the automated detection of biological warfare agents (SEB, Botulinium neurotoxin A, B, E) in the low ng mL^{-1} range. The detection principle relies on an ELISA procedure. Antibodies are immobilized on gold electrodes, which are attached to a disposable toxin chipstick. The toxin is detected by measuring the electric current of an enzymatic redox reaction. Hereby, the current correlates to the amount of toxin bound to the specific antibodies. The assay time is approximately 25 minutes.
Wojciechowski et al. have developed the CombiMatrix antibody microarray for the simultaneous detection of SEB, *Yersinia pestis* and *Bacillus anthracis*. The approach is based on the generation and transduction of electrochemical signals following the antigen binding to surface antibodies [121]. A LOD of 5 pg mL^{-1} was obtained.

Nanoparticle-based detection methods for SEB

Due to their unique physical and chemical properties, nanoparticles are of increasing interest for the application in various detection methods. Functionalization of a nanoparticle surface with biomolecules and detection labels offers a high assay set-up diversity. In particular, the application of magnetic nanoparticles for toxin detection is promising, because of the fast and simple possibility of IMS and thus concentration and purification of the analyte prior detection. Table 2.4 shows a brief overview of nanoparticle-based SEB detection methods.

An important commercially available multiplex platform is the suspension array technology, also called Luminex xMAP technology (Luminex Corp., Austin, USA). In principle, the conventional suspension array technology applies polystyrene microspheres with incorporated red and infrared fluorescent dyes. Thus an array of 100 spectrally unique bead sets is generated which can easily be distinguished by flow cytometry. The assay principle is based on a sandwich ELISA. Distinct coloured microbeads are functionalized with specific monoclonal antibodies for various antigens. Thus a simultaneous detection of multiple antigens is possible. The bound analytes are subsequently detected by biotinylated detection antibodies and the fluorescent reporter streptavidin-phycoerythrin. The luminex flow cytometer measures the fluorescent signature of the microbeads and the intensity of the reporter signal per microbead set [3].

Garber et al. applied the conventional suspension array technology for the simultaneous detection of abrin, ricin, botulinum toxins, and SEs A - C in food. A LOD for SEB of 10-20 ng L^{-1} was obtained [122].

Additionally, a suspension array-based multiplexed immunoassay for the simultaneous detection of biothreat agents including SEB in powder samples was developed with a LOD of 200 ng L^{-1} [123].

Pauly et al. advanced the existing conventional suspension array technology and applied magnetic fluorescent microspheres instead of the conventional fluorescent polystyrene microspheres to generate a multiplexed fluorescent magnetic suspension array for the parallel detection of five bacterial and plant toxins from complex food matrices. The magnetic fluorescent beads were applied in a prior IMS step in order to isolate and enrich the analytes from the food matrix. Thus, the sensitivity could be decreased to 0.3 ng L^{-1} for SEB in a sample volume of 0.5 mL (enrichment factor: 10) [3].

By application of fluoresecent nanoparticles, a sensitive multiplex antibody microarray system has been reported for the detection of ricin, cholera toxin and SEB in complex food matrices. For SEB a LOD of 100 ng L^{-1} in spiked apple cider or milk was obtained [124].

A novel method based on the application of immunoaffinity capture and matrix-assisted laser desorption / ionization - time-of-flight mass spectrometry (MALDI-TOF-MS) for the selective isolation and detection of SEB in food was developed by Schlosser et al. [125]. Anti-SEB antibodies were conjugated to magnetic nanoparticles for a selective purification and isolation of SEB from complex food matrices (e.g. raw milk). Subsequently, SEB was quantified by MALDI-TOF-MS.

Miyamoto et al. reported a rapid method for the detection of SEB in raw and dry milk samples based on antibody-based IMS and combined it with flow cytometry [126].
Shlyapnikov et al. have developed a microarray-based analytical method for the simultaneous detection of five bacterial toxins (cholera toxin, *E.coli* heat-labile toxin, SEA, SEB, TSST-1) by magnetic nanoparticles. Basically, toxins were captured on an antibody microarray. Subsequently, biotin-labeled secondary antibodies bind to the captured toxins. The microarray surface is subsequently analyzed by applying streptavidin-coated magnetic beads in a shear flow and magnetic field. The analysis was performed in milk and meat extracts with a LOD of 1 ng L^{-1} in less than 10 mins [127].

TABLE 2.4: Overview of nanoparticle-based detection methods for SEB.

Detection system	**LOD (ng L^{-1})**	**Matrix**	**Time**	**Reference**
xMAP technology	200	environmental	75 min	[123]
xMAP technology	10 - 30	food	-	[122]
Magnetic xMAP technology	3	food	210 min	[3]
	0.3	food	24 h	
Fluorescent antibody microarray	100	food	6 h	[124]
Immunomagnetic fluorogenic detection	100	buffer	30 min	[128]
IMS, MALDI-TOF MS	2 ng	food	15 min	[125]
IMS, Flow cytometry	250	food	3 h	[126]
Magnetic antibody microarray	1	food	15 min	[127]

Commercially available detection methods for SEs

Currently, several detections kits based on immunoassays are commercially available. A selection of commercially available kits for the detection of SEs is listed in Table 2.5. One important testing kit is the TRANSIA®PLATE SET Test. The EU Community Reference Laboratory for milk and milk products (CRL) is recommending TRANSIA PLATE SET for official testing of milk and dairy products throughout Europe.
VIDAS®Staph enterotoxin II is an automated enzyme-linked fluorescent immunoassay (ELFA) for the detection of SEA - SEE. This method is approved by AOC (AOAC Official Method 2007.06, 2010). Here, the Solid Phase Receptacle (SPR) is coated with anti-SE antibodies. The SE in the food matrix bind to the antibodies. After washing steps, alkaline phosphatase-labeled antibodies are cycled in and out of the solid phase. After addition of the substrate 4-methylumbelliferylphosphate, alkaline phosphatase catalyze the hydrolysis of the substrate into the fluorescent product 4-methylumbelliferone, which can be measured at 450 nm.
The Ridascreen SET Total (R-Biopharm AG) is a manual enzyme linked immunoassay which is performed in wells coated with polyvalent antibodies. The Ridascreen kit has been validated and verified thorough ring trials and third party validation studies led by European Union Reference Laboratory for Coagulase Positive Staphylococci for the European Committee for Standardization.
All those methods require extraction of enterotoxin from food prior to analysis. The method sensitivity and selectivity may be improved with dialysis concentration of the food extract. Furthermore, false-positive results due to the inference of food compontents represent a major challenge.

TABLE 2.5: Selection of commercially available immunoassays for the detection of SEs in food matrix.

Test Kit	Supplier	SE	LOD	Assay time
RIDASCREEN [129]	R-Biopharm AG	SEA - SEE	0.2 - 0.7 $\mu g\,L^{-1}$	2.5 h
Tecra Staph Enterotoxins Visual Immunoassay [130]	3M	SEA - SEE	1.0 $\mu g\,L^{-1}$	4 h
TRANSIA®Plate SEs [131]	Transia-Diffchamp	SEA - SEE	$< 0.2\ \mu g\,L^{-1}$	2 h
VIDAS SET II [71]	BioMériuex	SEA - SEE	0.25 $\mu g\,L^{-1}$	2 h
SET-RPLA Kit [96]	Oxoid	SEA - SED	0.25 $\mu g\,L^{-1}$	24 h

Chapter 3

Materials and Methods

3.1 Materials

3.1.1 Instruments

- BioOdyssey Calligrapher MiniArrayer (Bio-Rad Laboratories, Munich, Germany)
- Centrifuge 5804 R (Eppendorf, Hamburg, Germany)
- Drying cabinet (Memmert, Buchenbach, Germany)
- Drying oven 20 - 250 °C (Memmert, Buchenbach, Germany)
- Engraving pen MICROMOT 50/E (Proxxon, Niersbach, Germany)
- Havard Apparatus Pump 11 (Holliston, USA)
- Heating mantle, 450 °C (Carl Roth, Karlsruhe, Germany)
- ICP/MS Elan 6100 (Perkin Elmer, Hamburg, Germany)
- Lab-RAM HR Raman microscope (Horiba Scientific, Japan)
- Magnetic incubation unit (Institut für Wasserchemie und Chemische Balneologie, Munich, Germany)
- Magnetic separator, Magna Rack (Invitrogen, Life Technologies, Carlsbad, USA)
- Magnetic stirrer with heating function MR 3002 S (Heidolph, Kelheim, Germany)
- Milli-RO 5 Plus, Milli-Q185 Plus (Millipore, Eschborn, Germany)
- Munich Chip Reader 3 SLT (GWK Präzisionstechnik, Munich, Germany)
- Nanodrop 1000 (Thermo, Wilmington, USA)
- NiCr-Ni temperature sensor, HKMTIN-IM100U.150 (OMEGA, Newport Electronics GmbH, Deckenpfronn, Germany)
- Overhead shaker REAX2 (Heidolph, Schwabach, Germany)

- pH / conductivity cell Multi 3401 (WTW, Weilheim, Germany)
- Quantum Design superconducting quantum interference device (SQUID) magnetometer, MPMS XL-7 (Walther-Meissner-Institut, Garching, Germany)
- Reader Synergy HT (BioTek, Bad Friedrichshall, Germany)
- Refrigerated Incubator Shaker C24KC (New Brunswick Scientific Classic Series, EDISON, USA)
- Rotavapor RE 121 (Buechi, Flawil, Switzerland)
- Shaker Easyshaker EAS 2/4 (SLT, Crailsheim, Germany)
- Stealth solid spotting pin SNS9 (ArrayIt, Sunnyvale, USA)
- Synergy HT (BioTek, Bad Friedrichshall, Germany)
- TEM JEM 100 CX microscope (JEOL LTd., Tokyo, Japan)
- Ultrasonic bath Sonorex Super RK106 (Bandelin, Berlin, Germany)
- UV/Vis spectrometer DU 650 (Beckman, Fullerton, USA)
- Vario Pump-System (Ismatec /Idex, Glattbrug, Switzerland)
- Vortex mixer TopMix FB1 5024 (Fisher Scientific, Schwerte, Germany)
- Washing automat ELx 405 Select (BioTek, Bad Friedrichshall, Germany)
- Zetasizer Nanoseries NanoZS (Malvern Instruments GmbH, Herrenberg, Germany)

3.1.2 Software

- AVIS V.F. Viewer (MSB di F. Cavicchio, Ravenna, Italy)
- BioOdyssey Calligrapher 2.0 (Bio-Rad Laboratories GmbH, Munich, Germany)
- ChemBioDraw Ultra 14.0 (Perkin Elmer, Waltham, MA, USA)
- Gen5 (BioTek, Bad Friedrichshall, Germany)
- Laboratory balance AT 261 Delta Range (Mettler-Toledo GmbH, Giessen, Germany)
- Laboratory balance PM 4600 Delta Range (Mettler - Toledo GmbH, Giessen, Germany)
- MCR ImageAnalyzer Ver. 03.2.1 (GWK, Munich, Germany)
- MCRImageAnalyzer (ODEVIS AG, Burghausen, Germany)

- Microsoft Office 2010 (Microsoft, Redmond, WA, USA)
- Origin Pro 2015G und 2016G (OriginLab Corporation, Northampton, USA)
- Origin Pro 2017G (OriginLab Corporation, Northampton, USA)

3.1.3 Materials and Chemicals

Material

- Adhesive foil, ARcare 90106, Acryl-hybride (Adhesive Research Ireland, Limerick, Ireland)
- Amicon Ultra- 0.5 mL centrifugal filter units, Ultracel 30 K (UFC503024, Sigma Aldrich, Taufkirchen, Germany)
- Autoclave bags (0384.1, Carl Roth, Karlsruhe, Germany)
- Carrier for staining microscopy carriers PP (2291.1, Carl Roth, Karlsruhe, Germany)
- Centrifugation tubes PP, 15 mL, non-sterile (AN76.1, Carl Roth, Karlsruhe, Germany)
- Centrifugation tubes PP, 50 mL, non-sterile (AN78.1, Carl Roth, Karlsruhe, Germany)
- Disposable syringe, Injekt-F, PP/PE, 25 mL (T987.3, Carl Roth, Karlsruhe, Germany)
- Disposable syringes Omnifix®-F, PP/PS, 1 mL (H999.1, Carl Roth, Karlsruhe, Germany)
- Double-sided adhesive foil (ARcare 90106)
- Eppendorf pipettes (1 - 10 µL, 10 - 100 µL, 100 - 1000 µL, 1 - 5 mL (Eppendorf, Hamburg, Germany)
- Glass slides, 76 x 26 x 1 mm, (0656.1, Carl Roth, Karlsruhe, Germany)
- Gloves, nitrile (P778.1, Carl Roth, Karlsruhe, Germany)
- Microtiter plate, 96-well, flat bottom, high binding capacity (655061, Greiner Bio-One, Frickenhausen, Germany)
- Neodym-iron-boron magnet, 40 x 20 x 10 mm, magnetisation: N42 (Q-40-20-10-N, Webcraft GmbH, Uster, Switzerland)
- Parafilm (H666.1, Carl Roth, Karlsruhe, Germany)
- Pasteur pipette (4522, Carl Roth, Karlsruhe, Germany)

- PMMA carrier, black (Institut für Wasserchemie und Chemische Balneologie, Munich, Germany)
- Protein LoBind Tubes, 1.5 mL (0030108.116, Eppendorf, Hamburg, Germany)
- Reaction flask, 1.5 mL (4190.1, Carl Roth, Karlsruhe, Germany)
- Roll edge glass, 10 mL (X655.1, Roth, Karlsruhe, Germany)
- Roll edge glass, 25 mL (X659.1, Roth, Karlsruhe, Germany)
- Roll edge glass, 40 mL (X662.1, Roth, Karlsruhe, Germany)
- Sealing foils for microtiter plates (EN76.1, Carl Roth, Karlsruhe, Germany)
- Single-use syringe filter, reg. cellulose, pore size 0.20 µm (5824.2, Carl Roth, Karlsruhe, Germany)
- Single-use syringe, 1 mL (H.999.1, Carl Roth, Karlsruhe, Germany)
- Single-use syringe, 10 mL (0058.1, Carl Roth, Karlsruhe, Germany)
- Single-use syringe, 5 mL (0057.1, Carl Roth, Karlsruhe, Germany)
- Staining shell TPX (2290.1, Carl Roth, Karlsruhe, Germany)
- Tygon tube R3607, IDEX Ismatec, TYGON LMT-55, inner diameter: 3.17 mm, wall 0.9 mm, color code: Black and White, (070535-25I-ND SCO224 T, Ismaetec, Wertheim, Germany)
- UV StarR 384 well plate (Greiner Bio-one GmbH, Frickenhausen, Germany)

Chemicals and Reagents

- (3-Glycidyloxypropyl)trimethoxysilane > 98% (440167, Sigma Aldrich, Germany)
- 1-Octadecene, 95% (74740, Sigma Aldrich, Germany)
- 2-Amino-2-hydoxymethylpropane-1,3-diol, Sigma 7-9 (T1378, Sigma Aldrich, Taufkirchen, Germany)
- (3-Aminopropyl)triethoxysilane, 97% (440167, Sigma Aldrich, Taufkirchen, Germany)
- (3-Aminopropyl)trimethoxysilane, 97% (281778, Sigma Aldrich, Germany)
- Acetone > 99.8% (9372.5, Carl Roth, Karlsruhe, Germany)
- Amine-PEG3-Biotin (21347, Thermo Scientific, Waltham, USA)

- Biotin-X-X-NHS, Biotinamidohexanoyl-6-aminohexanoic acid N-hydroxysuccinimide (B3295, Sigma Aldrich, Taufkirchen, Germany)
- BSA, albumine from bovine serum (A3912, Sigma Aldrich, Taufkirchen, Germany)
- Carboxyethylsilianetriol, sodium salt, 25% in water (110934, ABCR, Karlsruhe, Germany)
- Caseine from bovine milk (C5890, Sigma Aldrich, Taufkirchen, Germany)
- D(+)-Trehalose dehydrate (90210, Fluka, Steinheim, Germany)
- Dimethyl sulfoxide anhydrous, 99.9% (276855, Sigma Aldrich, Taufkirchen, Germany)
- Dimethylaminopyridine (522805, Sigma Aldrich, Taufkirchen, Germany)
- Di-Potassium hydrogen phosphate (Merck, Darmstadt, Germany)
- Disuccinimidyl suberate (21658, Thermo Scientific, Waltham, USA)
- Ethanol absolute, > 99.8%) (32205, Sigma Aldrich, Taufkirchen, Germany)
- Fixogum (Marabu GmbH & Co. KG, Tamm, Germany)
- Hydrochloric acid, 37% (84422, Sigma-Aldrich, Taufkirchen, Germany)
- Iron(III) chloride hexahydrate, > 99% (31232, Sigma Aldrich, Taufkirchen, Germany)
- JEFFAMINE® ED-2003 (XTJ-502, Huntsman, Rotterdam, Holland)
- Methanol, > 99% (65548, Sigma-Aldrich, Taufkirchen, Germany)
- N,N-Dimethylformamide anhydrous, 99.8% (227056, Sigma Aldrich, Taufkirchen, Germany)
- N,N'-Disuccinimidyl carbonate, 95% (225827, Sigma Aldrich, Taufkirchen, Germany)
- n-hexane (7339.1, Carl Roth, Karlsruhe, Germany)
- N-Hydroxysulfosuccinimide sodium salt (56485, Sigma Aldrich, Taufkirchen, Germany)
- Ninhydrin reagent solution, 2% (N7285 Sigma Aldrich, Taufkirchen Germany)
- Oleic acid, > 99% (7213.2, Sigma Aldrich, Taufkirchen Germany)
- Peroxidase from horseradish (P8375, Sigma Aldrich, Taufkirchen Germany)

- Pluronic F® 127 (P2443, Sigma Aldrich, Taufkirchen, Germany)
- Potassium dihydrogen citrate hydrate, 99%, dry basis (866-83-1, Alfa Aesar, Haverhill, USA)
- Potassium dihydrogenphosphate (60230, Sigma Aldrich, Taufkirchen, Germany)
- Potassium sorbate (85520, Sigma Aldrich, Taufkirchen Germany)
- Silica nanoparticles, mesoporous, 200 nm particle size (748161, Sigma Aldrich, Taufkirchen, Germany)
- SM(PEG)12 Crosslinker, NHS-PEG12-Maleimide (22112, Thermo Scientific, Waltham, USA)
- Sodium azide (S2002, Sigma Aldrich, Taufkirchen, Germany)
- Sodium carbonate, anhydrous (73151, Fluka, Buchs, Switzerland)
- Sodium chloride (13565, Sigma Aldrich, Taufkirchen, Germany)
- Sodium hydrogen carbonate (401676, Sigma Aldrich, Taufkirchen, Germany)
- Sodium hydroxide (S0899, Sigma Aldrich, Taufkirchen, Germany)
- Sodium oleate (8856.1, Carl Roth, Karlsruhe, Germany)
- Streptavidin-horseradish peroxidase (SA-5004, Vector Laboratories, Burlingam, USA)
- Streptavidin poly-HRP 40 (2.8.1.1., Senova, Weimar, Germany)
- Succinic anhydride, 99% (239690, Sigma Aldrich, Taufkirchen, Germany)
- Sulfuric acid, 97% (84720, Sigma-Aldrich, Taufkirchen, Germany)
- Tergazyme, enzyme detergent (Z273287-1EA, Sigma-Aldrich, Steinheim)
- Tetrahydrofurane, anhydrous, > 99.9%, inhibitor-free (401757, Sigma Aldrich, Taufkirchen, Germany)
- Toluene anhydrous, 99.8% (244511, Sigma Aldrich, Taufkirchen, Germany)
- Trauts reagent, 2-Iminothiolane HCl (26101, Thermo Scientific, Waltham, USA)
- Triethylamine, 99.5%, anhydrous (471283, Sigma Aldrich, Taufkirchen, Germany)
- Tween 20 (8.17072, Merck, Darmstadt, Germany)
- Ultra pasteurized milk, 1.5% fat (Penny Market, Germany)

- WESTAR SUPERNOVA ELISA Luminol solution (XLSE2L, 0250, Cyanagen, Bologna, Italy)
- WESTAR SUPERNOVA ELISA Peroxide solution (XLSE2P, 0250, Cyanagen, Bologna, Italy)

Antibodies and Antigens

- mAb 1D6, anti-SEB (mouse), c = 1.0 $\mathrm{mg\,mL^{-1}}$ (Ludwig-Maximilians-Universität München, Chair for Hygiene and Technology of Milk, Prof. Märtlbauer, Oberschleißheim, Germany)
- mAb 1D6, anti-SEB, biotin-conjugated (mouse), c = 1.0 $\mathrm{mg\,mL^{-1}}$ (Ludwig-Maximilians-Universität München, Chair for Hygiene and Technology of Milk, Prof. Märtlbauer, Oberschleißheim, Germany)
- mAb S1001/4/6, anti-SEB (mouse), c = 1.26 $\mathrm{mg\,mL^{-1}}$ (Robert Koch-Institut, Centre for Biological Threats and special pathogens, Dr. Dorner, Biological Toxins (ZBS3), Berlin, Germany)
- mAb S419/5/5, anti-SEB (mouse), c = 1.39 $\mathrm{mg\,mL^{-1}}$ (Robert Koch-Institut, Centre for Biological Threats and special pathogens, Dr. Dorner, Biological Toxins (ZBS3), Berlin, Germany)
- SEB from *Staphylococcus aureus* (S4881, Sigma Aldrich, Taufkirchen Germany)

Buffers

All buffers and solutions were prepared using purified water from a MilliQ-plus 185 system.

Phosphate buffered saline (PBS 10 x)

- 244 g (70 mmol) K_2HPO_4
- 27,2 g (10 mmol)KH_2PO_4
- 170 g (145 mmol) NaCl
- H_2O, ad 2000 mL

0.1 M Bicarbonate buffer, pH 9.3

- 1.5 g Na_2CO_3
- 2.93 g $NaHCO_3$
- H_2O, ad 2000 mL
- pH was adjusted to pH 9.3

PBS, Tween, pH 7.4

- 0.5 g Tween 20
- PBS, ad 1000 mL

1 M Sodiumhydrogencarbonate buffer, pH 8.3

- 2.1 g $NaHCO_3$
- H_2O, ad 25 mL
- pH was adjusted to pH 8.3

Spotting Buffer (MCR 3)

- 0.5 mg Pluronic F127
- 1 g Trehalose-D(+) Dihydrate
- PBS, ad 10 mL

Running buffer A, Caseine 0.5% (MCR 3)

- 5 g caseine from bovine milk
- PBS, ad 1000 mL

Running buffer B, Caseine 0.5%, 0.01% Pluronic® F127 (MCR 3)

- 5 g Casein
- 0.1 g Pluronic F 127
- PBS, ad 1000 mL

Blocking buffer, TRIS-HCl, pH 8.5

- 121.1 g TRIS (1M)
- 8.8 g NaCl (150 mM)
- H_2O, ad 1000 mL
- pH was adjusted to pH 8.5 with hydrocloric acid (37% v/v)

Cleaning buffer A (MCR 3)

- 10 g Tergazyme (10% w/v)
- H_2O, ad 1000 mL

Cleaning buffer B (MCR 3)

- 20 mL Hellmanex (2% w/v)
- H_2O, ad 1000 mL

3.2 Methods

3.2.1 Synthesis of iron oxide-shell silica-core nanocomposites

The iron(III) oleate complex was prepared according to the method published by [13]. For the synthesis of the iron oleate precursor, 4.05 g (15 mmol) Iron(III) chloride hexahydrate and 13.69 g (45 mmol) sodium oleate were dissolved in a mixture of 30 mL ethanol, 22.5 mL ultrapure water and 52.5 mL hexane. The resulting reaction mixture was heated to 70 °C for 4 hours. Then, the upper layer containing the iron-oleate precursor was washed repeatedly with ultrapure water in a separatory funnel. The hexane was evaporated using a rotavapor resulting in a brown waxy solid. The iron(III) oleate was stored at 4 °C until further use.

2.68 g (2.8 mmol) iron(III) oleate, 0.68 g oleic acid (2.4 mmol) and 120 mg silica nanoparticles were combined in 28 mL 1-octadecene in a three-neck round flask. For a controlled heating procedure during nanoparticle synthesis a temperature sensor was connected to a heating mantle thermocontroller by the workshop of the IWC. The setup of the synthesis apparatus is shown in Figure 3.1. The mixture was gently stirred for one hour at RT, subsequently heated to 320 °C and incubated for 5 min. After cooling to RT, the reaction mixture was centrifuged (4500 rpm, 10 min) to remove unbound iron oxide nanoparticles. The precipitate containing the nanocomposites was washed by performing two sequential cycles of centrifugation and resuspension in hexane. Magnetic separation in hexane was performed to remove vacant silica nanoparticles (Figure 3.2A). The above process can be scaled up to the desired amount of nanomaterial. After drying under vacuum, the oleic acid-capped nanocomposites were dispersed in hexane and stored at 4 °C for further use. The small iron oxide nanoparticles were additionally analyzed. After the first centrifugation step the reaction mixture supernatant was therefore precipitated by adding 10 mL of ethanol. The reaction mixture was centrifuged at 4500 rpm for 20 minutes. The precipitate containing the small iron oxide nanoparticles was washed by performing two sequential cycles of centrifugation and resuspension in hexane (Figure 3.2B).

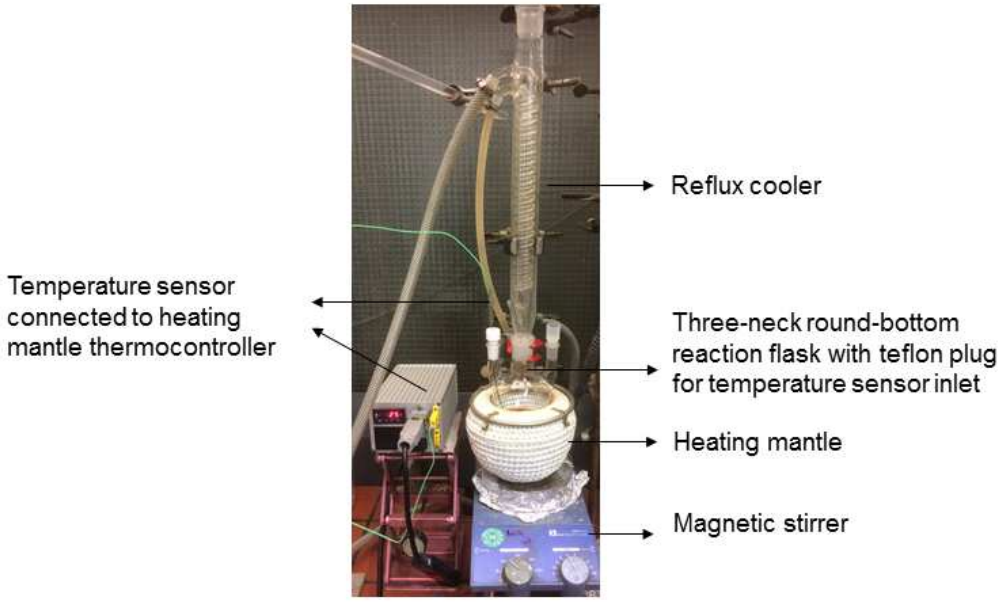

FIGURE 3.1: Setup of synthesis apparatus for preparation of iron oxide-shell silica-core nanocomposites.

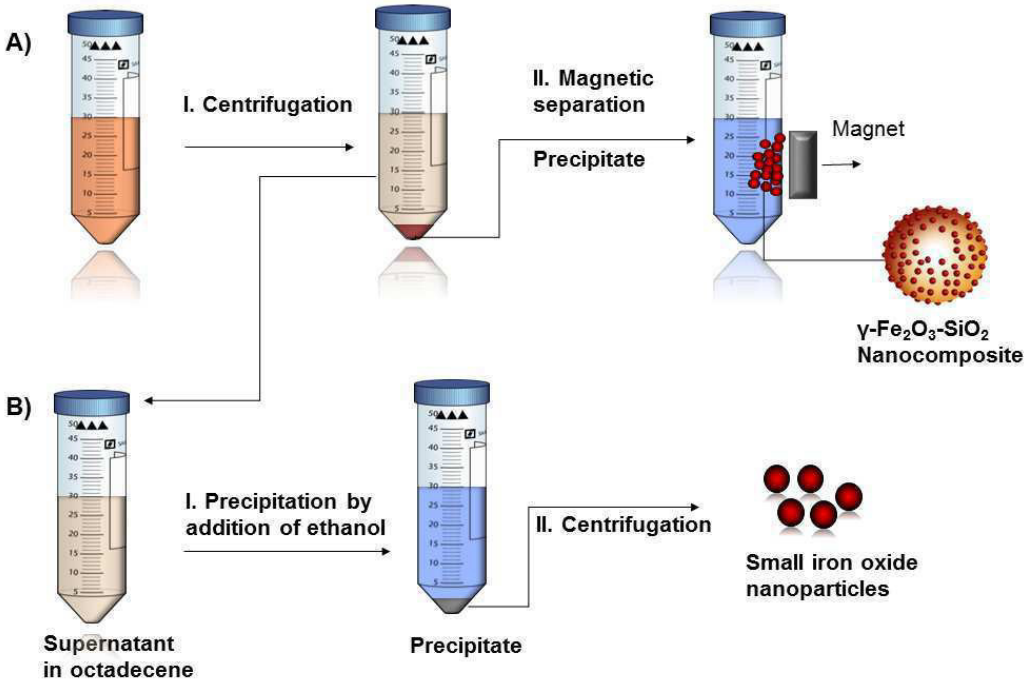

FIGURE 3.2: Separation and purification of iron oxide-shell silica-core nanocomposites.

3.2.2 Functionalization of iron oxide-shell silica-core nanocomposites

The hydrophobic oleic acid-capped nanocomposites were converted to hydrophilic ones by using a rapid ligand exchange method with either APTES or GOPTS to produce amino-functionalized or epoxy-functionalized nanocomposites, respectively. The protocol for coating of small iron oxide nanoparticles according to [35] was adjusted with minor modifications in order to functionalize the nanocomposites with organosilanes. In detail, 20 mg oleic acid-capped nanocomposites in 1 mL hexane stock solution were mixed with 10 mL toluene, 500 µL triethylamine, 10 µL ultrapure water and 100 µL APTES or GOPTS. The flask was sealed and placed in an ultrasonication bath for 5 hours under ambient conditions. The aminosilane-functionalized nanocomposites were subsequently separated by a neodymium magnet and washed three times with ethanol. Nanocomposites functionalized with GOPTS were washed three times with anhydrous tetrahydrofurane. After drying under vacuum, nanocomposites were weighed and dispersed in the appropriate aqueous medium.

3.2.3 Synthesis of maghemite and magnetite nanoparticle reference materials

Synthesis of nanoparticle reference materials was performed by Carolin Hartmann according to following protocol. Magnetite nanoparticles were synthesized by precipitation under alkaline conditions as published elsewhere [132]. 1.5 g $FeCl_2$ x 4 H_2O (75.4 mM) and 4.99 g $FeCl_3$ x 6 H_2O (184.6 mM) were dissolved in 100 mL ultrapure water and heated with vigorous stirring at 90 °C under nitrogen atmosphere. 10 mL of 25 wt % ammonium hydroxide solution were added dropwise. Hereby, a rapid color change from red brown to black was observed. To avoid agglomeration between the nanoparticles the coating agent oleic acid (1% (v/v), 1 mL) was added to the solution and stirred for about 15 minutes. The magnetic nanoparticles were filtered and thoroughly washed with ultrapure water and ethanol and subsequently dried under vacuum for 24 hours. To obtain maghemite nanoparticles, magnetite nanoparticles were heated under ambient conditions at 250 °C for 5 hours [133].

3.2.4 Characterization of iron oxide-shell silica-core nanocomposites

Characterization of size and morphology

Transmission electron microscopy (TEM) images were obtained with a JEM 100 CX microscope (JEOL Ltd., Tokyo/Japan) at 100 kV. Measurements were performed by Dr. M. Hanzlik (Electron Microscopy, TUM). 5 µL of the 1 $mg\,mL^{-1}$ nanocomposite suspension was applied to a 300 mesh grid coated with carbon. Scanning electron microscopy (SEM) images were performed

by Dr. G. Ganskow and C. Sternkopf with a SIGMA VP 300 (Carl Zeiss AG, Germany) microscope at 2.50 - 3.00 kV. 10 µL of the 10 mg mL^{-1} nanocomposite suspension was applied to an aluminium sample stub. The size distribution of the nanoparticle cores was determined from the TEM and SEM images with *Analyze Particle* feature of the image-processing software Image J.
A Zetasizer Nanoseries NanoZS (Malvern Instruments GmbH, United Kingdom) at the Munich School of BioEngineering, TUM, was used to determine the hydrodynamic diameter of the nanoparticles. The particles were suspended in ultrapure water with the addition of 1 mM NaCl for the measurements. Samples were analyzed in triplicates, each triplicate with 10 sub-runs. The average diameter and polydispersity were calculated by the Malvern Dispersion Technology software.

Analysis of magnetic properties

Magnetic properties of the iron oxide-shell silica-core nanocomposites were investigated in a Quantum Design superconducting quantum interference device (SQUID) magnetometer (MPMS XL-7) with a magnetic field of up to 5 T applied in plane. Measurements were performed by Dr. Mathias Opel, Walther-Meißner-Institute for Low Temperature Research, Garching.
Around 10 mg of either bare or functionalized vacuum-dried nanomaterial were embedded in Fixogum rubber cement (Marabu GmbH & Co. KG) and placed in a holder tube. M(H) measurements were performed at 300 K in a magnetic field from -4000 kA m^{-1} to 4000 kA m^{-1}. The average magnetic moment per nanoparticle was calculated by fitting the data to the Langevin function after subtracting the diamagnetic contribution. The zero field-cooled (ZFC) and field-cooled (FC) magnetization measurements were performed while warming at a measuring field of 8 kA m^{-1} after having cooled the sample down from RT to 5 K either at 0 kA m^{-1} (ZFC) or at 4000 kA m^{-1} (FC), respectively. The M_S value was calculated per gram γ-Fe_2O_3. In order to determine the iron content in the nanocomposites ICP-MS measurements were performed as described below.

Determination of iron conent by ICP-MS measurements

The iron content was kindly performed by C. Sternkopf at a Perkin Elmer ICP/MS Elan 6100. Nanocomposites were treated in a microwave-assisted acid extraction procedure with hydrofluoric acid and nitric acid (10 min at 130 °C, 10 min at 180 °C and 30 min at 210 °C. Iron content was quantified by ICP-MS measurements (Perkin Elmer ICP/MS Elan 6100).

Raman microspectroscopy (RM)

For Raman analysis a Lab-RAM HR Raman microscope (Horiba Scientific, Japan) with an integrated Olympus BXFM microscope was used. Measurements were conducted by Dr. Natalia P. Ivleva and Carolin Hartmann at the IWC. A He-Ne laser (633 nm, max. 4 mW at the sample) was applied for all

measurements. Wavelength calibration was accomplished by the characteristic first-order phonon band of Si at 520.7 cm^{-1}. The samples were air-dried and measured on CaF_2 plates. The laser beam was focused onto the sample with a 100 x objective (Olympus MPlan N, NA = 0.9). The laser power was reduced down to 0.4 mW in order to avoid thermal decompositions of the samples. The integration time for one spectrum was set to 10 s, and the number of accumulation of 25 or 50 was chosen to obtain an acceptable signal-to-noise ratio.

Fouriertransformed infrared spectroscopy (FT-IR)

FT-IR spectra were measured on a Nicolet 6700 FT-IR spectrometer (Thermo Fisher Scientific Inc., Waltham, USA) by using an attenuated total reflectance (ATR) sampling accessory. 1 mg of dried nanoparticles were applied on the sampling accessory. Before each measurement, the background was distracted by a blank measurement in air.

Mössbauer spectroscopy

Mössbauer spectroscopy measurements were conducted by Prof. Dr. F. Wagner, TUM. The Mössbauer measurements were performed at temperatures of 298 K and 4.2 K. Around 100 mg of dried nananoparticles were put in a liquid helium bath cryostat with the source of ^{57}Co in rhodium. The samples were kept in liquid nitrogen until being transferred into the Mössbauer sample holders in a nitrogen atmosphere. They were subsequently cooled in liquid nitrogen and transferred into the liquid helium bath of the cryostat.

Analysis of zeta potential

A Zetasizer Nanoseries NanoZS (Malvern Instruments GmbH, United Kingdom) at the Munich School of BioEngineering, TUM, was used to determine the zeta potential at various pH values. First, the nanocomposites were diluted to 0.1 $mg\,mL^{-1}$ in a volume of 1 mL using 1 mM NaCl. The pH was carefully adjusted to the desired value using concentrations of 10 mM and 100 mM of KOH and HNO_3. Finally, the volume was adjusted with 1 mM NaCl to a total volume of 1.5 mL. After incubation at RT for 30 min the pH was verified and adjusted if necessary. The Zeta potential was determined using the high concentration dip cell from Malvern. Both, pH and zeta potential, were recorded to determine the pH stability of the nanoparticle dispersion.

Ninhydrin colorimetric assay

Quantification of primary and secondary amines on the nanoparticle surface was performed by the ninhydrin colorimetric assay. For the preparation of the standard curve stock solutions of the amino acid glycine was diluted in 0.05% glacial acetic acid at different concentrations according to the supplier information (Sigma Aldrich N 7285). For both standards and samples, 1 mL of the ninhydrin reagent was added and mixed gently. The tubes were placed

into a boiling water bath for 10 minutes and subsequently cooled to RT. 5 mL of 95% ethanol were added to each tube. The absorbance was recorded at 570 nm on a microplate plate reader Synergy HT (BioTek, Bad Friedrichshall). The amine content was quantified using the glycine standard curve.

Separation capability of magnetic nanocomposites in milk

2.5 mg magnetic nanocomposites were added to 100 mL milk (ultra-pasteurized milk, 1.5% fat, Penny Market, Germany) and magnetically separated by using different separation strategies. To compare the separation capability the magnetic nanocomposites were either separated manually (a) or automatically separated by syringe pump (b) or peristaltic pump (c). For the manual separation 25 mL each of the magnetic nanocomposites spiked milk were filled in a glass container. The magnetic nanocomposites were attracted by applying a neodymium permanent magnet for 5 minutes. The milk was removed by using a disposable pipette. This step was repeated until 100 mL of the spiked milk were separated. For the automatic separation two adjustable neodymium magnets were used and connected to a peristaltic pump and a syringe pump for an automated flow of the spiked milk. To increase the interaction time of the magnetic nanocomposites in the magnetic field, a tube sample loop was created. The setup for the automated IMS is illustrated in Figure 4.47. To compare the separation ability of the magnetic nanocomposites in large volumes of complex food matrices, the iron content before and after separation in milk was analyzed. The iron content was quantified by ICP-MS measurements (Perkin Elmer ICP/MS Elan 6100) and kindly performed by C. Sternkopf. Prior to analysis a pressure-assisted acid microwave digestion procedure with hydrofluoric acid and nitric acid (1:3 v/v) for 10 at 130 °C, 10 min at 180 °C and 30 min at 210 °C was performed. Each sample was diluted in ultrapure water at the appropriate concentration.

3.2.5 Biotinylation of anti-SEB antibody S419/5/5/5

Biotinamidohexanoyl-6-aminohexanoic acid N-hydroxysuccinimide ester was dissolved in anhydrous DMSO at a concentration of 13.4 mM. The mixture was aliquoted and stored at -20 °C until further use. The anti-SEB antibody S419/5/5/5 (c = 1.39 mg mL^{-1}) stock solution was diluted in PBS to a concentration of 1 mg mL^{-1}. 25 µL of a freshly prepared 1 M sodium hydrogen carbonate buffer (pH 8.3) was added to 250 µL of the antibody solution and gently mixed. 2.5 µL of the Biotin-NHS-DMSO solution was added to the antibody (molar ratio 1:20) and incubated in a thermomixer at 23 °C and 600 rpm for one hour. The conjugation was stopped by adding 5 µL of 10% sodium azide in PBS. Removal of excess non-reacted biotin and reaction byproducts was accomplished in Amicon® ultracentrifugation filter units (nominal molecular weight limit: 30 kDa) by concentrating the sample, discarding the filtrate, then reconstituting the concentrate to the original sample volume with 0.5% (w/v) sodium azide in PBS. This process was repeated twice.

The concentration of the biotinylated antibody was measured by a nanophotometer. Hereby, 3 µL of the biotinylated antibody solution were carefully applied onto the measuring window of the nanometer. After closing the lid, the protein concentration was quantified by measuring the absorbance at 280 nm. Prior to each measurement, a blank measurement with 0.5% (w/v) sodium azide in PBS was performed at 280 nm. The total volume of the biotinylated antibody was determined. After each biotinylation 1/50 of the determined volume of 10% BSA was added.

3.2.6 IMS of SEB for MNC-SMIA I

Antibody functionalization of iron oxide-shell silica core nanocomposites

For the conjugation of biotinylated anti-SEB antibody S419/5/5/5 to the magnetic nanocomposites, 200 µL of biotinylated anti-SEB antibody S419/5/5/5 in bicarbonate puffer, pH 9.3 (c = 37.5 $\mu g\,mL^{-1}$, m = 7.5 µg , antibody to nancomposite ratio = 1:166) were added to 1.25 mg dried epoxy-functionalized magnetic nanocomposites. The reaction mixture was gently mixed in an overhead shaker for 24 hours at RT. After 24 hours, the magnetic nanocomposites were magnetically separated in a magnetic separation rack (MagnaRack™, Invitrogen) and washed three times with PBS, Tween (0.05% v/v). To block the unspecific binding sites, magnetic nanocomposites were resuspended in 1 mL of BSA (5% w/v) in PBS and subsequently mixed in an overhead shaker for two hours. Consequently, the antibody-functionalized magnetic nanocomposites were washed with PBS (see Figure 3.3). The antibody-functionalized magnetic nanocomposites were immediately used for IMS of SEB in milk.

IMS step of SEB in 0.6 mL milk

For each IMS procedure, a 0.6 mL-sample milk and 1.25 mg of biotinylated anti-SEB antibody-functionalized magnetic nanocomposites were used (c = 2.1 $mg\,mL^{-1}$). First, the antibody-functionalized magnetic nanocomposites in PBS were magnetically separated in a magnetic separation rack (MagnaRack™, Invitrogen). The liquid was removed and 600 µL of SEB spiked milk at the desired concentration was added. Due to the high binding affinity Protein LoBind Tubes (Eppendorf) were used. The reaction mixture was gently mixed in an overhead shaker for 2 hours at RT. After washing three times with PBS, Tween 20 (0.05% v/v) the magnetic nanocomposites were resuspended in 52 µL of casein 0.5%, Pluronic® F127 0.01% (w/v), which is nearly the sample volume capacity for the flow-channel in the microarray chip. A schematic illustration can be seen in Figure 3.3.

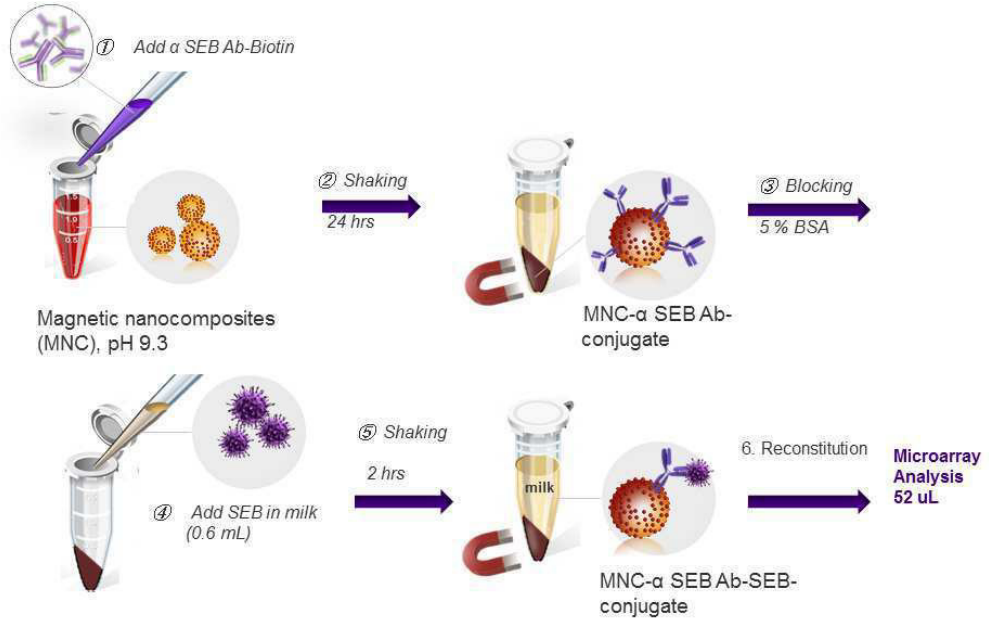

FIGURE 3.3: Schematic illustration of antibody functionalization and IMS of SEB with iron oxide-shell silica-core nanocomposites in milk.

3.2.7 IMS of SEB for MNC-SMIA II

Antibody functionalization of iron oxide-shell silica core nanocomposites

In order to conjugate the biotinylated anti-SEB antibody S419/5/5/5 to the magnetic nanocomposites, 200 µL of biotinylated anti-SEB antibody S419/-5/5/5 in bicarbonate puffer, pH 9.3 (c = 75 µg mL^{-1}, 15 µg, antibody to nancomposite mass ratio = 1:166) were added to 2.5 mg dried epoxy-functionalized magnetic nanocomposites. All following steps were carried out analogously to the previouisly described antibody functionalization of iron oxide-shell silica-core nanocomposites in small milk volumes.

IMS of SEB in 100 mL milk

For the IMS step 2.5 mg biotinylated anti-SEB antibody S419/5/5/5-functionalized magnetic nanocomposites were used. The antibody-conjugated magnetic nanocomposites were magnetically separated in a magnetic separation rack in order to remove the liqud (MagnaRack™, Invitrogen). SEB was spiked to 100 mL milk at the desired concentration (0 - 100 µg L^{-1}) and thoroughly mixed. Due to the high binding affinity of SEB a disposable 100 mL glass beaker was used. The antibody-functionalized magnetic nanocomposites were added to the SEB spiked milk samples. The reaction mixture was gently incubated in an overhead shaker for one hour at RT in order to conjugate the analyte SEB to the magnetic nanocomposites. For the IMS of the magnetic nanocomposites-SEB conjugates, the reaction mixture was consecutively transferred (15 mL each) in a small glass container. To attract the magnetic nanocomposites a neodymium magnet was manually attached for several minutes. The liquid was removed with a disposable plastic pipette.

This process was repeated until 100 mL of milk were completely separated. The magnetic nanocomposites were redispersed in 1 mL of PBS and transferred to a Protein LoBind Tube. After washing three times with PBS, Tween 20 (0.05%, w/v) in a magnetic separation rack the magnetic nanocomposites were resuspended in 52 µL of 0.5% casein, 0.01% Pluronic® F127 (w/v).

3.2.8 Microarray Chip Production

Microarray surface chemistry

JEFFAMINE coated glass slides were produced in-house and used as solid support. The coating procedure was performed as described in detail elsewhere [134, 135] with minor deviations. JEFFAMINE® ED-2003 was used instead of poly(ethylene glycol) diamine (DAPEG). A schematic illustration of the microarray chip surface chemistry is displayed in Figure 3.4.

1. Pretreatment of glass slides

In detail, engraved glass slides (26 mm x 76 mm x 1 mm) were cleaned by sonication in Hellmanex (2% in ultrapure water) for one hour, shaked overnight and subsequently sonicated for 30 minutes. Afterwards, the glass slides were washed with ultrapure water and treated with a freshly prepared mixture of 37% HCl and methanol (1:1 v/v) for one hour under gentle shaking. After a washing step in ultrapure water, the slides were treated with 97% sulfuric acid for one hour under gentle shaking. The glass slides were cleaned in ultrapure water, dried under a nitrogen stream and stored in a compartment dryer for 15 minutes at 100 °C.

2. Silanization

The pretreated glass slides were directly silanized with GOPTS by using a sandwich technique. Two glass slides were incubated at RT in a sandwich format with 600 µL of GOPTS for 3 hours in a closed chamber with freshly dried silica to reduce humidity. The glass slides were separated and thoroughly cleaned in ethanol. They were further cleaned by sonication in ethanol, methanol, and finally ethanol for 15 minutes each. Finally the glass slides were carefully dried under a nitrogen stream. Within this silanization process a self-assembled monolayer (SAM) of GOPTS was generated introducing epoxy groups.

3. PEG layer preparation

The silanized glass slides were coated with JEFFAMINE® ED-2003. JEFFAMINE® ED-2003 was melted at 98 °C. Two silanized glass slides were incubated overnight in a sandwich format with 600 µL of JEFFAMINE® ED-2003 at 98 °C. The sandwiches were separated, thoroughly washed in ultrapure water and subsequently sonicated for 15 minutes. Afterwards, the slides were dried under a nitrogen stream and stored in a desiccator under nitrogen atmosphere at RT.

4. NHS activation of microarray glass slide

JEFFAMINE-coated glass slides were activated using a mixture of 160 mg N,N′-disuccinimidyl carbonate (0.62 mmol) and 8 mg 4-(dimethylamino)pyridine (0.065 mmol) dissolved in 3.2 mL dry N,N′-dimethylformamide and 250 µL dry triethylamine. Two activated glass slides were incubated at RT in a sandwich format with 600 µL of the prepared solution for four hours. Afterwards, the glass sandwiches were carefully separated, washed and sonicated for 15 min in methanol and dried under nitrogen atmosphere.

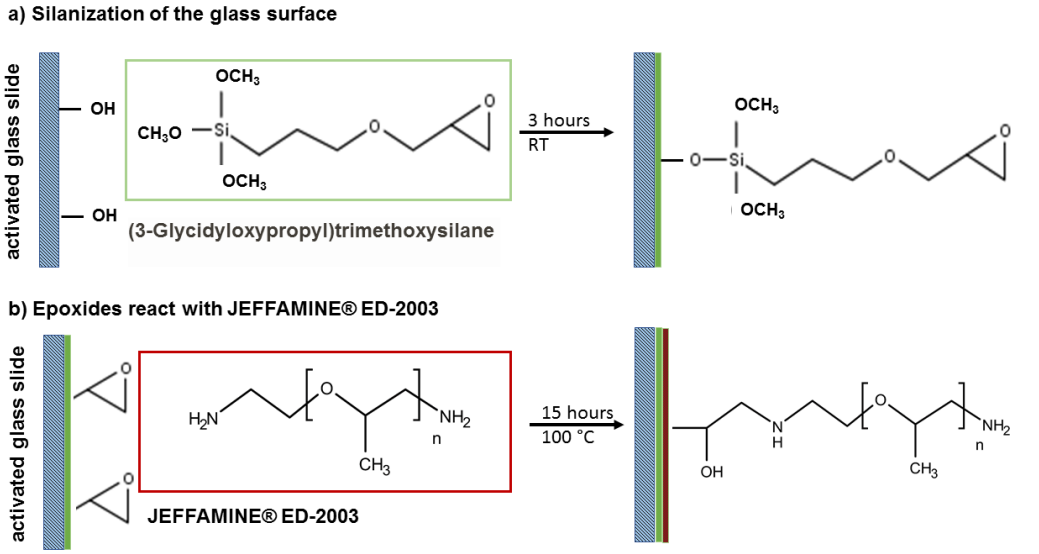

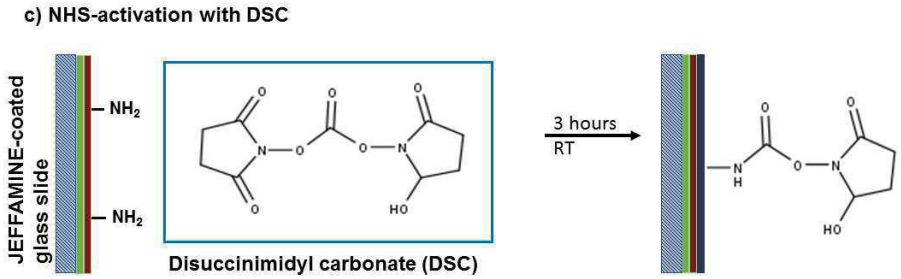

FIGURE 3.4: Schematic illustration of microarray chip surface chemistry. Adapted and modified from [134].

Immobilization of antibodies

Antibodies were covalently immobilized on the NHS-activated microscopy glass slides after deposition by contact printing (spotting). The antibody microarrays were generated using the BioOdyssey Calligrapher miniarrayer from Bio-Rad (Munich, Germany) and a solid pin SNS 9 from ArrayIT (Sunnyvale, CA, USA). The monoclonal capture antibody S1001/4/6 (anti-SEB) was dissolved in spotting buffer containing 20% trehalose and 0.05% Pluronic® F127 (c = 0.63 mg mL^{-1}). The spotting solutions (35 µL) were prepared in a polypropylene microtiterplate (MICROPLATTE, 384 deep well, Greiner bio-one). A negative control (spotting buffer) and positive control (anti-mouse IgG peroxidase, c = 11 mg mL^{-1} in spotting buffer) were immobilized. Around 1 nL of antibody solution was immobilized on the activated glass slide. The conditions in the spotting chamber were set to a humidity of 55% and 20 °C. Each microarray slide consisted of two separate flow channels with a distance of 11.75 mm. Five replicates of each antibody solution were immobilized as spots on the microarray surface (y-direction). The spotting distance in y-direction was 1.1 mm and the distance between the rows in x-direction was 1.3 mm. After printing, the processed microarrays were stored in an incubator overnight at 25 °C and 55% humidity. To block free, active groups on the microarray chip surface, glass slides were treated consecutively with TRIS-HCl (1 M TRIS, pH 8.5), PBS and ultrapure water for 15 min each. The microarray chips were dried under nitrogen stream.

Preparation of microarray chips

The antibody microarray chip consisting of the prepared glass slide and a (poly)methyl methacrylate (PMMA) solid support was assembled via double-sided adhesive foil (Adhesives Research, Ireland) as published elsewhere [136]. A schematic illustration of the microarray chip is shown in Figure 3.5. One microarray chip contained two flow cells and therefore was used for two

experiments. The two flow-through channels on microarray chips were created by means of a double-sided acrylic adhesive film on PE foils containing laser-cutted microchannel structures (Volume: 62 µL). The PMMA carriers consisted of a drilled inlet and an outlet hole for a connection with the MCR3 flow chamber holder. The flow channels were filled with 60 µL of 1% bovine serum albumin (BSA) in phosphate buffered saline (PBS). The antibody microarray chips were stored at 4 - 8 °C. The microarray chip was inserted into the heatable microarray chip loading unit.

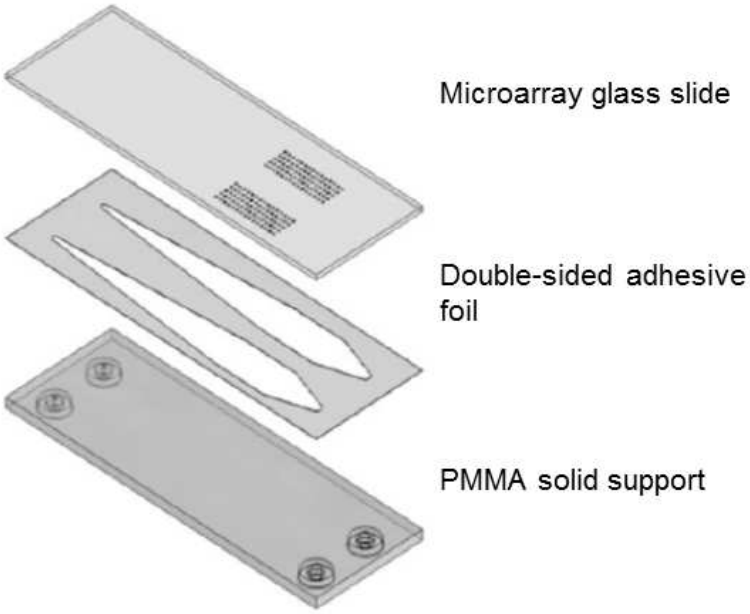

FIGURE 3.5: Schematic illustration of a microarray chip, consisting of the microarray glass slide (top), double-sided adhesive foil with two flow channels (middle) and a plastic carrier (bottom) [136].

3.2.9 MCR 3

The Munich Chip reader 3rd generation (MCR 3) was developed as a standalone microarray analysis platform for the automated processing of flow-based chemiluminescence microarrays at our institute over the last years and is described in detail elsewhere [112, 136]. It was built by GWK Präzisionstechnik GmbH (Munich, Germany).
For this thesis, the advanced microarray analysis platform MCR 3 SLT (sample loop and temperature controlled flow cell), constructed by GWK Präzisionstechnik GmbH, was used (Figure 3.6). The schematic fluidic plan is displayed in the appendix. Due to a reconstruction of the chip loading unit and the upgrade by a thermoelectric heating module as reported previously, the temperature on the microarray surface can now be controlled with a precision of $\pm$ 1 °C [137].

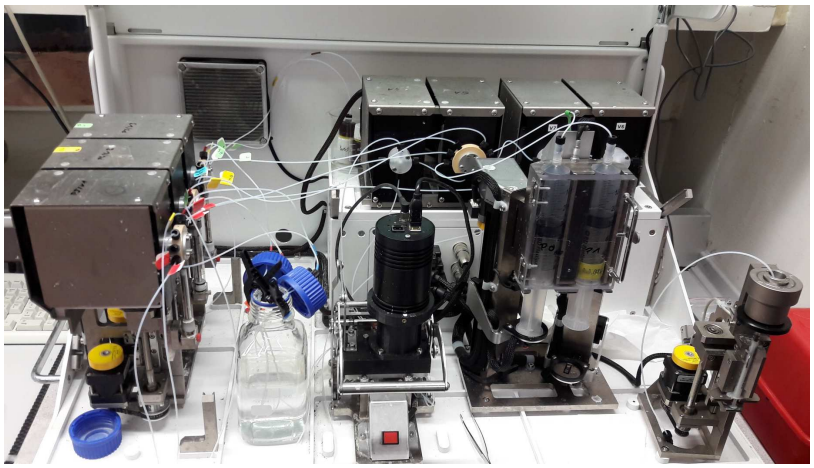

FIGURE 3.6: Microarray analysis platform MCR 3 SLT.

3.2.10 Procedure of CL-SMIA on analysis platform MCR 3

For all microarray experiments the microarray analysis platform MCR 3 SLT was used (Figure 3.6). Following reagents were used for the CL-SMIA: 1. Running and washing buffer (casein 0.5% w/v, 0.01% Pluronic® F127 in PBS pH 7.6), 2. Biotinylated detection antibody (S419/5/5/5, c = 0.9 µg mL^{-1} in casein 0.5% w/w, RKI, Germany), 3. Streptavidin poly-HRP (c = 0.2 µg mL^{-1} in casein 0.5% w/v, Senova, Germany), 4. CL substrates (luminol and hydrogen peroxide, 1:1, v/v, Cyanagen, Italy). 0.63 mg L^{-1} of the capture antibody S1001/4/6 were immoblized on the microarray surface. The MCR 3 SLT analysis platform was prepared as described previously. Therefore, syringes, tubes and valves of the MCR 3 SLT were washed using a washing program. Before the measurment, the process solution containers were connected with PTFE tubing of the MCR 3 SLT and loaded automatically in the instrumentation.
Prior to each measurement, a background image of the microarray chip was taken for 60 s with a CCD camera. The microarray chip was inserted in the

loading unit of the MCR 3 SLT. The total automated process of the CL-SMIA is summarized in Table 3.1. For the detection of SEB in milk, SEB was spiked at different concentrations to milk. The microarray channel temperature was set to 37 °C. 600 µL of the SEB spiked milk sample was injected manually into the microfluidic system using a disposable sample syringe. Then 60 µL of the sample was pumped stepwise (intervals of 30 s) through the flow channel at a flow rate of 5 $\mu L\,s^{-1}$. This step was repeated ten times. After a washing step (2000 µL of running buffer, 100 $\mu L\,s^{-1}$), the biotin-conjugated detection antibody solution was pumped in stop-flow mode through the microarray channel (60 µL increments at a flow rate of 2 $\mu L\,s^{-1}$, interaction time of 5 s). This step was repeated ten times. After a second washing step (2000 µL, 15 mL, 20 $\mu L\,s^{-1}$), 600 µL of streptavidin poly-HRP was pumped through the flow channel at a flow rate of 20 $\mu L\,s^{-1}$. After a third washing step (2000 µL, 100 $\mu L\,s^{-1}$), 200 µL of each CL reagent (hydrogen peroxide and luminol solution) premixed in a syringe (1:1, v/v) were pumped through the microarray chip at a flow rate of 20 $\mu L\,s^{-1}$. The assay duration is about 18 min. The chemiluminescence signal was recorded by the CCD camera for 60 s. The CL images of the SMIA were processed as described above. As previously described, washing steps of the microfluidic system were performed with with Tergazyme (c= 1%, v/v), Hellmanex (2% v/v) and subsequently with deionized water.

In order to obtain a calibration curve, a dilution series of SEB in milk was prepared (0 - 1000 $\mu g\,L^{-1}$). A sample aliquot of 600 µL was injected into the MCR 3 SLT. LOD was calculated by the mean CL signals of blank measurements using milk (n = 3) plus three times the standard deviation. The measurements were performed as triplicates. For determination of the recovery, milk samples with spiked SEB concentrations in the linear range of the sigmoidal calibration curve were performed and subsequently measured on the MCR 3. The SEB concentration was quantified by using the obtained calibration curve.

3.2.11 Procedure of the MNC-SMIA I and II on analysis platform MCR 3 SLT

As running buffer and as washing buffer casein (0.5% w/v) with Pluronic® F127 (0.01% w/v) in phosphate buffered saline was used. For the enzyme labeling, streptavidin poly-HRP (c = 0.4 $\mu g\,mL^{-1}$ in running buffer) was used. The CL reaction kit contains hydrogen peroxide, luminol, and enhancers as substrate. The concentration of the capture antibody S1001/4/6, immobilized on the microarray surface, was 0.63 $mg\,L^{-1}$. Before starting the experiment, all syringes, tubes and valves of the microarray analysis platform MCR 3 SLT were intensively washed. All process solution containers were connected with PTFE tubing of the MCR 3 and loaded automatically in the instrumentation before the measurement. Two measurements could be performed with one microarray, because one chip consists of two flow-through channels. Prior to the usage of each disposable chip, a background image of

TABLE 3.1: Total process of the automated CL-SMIA on the MCR 3 SLT, assay duration: 18 minutes.

Step	**Volume**	**Flowrate / T**
Heating of flow cell		37 °C
Sample injection	600 µL	
Washing step	2000 µL	100 µL s^{-1}
Detection antibody	600 µL	2 µL s^{-1}
Washing step	2000 µL	20 µL s^{-1}
HRP labeled streptavidin	600 µL, 600 µL	20 µL s^{-1}
Washing step	2000 µL	20 µL s^{-1}
CL substrates (luminol, hydrogen peroxide)	200 µL each	20 µL s^{-1}
Picture with CCD camera		60 s
Washing step	5000 µL	500 µL s^{-1}
Washing step	5 x 1000 µL	68 µL s^{-1}
Washing step	3 x 5000 µL	500 µL s^{-1}

the microarray chip was taken for 60 s with a CCD camera. In order to load 52 µL of the sample into the microarray channel, an in-house made adaptor for the flow-through microarray chips was used (Figure 3.7).

To achieve an optimal interaction between conjugated magnetic nanocomposites and immobilized antibodies, the filled microarray chip was sealed and inserted in a in-house made magnetic incubation unit and incubated for one hour at 37 °C under gentle shaking at 100 rpm (Figure 3.8). After the magnetic incubation step, the microarray chip was inserted in the heatable loading unit of the MCR 3 SLT. Then, all program steps are performed automatically. The flow-cell was heated to 37 °C during the assay. The flow cell was washed three times with 1 mL (100 µL s^{-1}) of running buffer. SEB immobilized to the biotinylated antibody-conjugated magnetic nanocomposites was bound by the anti-SEB capture antibodies immobilized on the microarray chip surface during the stop-flow incubation process and detected by streptavidin poly-HRP (600 µL, 2 µL s^{-1}). Unbound streptavidin poly-HRP was removed by a washing step with running buffer (1 mL, 100 µL s^{-1}). To start the CL reaction, 200 µL of each CL reagent (hydrogen peroxide and luminol solution) premixed in a syringe (1:1, v/v) were pumped through the microarray chip at a flow rate of 20 µL s^{-1}. The CL signal was recorded by the CCD camera for 50 s. All assay parameters are summarized in Table 3.2. The complete microfluidic system was rinsed two times with water. Every week, the microfluidic system was rinsed with Tergazyme (c = 1% v/v) and Hellmanex (2% v/v) and finally with deionized water to prevent any cross-contamination.

FIGURE 3.7: Direct injection of the reaction mixture in the microarray flow channel by using an housemade adapter.

For the calibration curve, a dilution series was prepared by spiking into milk at various concentrations in a range of 0 - 5000 $\mu g\,L^{-1}$. Samples were processed by IMS as described previously. LOD was calculated by the mean CL signals of blank measurements using antibody-functionalized magnetic nanocomposites in pure milk (n = 3) plus three times the standard deviation. All measurements were performed as triplicates. For recovery experiments SEB was spiked at three different concentrations in the linear range of the sigmoidal calibration curve and measured on the MCR 3 SLT as described previously. CL signals were quantified according to the calibration curve.

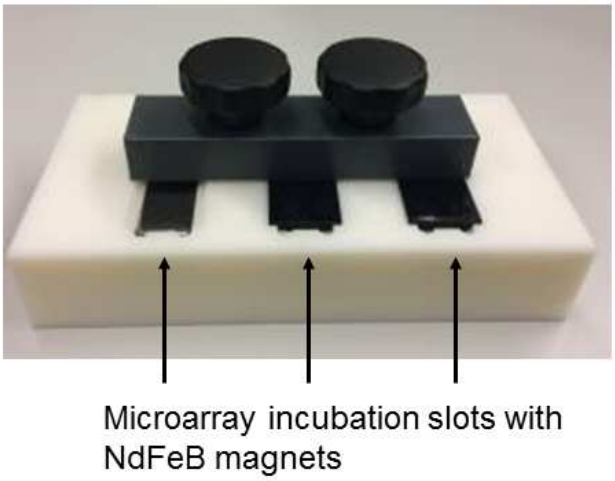

FIGURE 3.8: Magnetic chip incubation device (constructed by IWC workshop).

TABLE 3.2: Total process of the automated MNC-SMIA I and II on the MCR 3 SLT, assay duration: 8 minutes.

Step	**Volume**	**Flowrate / T**
Heating of flow cell		37 °C
Washing step (3x)	1000 µL	100 µL
HRP labeled streptavidin	150 µL, 600 µL	50 µL, 2 µL
Washing step (3x)	1000 µL	100 µL
CL substrates (luminol, hydrogen peroxide)	200 µL each	20 µL s^{-1}
Picture with CCD camera		50 s
Washing of the flow-system	150 µL each	500 µL s^{-1}
Washing of the microarray chip (3 x)	1000 µL each	68 µL s^{-1}

3.2.12 Read out and data analysis

Every MCR 3 measurement resulted in a 2-D CL image, which was automatically evaluated by the microarray analysis software (MCR Visualization 1.0.6, GWK Praezisionstechnik, Germany). The background image was substracted from each CL image. A grid was applied to separate the spots. The mean value of the ten brightest pixels per spot was taken, and an average value for each row, containing five spots, was calculated. CL spots with data deviating more than 15% from the average were marked as outlier and not included in the data analysis.

Chapter 4

Results and Discussion

4.1 Iron oxide-shell silica-core nanocomposites

One important task of this thesis was the design of iron oxide-based superparamagnetic nanocomposites, which exhibit individually tailored morphological, physical and chemical characteristics and are suitable for the application in IMS coupled with a sensitive microarray analysis.
For the IMS, two essential magnetic properties should be combined in one nanocomposite: 1) superparamagnetism for easily switching on / off the magnetic response and (2) simple magnetic manipulation by permanent magnets.

Parts of this chapter have been published in Journal of Magnetic Materials and Magnetism, 442 (2017), pp. 497–503:
"Production and characterization of long-term stable superparamagnetic iron oxide-shell silica-core nanocomposites", Angelika Nistler, Carolin Hartmann, Christine Rümenapp, Matthias Opel, Bernhard Gleich, Natalia P. Ivleva, Reinhard Niessner, and Michael Seidel.

4.1.1 Synthesis strategy of bare iron oxide-shell silica-core nanocomposites

A novel rapid and simple synthesis strategy based on thermal decomposition of iron(III) oleate for the production of superparmagnetic silica-core and iron oxide-shell nanocomposites was developed. It combines the *in situ* synthesis of small iron oxide nanoparticles composed of maghemite with their simultaneous highly uniform loading onto mesoporous silica nanoparticles.
One major drawback of current synthesis strategies for the preparation of silica-core iron oxide-shell nanocomposites is that magnetic nanoparticles usually have to be pre-synthesized and then subsequently doped onto the silica nanomaterial. This involves multiple complex and time-consuming synthesis steps. Until now, only few reports have been published about the *in situ* fabrication of magnetic nanoparticles and simultaneous deposition onto silica beads, but yet lack in shortness of synthesis time and operation steps [29, 30].

Thus, with regard to time-effectiveness and simplicity the proposed synthesis strategy appears to be a major advantage.

Firstly, the iron(III)oleate precursor is synthesized as published elsewhere [13]. Hereby the metal-oleate complex is generated *in situ* from the reaction of sodium oleate and iron(III) chloride at a temperature of 70 °C. Secondly, the precursor iron(III)oleate, oleic acid and commercially available poly-disperse mesoporous silica nanoparticles in 1-octadecene are stirred at RT and subsequently heated for either 5 or 30 minutes at 320 °C resulting in a simultaneous *in situ* growth of maghemite nanoparticles (8.4 $\pm$ 1.0 nm) and their stable deposition onto silica nanoparticles (381 nm $\pm$ 111 nm). The total synthetic procedure is summarized in Figure 4.1.
The reaction mixture was centrifuged (4500 rpm, 10 min) to remove unbound iron oxide nanoparticles. The precipitate containing the nanocomposites was washed by performing two sequential cycles of centrifugation and resuspension in hexane. Magnetic separation in hexane by using a permanent magnet was performed to remove vacant, non-magnetic silica nanoparticles.

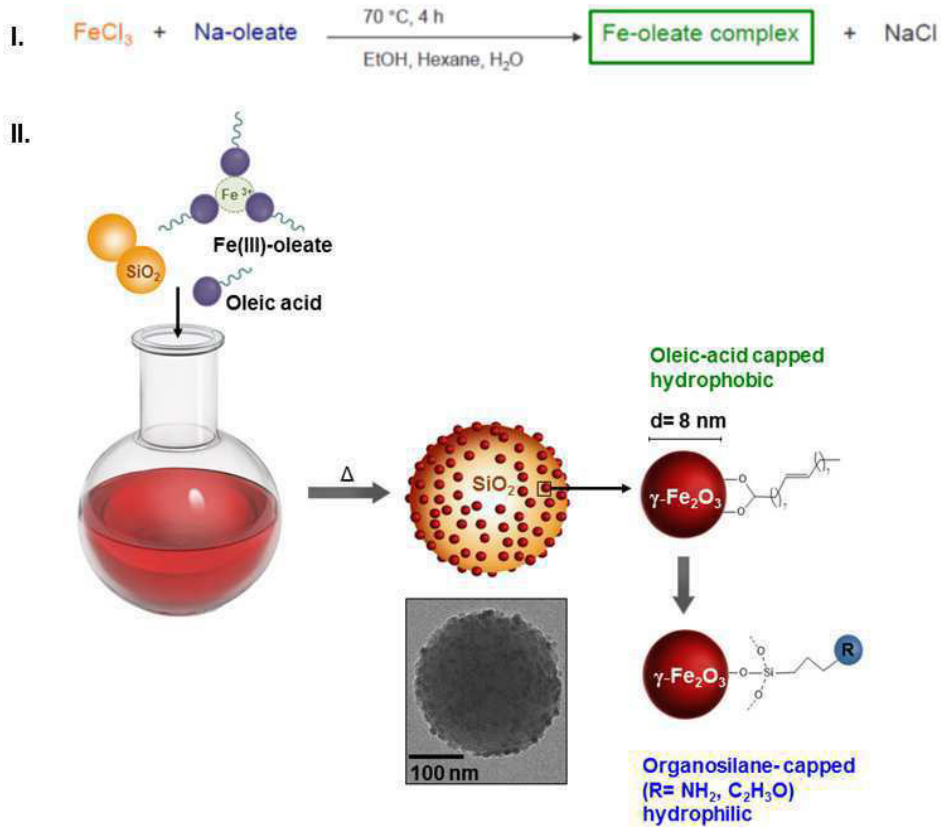

FIGURE 4.1: Schematic illustration of the synthesis procedures of I. Iron(III)oleate and II. Iron oxide-shell silica-core nanocomposites.

4.1.2 Characterization of bare iron oxide-shell silica-core nanocomposites

Iron oxide-shell silica-core nanocomposites were extensively characterized by several analytical techniques such as SEM, TEM, RM, Mössbauer spectroscopy and SQUID magnetometry to learn more about their size, morphology as well as their mechanical, magnetical and chemical characteristics.

Size and morphology

Electron microscopy (SEM and TEM) and Dynamic Light Scattering (DLS) were applied to characterize size and morphology of the iron oxide-shell silica-core nanocomposites. For our experiments, commercially available mesoporous silica nanoparticles with a pore size of 4 nm were used. As shown in Figure 4.2a, SEM image of the silica precursor reveals a relatively broad size distribution with an average size of 381 $\pm$ 111 nm. The mesoporous structure of the silica nanoparticle can be seen in the TEM image Figure 4.2b.
Both representative SEM images (Figure 4.3a, b) of bare nanocomposites clearly demonstrate that small iron oxide nanoparticles are highly uniformly deposited onto the surface of each silica nanoparticle. The nanocomposites exhibit a spherical, raspberry-shaped morphology (Figure 4.3). The size distribution of the nanocomposites was determined with the *Analyze Particle* feature of the image-processing software Image J from SEM images and revealed an average nanocomposite size of 329 $\pm$ 123 nm (n = 85).
For a better particle size determination of small iron oxide nanoparticles on the magnetic nanocomposite, the supernatant of the reaction mixture directly after the separation of magnetic nanocomposites by centrifugation was analyzed. TEM analysis revealed the presence of small iron oxide nanoparticles with a core diameter of 8.4 $\pm$ 1.0 nm (Figure 4.4). This confirms the assumption that, the supernatant after centrifugation only contains the excessive, vacant small nanoparticles.

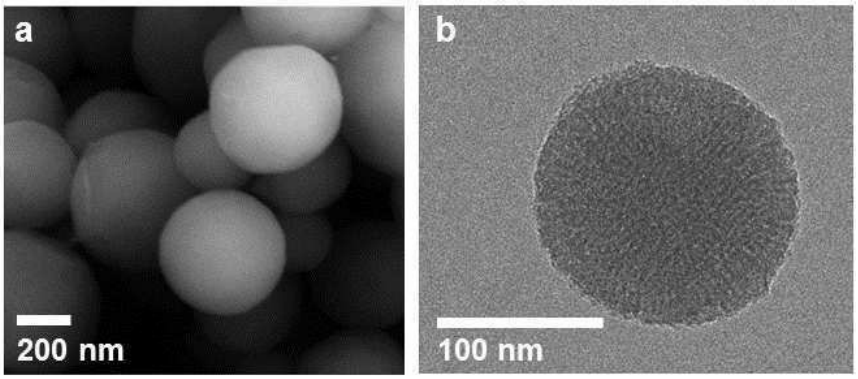

FIGURE 4.2: Representative electron microscopy images of bare silica nanoparticles: Field emission SEM image a) and TEM image b).

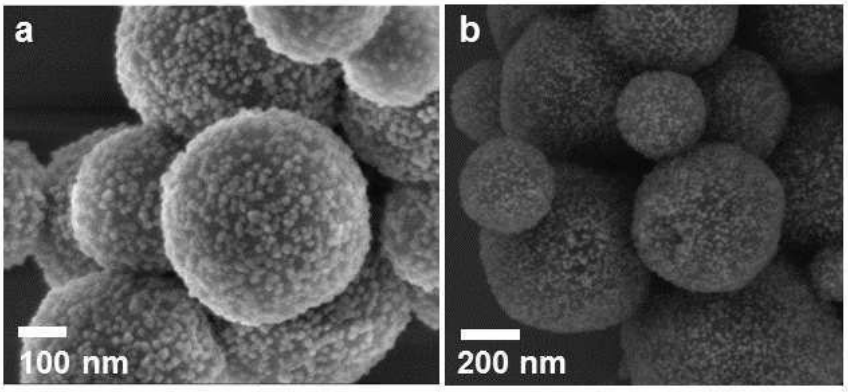

FIGURE 4.3: Representative field emission SEM images of bare iron oxide-shell silica-core nanocomposites.

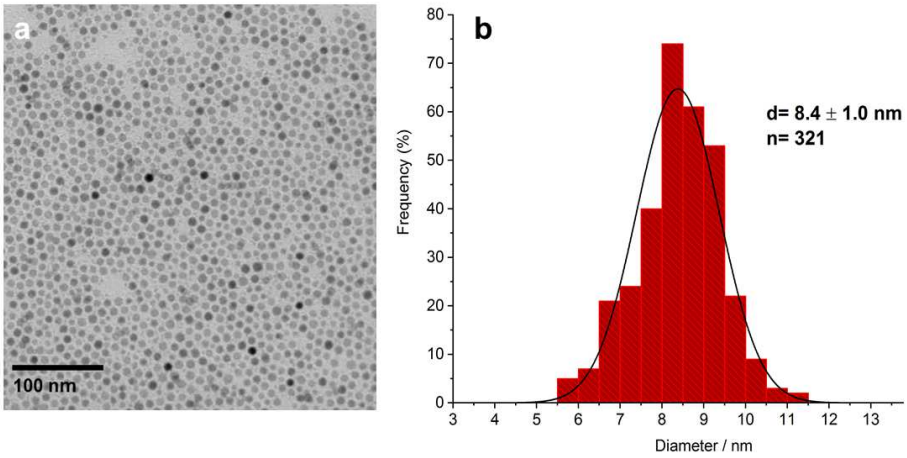

FIGURE 4.4: Small iron oxide nanoparticles: TEM image a), analysis of size distribution b).

Magnetic characteristics

Magnetic properties of iron oxide-shell silica-core nanocomposites were investigated in a SQUID magnetometer (MPMS XL-7) with a magnetic field of up to 5 T applied in plane. In order to analyze the magnetic behaviour of nanocomposites the magnetization M as a function of the magnetic field H was measured by SQUID magnetometry.
When an external magnetic field is applied to superparamagnetic nanoparticles, the magnetic moments in particles generally align towards the applied field and a net magnetization is generated. In absence of a magnetic field, thermal fluctuations outcompete the dipole-dipole interactions in particles, a random flip of the magnetization is induced, and the particles do not show any remanent magnetization (M_r) at zero field [11]. Thus, for superparamagnetic particles the magnetization as a function of the applied magnetic field shows a reversible sigmoidal (S-shaped) curve at RT [12] but no hysteresis.
The obtained M(H) curve of the nanocomposites clearly demonstrates a sigmoidal shape at 300 K (Figure 4.5). Additionally, our data does not show any remanent magnetization at zero field (see inset Figure 4.5), revealing the desirable superparamagnetic characteristics of our nanocomposites. The slight shift, which can be seen in the inset of Figure 4.5 is caused by measurement artefacts and not due to hysteresis.

In general, superparamagnetism is only present in very small iron oxide nanoparticles below the size of 30 nm [11]. As described previously, TEM measurements demonstrated a nanoparticle size of around 8.4 ± 1.0 nm for the small iron oxide nanoparticles immobilized onto the silica sphere. Thus, the presence of superparamagnetism in our nanocomposites is perfectly consistent with the nanoparticle size limit in literature for superparamagnetic nanoparticles.
Next, M_S was calculated according to the obtained M-H curve. M_S is the maximum magnetic saturation, when all the magnetic dipoles of the particles are aligned with the external magnetic field. Since the nanocomposite is composed of both iron oxide nanoparticles and silica, it is essential to note that the M_S value was calculated per gram maghemite.
Overall, the obtained M_S value is around 17 $A\,m^2\,kg^{-1}$(γ-Fe_2O_3), which is higher than those observed for similar silica core iron oxide shell nanocomposites published elsewhere [24, 25, 30].

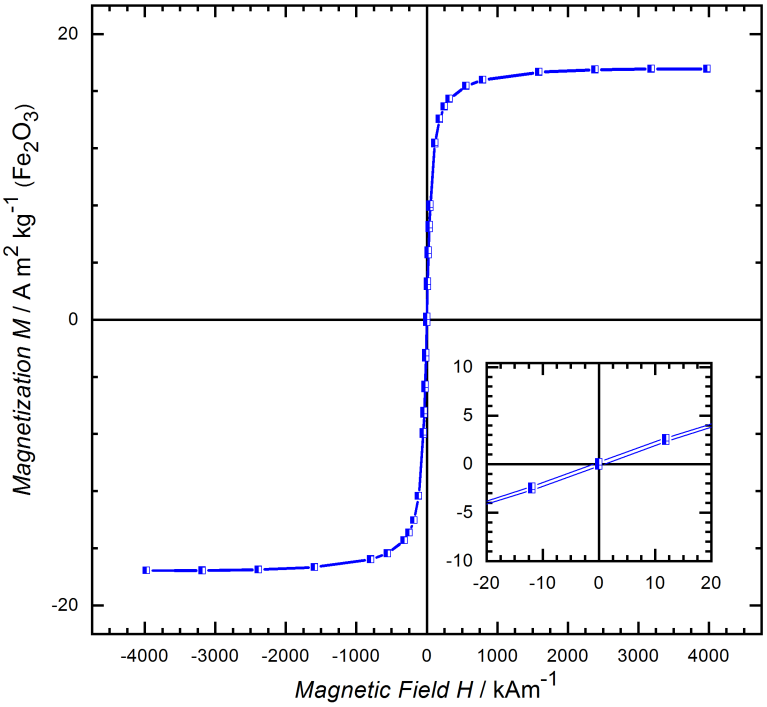

FIGURE 4.5: Magnetization measurement of bare iron oxide-shell silica-core nanocomposites as a function of the applied magnetic field at 300 K.

To further verify the nature of magnetism of our nanocomposites, we performed zero field (ZFC) and field-cooled (FC) measurements of the temperature dependence of the magnetization. As displayed in Figure 4.6, M(T) is plotted for the sample cooled down from 300 K to 4 K at 0 T (ZFC) or 5 T (FC), resepectively. Then, M(T) was measured while warming up the sample at a small measuring field of 10 mT [12]. As expected for superparamagnetic particles, a clear difference between the ZFC and FC data at low temperatures was evident (Figure 4.6). The curve obtained after ZFC shows a maximum around 65 K giving the blocking temperature T_B of the synthesized nanocomposites. T_B indicates the transition between superparamagnetic behavior and blocked state [138]. T_B is far below RT. Hence, the magnetic precondition for their bio-application is fulfilled.

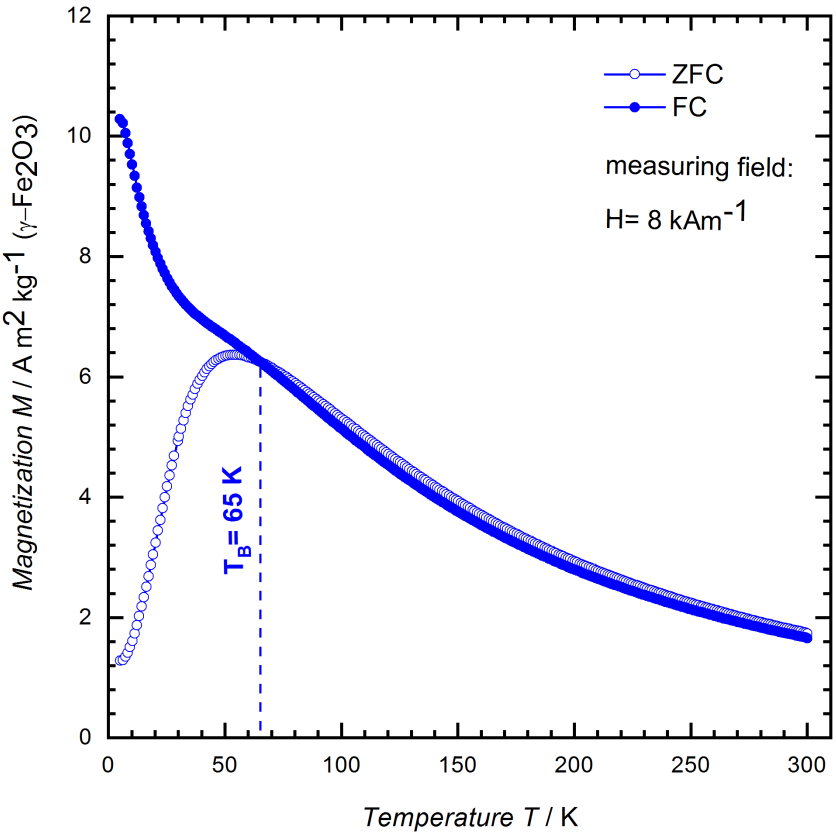

FIGURE 4.6: Magnetization measurement of bare iron oxide-shell silica-core nanocomposites as a function of the temperature, taken at an applied field of 8 kA m^{-1} after coooling in 4000 kA m^{-1} (field-cooled, closed symbols) or in zero field (open symbols).

This magnetic behavior can be utilized to rapidly attract nanocomposites in hexane towards a permanent magnet (< 30 s) and to re-disperse them by gentle tapping after removal of the external magnetic field (Figure 4.7a).
As expected, individual iron oxide nanoparticles with an average core diameter of about 9 nm, present in the synthesis supernatant, were not separable by a permanent magnet (Figure 4.7a). This can be explained by the fact, that maghemite nanoparticles below 30 nm show a higher thermal energy than the magnetic anisotropy at RT [8, 139].
In summary, the small superparamagnetic iron oxide nanoparticles attached on the silica sphere in the nanocomposite, form a magnetic cluster domain, which contributes to the magnetic attraction towards an external magnetic field. This resulted in a rapid separation of the whole nanocomposite [139], whereas the small iron oxide particles were not separable by a permanent magnet.
Hence, the investigation of the magnetic properties confirmed that the synthesized iron oxide-shell silica core nanocomposites combine both desirable magnetic features - the easy manipulation by permanent magnets and superparamagnetism for easily switching on and off the magnetic response.

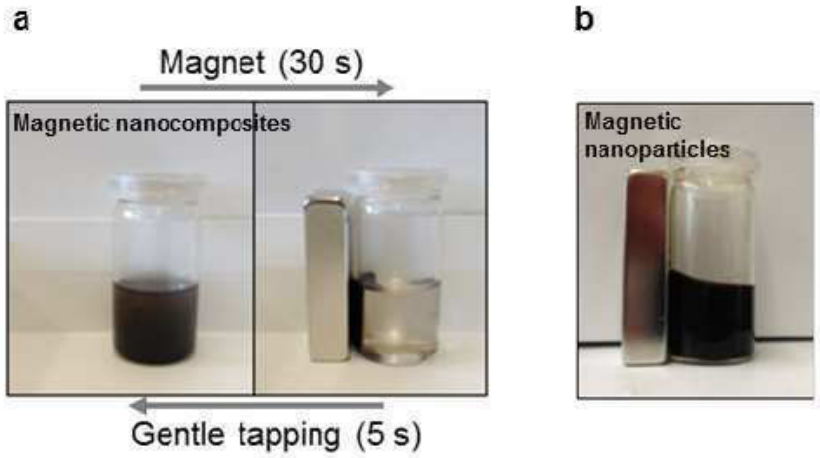

FIGURE 4.7: Attraction and re-dispersion of iron oxide-shell silica-core nanocomposites in absence and presence of a magnet in hexane a), iron oxide nanoparticles (8.4 nm +- 1.0 nm) in hexane b).

Chemical characteristics

Raman Microspectroscopy

Both iron oxides magnetite (Fe_3O_4), a mixed Fe (II)-Fe(III) oxide, and maghemite (γ-Fe_2O_3), a Fe(III) oxide exhibit magnetic characteristics, and therefore can be used for the synthesis of magnetic nanoparticles [52]. RM and Mössbauer spectroscopy were applied to analyze the oxidation state of the iron core in our magnetic nanocomposites.

RM has already been successfully applied for analysis of different magnetic nanoparticles [59, 60] and various iron oxides [58, 59, 61, 62]. Magnetite typically shows a noticeable band at 665 cm^{-1} and a weak broad band at 540 cm^{-1}. The spectral signature of maghemite is not well defined and seems to depend on sample preparation or sort of precursor, because it is directly related to the degree of crystallinity of the material [61]. In most publications the Raman spectra of maghemite can be characterized by two broad bands around 370 cm^{-1}, 500 cm^{-1} with approximately similar intensities and a strong broad band around 700 cm^{-1} [61, 62].

Although magnetite and maghemite have been intensively studied by RM, there are still discrepancies in the published data. A comparison of various publications reveal slight differences in spectral band positions of magnetite and maghemite. Hence, for a reliable characterization of the iron oxidatation state in the magnetic composites, magnetite and maghemite nanoparticle references have been synthesized.

Figure 4.8 shows Raman spectra of reference iron oxide-based nanoparticles (magnetite and maghemite) as well as a spectrum of the freshly prepared suspension of iron oxide-shell silica-core nanocomposites. It revealed three broad bands around 350 cm^{-1}, 500 cm^{-1} and 700 cm^{-1}. Here, a perfect match of the spectral signature of nanocomposites and maghemite nanoparticles could be demonstrated. Additionally, the absence of any other iron oxide forms could be verified.

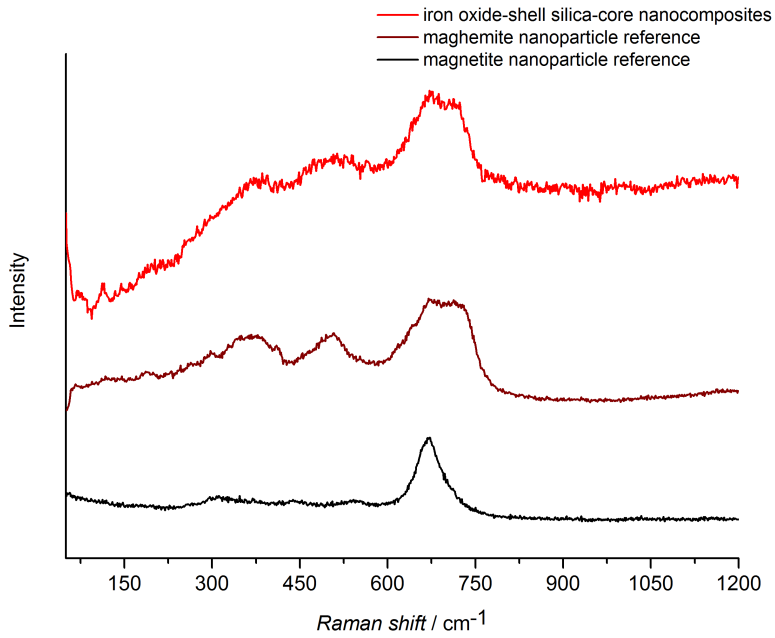

FIGURE 4.8: Raman spectra of iron oxide-shell silica-core nanocomposite, magnetite and maghemite nanoparticle references.

Mössbauer spectroscopy

A further method for a distinction between Fe(II) and Fe(III) is Mössbauer spectroscopy. Mössbauer spectroscopy is very sensitive to different iron oxides and iron oxide-hydroxides and allows a reliable confirmation of the Raman data [52, 63].
For the determination of the oxidation state of the iron oxide-shell silica-core nanocomposites Mössbauer spectroscopy was performed at a temperature of 4.2 K. Maghemite and magnetite reference nanoparticles were analyzed analogously at 4.2 K.
Maghemite and magnetite nanoparticles in a size range smaller than 10 nm are superparamagnetic at ambient temperature [140]. This leads to a collapse of the magnetic splitting giving a broad pattern with only little structure, which makes it hard or even impossible to distinguish Fe(II) and Fe(III) and therefore magnetite and maghemite [141]. At low temperatures like 4.2 K this superparamagnetic relaxation is blocked and the spectra are magnetically splitted with narrow lines as shown in Figure 4.9, and Figure 4.10 [142, 143]. The Mössbauer spectrum of magnetite nanoparticles is shown in Figure 4.9. In the spinel structure of magnetite (Fe_3O_4) the octahedral sites are occupied by one Fe(II) and one Fe(III), the tetrahedral sites are occupied by one Fe(III) per formula unit.
Due to the different isomer shifts of Fe(II) and Fe(III) the Mössbauer spectrum of magnetite consists of two discrete sextets of its magnetic hyperfine splitting, which are slightly shifted from each other [63]. As displayed in Figure 4.9 the most prominent feature caused by the presence of Fe(II) is the peak at the position indicated by an asterisk (*).

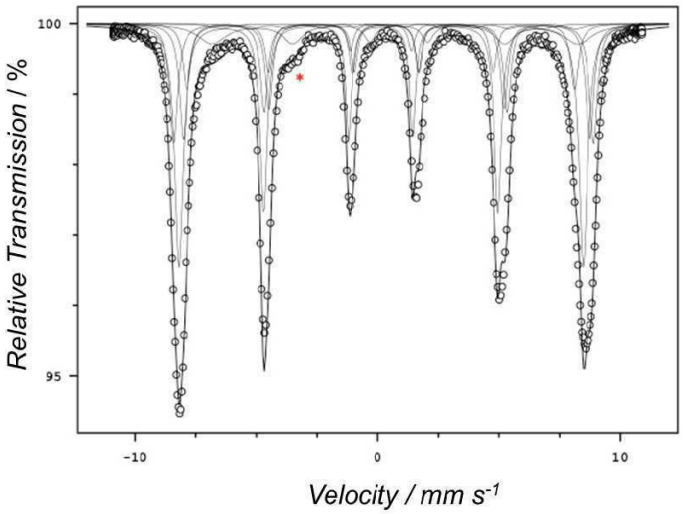

FIGURE 4.9: Mössbauer spectrum of magnetite nanoparticles at 4.2 K.

In maghemite (γ-Fe_2O_3), Fe(III) is on the octahedral and on the tetrahedral sites of the lattice sites. We expect to only obtain one sextet of its magnetic hyperfine splitting (Fe_3O_4), which is displayed in Figure 4.10a. Additionally, the absence of the Fe (II) peak is prominent.
The Mössbauer spectrum of iron oxide-shell silica-core nanocomposites clearly shows the typical sextet of maghemite (Figure 4.10b) and the absence of Fe(II). In summary, the iron oxide-shell silica-core nanocomposites are composed of maghemite, which confirms the previously described results of RM.

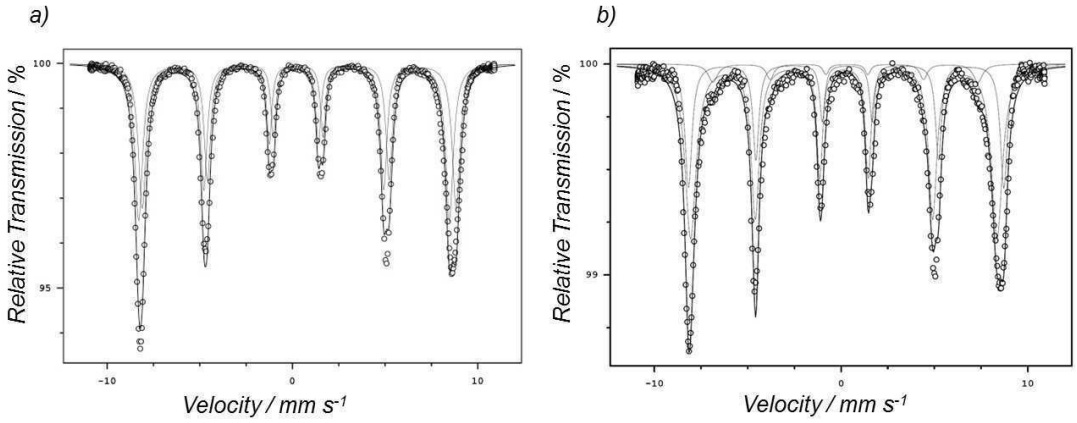

FIGURE 4.10: Mössbauer spectrum at 4.2 K of a) maghemite nanoparticles, b) iron oxide-shell silica-core nanocomposites.

Surface Characterization by Fouriertransformed Infrared Spectroscopy

FT-IR can be applied to analyze the surface characteristics of the magnetic nanocomposites due to the vibration and rotation of the molecules under the influence of infrared light [65]. Oleic acid is a commonly used surfactant, which forms a strongly bonded protective monolayer on the nanoparticle surface and stabilizes the iron oxide nanoparticles synthesized by thermal decomposition [35, 144]. To understand the adsorption mechanism of the oleic acid on the surface of small iron oxide nanoparticles, FT-IR measurements were performed of the surfactant oleic acid and the iron oxide-shell silica-core nanocomposite coated with oleic acid.

A FT-IR spectrum of the surfactant oleic acid was measured in order to verify the oleic acid-capping on the nanoparticle surface. The FT-IR spectrum of oleic acid (Figure 4.11 b, clearly shows the typcial C=O stretching peak at 1707 cm^{-1}. Two sharp bands at 2921 cm^{-1} and 2852 cm^{-1} were attributed to assymetric CH_2 and symmetric CH_2 stretch, respectively. The shoulder at 3004 cm^{-1} was determined as the =CH double bond. Additionally, the O-H in-plane and out-of-plane bands appeared at 1462 cm^{-1} and 934 cm^{-1}, respectively.

The FT-IR spectrum of iron oxide-shell silica-core nanocomposites is shown in Figure 4.11 a. The strong band at 1041 cm^{-1} can be attributed to the Si-O peak of the silica core in magnetic nanocomposite, confirming the presence of silica in magnetic nanocomposites. Smaller peaks at 2999 cm^{-1} and 2800 cm^{-1} indicated the CH_2 stretches.
The typical C=O band of the carbonyl group of oleic acid, which was present in the spectrum of the pure oleic acid, was absent in the spectrum of nanocomposites. The characteristic FT-IR bands for metal carboxylates are usually in the range of 1650 - 1510 cm^{-1} for the asymmetrical vibrations and 1400 - 1280 cm^{-1} for the symmetrical vibrations. As expected, two new bands appeared at 1539 cm^{-1} and at 1436 cm^{-1}, which are characteristic for the asymmetric COO- stretch and the symmetric COO- stretch, respectively. The wavenumber separation of the asymmetric and symmetric COO- stretch (Δ = 1539 cm^{-1} - 1436 cm^{-1} = 103 cm^{-1}) is an indication for the interaction between the carboxylate head of the oleic acid and the metal atom on the particle surface. For $\Delta > 200\ cm^{-1}$ a monodentate ligand can be expected. A $\Delta < 110\ cm^{-1}$ can be attributed to a bidentate ligand. A wavenumber separation of $140\ cm^{-1} < \Delta < 200\ cm^{-1}$ indicates a bridging ligand [144, 145]. Since the wavenumber separation difference is smaller than 110 cm^{-1}, a chelating bidentate interaction can be proposed from the spectrum. This means one metal ion on the nanoparticle surface is binding with two carboxylate oxygens of the oleic acid [145]. A schematic illustration of the interaction between the surfactant oleic acid and the nanoparticle surface can be seen in Figure 4.12. Subsequently, the oleic acid capped-iron-oxide shell silica-core nanocomposites are hydrophobic, since the polar end groups are attached to the surface.

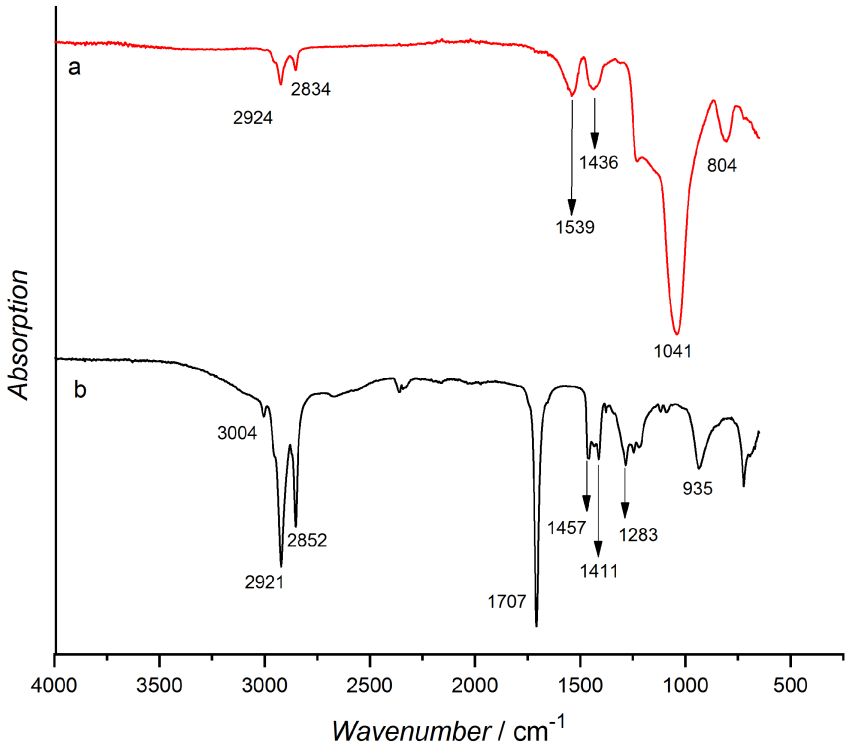

FIGURE 4.11: FT-IR spectra: oleic acid-capped nanocomposites a), oleic acid b).

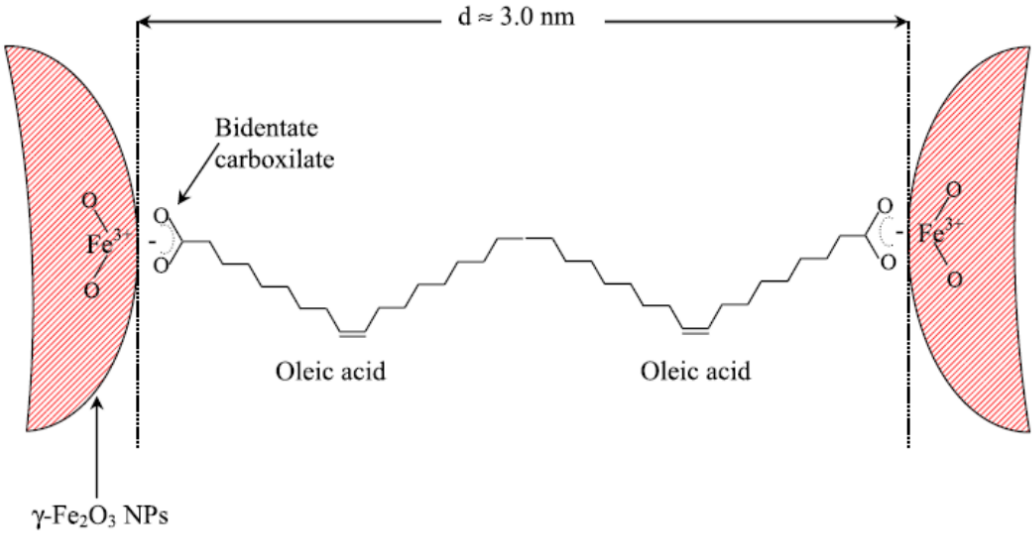

FIGURE 4.12: Schematic representation of the chelating bidentate interaction between the COO^- group of oleic acid and the iron atom on the nanoparticle surface [145].

4.1.3 Influence of synthesis reaction time on characteristics of iron oxide-shell silica-core nanocomposites

The nucleation and growth process during nanoparticle synthesis has a crucial influence on the size and morphology of the nanoparticles [13]. Therefore, we analyzed the influence of the synthesis reaction time on composition, size and morphology as well as magnetic characteristics of the iron oxide-shell silica-core nanocomposites in order to determine the optimal synthesis reaction conditions. Magnetic nanocomposites which exhibit the highest possible M_S and superparamagnetism but still preserve their unique raspberry-shaped morphology should be obtained.

Influence on size and morphology

In Figure 4.13 representative TEM images of nanocomposites at various particle ageing times from 5 minutes up to 60 minutes are shown. In all nanocomposites the small iron oxide nanoparticles are highly uniformly deposited onto the surface of each silica sphere, forming the typical spherical, raspberry-shaped morphology. As displayed in Figure 4.14, TEM analysis of the supernatant containing the vacant small iron oxide nanoparticles revealed an increase of the particle core diameters from 8.4 ± 1.0 nm at 5 min, 10.7 ± 1.0 nm at 30 min to 15.9 ± 2.6)m after 60 minutes. Along with a larger particle core diameter, the iron oxide nanoparticles at a reaction time of 60 minutes clearly show an undersirable increased agglomeration tendency in the TEM image (Figure 4.14c).

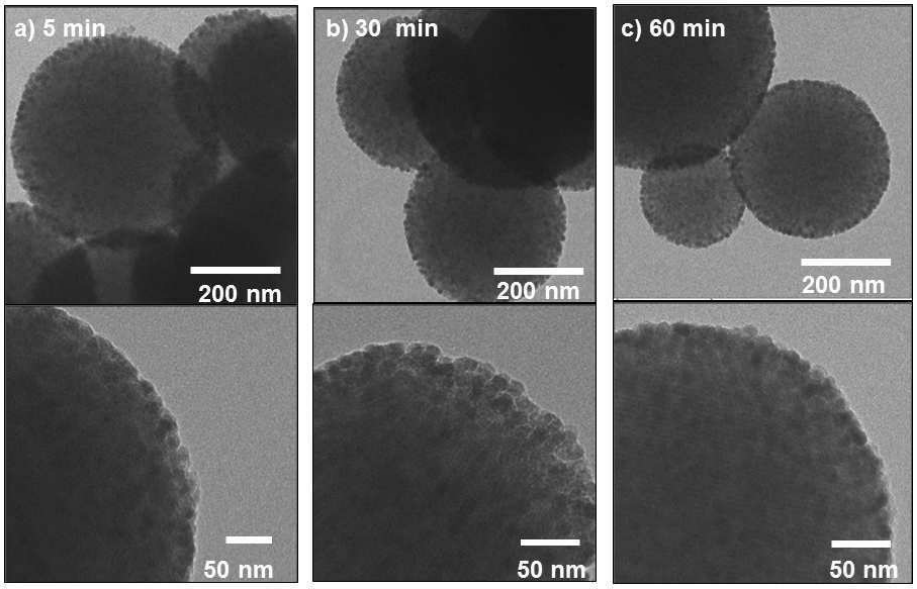

FIGURE 4.13: Representative TEM images of bare iron oxide-shell silica-core nanocomposites at reaction time of 5 min a), 30 min b) and 60 minutes c).

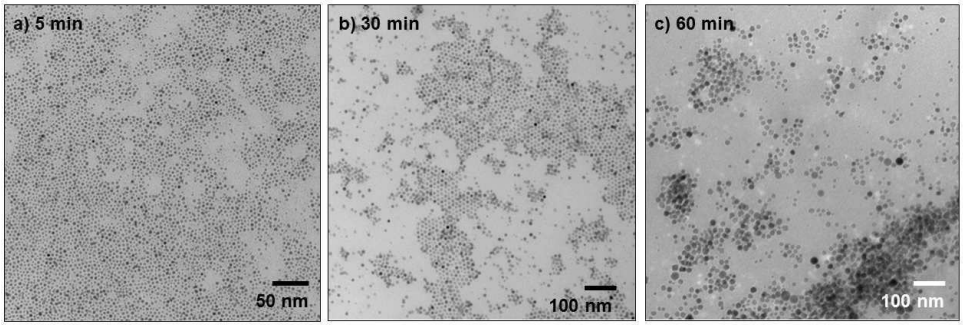

FIGURE 4.14: Representative TEM images of small iron oxide nanoparticles in the synthesis supernatant at reaction time of 5 min a), 30 min b), 60 minutes c).

Size distribution analysis by DLS of iron oxide nanoparticles at different reaction times verified the TEM results and revealed hydrodynamic core diameters of 9.1$\pm$ 2.7 nm after 5 min, 12.9 $\pm$ 3.9 nm after 30 min and 19.0 $\pm$ 5.9 nm after 60 min.
The core diameter obtained by DLS measurements is slightly larger than by TEM analysis. This can be attributed to the intrinsic characteristics of the methods. Whereas TEM determines the core diameter, DLS is measuring the hydrodynamic diameter. When a dispersed particle moves through a liquid medium, a thin electric dipole layer adheres to its surface and affects its movement. Thus, the so called hydrodynamic diameter measured by DLS, is usually above the diameter obtained by TEM [51–53].

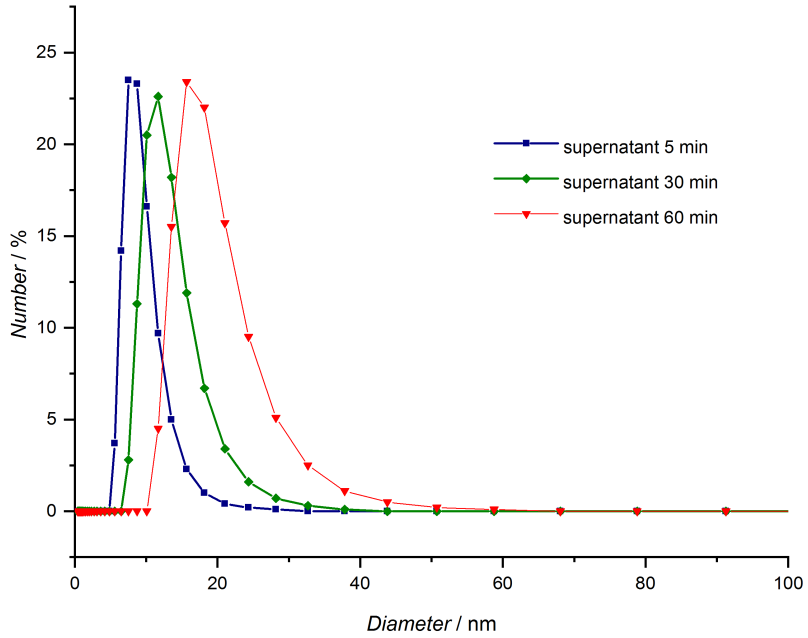

FIGURE 4.15: DLS measurements of iron oxide nanoparticles at a synthesis reaction time of 5 minutes, 30 minutes and 60 minutes.

Influence on composition

ICP-MS measurements were performed to determine the iron concentration of nanocomposites aged at various synthesis reaction times. Iron oxide-shell silica-core nanocomposites aged at 5 minutes, 30 minutes and 60 minutes reaction time were treated in a microwave-assisted acid extraction procedure with hydrofluoric acid and nitric acid. Subsequently, their iron content was quantified by ICP-MS measurements. As shown in Figure 4.16 iron contents of 10.1 $\pm$ 0.8 %Fe (w/w) for 5 minutes, 12.9 $\pm$ 0.7 % Fe (w/w) for 30 minutes and 12.9 $\pm$ 0.3 % Fe (w/w) for 60 minutes were measured. Overall, ICP-MS measurements exhibited a slight increase in the iron content from 5 minutes to 30 minutes or 60 minutes. This might be attributed to the increase in particle core diameter at higher reaction times.

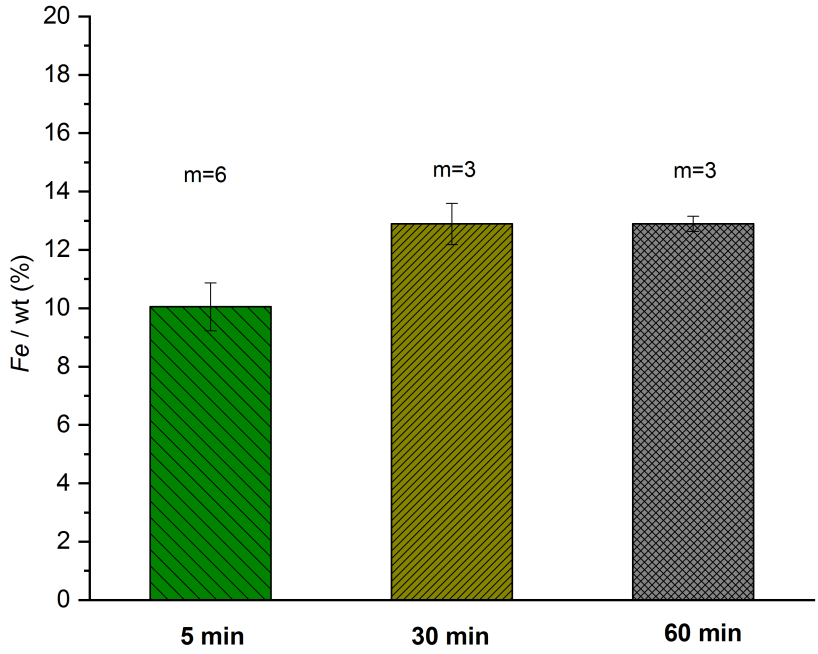

FIGURE 4.16: Determination of iron content of iron oxide-shell silica-core nanocomposites aged at 5 minutes, 30 minutes and 60 minutes by ICP-MS.

Influence on magnetic characteristics

Along with the particle size, longer reaction times during particle synthesis also resulted in a variation in the magnetic properties. Figure 4.17 shows the magnetization plots of bare nanocomposites at 300 K at various durations of particle synthesis. The typical sigmoidal-shape curve and the absence of hysteresis can be seen in all nanocomposites, revealing the desirable superparamagnetic characteristic. An increase in the particle ageing time during the synthesis process from 5 min over 30 min to 60 min resulted in a drastic increase of the M_S values from 17.3 $A\,m^2\,kg^{-1}$(γ-Fe_2O_3) to 35.9 $A\,m^2\,kg^{-1}$ (γ-Fe_2O_3) and 45.3 $A\,m^2\,kg^{-1}$ (γ-Fe_2O_3), respectively. Overall, the obtained M_S values ranging from 17-45 $A\,m^2\,kg^{-1}$ (γ-Fe_2O_3) are higher than those observed for similar silica core/iron oxide shell nanocomposites, published elsewhere [23–25, 30]. The decrease of M_S with decreasing particle size has been previously reported in literature and was explained by an increased spin canting effect of smaller nanoparticles, ascribed to their increase in surface area-to-volume ratio [22, 146].

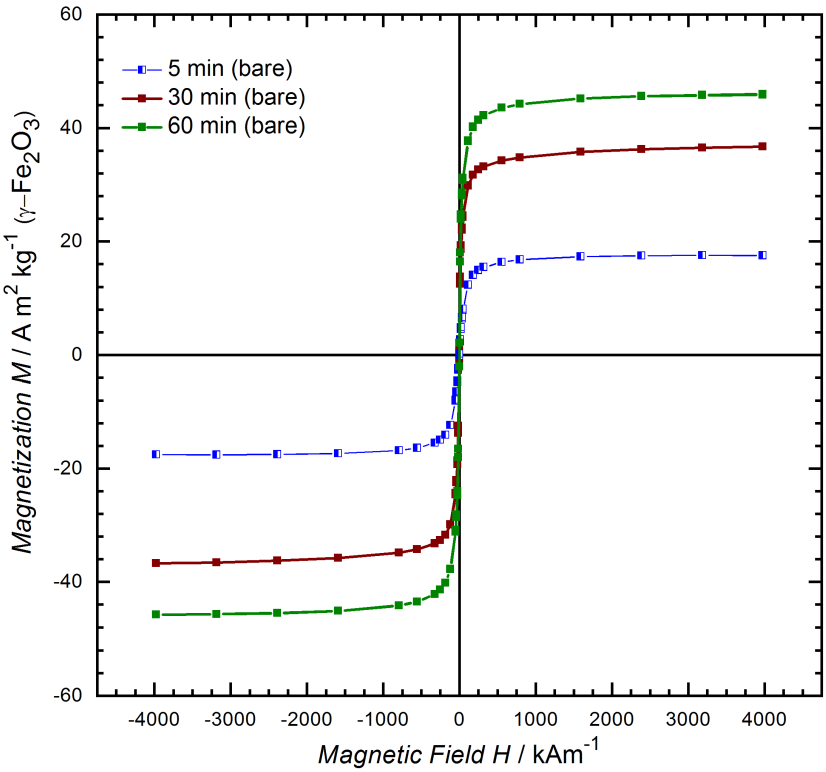

FIGURE 4.17: Magnetization measurements of bare iron oxide-shell silica-core nanocomposites at various durations of particle synthesis as a function of the applied magnetic field at 300 K.

To analyze the magnetic properties in detail, zero field (ZFC) and field-cooled (FC) measurements were performed. As expected for superparamagnetic particles, a difference between the ZFC and FC data at low temperatures is visible (Figure 4.18). The curves obtained after ZFC show maxima around 65 K (5 min), 120 K (30 min) and 115 K (60 min) giving T_B of the synthesized nanocomposites. The shift of T_B towards higher temperatures with

increasing nanoparticle sizes is already reported and can be attributed to an increase of the magnetic anisotropy energy of larger nanoparticles [138, 147–149]. Since T_B is far below RT for all nanocomposites, the magnetic condition for their application in bioseparation is fulfilled. Consequently, by extending the duration of the particle synthesis from the standard 5 min up to 60 min at 320 °C, both the magnetic characteristics and the nanoparticle size could be modified.

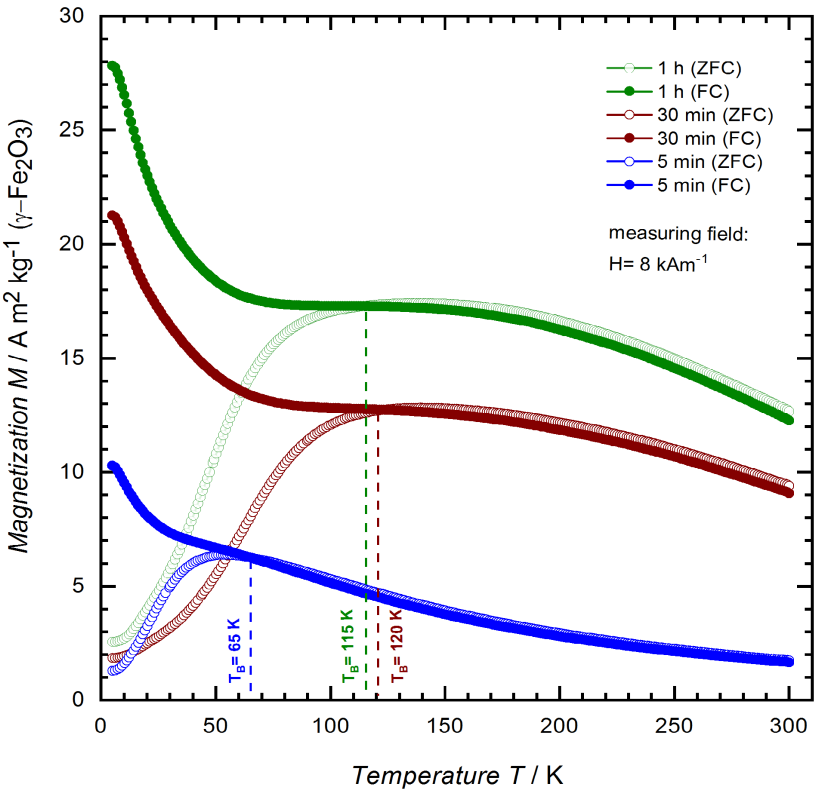

FIGURE 4.18: Magnetization measurements as a function of the temperature, taken at an applied field of 8 kA m^{-1} after cooling in 4000 kA m^{-1} (field-cooled, closed symbols) or in zero field (open symbols).

A summary of the results can be seen in Table 4.1. For our further experiments nanocomposites with both a high M_S value for optimal separation capability and a high colloidal stability are favoured. Since nanocomposites at a reaction time of 30 minutes show superparamagnetic characteristics, a high M_S value without any agglomeration tendency, these synthesis reaction time of 30 minutes was chosen for our further experiments.

TABLE 4.1: Influence of synthesis reaction time on size and magnetic characteristics of iron oxide-shell silica-core nanocomposites

Reaction time (nm)	**d, TEM (nm)**	**d, DLS (nm)**	**M_S (γ-Fe_2O_3)**	**T_B (K)**	**Fe (%, w/w)**
5 min	8.4 ± 1	9.1 ± 2.7	17.3	65 K	10.1 ± 0.8
30 min	10.7 ± 1	12.9 ± 3.9	35.9	120 K	12.9 ± 0.7
60 min	15.9 ± 2.6	19.0 ± 5.9	45.3	115 K	12.9 ± 0.3

4.1.4 Functionalization of iron oxide-shell silica-core nanocomposites

The bare iron oxide-shell silica-core nanocomposites are oleic acid-capped and therefore initially hydrophobic (see 3.1.2.). For our final application in the IMS process of SEB in milk, an appropriate hydrophilic functionalization approach is required which broadens their use from nonpolar to aqueous systems, improves their colloidal stability and also provides an ideal anchorage for the covalent binding of the anti-SEB antibodies. In this section, we propose a hydrophilic functionalization strategy by organosilane chemistry for our iron oxide-shell silica-core nanocomposites as well as a detailed surface characterization of the coating.

Functionalization strategy

The hydrophobic oleic acid-capping of the iron oxide nanoparticles has to be replaced with a hydrophilic coating. To achieve a hydrophilic coating we chose the so-called ligand exchange with trialkoxysilanes [35]. This ligand exchange method was chosen because it rapidly transfers the whole magnetic nanocomposite from organic to aqueous phase and introduces functional groups. By using ultrasonic energy for this ligand exchange step, the reaction time could drastically be reduced from days to only several hours [35]. At the same time, crosslinking can be avoided and therefore monodispersity can be preserved.
In our experiments the two organosilanes GOPTS and APTES were tested to introduce terminal epoxy-groups or amine-groups on the nanocomposite surface, respectively. A schematic illustration of the functionalization process can be seen in Figure 4.19.
As shown in Figure 4.20 bare oleic acid-capped and aminosilane-functionalized iron oxide-shell silica-core nanocomposites were added to a small volume of hexane and water to verify the phase transfer and therefore the water dispersibility. A phase transfer from the organic upper phase to the aqueous lower phase was observed after functionalization with organosilanes, confirming a successful ligand exchange. The same phase transfer could also be observed for the epoxy-functionalized nanocomposites (data not shown).

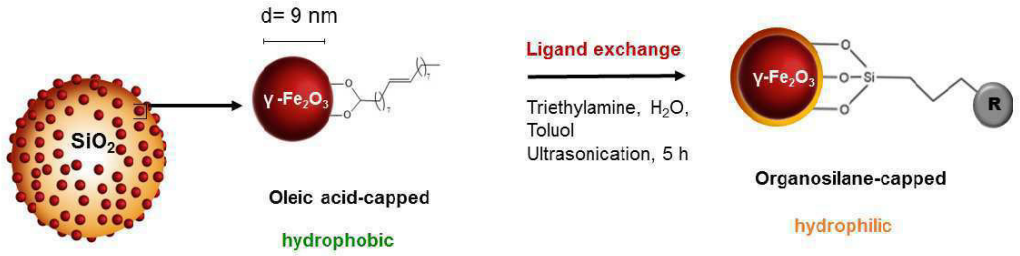

FIGURE 4.19: Schematic illustration of the functionalization of iron oxide-shell silica-core nanocomposites with organosilanes.

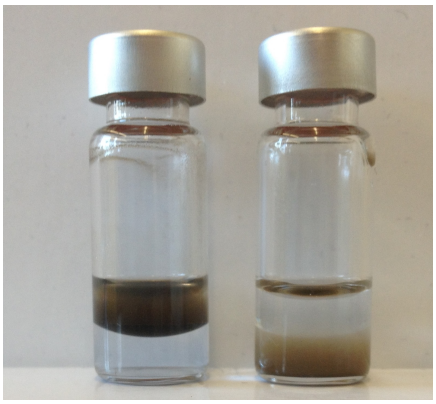

FIGURE 4.20: Bare nanocomposites in organic phase (upper phase) and organosilane-functionalized nanocomposites in aqueous phase (lower phase).

Surface characterization of organosilane-functionalized iron oxide-shell silica-core nanocomposites

Transmission Electron Microscopy

TEM measurements were performed to verify the presence of the organosilane functionalization on the nanocomposite surface and to control the preservation of the raspberry-like morphology after the coating process.
Representative TEM images of epoxysilane-functionalized nanocomposites (Figure 4.23) confirmed the desired raspberry-shaped morphology of hydrophilic nanocomposites. Thus, during the phase transfer by a tempered ultrasonication step for 5 hours, nanocomposites retained their raspberry-shaped morphology. Although no covalent coupling or stabilization chemistry was used, magnetic nanoparticles were not detached from the silica spheres by ultrasonication.
In the inset in Figure 4.23b, a shade of grey around the iron oxide particles can be seen, which appears clearly distinct from the background. This demonstrates the thin organosilane layer of a few nanometers around the entire nanocomposite. Until now, this ligand exchange method using ultrasonic energy was only applied for the functionalization of small iron oxide nanoparticles [35]. Based on our results, we can verify that this ligand exchange method with minor modifications can also be used as functionalization strategy for entire nanocomposites.

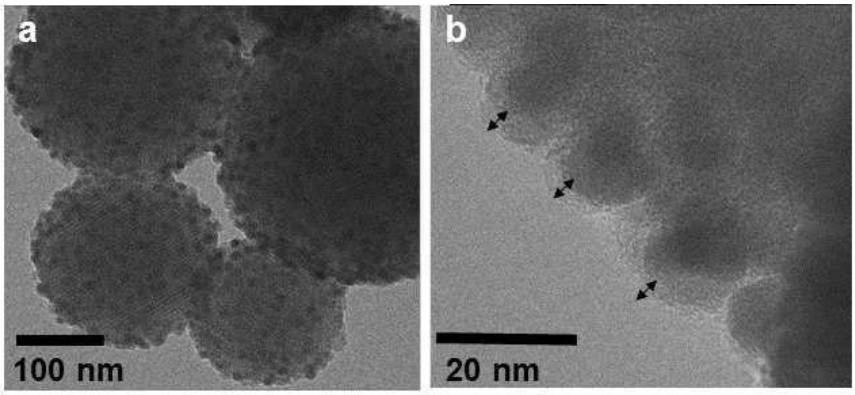

FIGURE 4.21: Representative TEM images of hydrophilic iron oxide-shell silica-core nanocomposites: aminosilane-functionalized iron oxide-shell silica-core nanocomposites a), inset of epoxysilane-functionalized nanocomposites b).

Ninhydrin colorimetric method

The Ninhydrin colorimetric assay is a commonly used method for the quantification of primary or secondary amines by producing a deep purple colour known as Ruhemans´s purple. The absorbance of the Ruhemann´s complex at 570 nm is proportional to the density of free primary amino groups on the surface [150]. Hence, this colorimetric assay was applied to detect and quantify the primary amino groups on the nanoparticle surface of aminosilane-functionalized nanocomposites. As displayed in the image in Figure 4.22, after the treatment with ninhydrin, aminosilane-functionalized nanocomposites clearly show a dark purple colour reaction, which confirms the presence of free aminogroups on the nanoparticle surface.
As reference for the quantification of free amino groups on the nanoparticle surface, a standard curve with the amino acid glycine was performed. Measurements of the UV-absorbance of the Ruhemann´s complex indicated an amine density on the nanoparticle surface of 0.95 ± 0.16 µmol mg^{-1} nanocomposites, which is similar to results for aminosilane-coated nanoparticles in literature [150].

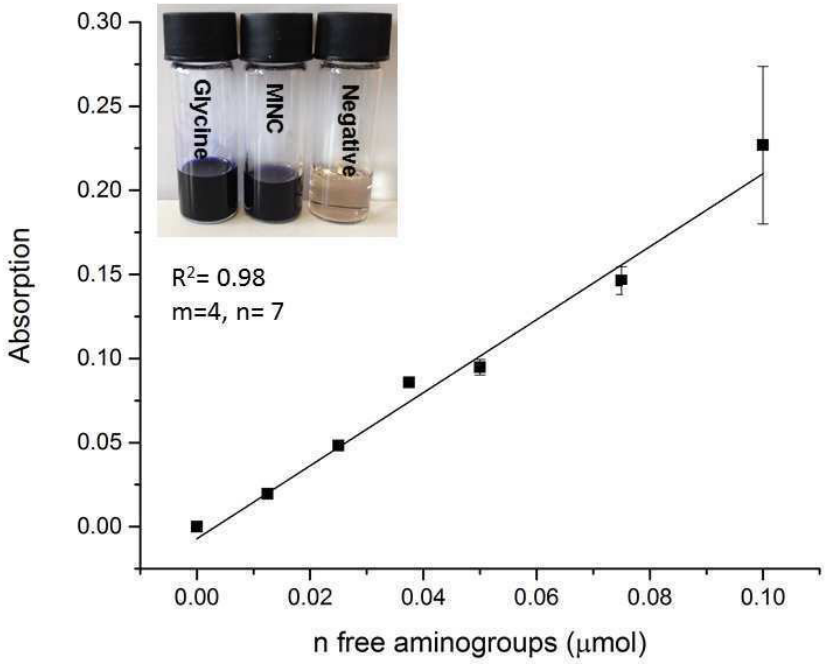

FIGURE 4.22: Standard curve of glycine by Ninhydrin colorimetric assay and image of the colour reaction with ninhydrin.

Analysis of the zeta potential

The stability of nanoparticles dispersed in aqueous media can be expressed by zeta potential. The zeta potential describes the electric potential between the inter-facial double layer of ions surrounding a dispersed particle and the the bulk dispersion. The value of the zeta potential is related to the stability of a colloidal nanoparticle dispersion. If the absolute value is higher than 20 - 25 mV, the nanoparticles are usually electrostatically stable [35].
Figure 4.23a shows the zeta potential at various pH values for aminosilane- and epoxysilane-functionalized iron oxide-shell silica-core nanocomposites. When the pH increases, a downward trend for the zeta potential of amino-functionalized nanocomposites is visible. This might be attributed to the decrease in the surface charge due to the deprotonation of the amine at high pH values [35]. In comparison, the curve of the epoxysilane-functionalized nanocomposites is shifted to a more acidic pH range. The point of zero charge (Isoelectric point, IEP) is 4.2 for epoxysilane-functionalized and 8 for aminosilane-functionalized nanocomposites. Since the IMS is perfomed in milk (pH = 6.5) and the SMIA in PBS (pH = 7.0), the zeta potential value of the nanocomposites at around neutral pH is especially crucial. As shown in Figure 4.23 b) epoxy-nanocomposites show a better electrostatic stability at neutral pH with a zeta potential of - 32.9 mV compared to amino-nanocomposites (+ 14.7 mV). Due to their high colloidal stability at neutral pH, epoxysilane-functionalized iron oxide-shell silica-core nanocomposites appeared to be beneficial. Therefore, the epoxy-nanocomposites were used for our further experiments in the complex food matrix milk.

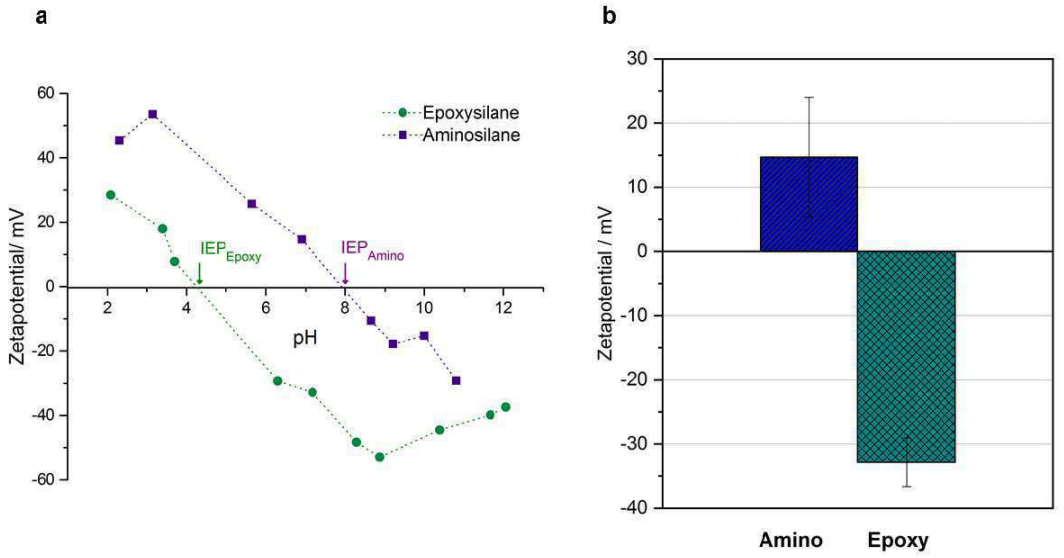

FIGURE 4.23: Changes in zeta potential values for amino- and epoxy-functionalized iron oxide-shell silica-core nanocomposites: at different pH values a), at neutral pH b).

Magnetic characteristics of organosilane-functionalized iron oxide-shell silica-core nanocomposites

Magnetic properties of organosilane-functionalized nanocomposites were investigated with a SQUID magnetometer. Figure 4.24 shows the magnetization plots of bare and silane-functionalized nanocomposites at 300 K. A typical sigmoidal-shape curve can be seen, revealing superparamagnetic characteristics with a M_S of 17.4 $A\,m^2\,kg^{-1}$ (γ-Fe_2O_3) for bare and 17.9 $A\,m^2\,kg^{-1}$ (γ-Fe_2O_3) for organosilane-functionalized nanocomposites.
As displayed in Figure 4.24, M_S of the organosilane-functionalized nanocomposites is slightly higher compared to the bare nanocomposites. This may be attributed to the existence of magnetic disorders on the nanoparticle surface due to interactions between particles. Consequently, the organosilane coating could weaken these interactions, which may reduce the disorder of the spins on the surface and thus increasing the magnetization [151].
Since our main interest is to apply the magnetic nanocomposites in the complex and viscous matrix milk, attraction and re-dispersion of hydrophilic nanocomposites in absence and presence of a permanent magnet was tested. As shown in Figure 4.25, organosilane-functionalized nanocomposites in milk were rapidly attracted towards a magnet (< 2 mins) and could be re-dispersed by gentle tapping after removal of the external magnetic field. Hence, the designed nanocomposites are applicable for the IMS in milk by using a permanent magnet.

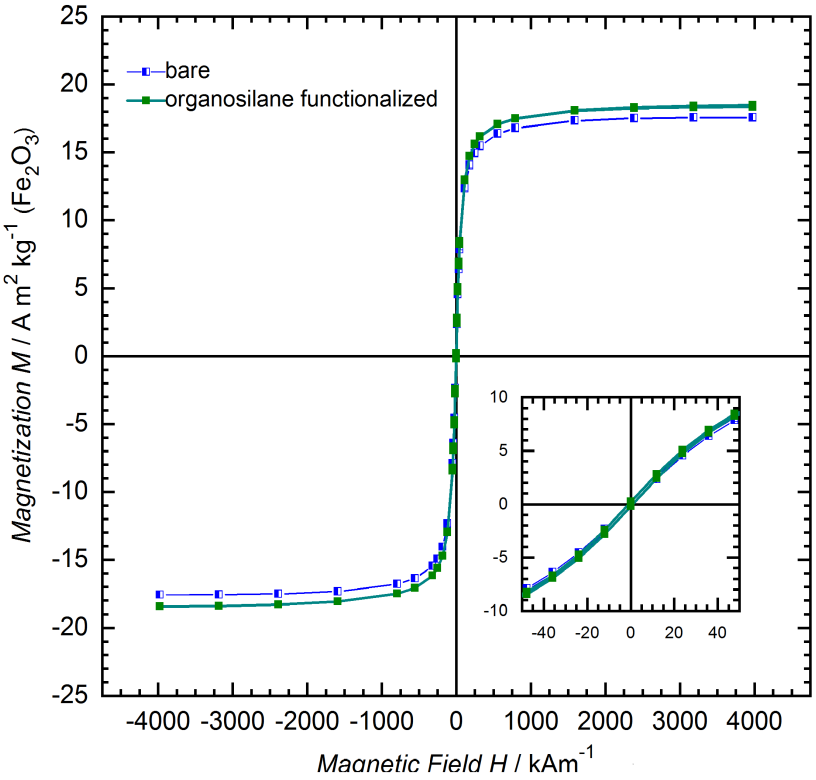

FIGURE 4.24: Magnetization measurements of bare and organosilane-functionalized iron oxide-shell silica-score nanocomposites (reaction time: 5 min) as a function of the applied magnetic field at 300 K.

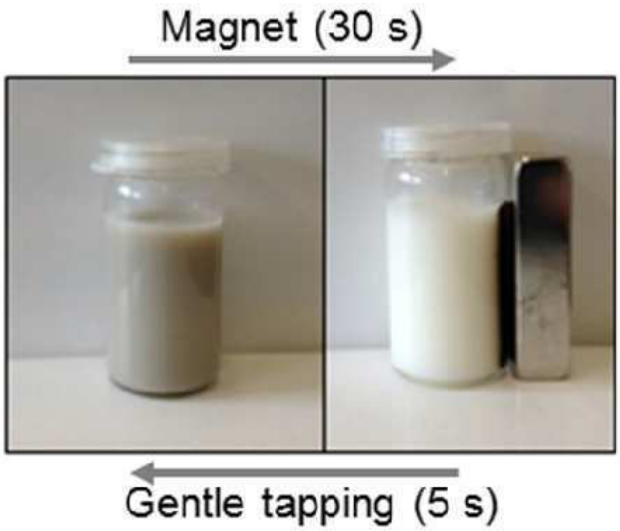

FIGURE 4.25: Attraction and re-dispersion of organosilane-functionalized iron oxide-shell silica-core nanocomposites in absence and presence of a permanent magnet in milk.

4.1.5 Long-term stability of iron oxide-shell silica-core nanocomposites

As handling and storage of nanoparticles can greatly influence their properties, a good knowledge of their stability over long-term storage is very important to guarantee highly stable nanoparticles with constant material characteristics.
Long-term stability of the nanocomposites over several months was tested by SQUID magnetometry and by RM.
The comparison of Raman spectra of fresh nanocomposites and aged nanocomposites for 2 weeks and 5 months revealed three broad bands around 350 cm^{-1}, 500 cm^{-1} and 700 cm^{-1}, perfectly matching to the spectral signature of maghemite (Figure 4.26). Furthermore RM indicated no changes and hence reassured the long-term stability of the nanocomposites over several months.
Previous work has already demonstrated that synthesis procedure, post-synthesis work up and storage of magnetite nanoparticles in the presence of atmospheric oxygen leads to an oxidation to maghemite [52]. Hence, maghemite nanoparticles can be recommended for use, because, although magnetite has a slightly higher magnetization, the main advantage of maghemite is its chemical stability [152].

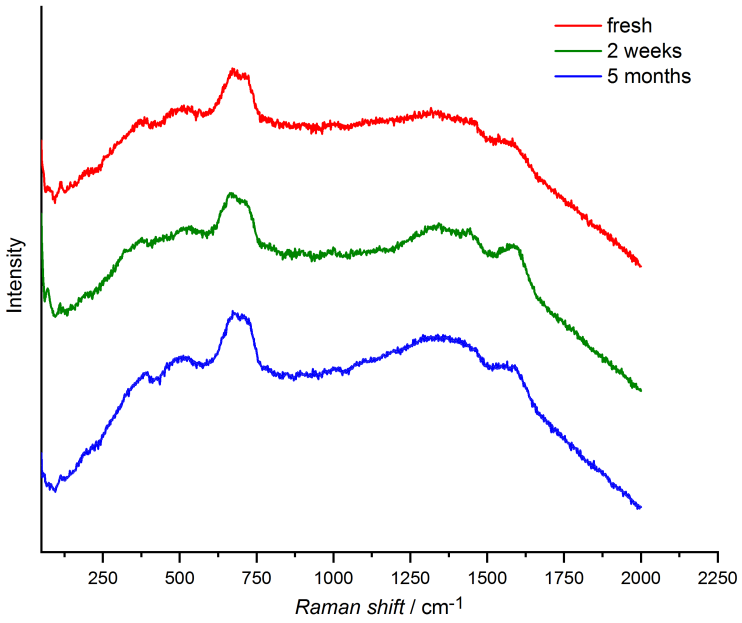

FIGURE 4.26: Raman spectra of iron oxide-shell silica-core nanocomposites over 5 months.

Since the preservation of a constant magnetization of magnetic nanocomposites is essential for future applications, magnetic long-term stability was confirmed over six months by periodical SQUID magnetization measurements at different particle ageing times.
M_S was 16.3 A m^2 kg^{-1} (γ-Fe_2O_3) for freshly prepared bare magnetic nanocomposites, 17.3 A m^2 kg^{-1} (γ-Fe_2O_3) after 35 days, 17.4 A m^2 kg^{-1} (γ-Fe_2O_3)

after 50 days, 16.4 A m^2 kg^{-1} (γ-Fe_2O_3) after 76 days, and 16.4 A m^2 kg^{-1} (γ-Fe_2O_3) after 184 days (Figure 4.27). The deviations are negligible low and can be attributed to measurement artefacts.
The same behavior was observed for organosilane-functionalized nanocomposites with a M_S value of 17.9 A m^2 kg^{-1} (γ-Fe_2O_3) after 77 days. Additionally, the nearly constant M_S values over 6 months confirm the highly stable deposition of maghemite nanoparticles onto silica spheres. For our nanocomposites excellent long-term stability could be demonstrated by SQUID magnetometry and by RM.

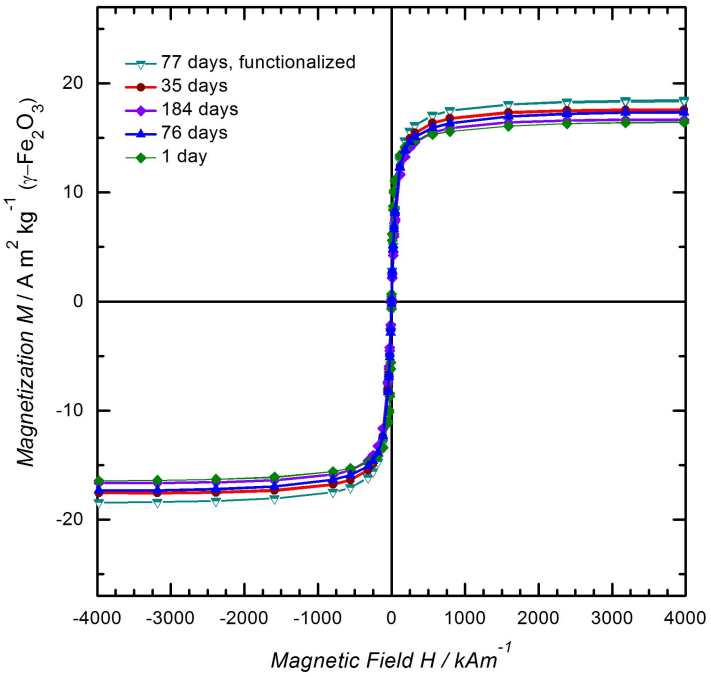

FIGURE 4.27: Magnetization measurements of bare and organosilane-functionalized magnetic nanocomposites at various particle ageing times as a function of the applied magnetic field at 300 K.

4.1.6 Summary

In summary, a rapid low-cost method for the preparation of superparamagnetic iron oxide-shell silica-core nanocompsoites by combining simultaneous *in situ* growth of iron oxide nanoparticles and nanocomposite synthesis was shown in this section. By a homogeneous deposition of small iron oxide nanoparticles onto a mesoporous silica core, a magnetic cluster domain is formed. The formation of a nanocomposite combines both desired magnetic characteristics: 1) Superparamagnetism and 2) Magnetic manipulation by permanent magnets.
The fast hydrophilic functionalization approach by organosilane chemistry broadens their use from nonpolar to aqueous systems and also provides ideal anchorage for the future covalent binding of antibodies. Excellent long-term stability over several months was verified by RM and SQUID magnetometry. Magnetic separation experiments in milk demonstrated their promising potential for bioseparation in complex matrices. For our following bioseparation and microarray analyis experiments the iron oxide-shell silica-core nanocomposite at a synthesis reaction time of 30 min with constant and specific material characteristics were used. A summary of all nanocomposite characteristics and chosen synthesis reaction parameters are shown in Table 4.2.

TABLE 4.2: Summary: Characteristics and reaction parameters of iron oxide-shell silica-core nanocomposites.

Parameter	
Synthesis parameters	30 min, 320 °C
Nanocomposite size (TEM)	329 $\pm$ 123 nm
Nanoparticle size (TEM)	10.7 $\pm$ 1 nm
Nanoparticle size (DLS)	12.9 $\pm$ 3.9 nm
Magnetic saturation (M_S)	35.9 (γ-Fe_2O_3)
Blocking temperature	120 K
Iron content (w/w)	12.9 $\pm$ 0.7 %
Surface functionalization	Epoxysilane

4.2 Chemiluminescence sandwich microarray immunoassay (CL-SMIA) for detection of SEB in milk

The second aim of this thesis is the development of a rapid and sensitive detection and quantification method for SEB in the complex food matrix milk. In a first step, a flow-based CL-SMIA on the microarray analysis platform MCR 3 SLT was developed in order to quantify SEB directly in milk. For the CL-SMIA the capture antibody S1001/4/6 and biotinylated detection antibody S419/5/5/5-biotin (Robert-Koch Institute, Berlin, Germany) were used. This antibody pair was considered optimal since in a previous report by Pauly et al. it specifically detected the antigen SEB with high sensitivity, without cross-reacting with any other SEs [3].
Therefore, SEB was directly spiked in ultra-pasteurized milk and subsequently measured on the flow-based microarray analysis platform by injecting a sample aliquot of 600 µL into the MCR 3 SLT. The SEB in the milk is bound by the anti-SEB capture antibodies immobilized on the microarray chip surface during the stop-flow incubation process. The sandwich is formed by using a biotin-labeled monoclonal detection antibody against SEB. For the CL detection first streptavidin poly-HRP and then the CL reagents (luminol and hydrogen peroxide) are pumped through the microarray channel. The CL signal is recorded by a CCD camera. The CL images of the SMIA were analyzed to get a quantitative information. The total assay duration is about 18 min. A schematic illustration of the assay principle of the CL-SMIA is displayed in Figure 4.28.

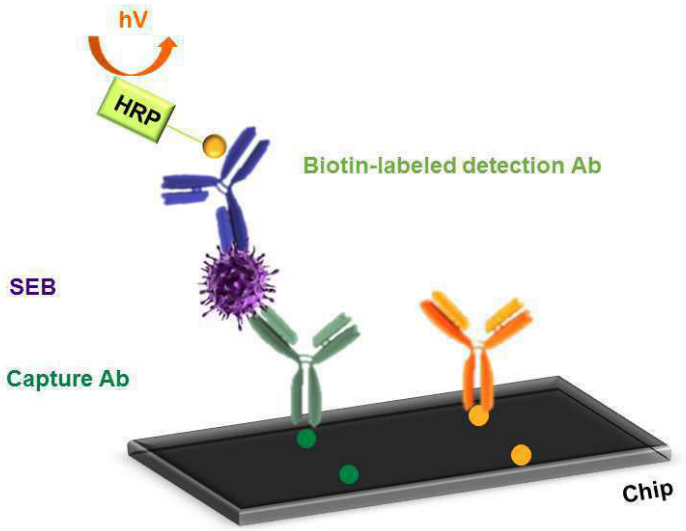

FIGURE 4.28: Schematic illustration of the CL-SMIA assay for the detection of SEB in milk.

4.2.1 Calibration of CL-SMIA

Various concentrations of SEB in a range of 0 - 1000 µg L^{-1} in milk were measured to obtain a calibration curve for the quantification of SEB in milk by CL-SMIA. Biotinylated detection antibody (S419/5/5/5, c = 0.9 µg mL^{-1} in casein 0.5% w/v, Robert-Koch Institute, Germany) and streptavidin poly-HRP (c = 0.2 µg mL^{-1} in casein 0.5% (w/v, Senova, Germany) were used. The capture antibody S1001/4/6 was immobilized on the micoarray chip surface at a concentration of 0.63 mg mL^{-1} in spotting buffer containing 20% (w/v) trehalose and 0.05% (w/v) Pluronic® F127.
As shown in Figure 4.29 a sigmoidal correlation of the CL signal as a function of the decadic logarithm of the SEB concentration was obtained. By calculating the mean CL signals of blank measurements using milk (n = 3), plus three times the standard deviation, a LOD of 0.13 µg L^{-1} was achieved. A broad working range (WR) from 4.6 µg L^{-1} to 45.8 µg L^{-1} was further obtained. Consequently, it can be concluded that the sandwich antibody pair S1001/4/6 and S419/5/5/5-biotin are perfectly suitable for the detection of SEB directly in milk on the MCR 3 SLT.

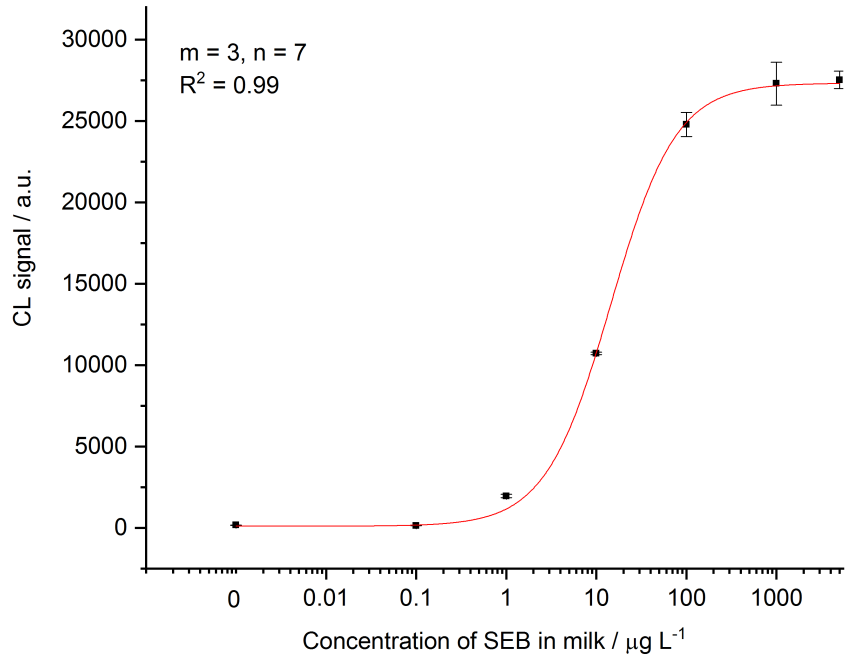

FIGURE 4.29: Calibration curve for the quantification of SEB in milk analzyed by CL-SMIA. Standard deviations (n = 3) are indicated as error bars.

4.2.2 Recovery experiments

In order to determine recoveries of the established analytical method, milk samples were spiked with SEB at three different concentrations in the linear WR of the calibration curve. At that time of the experimental phase only a limited amount of detection antibody was provided. Therefore, recovery experiments were performed in single measurements.
Recovered concentrations were calculated from the CL signals of the SMIA according to the previously determined calibration curve. For spiked SEB concentration of 10 µg L^{-1}, 15 µg L^{-1}, and 25 µg L^{-1}, recoveries of 95.6%, 97.2% and 98.4% were obtained, respectively. An average recovery of 97.1 $\pm$ 1.4 % was calculated. This result indicated that the CL-SMIA is highly reproducible in milk.

4.3 Magnetic nanocomposite based chemiluminescence sandwich microarray immunoassay (MNC-SMIA I)

Next, the synthesized superparamagnetic iron oxide-shell silica-core nanocomposites were applied for IMS in order to concentrate SEB from milk samples. IMS was combined with a subsequent microarray analysis on the flow-based microarray analysis platform MCR 3 SLT for sensitive and rapid detection of SEB in milk.
Many biosensor technologies commonly work well in buffer systems but fail when applied in complex matrices, since the food matrix components may interfere with reagents (e.g. enzymes) or the technical equipment. Introducing an IMS step prior to analysis offers the advantage of simple and specific isolation of the analyte SEB from the complex food matrix [3].
Moreover, a selective pre-enrichment and concentration step by IMS may increase the assay sensitivity, reduces the total assay time and even enables the possibility to rapidly analyze larger amounts of food samples in an urgent case of a foodborne outbreak.
In the following thesis section, we developed and subsequently optimized the MNC-SMIA I.

4.3.1 Development of MNC-SMIA I

In a proof-of-principle study, the feasibility of the MNC-SMIA I on the microarray analysis platform MCR 3 SLT was tested. The total process of the MNC-SMIA I is illustrated in Figure 4.30, and shows a schematic illustration of the pre-enrichment and isolation of SEB by IMS combined with the sensitive CL-SMIA on the MCR 3 SLT.
For the principle study, following sandwich antibody pairs (detection antibody and capture antibody) were used: S419/5/5-biotin and S1001/4/6, mAB 1D6-biotin and S1001/4/6a, mAB 1D6-biotin and pAB (R-Biopharm AG).
First, iron oxide-shell silica-core nanocomposites functionalized with biotinylated anti-SEB detection antibodies were incubated in milk containing the analyte SEB. The milk volume was initially set to 0.6 mL since this is the standard sample volume capacity in the sample loop of the MCR 3 SLT, and therefore, allows a direct comparison to the CL-SMIA.
The magnetic nanocomposites coupled to biotinylated secondary antibodies bind the SEB in the liquid phase by an affinity reaction. For the selective enrichment and isolation of SEB in the complex matrix the whole sandwich construct consisting of MNC, anti-SEB antibody, and SEB can subsequently be separated by IMS using a permanent magnet (Figure 4.30 b). After several magnetic washing steps the magnetic nanocomposites were resuspended in 52 µL of running buffer containing 0.5% (w/v) casein and 0.01% (w/v) Pluronic® F127, which is nearly the volume capacity of the microarray channel flow cell. The initial sample volume of 0.6 mL is therefore enriched

and concentrated to 52 µL, which equals a volumetric concentration factor of around 11.5.
The sandwich construct (MNC, anti-SEB antibody, SEB) was directly injected in the microarray flow channel and the microarray chips were subsequently incubated at 37 °C for 60 minutes at a constant shaking rate of 98 rpm.
Next, SEB was quantified by a CL-SMIA on the MCR 3 SLT. Hereby, the SEB in the sandwich construct is bound by the anti-SEB capture antibodies immobilized on the microarray chip surface during incubation process and forms the antibody sandwich. For the CL detection streptavidin poly-HRP and subsequently CL reagents (luminol and hydrogen peroxide) are pumped through the microarray channel. The CL signal is recorded by a CCD camera for 50 seconds. The CL images of the MNC-SMIA I were analyzed to get a quantitative information.

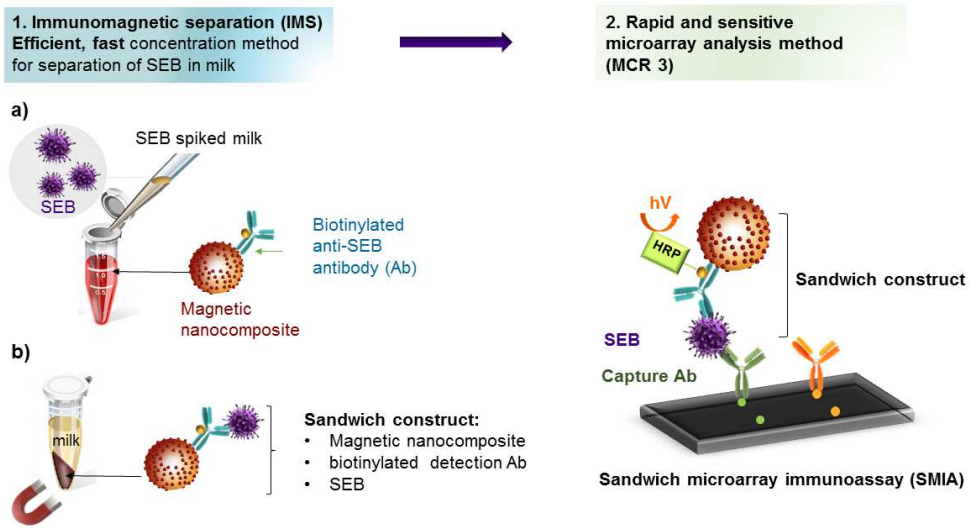

FIGURE 4.30: Schematic scheme of the IMS coupled MNC-SMIA I for the detection of SEB in milk.

The initial automated MCR program was adapted from Kunze et al. [153] with minor modifications. In detail, the original washing step was slightly modified by setting the velocity of the washing step from 200 µL s^{-1} to 100 µL s^{-1}. Additionally, the incubation time in the automated MCR 3 program was removed. Throughout the experimental phase of the PhD thesis the MCR 3 program as well as reaction conditions and parameters were continuously modified to obtain a highly sensitive, selective and time-effective assay protocol. An overview of the initial MCR 3 program and applied reaction parameters are summarized in Table 4.3.

TABLE 4.3: Total process of the automated MNC-SMIA I on the MCR 3, assay duration: 8 minutes.

Preincubation of microarray chips: 37 °C, shaking at 98 rpm for 60 minutes.		
Step	**Volume**	**Flowrate / T**
Heating of flow cell		37 °C
Washing step (3x)	1000 µL	100 µL
HRP labeled streptavidin	150 µL, 600 µL	50 µL, 2 µL
Washing step (3x)	1000 µL	100 µL
CL substrates (luminol, hydrogen peroxide)	200 µL each	20 µL s^{-1}
Picture with CCD camera		60 s
Washing of the flow-system	150 µL each	500 µL s^{-1}
Washing of the microarray chip (3 x)	1000 µL each	68 µL s^{-1}

The CL image with the sandwich antibody pair S419/5/5-biotin and S1001/-4/6 (Figure 4.31a clearly shows distinct CL spots at the location of the immobilized anti-SEB capture antibodies (13,270 a.u.). In comparison the no target control (NTC), which only contains spotting buffer (PBS, trehalose, Pluronic® F127), shows a CL signal of only 3,500 a.u.
The CL image (Figure 4.31 b with the anti-SEB detection antibody 1D6-biotin shows similar results by exhibiting visible CL spots at the location of the immobilized polyclonal anti-SEB antibody (22,000 a.u.) and S1001/4/6 (11,700 a.u.). In contrast, the NTC displays a low CL signal around 3,300 a.u.
A deviation in spot size and spot homogenity in the replicates in each row can be attributed to technical difficulties during antibody immobilization with the BioOdyssey Calligrapher miniarrayer at that time of experimental phase.

For the first time, we could demonstrate in a proof-of-principle study, that the MNC-SMIA I, which combines an IMS step prior to microarray analysis, could successfully be performed on the flow-based microarray analysis platform MCR 3 SLT for the detection of SEB in milk. However, the microarray image clearly shows relatively low CL signals and a high, inhomogeneous background signal over the entire chip surface (3,700 $\pm$ 300 a.u.). Consequently, the optimization of important assay parameters as well as the adjustment of MCR 3 program is required to obtain a sensitive and rapid analytical method for the detection and quantification of low amounts of SEB in milk.

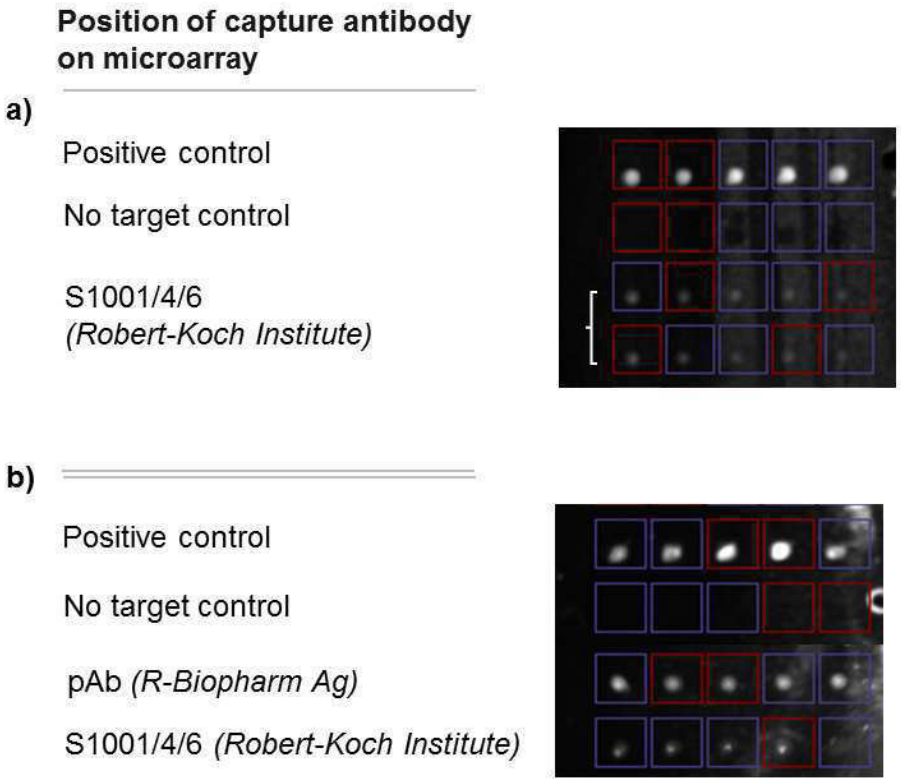

FIGURE 4.31: CL images for MNC-SMIA I. 2.5 mg magnetic nanocomposites were conjugated to a) anti-SEB Ab S419/5/5-biotin (c = 75 mg L^{-1}) or b) anti-SEB mAB 1D6 (c = 75 mg L^{-1}) and incubated with 10 mg L^{-1} SEB in milk. The microarray contains a spotting control (anti-HRP antibody), NTC (only spotting buffer) and the anti-SEB capture antibodies.

4.3.2 Optimization of MNC-SMIA I

An important task during this PhD thesis was the step-by-step optimization of the developed MNC-SMIA I in order to overcome the previously discussed problems such as low CL signals and high, inhomogeneous backgrounds signals. The aim of the optimization was to achieve an increase in the CL signal, a short assay duration as well as a high assay sensitivity.
In accordance with an analytical approach, one parameter at a time was changed to investigate the influence on the CL signal.
Following parameters were analyzed during the optimization:

- Conditions of microarray chip incubation
- Influence of buffer systems
- Concentration of antibodies and enzymes
- Nanocomposite to antibody mass ratio
- MCR 3 program

Selection of antibodies

The thesis was part of the BMBF Project "Lebensmittelversorgung und Analytik" (13N12613) covering the production of monoclonal and polyclonal antibodies for several foodborne pathogens and toxins including SEB. Consequently, the earlier optimization experiments were partly performed with the anti-SEB antibodies provided by the cooperation partners of the LEVERA project. Due to the shortage of anti-SEB antibodies in the end phase of the LEVERA project, the measurements for assay optimization could only be performed in single measurements. Since the project ended after one and a half year of my experimental phase, I finished my experimental work with more sensitive antibody pair S419/5/5-biotin and S1001/4/6 kindly allocated by the Robert-Koch Insitute, Berlin. The final assay was also performed with this sensitive antibody pair. Table 4.4 displays an overview of the applied sandwich anti-SEB antibody pairs.

TABLE 4.4: Overview of applied sandwich anti-SEB antibody pairs (polyclonal antibody: pAb, monoclonal antibody: mAb).

Capture antibody (supplier)	Detection antibody (supplier)
S1001/4/6 (*Center for Biological Safety, Microbial Toxins, Robert Koch-Institute, Berlin*)	**S419/5/5-biotin** (*Center for Biological Safety, Microbial Toxins, Robert Koch-Institute, Berlin*)
S1001/4/6 (*Center for Biological Safety, Microbial Toxins, Robert Koch-Institute, Berlin, Germany*)	**mAB 1D6-biotin** (*Prof. Maertlbauer, Institute of Milk Hygiene, Milk Technology and Food Science, LMU, Oberschleissheim*)
pAb-biotin (*R-Biopharm AG, Darmstadt*)	**mAB 1D6-biotin** (*Prof. Maertlbauer, Institute of Milk Hygiene, Milk Technology and Food Science, LMU, Oberschleissheim*)

Conditions of microarray chip incubation

First, the conditions of microarray chip incubation were investigated. After the sandwich construct (MNC, biotinylated anti-SEB antibody, SEB) was directly injected in the microarray flow channel, the microarray chips were subsequently incubated for a period of time. During this microarray chip incubation process, SEB in the sandwich construct is bound by the anti-SEB capture antibodies immobilized on the microarray chip surface and the desired antibody sandwich is formed, which can be detected by CL reaction.
Generally, the microarray chip is inserted with its glass surface on top in the microarray chip loading unit in the MCR 3 SLT. The relative large antibody-functionalized magnetic nanocomposites usually tend to settle down to the bottom of the microarray channel over time, which could drastically decrease the interaction time for the formation of the desired antibody sandwich and therefore the sensitivity of the CL assay.
To overcome this problem, the microarray chips were filled with the sample containing the sandwich construct and directly placed on a magnet holder for 30 minutes. Therefore, a perfect attraction of the antibody-functionalized magnetic nanocomposites towards the capture antibodies on the microarray glass slide could be guaranteed during the total incubation time, which increases the interaction time between the immobilized SEB in the magnetic nanocomposites and the capture antibodies. A schematic illustration of the magnetic incubation can be seen in Figure 4.32. The application of a magnetic field to attract magnetic nanoparticles towards an antibody microarray, which increases the assay sensitivit, has already been applied in literature [127].

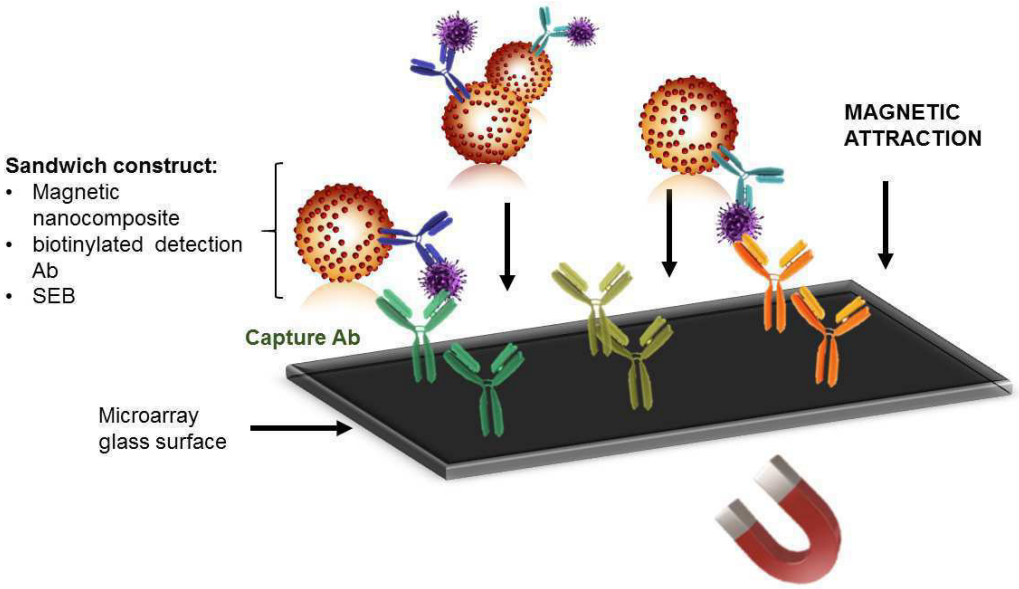

FIGURE 4.32: Schematic illustration of magnetic incubation of microarray chips.

In order to investigate the influence of the magnetic chip incubation, the non-magnetic chip incubation was compared to the magnetic chip incubation on a magnetic holder (30 minutes at 37 °C).
As shown in Figure 4.33 the magnetic incubation revealed an increase in the CL signal of 23% for the capture antibodies S1001/4/6 and 18% for the polyclonal capture antibody, respectively. This result is in accordance with literature, where a magnetic field underneath the microarray could increase the assay sensitivity [127, 154].
Since the effect of magnetic incubation is advantageous but rather weak, additional parameters of microarray chip incubation were further investigated.

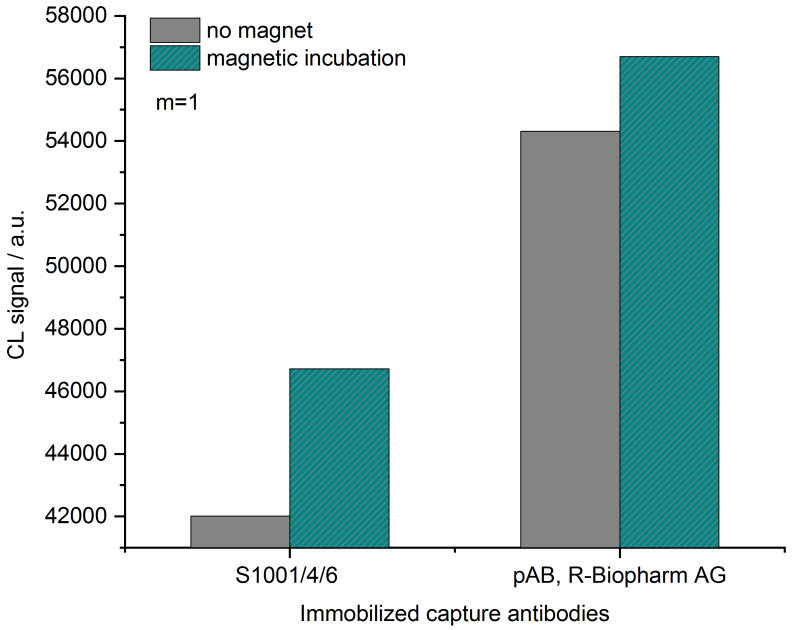

FIGURE 4.33: Comparison of MNC-SMIA I with and without magnetic incubation of microarray chips for 30 minutes at 37 °C. 2.5 mg magnetic nanocomposites were conjugated to anti-SEB mAB 1D6-biotin (c = 125 µg mL^{-1}) and incubated with SEB 10 mg L^{-1} in milk.

Second, the influence of the type of magnetic incubation was investigated. During static magnetic incubation, the microarray chip was placed on a magnetic holder for 30 minutes at 37 °C. In another setup, the magnet was slowly moved from one end to the other end of the microarray chip for 5 minutes. Subsequently the magnet was removed and incubated for 25 minutes at 37 °C. By moving the magnet, the sample is completely spread on the entire microarray channel which might increase the interaction between nanocomposites and the immobilized capture antibodies. However, as shown in Figure 4.34 the moving magnetic incubation exhibits a decrease in the CL signals for both capture antibodies.
For the polyclonal antibody, the static magnetic incubation showed a CL signal of 55,000 a.u., whereas a moving magnetic incubation only showed a CL signal of 18,500 a.u. Using the static magnetic incubation therefore means an increase in the CL signal of around 34%. The monoclonal capture antibody S1001/4/6 exhibited an increase in the CL signal of 31% (static magnetic inbuation: 27,000 a.u., moving magnetic incubation: 8,600 a.u.).
Since a static incubation is highly favoured, a housemade magnetic incubation unit was built by the IWC workshop in order to simultaneously incubate multiple microarray chips (see Materials and Methods 3.2.10).

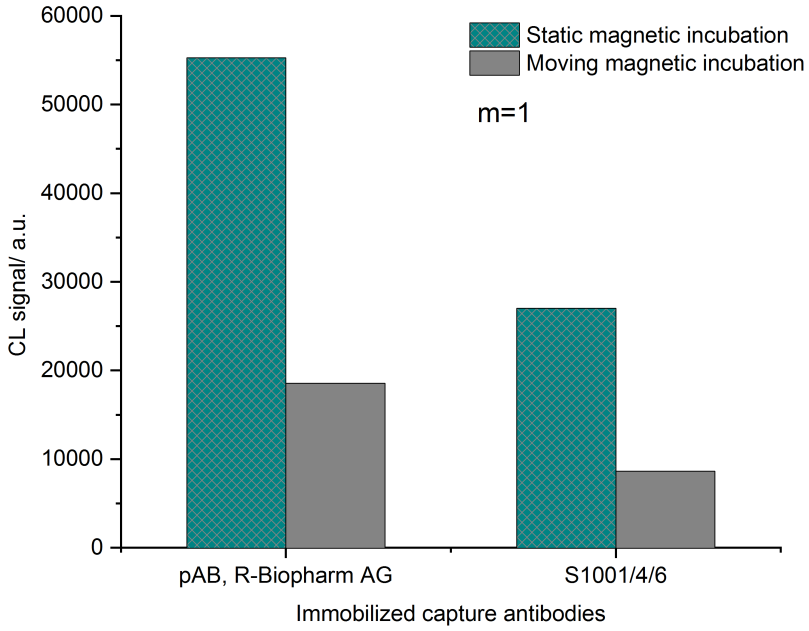

FIGURE 4.34: Comparison of MNC-SMIA I with static and moving magnetic incubation of microarray chips for 30 minutes at 37 °C. 2.5 mg magnetic nanocomposites were conjugated to anti-SEB mAB 1D6-biotin (c= 125 µg mL^{-1}) and incubated with SEB 1000 µg L^{-1} in milk.

Since the reaction time can significantly affect the performance of the immunoassay [66], we investigated the effect of incubation time of the microarray chips on the CL signals. As shown in Figure 4.35 the highest CL signal of 58,000 a.u. could be achieved at an incubation time of 60 minutes. Both, a shorter and a longer incubation time led to a decrease in the CL signal. A shorter incubation time might not be enough for a sufficient interaction between the SEB on the nanocomposites and the capture antibodies on the glass slides. A long incubation at 37 °C could result in a slight activity loss of the antibodies [155], which may eventually decrease the CL signal. The decrease in the CL signal for longer incubation times may also be attributed to a phenomen called Hook effect. Hereby, the capture antibody becomes saturated due to an antigen excess. In this case, free SEB is in competition with captured SEB for detection antibody binding. In summary, the optimal microarray chip incubation condition is a static magnetic incubation for 60 minutes at 37 °C.

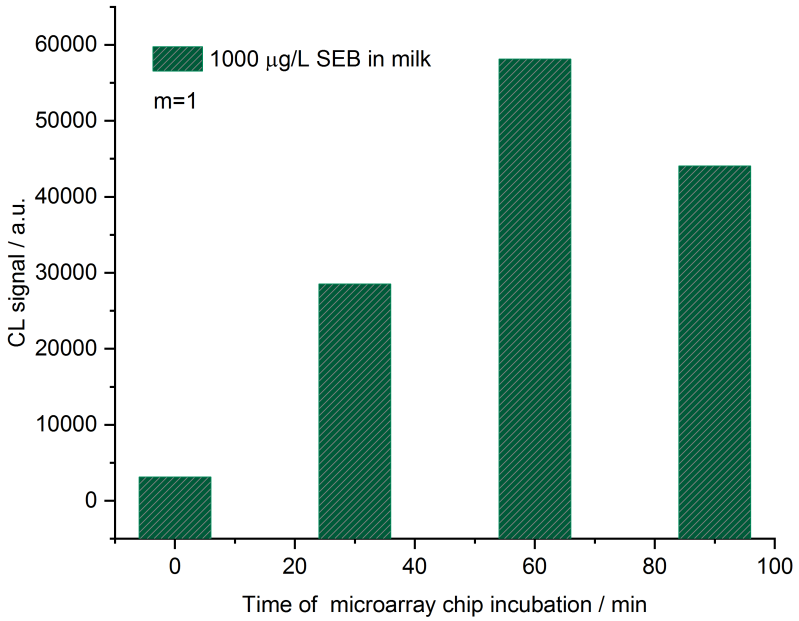

FIGURE 4.35: MNC-SMIA I with static magnetic incubation at various incubation times at 37 °C. 1.25 mg magnetic nanocomposites were conjugated to anti-SEB S419/5/5 (c = 75 µg mL^{-1}) and incubated with SEB 1000 µg L^{-1} in milk.

Influence of blocking buffer on background signal

In order to overcome the previously described problem of high background signal on the microarray surface the influence of blocking buffer was further investigated.
A blocking buffer consists of formulations of proteins designed to prevent non-specific binding and to maximize the signal-to-background ratio. Generally, the optimal blocking buffer should not react with the applied antibodies or target analyte [156].

Prior usage, the microarray chips with immobilized antibodies are filled with the blocking buffer TRIS-HCl in order to block the unspecific binding sites on the microarray chip surface. However, the buffer composition for the further microarray analysis or the sample preparation may have a crucial influence on the CL signals.
In general, the blocking buffer is used for several applications in the MNC-SMIA I.
First, it is applied as running buffer for the MCR 3 SLT. Before starting the experiment, all syringes, tubes and valves of the microarray analysis platform MCR 3 SLT are intensively washed to avoid any unspecific binding of the assay components in the system.
During the automated washing step of the MCR 3 program, running buffer is flushed through the microarray channel and removes unbound assay substrates.
Second, sample containing the sandwich construct is dissolved in blocking buffer (sample buffer). After the direct injection and incubation of the sample in the microarray channel, ideal blocking buffer components such as casein or BSA passively adsorb to all potential sites of nonspecific interaction on the microarray chip surface, which are not occupied by the immobilized antibody, and eliminate background without altering or obscuring the epitope for antibody binding (Figure 4.36). Another important additive of blocking buffer are surfactants e.g. Pluronic® F127. The PEG-block-copolymer Pluronic® F127 is forming a micellar structur, which embeddes the antibody and consequently avoids its unspecific binding to the surface of the microarray [157].

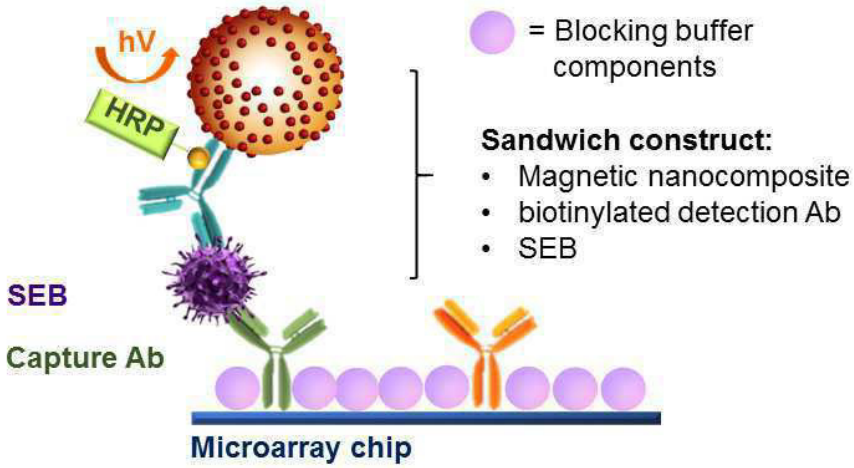

FIGURE 4.36: Scheme of MNC-SMIA I illustrating the blocked unspecific binding sites by blocking buffer components.

For the CL-SMIA on the microarray platform MCR 3 the commonly used running buffer system is casein 0.5% (w/v) in PBS [112, 136].
In order to evaluate the influence of the blocking buffer several buffer compositions were tested:

- Casein/ PBS (0.5% w/v)
- Casein (0.5% w/v)/Pluronic® F127 (0.01% w/v)
- PBS/Pluronic® F127 (0.01% w/v)

To compare the influence of the different blocking buffer systems, the signal-to-no target control (signal/NTC) was calculated according to Equation 4.1. NTC means that only spotting buffer (PBS, trehalose, Pluronic® F127) was spotted on the microarray surface. Consequently, the NTC serves as an indicator for unspecific binding on the microarray.

$$\frac{\text{CL signal (SEB)}}{\text{CL signal (no target control)}} = \text{signal/no target control (\%)} \tag{4.1}$$

2.5 mg magnetic nanocomposites were subsequently conjugated to 200 µL of anti-SEB S419/5/5-biotin (c = 75 µg mL^{-1}, 15 µg). The concentration of the capture antibody S1001/4/6 was set to 0.63 mg L^{-1}. The antibody-functionalized magnetic nanocomposites were incubated in 0.6 mL milk spiked with 1000 µg L^{-1} SEB for two hours. After IMS, the sample was resuspended in the respective blocking buffer and measured by MNC-SMIA I.

The aim of this study was to obtain the highest possible signal/NTC ratio. As shown in Figure 4.37, the typical used blocking buffer casein results in a signal/NTC ratio of 37 (Figure 4.38a).

Since surfactants usually minimize hydrophobic interactions between the blocking protein and the antigen or antibodies [157], the benefit from the addition of the nonionic, surfactant Pluronic® F127 to the blocking buffer was tested. Pluronic is a commonly used surfactant, which is already added to the spotting buffer for the immobilization of antibodies on activated microarray glass slides at the IWC. As displayed in Figure 4.37 the addition of Pluronic® F127 at a concentration of 0.01% (w/v) to 0.5 % (w/v) casein buffer significantly improved the signal/NTC ratio to 104, whereas its addition to only PBS resulted in a low signal/NTC of around 8.
Thus, both casein and Pluronic® F127 are essential blocking buffer components in order to achieve a high signal/NTC for the developed immunoassay.
The ideal blocking buffer system for our developed MNC-SMIA I, is therefore casein 0.5% with Pluronic® F127 (0.01% w/v).

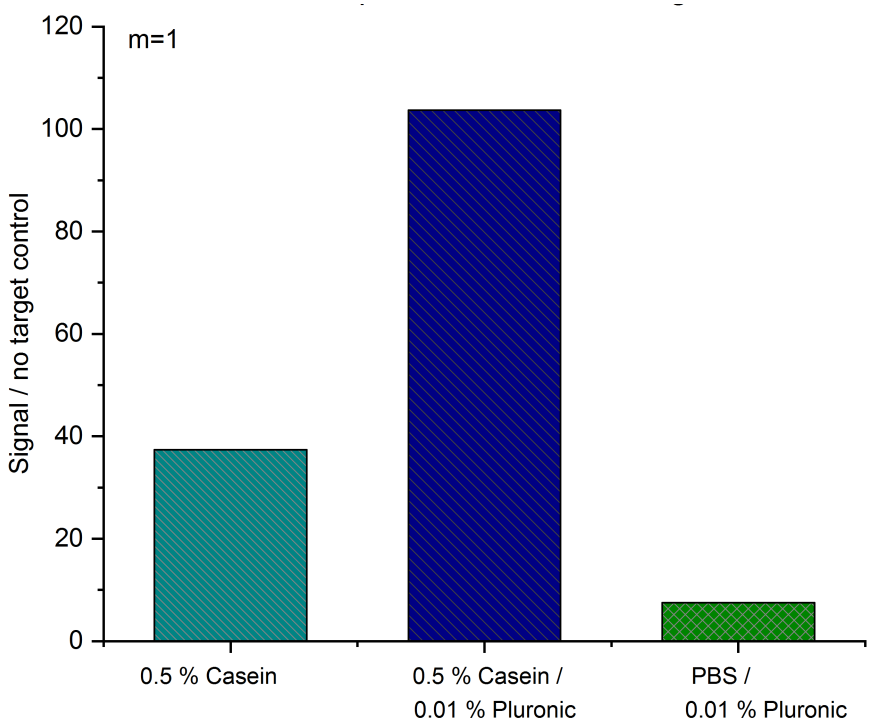

FIGURE 4.37: MNC-SMIA I with various blocking buffers. 2.5 mg magnetic nanocomposites were conjugated to anti-SEB S419/5/5-biotin (c = 75 µg mL^{-1}) and incubated with SEB 1000 µg L^{-1} in milk.

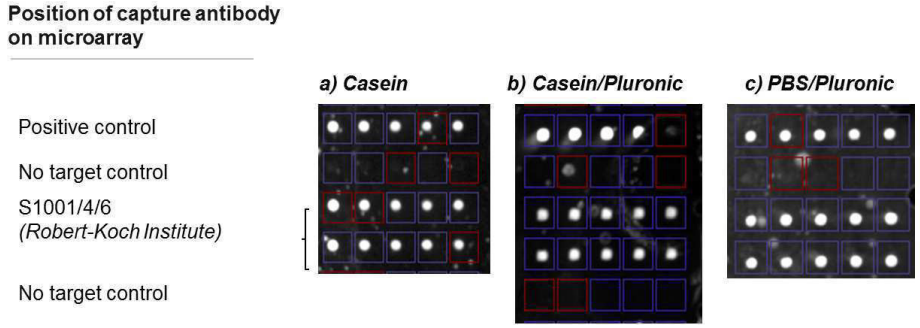

FIGURE 4.38: CL images of MNC-SMIA I with various blocking buffers: a) Casein, b) PBS / Pluronic® F127 and c) Casein / Pluronic® F127.

Influence of marker enzyme

The assay readout is performed by CL imaging after enzymatic reaction of HRP with luminol and peroxide on each spot of the microarray. Common marker enzymes for CL reactions are streptavidin-HRP or streptavidin poly-HRP. Basically, streptavidin binds to biotin at the biotinylated detection antibody with high affinity and the conjugated HRP provides enzyme activity for detection using the CL reagents peroxide and luminol.

In order to investigate the influence of marker enzymes on the developed immunoassay, the MNC-SMIA I was performed with either streptavidin-HRP and streptavidin poly-HRP. Streptavidin-HRP consists of one streptavidin protein that is covalently conjugated to HRP. In comparison, streptavidin poly-HRP conjugate is composed of five identical covalent HRP homopolymer blocks that are covalently coupled to multiple streptavidin molecules [39, 147]. All other assay parameters were kept constant. 1.25 mg magnetic nanocomposites were conjugated to 200 µl of anti-SEB S419/5/5-biotin (c = 37.5 µg mL^{-1}, 7.5 µg). The concentration of the capture antibody S1001/4/6 was set to 0.63 mg L^{-1}. After incubation with 1000 µg L^{-1} SEB in milk (0.6 mL) for two hours, the IMS step and detection by MNC-SMIA I was performed.
As shown in Table 4.5 the application of streptavidin-HRP (c = 0.4 mg mL^{-1}) results in a CL signal of 8400 a.u, wheras the usage of streptavidin poly-HRP (c = 0.4 mg mL^{-1}) reveals a 7-fold higher CL signal at the identical concentration (58,800 a.u.).
This can be explained by the composition of streptavidin-HRP conjugates. The increased molar ratio of HRP molecules to streptavidin results in more signal-generating HRP molecules being available per binding event to react with the substrate. This enables CL signal amplification and more sensitive detection of biotinylated antibodies.
It has to be noted, that the application of streptavidin poly-HRP not only increases the desired CL signal of the analyte but also the signal of the NTC. Hence, the signal/NTC ratio was calculated as described previously (Equation 4.1).
The best signal/NTC ratio of 41 could be achieved by using streptavidin

poly-HRP at a concentration of 0.4 mg mL^{-1}. Since the CL signal at 0.4 mg mL^{-1} is rather close to the saturation level of the CCD camera, a slightly lower concentration of 0.3 mg mL^{-1} was additionally tested. Nevertheless, the CL signal at this high analyte concentration is drastically decreased from 58,800 a.u. to only 9,400 a.u.
Thus, the lower streptavidin poly-HRP concentration is not beneficial for our application and the optimal enzyme marker for our MNC-SMIA I is streptavidin poly-HRP at a concentration of 0.4 mg mL^{-1}.

TABLE 4.5: Influence of marker enzymes streptavidin-HRP and streptavidin poly-HRP on CL signals of MNC-SMIA I.

Marker enzyme	**CL signal (SEB)**	**NTC**	**signal/NTC**
Streptavidin HRP, 0.4 mg mL^{-1}	8,400 a.u.	500 a.u.	17
Streptavidin poly-HRP, 0.3 mg mL^{-1}	9,400 a.u.	250 a.u.	37
Streptavidin poly-HRP, 0.4 mg mL^{-1}	58,800 a.u.	1,400 a.u.	41

Influence of exposure time

Next to the applied marker enzyme, the exposure time for the CCD camera may have a crucial effect on both the CL signal of the analyte SEB and the background. As described previously, the CL signal of SEB at 1000 µg L^{-1} is relatively high (59,000 a.u.) and very close to the saturation level of the CCD camera.

In this study, the exposure time of the CCD camera was varied between 30 seconds, 50 seconds and 60 seconds in order to slightly reduce the CL signal of the analyte, lower the background signal and optimize the signal/NTC ratio. Again, a signal/NTC ratio was calculated in order to evaluate the optimal exposure time for our application.
For this experiment, 1.25 mg magnetic nanocomposites were conjugated to 200 µl of anti-SEB S419/5/5-biotin (c = 37.5 µg mL^{-1}, 7.5 µg). The concentration of the immobilized capture antibody S1001/4/6 was 0.63 mg L^{-1}. After incubation with 1000 µg L^{-1} SEB in milk, the IMS step and a subsequent MCR 3 analysis by MNC-SMIA I was performed.

At an exposure time of 60 seconds a signal/NTC ratio of 41 was obtained. Both a high CL signal (59,000 a.u.) and a high NTC (1,000 a.u.) were achieved, which may decrease the assay sensitivity for the detection of low amounts of

SEB (Table 4.6). In comparison, an exposure time of 50 seconds, as desired, slightly reduces the CL signal of the analyte to 41,000 a.u. and simultaneously drastically lowers the NTC signal from 1,000 a.u. to 260 a.u.
A further decrease of the exposure time to 30 seconds significantly decreases the CL signal of SEB from 41,000 a.u. to only 16,700 a.u., whereas the NTC only reveals a slight decrease in the CL signal (176. a.u).
The lowering of the NTC signal and CL signal of the analyte with decreasing exposure times is also demonstrated in the CL images (Figure 4.39).
Overall, the best signal/NTC ratio of 157 could be achieved at 50 seconds, since this exposure time equally shows a high CL signal for SEB but also an acceptable low NTC signal. Thus, for our further experiments, an exposure time of 50 seconds was applied.

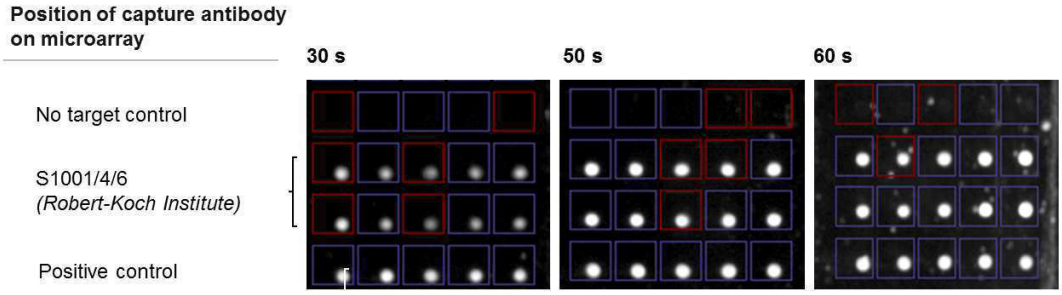

FIGURE 4.39: CL images of MNC-SMIA I with varying exposure times. The microarray contains the spotting control (anti-HRP antibody), the NTC (only spotting buffer) and the anti-SEB capture antibodies S1001/4/6.

TABLE 4.6: Influence of exposure time on CL signals of MNC-SMIA I.

Exposure time	**CL signal (SEB)**	**NTC**	**signal/NTC**
30 seconds	16,700 a.u.	176 a.u.	94
50 seconds	41,000 a.u.	260 a.u.	157
60 seconds	59,000 a.u.	1,000 a.u.	41

Concentration of capture and detection antibody

In this section, we evaluated the optimum concentration of the capture antibody S1001/4/6. Therefore the microarray chip was immobilized with several dilutions of the capture antibody in spotting buffer ranging from 0.04 $mg\,mL^{-1}$ to 0.84 $mg\,mL^{-1}$.
2.5 mg magnetic nanocomposites were conjugated to anti-SEB S419/5/5-biotin (c = 75 $\mu g\,mL^{-1}$, 15 µg). After incubation with 25 $\mu g\,L^{-1}$ SEB in milk (0.6 mL), the IMS followed by MNC-SMIA I were performed. Consequently, the CL signal at different immobilized capture antibody concentrations were compared. The aim of this study was to achieve a maximum CL signal.

Figure 4.40 displays the different CL signals at varying concentrations of the capture antibody. As expected, the dilution series of capture antibodies results in a saturation curve. The ideal concentration of the antibody lies in the saturation level of the curve, since these values display the maximum of the CL signal but are also relatively stable in this region and therefore show the smallest deviations in case of slight unexpected changes in the assay protocol (e.g. temperature, humidity).
An ideal concentration of the capture antibody S1001/4/6 of 0.625 $mg\,mL^{-1}$ was chosen and applied for further experiments, since this concentration exhibits the highest possible CL signal of 51,000 a.u. The application of a higher concentration of 0.84 $mg\,mL^{-1}$ was not necessary since this concentration did not result in an increase in the CL signal.

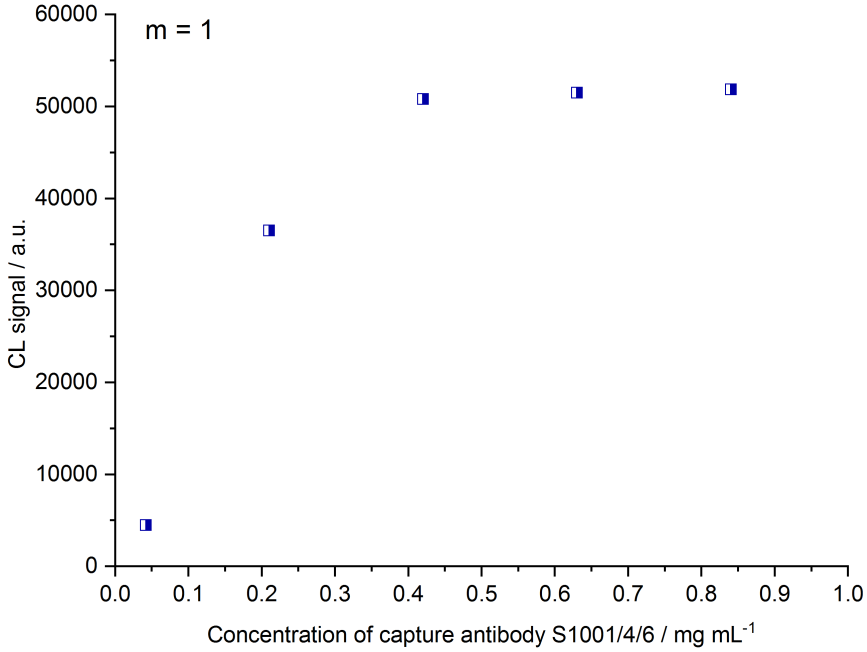

FIGURE 4.40: Influence of varying concentrations of the capture antibody S1001/4/6 on the CL signals of the MNC-SMIA. 1.25 mg magnetic nanocomposites were conjugated to anti-SEB S419/5/5-biotin (c = 37.5 µg mL^{-1}) and incubated with SEB 25 µg L^{-1} in milk, m = 1.

Next, the ideal concentration of the biotinylated detection antibody was investigated. Therefore, a constant amount of 2.5 mg magnetic nanocomposites were incubated with 200 µl of either 25 µg mL^{-1}, 75 µg mL^{-1} or 125 µg mL^{-1} anti-SEB antibody S419/5/5biotin. This equals an antibody to nanocomposite mass ratio of 1:500, 1:166 and 1:100, respectively. The concentration of the capture antibody S1001/4/6 was set to 0.63 mg L^{-1}. The antibody-functionalized magnetic nanocomposites were incubated with 1000 µg L^{-1} SEB in 0.6 mL milk for two hours. IMS and microarray analysis by MNC-SMIA I were done as described previously. The CL signals at various concentrations of the detection antibody were compared, aiming for the highest possible CL signal. In order to choose the ideal amount of antibody related to the applied nanocomposites, the antibody to nanocomposite mass ratio was calculated.

As shown in Figure 4.41 the highest possible CL signal could be achieved at an antibody to nanocomposite mass ratio of 1:166. The data clearly shows that the immunoassay response scales with the concentration of antibodies, increasing initially and decreasing at higher antibody concentrations.

The decrease in the CL signal at high antibody concentrations may be attributed to the inaccessibility of active antibodies due to overlaying effects at high antibody coverage rates, which can impair the availability of the

antigen-binding fragments (Fab) to capture antigen molecules [158].
In contrast, the decrease in the CL signal by addition of low amounts of antibody may be explained by the availability of free surface area causing disorientation and denaturation and thereby affecting their affinity toward the antigen [158]. Another explanation would be that the coverage of antibody on the nanoparticle surface is simply too low to effectively capture the offered amount of SEB.
Thus, for further experiments an antibody to nanocomposite mass ratio of 1:166 was chosen.

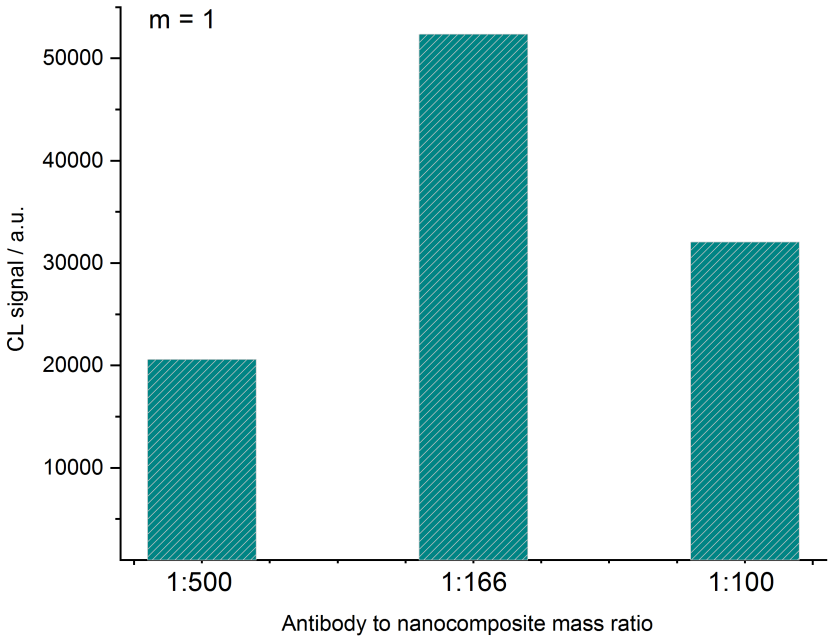

FIGURE 4.41: Influence of varying concentrations of the detection antibody anti-SEB S419/5/5-biotin on the CL signals of the MNC-SMIA I. 2.5 mg magnetic nanocomposites were conjugated to anti-SEB S419/5/5-biotin at 25, 75 or 125 µg mL^{-1} and incubated with 25 µg L^{-1} SEB in milk, m = 1.

Titration of magnetic nanocomposite-antibody conjugate

In a preliminary test, the optimal antibody to nanocomposite mass ratio was found to be at 1:166. Since both nanocomposites and detection antibody may have a crucial influence on the CL signals of the MNC-SMIA I, we titrated the entire magnetic nanocomposite-antibody conjugate, but kept the optimal antibody to nanocomposite mass ratio constant at 1:166.
To obtain a titration curve, several dilutions of the antibody-functionalized magnetic nanocomposites in 0.6 mL SEB spiked milk were prepared. The aim of this study was to identify the required amount of magnetic nanocomposite-to-antibody conjugate, which leads to the highest possible CL signal but also avoids a waste of both nanomaterial and antibody.

Therefore, a serial dilution of antibody-functionalized nanocomposites (antibody to nanocomposite mass ratio: 1:166) was performed in 0.6 mL of SEB spiked milk (c = 25 $\mu g\,L^{-1}$) ranging from 0.42 $mg\,mL^{-1}$ to 4.2 $mg\,mL^{-1}$ nanocomposite-antibody conjugate. After an incubation of 2 hours and several washing steps, the detection of SEB was performed by MNC-SMIA. As usual, the concentration of the capture antibody S1001/4/6 immobilized on the microarray surface was 0.63 $mg\,L^{-1}$.
As expected, the dilution series of capture antibodies results in a saturation curve (Figure 4.42). An optimal CL signal could be achieved at 2.1 $mg\,mL^{-1}$ of magnetic nanocomposite-antibody conjugate (mass: 2.5 mg). At this concentration the CL signal saturates, and the highest possible signal was obtained. The application of a higher concentration of antibody-functionalized nanocomposites (4.2 $mg\,mL^{-1}$) was not required, since no further increase in the CL signal can be observed.

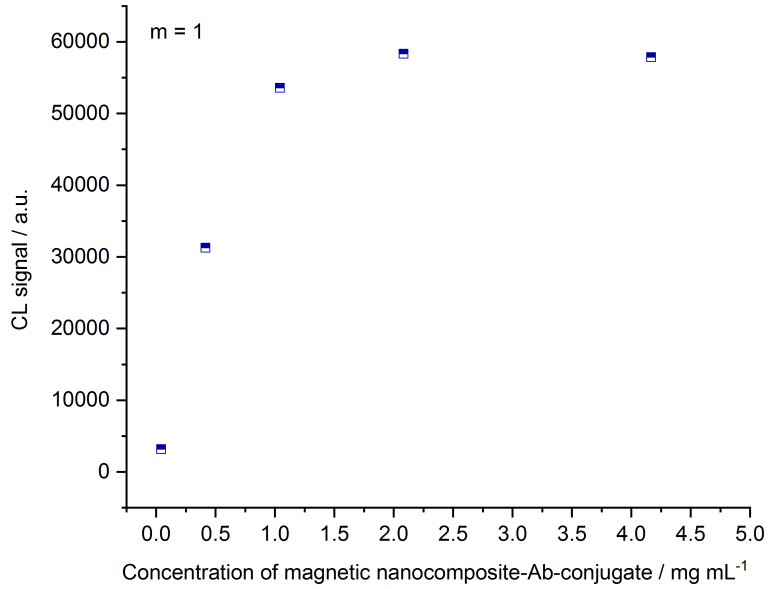

FIGURE 4.42: Influence of varying amounts of magnetic nanocomposite-antibody conjugate on MNC-SMIA I, m = 1.

Summary

The influence of several parameters on the CL signals of the MNC-SMIA I such as conditions of microarray chip incubation, influence of buffer systems, concentration of antibodies and enzymes, nanocomposite to antibody mass ratio as well as exposure time of the CCD camera were investigated during the stepwise assay optimization.
In summary, the MNC-based SMIA was successfully optimized. The aims were to achieve an increase in the CL signal intensity and a decrease in the background signal of the microarray chip surface resulting in a high assay sensitivity.
Even at a significant lower SEB concentration of 25 µg L^{-1} compared to the initial applied 5000 µg L^{-1} SEB, the assay optimization led to a significant increase in the CL signal intensity (Figure 4.43). Additionally the unspecific binding of the substances on the microarray chip surface, which resulted in a relatively high background signal and inhomogeneous chips surface, was drastically reduced. A summary of all optimized parameters are listed in Table 4.7.

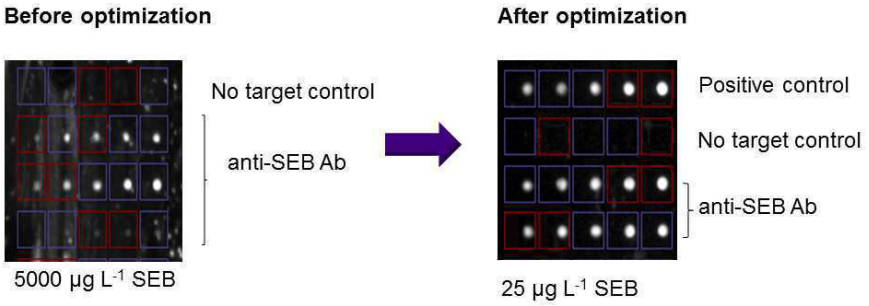

FIGURE 4.43: CL images of the MNC-SMIA I before and after assay optimization.

TABLE 4.7: Summary of optimized parameters of the MNC-SMIA I

Parameter	
Analyte incubation time	2 hours, rotary shaker
Conditions of microarray chip incubation	Magnetic static incubation, 2 hours at 37 °C, 98 rpm
Buffer system	Casein 0.5%, Pluronic® F127 0.01%
Marker enzyme	Streptavidin poly-HRP, c = 0.4 mg mL^{-1}
Exposure time	50 seconds
Capture antibody	S1001/4/6, c = 0.63 mg mL^{-1}
Detection antibody	S419/5/5-biotin Antibody to nanocomposite mass ratio = 1:166 (1.25 mg MNC, 7.5 µg Ab)
Magnetic nanocomposite-antibody conjugate	2.1 mg mL^{-1}

4.3.3 Calibration of MNC-SMIA I

After the stepwise assay optimization, a calibration curve for the quantification of SEB in milk by MNC-SMIA I was performed by applying optimal assay parameters.
1.25 mg nanocomposites were functionalized with 200 µl of 37.5 µg L^{-1} S419/5/5-biotin (antibody to nanocomposite mass ratio = 1:166). Antibody-functionalized magnetic nanocomposites were incubated in 0.6 mL of SEB spiked

milk samples in the range of 0 - 1000 µg L^{-1}. During the incubation time of two hours under gentle mixing on an overhead shaker, the analyte SEB bound to the antibody-functionalized magnetic nanocomposite in an affinity reaction. Subsequently, SEB was isolated and separated from the milk by IMS using a magnetic separation rack. The initial sample volume of 0.6 mL is concentrated to 52 µL, which equals a volumetric concentration factor of around 11.5. After the injection of the sandwich construct consisting of nanocomposite, biotinylated detection antibody and SEB in the microarray channel of the chip, the microarray chip was incubated on a magnetic chip holder for two hours at 37 °C at a shaking rate of 98 rpm.
For the detection via MNC-SMIA I the capture antibody S1001/4/6 was immobilized on the chip surface at a concentration of 0.63 mg mL^{-1}. The assay readout was performed by CL imaging after enzymatic reaction of HRP with luminol and hydrogen peroxide on each spot of the microarray. As marker enzyme, streptavidin poly-HRP at a concentration of 0.4 mg mL^{-1} was applied.
As shown in Figure 4.44, a sigmoidal correlation of the CL signal as a function of the decadic logarithm of the SEB concentration was obtained. By calculating the mean CL signals of blank measurements using milk (n = 3) plus three times the standard deviation, a LOD of 0.05 µg L^{-1} was obtained. A WR from 1.9 µg L^{-1} to 10.3 µg L^{-1} and EC50 value of 4.4. µg L^{-1} were achieved.

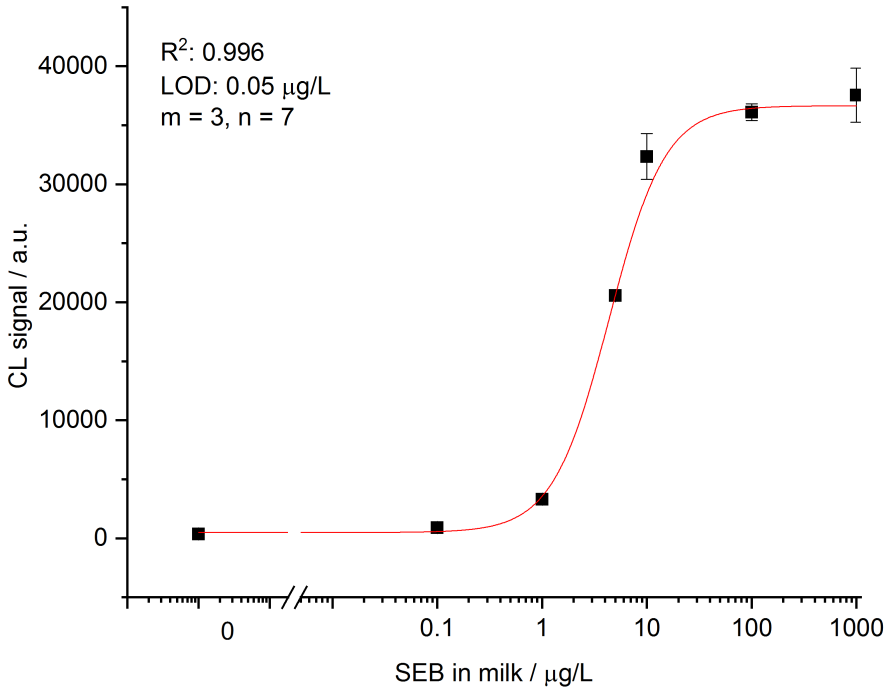

FIGURE 4.44: Calibration curve for the quantification of SEB in milk analyzed by MNC-SMIA I. Standard deviations (n = 3) are indicated as error bars.

4.3.4 Recovery experiments

Recovery experiments were performed to verify the established MNC-SMIA I. To determine recoveries of the developed analytical method, milk samples were spiked with SEB at three different concentrations (2.5 µg L^{-1}, 5 µg L^{-1} and 7.5 µg L^{-1}) in the linear WR of the calibration curve.
Samples were freshly prepared as described previously and measured analogously by MNC-SMIA I. All experiments were performed in triplicates. Recovered concentrations were calculated from the CL signals of the MNC-SMIA I according to the previously determined linear fit curve (Figure 4.44). For SEB concentrations of 2.5 µg L^{-1}, 5 µg L^{-1}, and 7.5 µg L^{-1} in milk samples, recoveries of 90.6 $\pm$ 7.1 %, 94.7 $\pm$ 8.3% and 101.2 $\pm$ 15.2 % were obtained, respectively (Table 4.12). An average recovery of 95.8 $\pm$ 5.9 % was calculated. This result indicated that the MNC-SMIA I was highly reproducible in milk.

TABLE 4.8: Table of recovery experiments (m = 3, n = 3). The concentration of the used sample,the recovery values and the averaged recovery are displayed.

Concentration of SEB / µg L^{-1}	**Recovery / %**	**Averaged recovery / %**
2.5	98.8 87.3 85.7	90.6 $\pm$ 7.1
5	102.5 127.4 95.4 86	94.7 $\pm$ 8.3
7.5	90.4 119.4 96.6	101.2 $\pm$ 15.2%

4.3.5 Comparison of CL-SMIA and MNC-SMIA I

As displayed in Figure 4.45, the CL-SMIA was compared to the MNC-SMIA I, which combines a prior IMS step with the sensitive microarray analysis detection.
For the CL-SMIA, 0.6 mL of the milk sample spiked with SEB is directly injected into the sample loop of the MCR 3 SLT.
In comparison, in the MNC-SMIA I the analyte SEB in 0.6 mL milk is first isolated and separated from the food matrix. Additionally, the initial sample volume of 0.6 mL is enriched and concentrated to 52 µL, which equals a volumetric concentration factor of around 11.5. The application of the IMS based on superparamagnetic nanocomposites was initially implemented to decrease the LOD and EC_{50} and therefore improve the assay sensivity (Figure 4.45).

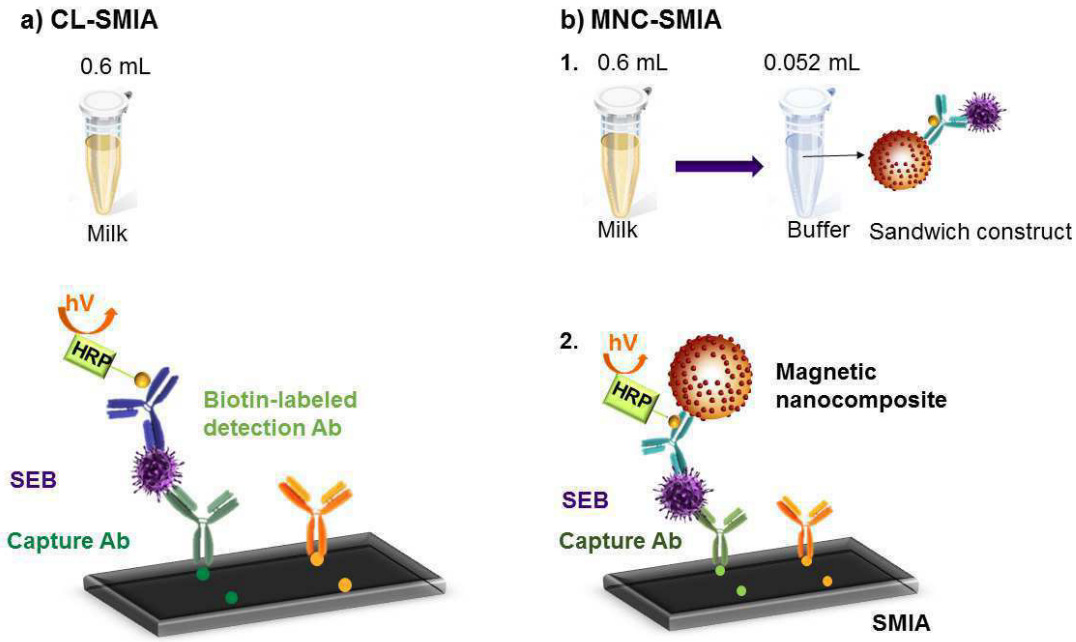

FIGURE 4.45: Schematic illustration of of CL-SMIA a) and MNC-SMIA I b).

By applying the CL-SMIA a LOD of 0.13 µg L^{-1} and EC_{50} of 14.5 µg L^{-1} was obtained. In the MNC-SMIA I, which involves a prior IMS, both LOD and EC_{50} could be slightly improved to 0.05 µg L^{-1} and 4.4 µg L^{-1}, respectively (Table 4.9). Advancing the existing antibody-based microarray principle, the novel superparamagnetic iron oxide-shell silica-core nanocomposites proved amenable to enrichment procedures, by further increasing sensitivity, starting from a sample volume of 0.6 mL.

TABLE 4.9: Comparison of MNC-SMIA I and CL-SMIA

	LOD / µg L^{-1}	**EC50 /** µg L^{-1}	**WR /** µg L^{-1}
CL-SMIA	0.13	14.5	4.6 - 45.8
MNC-SMIA I	0.05	4.4	1.9 - 10.3

4.4 Development of MNC-SMIA II in large volumes of milk

4.4.1 Assay principle MNC-SMIA II in large volumes of milk

After establishing the rapid, sensitive and cost-effective MNC-SMIA, the suitability of this analytical approach should be tested for large-scale screening of food samples from the food supply chain. The sample volume was therefore upscaled from 0.6 mL to 100 mL of ultra-pasteurized milk. Basically, a further decrease of the assay sensitivity due to the concentration step should be achieved. A schematic illustration of the assay principle of the MNC-SMIA II in 100 mL milk is displayed in Figure 4.46.

The iron oxide-shell silica-core nanocomposites were functionalized with biotinylated anti-SEB detection antibody S419/5/5-biotin and incubated in 100 milk containing the analyte SEB. The magnetic nanocomposites coupled to biotinylated secondary antibodies bound the SEB in the liquid phase by an affinity reaction. In order to selectively enrich and isolate SEB from the complex food matrix milk the whole sandwich construct consisting of MNC, biotinylated anti-SEB detection antibody and SEB was separated by IMS. After several magnetic washing steps the magnetic nanocomposites were resuspended in 52 µL of buffer (casein 0.5% (w/v), Pluronic® 0.01% (w/v), which is nearly the volume capacity of the microarray channel flow cell. This concentration step, starting from 100 mL milk, means the initial sample was concentrated by a volumetric concentration factor of 1923. The quantification of SEB by sandwich microarray immunoassay on the analysis platform MCR 3 SLT was performed as described before (see 4.3.1).

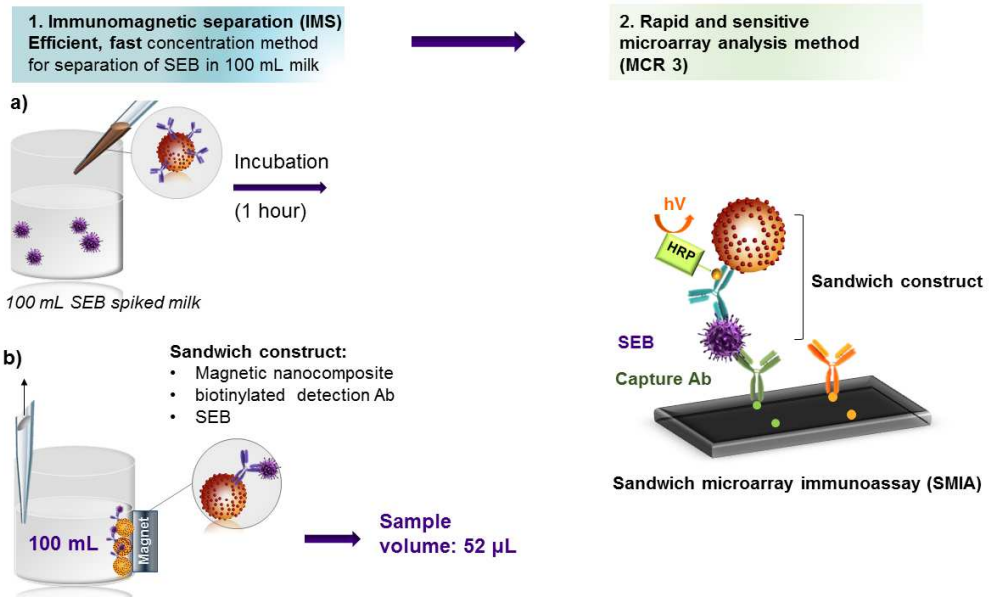

FIGURE 4.46: Schematic illustration of MNC-SMIA II in 100 mL milk. Pre-enrichment and isolation of the analyte SEB from the food matrix milk by IMS a) is combined with a rapid and sensitive microarray analysis b).

4.4.2 Separation capability of iron oxide-shell silica-core nanocomposites in milk

In this section, a rapid and efficient IMS step for the magnetic separation capability of the iron oxide-shell silica-core nanocomposites in a large volumes of the complex food matrix milk was developed.
In order to achieve an optimal separation capability of nanocomposites and also a time-efficient, cost-effective and convenient IMS step, magnetic separation of iron oxide-shell silica-core nanocomposites in milk was evaluated by using various separation techniques.
We demonstrate three types of separation techniques: a) manual separation in a glass container, b) automatic separation via syringe pump and c) automatic separation via peristaltic pump.
The setups for the automated and manual magnetic separation techniques are illustrated in Figure 4.47. In order to compare the separation techniques, the iron content of the nanocomposites and therefore the recovery of the nanocomposites, before and after separation in milk, was quantified by ICP-MS measurements.

Before each separation, 2.5 mg epoxysilane-functionalized magnetic nanocomposites were spiked to 100 mL milk.
In detail, for the manual separation, 25 mL of the magnetic nanocomposites spiked milk were filled in a small glass container. The magnetic nanocomposites were attracted by applying a magnet between both filled glasses (Figure 4.47a). After five minutes, the milk was carefully removed. This step was repeated until 100 mL of the spiked milk were separated. In total, this separation process took approximately 10 minutes.

For the automatic separation two adjustable permanent magnets were used and connected by a tube to either a peristaltic pump or a syringe pump for an automated flow of the spiked milk. For the automatic separation by syringe pump, 50 mL of milk each were filled in a disposable syringe. For the peristaltic pump the tube was placed in the milk reservoir and slowly pumped across the created magnetic field. To increase the interaction time and interaction area of the magnetic nanocomposites in the magnetic field, a tube sample loop was created (Figure 4.47b, c).

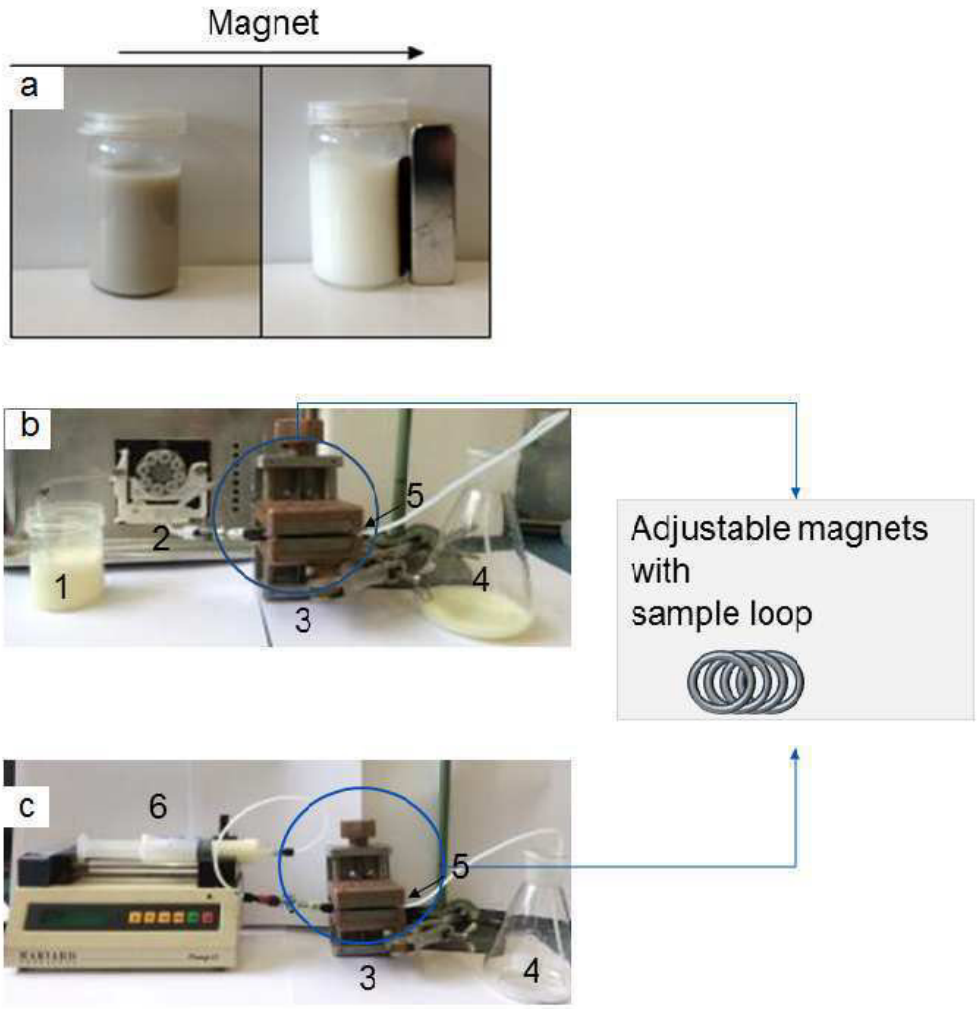

FIGURE 4.47: Automatic separation of iron oxide-shell silica-core nanocomposites in 100 mL milk: a) manual separation, b) syringe pump, c) peristaltic pump. The technical separation setup consists of: 1) milk reservoir, 2) peristaltic pump, 3) permanent magnet holder, 4) waste bottle, 5) tube including sample loop, 6) syringe pump.

Both automatic separation procedures by using a peristaltic pump or syringe pump led to a significant decrease in the recovery rate. By automatic separation via syringe pump recoveries of only 62% at a pump flow rate of 0.35 mL min^{-1}, 61% at 0.85 mL min^{-1} and 50% at 1.5 mL min^{-1} were obtained. A separation of 100 mL milk at an optimal pump flow rate of 0.85 mL min^{-1} took around 1.5 hours, and is therefore relatively time-consuming (Table 4.10).
The magnetic separation via peristaltic pump showed decreasing recovery rates with increasing pump flow rates of 49% at a pump flow rate of 0.35 mL min^{-1}, 27% at 0.85 mL min^{-1} and 22% at 1.5 mL min^{-1}, respectively. The separation of 100 mL at the best flow rate of 0.35 mL min^{-1} took approximately 5 hours (Table 4.10).
The low recoveries for the automated magnetic separation may possibly attributed to the fact, that the magnetic attraction of the nanocomposites towards the permanent magnet was not sufficient under a continous flow. Additionally, an automatic separation was highly time-consuming, since the pump flow rate has to be drastically decreased to guarantee a high recovery rate. In comparison, ICP-MS measurements reveal that magnetic nanocomposites can be manually separated with a relatively high recovery rate of 83.6 $\pm$ 3.0 % (Figure 4.48). Since the manual separation only took around 10 minutes, this separation strategy was both highly effective and time-efficient. Additionally it does not require any technical setup (e.g. pumps, tubes), which makes it rather convenient and practically applicable anywhere.
Overall, whereas the magnetic separation in a static system such as the glass container revealed high recovery rates, the automatic flow-based separation technique resulted in significantly lower recovery rates. Since the aim of this study was to achieve a rapid and simple separation technique, the manual separation was favoured due to their high recovery rate, economy of time and practicability.

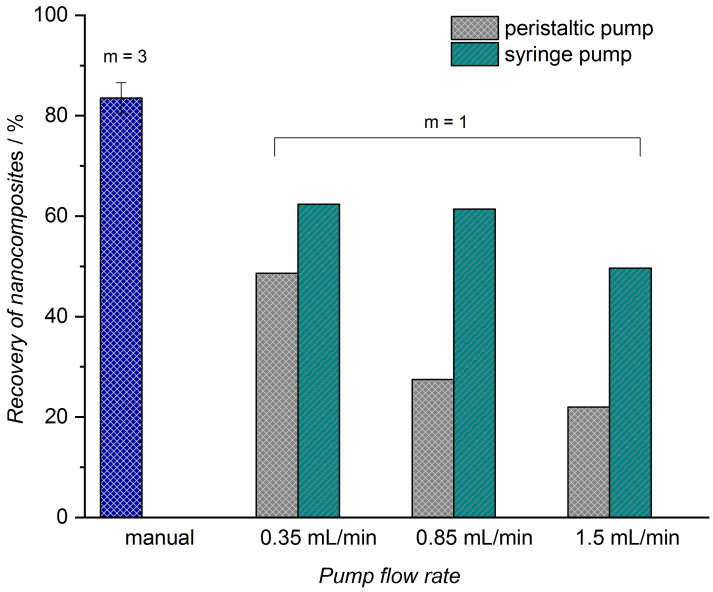

FIGURE 4.48: Recovery experiments of hydrophilic iron oxide-shell silica-core nanocomposites in 100 mL milk by various separation techniques. The iron content before and after separation in milk was quantified by by ICP-MS.

TABLE 4.10: Separation capability

Separation technique	**Flowrate /mL min^{-1}**	**Recovery / %**	**Time**
Manual separation	-	83.6 $\pm$ 3.0 (m = 3)	10 min
Syringe pump (automated)	0.35	62	
	0.85	61	1.5 h
	1.5	50	
Peristaltic pump (automated)	0.35	49	
	0.85	27	5 h
	1.5	22	

4.4.3 Optimization of MNC-SMIA II in large volumes of milk

On the basis of the optimized parameters for the previously described MNC-SMIA I in small volumes (see 4.3) the MNC-SMIA II in 100 mL was developed.
Due to time shortage at the end of the experimental phase, the assay optimization could only be focused on two assay parameters: 1) incubation time of the analyte and 2) titration of the magnetic nanocomposite-antibody conjugate. All remaining assay parameters including the MCR 3 program were adapted from the MNC-SMIA I (0.6 mL).

Titration of magnetic nanocomposite-antibody conjugate

A higher milk sample volume may require an increased amount of magnetic nanocomposite-antibody conjugates to efficiently capture the analyte SEB in the large volume. In this experiment the required amount of magnetic nanocomposite-to-antibody conjugate, leading to the highest possible CL signal with a simultaneous economic usage of both nanomaterial and antibody, should be evaluated.

Magnetic nanocomposites were functionalized with the detection antibody S419/5/5-biotin at an antibody to nanocomposite mass ratio of 1:166. A serial dilution of the nanocomposite-antibody conjugate was performed in 100 mL of SEB spiked milk (c = 100 µg L^{-1}) at a nanocomposite-antibody conjugate concentration of 6.25 mg mL^{-1}, 4.2 mg mL^{-1} and 2.1 mg mL^{-1}, respectively.
After gentle mixing of the sample on an overhead shaker for two hours, IMS was performed by applying a permanent magnet. SEB was subsequently quantified by MNC-SMIA.
Figure 4.49 shows that the highest possible CL signal could be achieved at magnetic nanocomposite-antibody conjugate concentration of 4.2 mg mL^{-1}. Both higher (6.25 mg mL^{-1}) and lower (2.1 mg mL^{-1}) concentrations of the magnetic nanocomposite-antibody conjugate result in a decreased CL signal. Compared to the 0.6 mL, the sample volume was increased 167-fold in the 100 mL sample. As expected, a higher amount of magnetic nanocomposite-antibody conjugate was required in order to bind the analyte SEB in the larger volume. Whilst the sample volume was increased 167-fold, double the amount of nanocomposite-antibody conjugates had to be applied for MNC-SMIA in 100 mL milk compared to 0.6 mL milk.

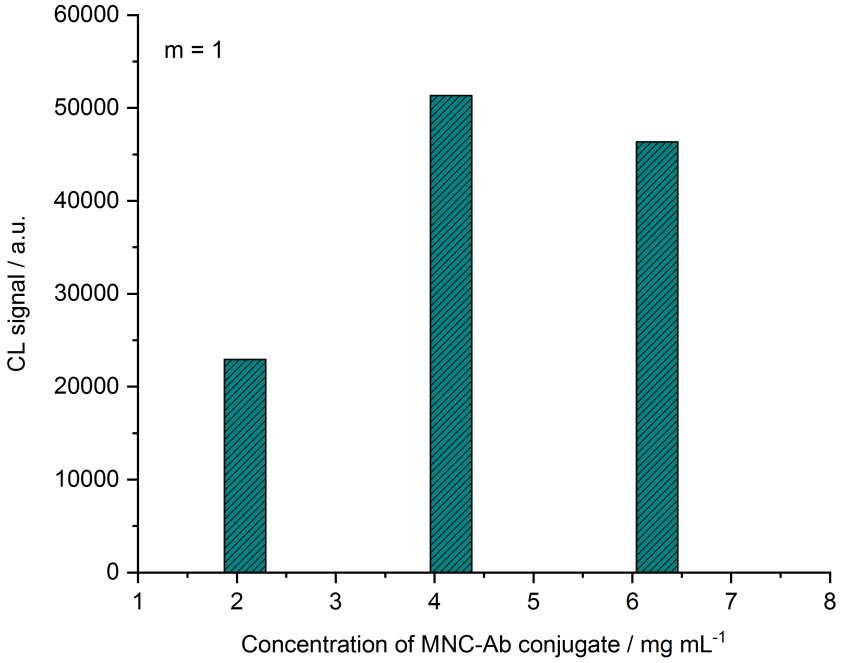

FIGURE 4.49: Influence of varying concentrations of magnetic nanocomposite-S419/5/5-biotin-conjugate on the CL signals of MNC-SMIA II. Antibody-nanocomposite conjugates were added to 100 mL of SEB spiked milk (c = 100 µg L^{-1}) , m = 1.

Influence of analyte incubation time

Due to the increase in the sample volume, a longer incubation time may be beneficial in order to efficiently capture the SEB in 100 mL milk. As previously described in literature, an increase in the analyte incubation time from two hours to 16 hours showed a positive effect on the assay sensitivity for the detection of bacterial toxins by multiplexed fluorescent magnetic suspension assay [3].
In order to improve the assay sensitivity, the influence of the analyte incubation time, which means the incubation of antibody-functionalized magnetic nanocomposites in milk spiked with SEB, was investigated in detail.
The antibody-functionalized magnetic nanocomposites were added to 100 mL of SEB spiked milk (c = 100 µg L^{-1}) at a concentration of 2.1 mg mL^{-1}. Then, the milk samples were gently mixed on a rotary shaker from 0.5 hour to 24 hours.
After IMS, SEB was detected and quantified by MNC-SMIA II. All remaining assay parameters were kept constant, as described above.
Figure 4.50 shows, that an analyte incubation time of one hour results in a high CL signal intensity of 57,000 a.u. An increase in the analyte incubation time to two or even four hours did not have a positive effect on the CL signals. In comparison, the incubation time of 30 minutes appears too short in order to achieve an optimal interaction between nanocomposites and the SEB in the milk, resulting in a lower CL signal of 42,000 a.u. Consequently, the optimal analyte incubation time for our immunoassay was one hour.

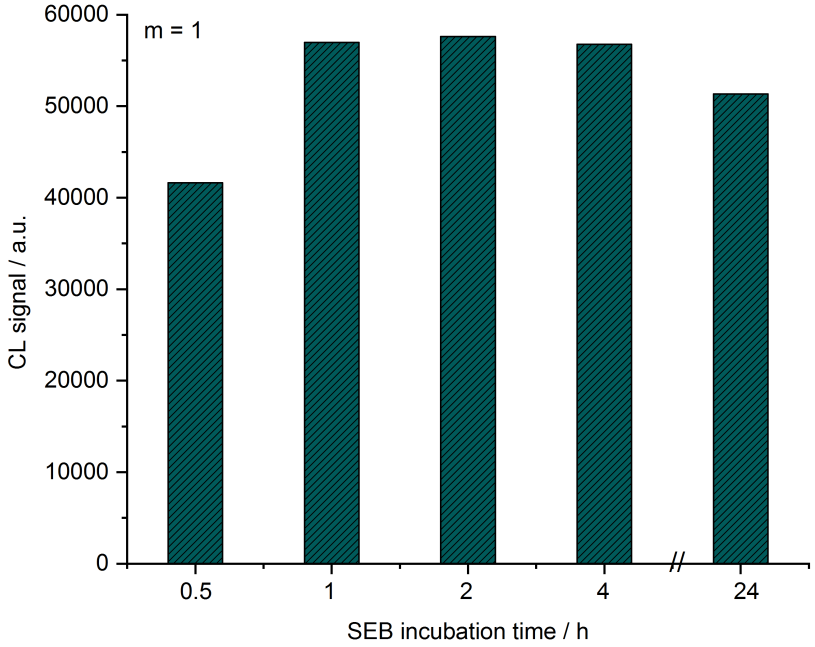

FIGURE 4.50: Influence of analyte incubation time on the CL signals of the MNC-SMIA II in 100 mL milk (c = 100 µg L^{-1} SEB), m = 1.

In summary, the MNC SMIA II in 100 mL milk was mostly adapted from the MNC-SMIA I in 0.6 mL milk. The influence of the two parameters 1) titration of the magnetic nanocomposite-antibody conjugates and 2) analyte incubation time were investigated during the stepwise assay optimization. A summary of all assay parameters are listed in Table 4.11.

TABLE 4.11: Summary: Optimized parameters of the MNC-SMIA II in 100 mL milk.

Parameter	
Analyte incubation time	1 hour, rotary shaker
Conditions of microarray chip incubation	Magnetic static incubation, 2 hours at 37 °C, 98 rpm
Buffer system	Casein 0.5%, Pluronic® F127 0.01%
Marker enzyme	Streptavidin poly-HRP, c = 0.4 mg mL^{-1}
Exposure time	50 seconds
Capture antibody	S1001/4/6, c = 0.63 mg mL^{-1}
Detection antibody	S419/5/5-biotin, Antibody to nanocomposite mass ratio = 1:166 (2.5 mg MNC, 15 µg Ab)
Magnetic nanocomposite-antibody conjugate	4.2 mg mL^{-1}

4.4.4 Calibration of MNC-SMIA II in 100 mL milk

After the stepwise assay optimization, a calibration curve for the quantification of SEB in milk by MNC-SMIA II in 100 mL was performed with the parameters listed in Table 4.11.
Therefore, 2.5 mg magnetic nanocomposites were functionalized (antibody to nanocomposite mass ratio = 1:166). After the antibody conjugation, the magnetic nanocomposites were incubated in 100 mL of SEB spiked milk samples in the range of 0 - 1000 µg L^{-1}. The samples were incubated on an overhead shaker for one hour under gentle mixing. The analyte SEB, bound to the antibody-functionalized magnetic nanocomposites, was separated from the milk by IMS. The initial sample volume of 100 mL was concentrated to 52 µL, which equals a volumetric concentration factor of approximately 1923. After injection of the sample containing sandwich construct (nanocomposite, biotinylated antibody and SEB) in the microarray channel of the chip, the microarray chip was incubated on a magnetic chip holder for 1 hour at 37 °C at constant shaking.
For the detection via MNC-SMIA II the capture antibody S1001/4/6 was immobilized on the chip surface at a concentration of 0.63 mg mL^{-1}. The assay readout was performed by CL imaging. The automated MCR 3 program took

8 minutes. In summary, the total assay duration was less than three hours, involving analyte incubation time (1 hour), IMS (0.5 hour), microarray chip incubation (1 hour) and microarray analysis (8 minutes).
As shown in Figure 4.51 a sigmoidal correlation of the CL signal as a function of the decadic logarithm of the SEB concentration was obtained. By calculating the mean CL signals of blank measurements using milk (n = 3) plus three times the standard deviation a LOD of 0.39 ng L^{-1} was obtained. A WR from 0.07 µg L^{-1} to 0.93 µg L^{-1} and EC_{50} value of 0.25 µg L^{-1} were achieved.
Overall, the LOD of 0.39 ng L^{-1} was lower compared to other nanoparticle-based SEB detection methods in literature [124, 125, 159] and similar to the previous published multiplexed fluorescent magnetic suspension assay [3]. Nevertheless, the large sample volume of 100 mL and the short assay time of less than 3 hours is highly advantageous compared to the previous published reports in literature.

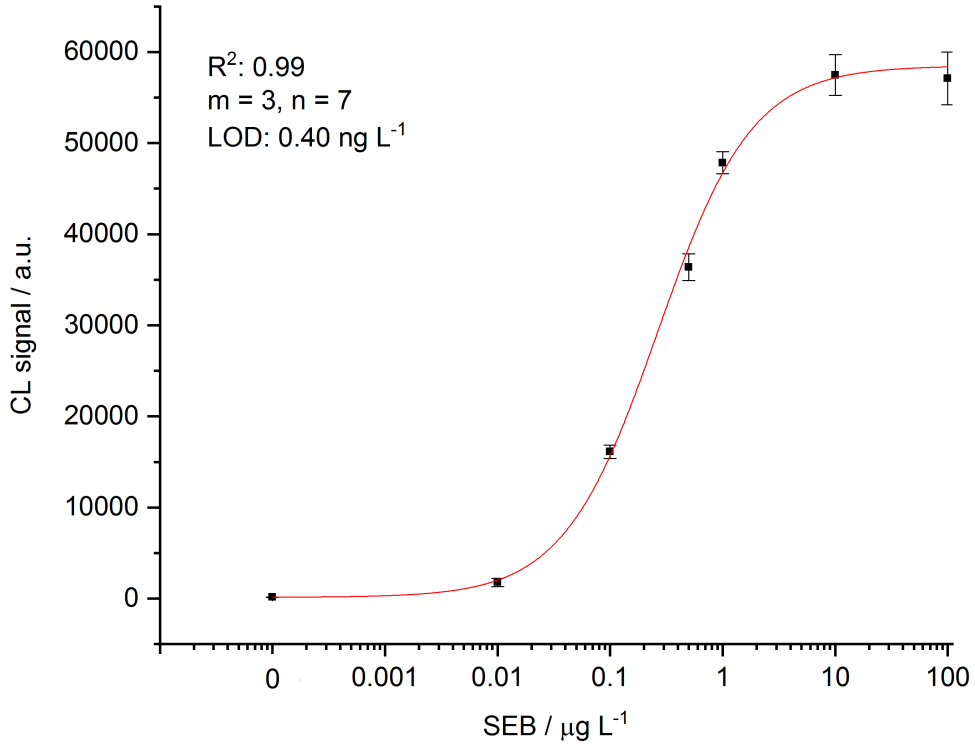

FIGURE 4.51: Calibration curve for the quantification of SEB in 100 mL milk analzyed by MNC-SMIA II . Standard deviations (n = 3) are indicated as error bars.

4.4.5 Recovery experiments

Recovery experiments were performed to verify the established MNC-SMIA II in 100 mL milk. To determine recoveries of this analytical method, milk samples were spiked with SEB at the concentrations 0.1 µg L^{-1} , 0.5 µg L^{-1} and 0.75 µg L^{-1}. Experiments were performed in triplicates. All samples were freshly prepared as described previously and measured by the developed MNC-SMIA II.
Recovered concentrations were calculated from the CL signals of the MNC-SMIA II according to the previously determined linear fit curve (Figure 4.51). For spiked SEB concentration of 0.1 µg L^{-1}, 0.5 µg L^{-1}, and 0.75 µg L^{-1}, recoveries of 93 $\pm$ 13.6 %, 91 $\pm$ 8.9 % and 94.7 $\pm$ 27.9 % were obtained, respectively (Table 4.12). An average recovery of 92.9 $\pm$ 1.9 % was calculated. This result indicated that the MNC-SMIA II was highly reproducible in milk.

TABLE 4.12: Table of recovery experiments (m = 3, n = 3). Listed is the concentration of used samples, recovery values and the averaged recovery.

Concentration of SEB / µg L^{-1}	**Recovery / %**	**Averaged recovery / %**
0.1	106.3 93.7 79.1	93 $\pm$ 13.6%
0.5	101.2 86.8 84.9	91 $\pm$ 8.9%
0.75	125.8 86.5 71.9	94.7 $\pm$ 27.9%

4.4.6 Comparison of SMIAs for the detection and quantification of SEB in milk

In this section, the three developed SMIAs: 1) CL-SMIA 2) MNC-SMIA I in small volumes (0.6 mL) and 3) MNC-SMIA II in large volumes (100 mL) are conclusively compared and summarized.
Whereas both MNC-SMIAs involve an isolation and enrichment by IMS prior to a sensitive microarray analysis, the milk sample containing the analyte SEB is directly measured in the CL-SMIA without any sample preparation.
Basically, the applied IMS in the MNC-SMIAs allows a concentration of the starting sample volume from either 0.6 mL and 100 mL to 0.052 mL, which equals a volumetric concentration factor of 11.5 and 1923, respectively. In principle, by implementing an IMS step based on magnetic nanocomposites, an effective separation of SEB from the food matrix milk should be achieved. Furthermore, the assay sensitivity should be improved by an effective concentration process via magnetic separation.

By comparing the MNC-SMIA I to CL-SMIA, Table 4.13 shows that the LOD could be enhanced to 0.05 µg L^{-1} compared to 0.13 µg L^{-1}. The EC_{50} value was improved from 14.5 µg L^{-1} to 4.4 µg L^{-1}. The left shift of the calibration curve of MNC-SMIA I can be seen in Figure 4.52. Thus, the prior IMS step in a sample volume of 0.6 mL milk by a volumetric concentration factor of 11.5 results in an increased assay sensitivity.

Advancing the developed MNC-SMIA I technology, the novel superparamagnetic nanocomposites proved suitable for large-scale enrichment procedures in 100 mL milk. Hereby, the assay sensitivity could be further decreased to a LOD of 0.39 ng L^{-1} and an EC_{50} value of 0.25 µg L^{-1} (Table 4.13). The left shift in the calibration curve can be observed in Figure 4.52.
When compared to previously reported nanoparticle-based SEB detection methods in literature [124, 125, 159] our developed MNC-SMIA II in 100 mL milk allows a more sensitive quantification of SEB.
The obtained assay sensitivity is comparable to the earlier published multiplexed fluorescent magnetic suspension assay for the parallel detection of five bacterial and plant toxins from food matrix [3]. Here, SEB was isolated and enriched by the application of commercial magnetic fluorescent beads. The assay sensitivity was 0.3 ng L^{-1} in a sample volume of 0.5 mL (enrichment factor: 10). The total assay time was approximately 24 hours.

Compared to the multiplex fluorescent suspension assay in 0.5 mL food sample our developed MNC-SMIA proved suitable for the enrichment of a larger sample volume of 100 mL. Additionally, the presented immunoassay is less time-consuming (3-4 hours), which is highly advantageous in an urgent case of a foodborne disease outbreak in the food supply chain. A crucial disadvantage of commerically available magnetic nanoparticles such as Dynabeads ™ is their high purchase price (100 mg Dynabeads™ M-280 Streptavidin: 2400 Euro), which may limit the high-throughput screening of food

samples. In comparison, our cost-effective in-house, economic and large-scale production of iron oxide-shell silica-core nanocomposites is highly beneficial. With regard to all used reagent and solvents, an approximate yield of 100 mg iron oxide-shell silica-core nanocomposites costs around 15 Euro. Magnetic nanocomposites per sample for MNC-SMIA I cost 20 Euro cents and 40 Euro cents for MNC-SMIA II.
In summary, the enrichment and isolation of the analyte SEB from a larger food sample (0.6 mL and 100 mL) by IMS combined with the sensitive microarray analysis were successfully applied to increase the assay sensitivity. On the basis of our results, the immunoassay appears to be a suitable and both time- and cost-effective approach for large-scale screening of samples from the food supply chain.

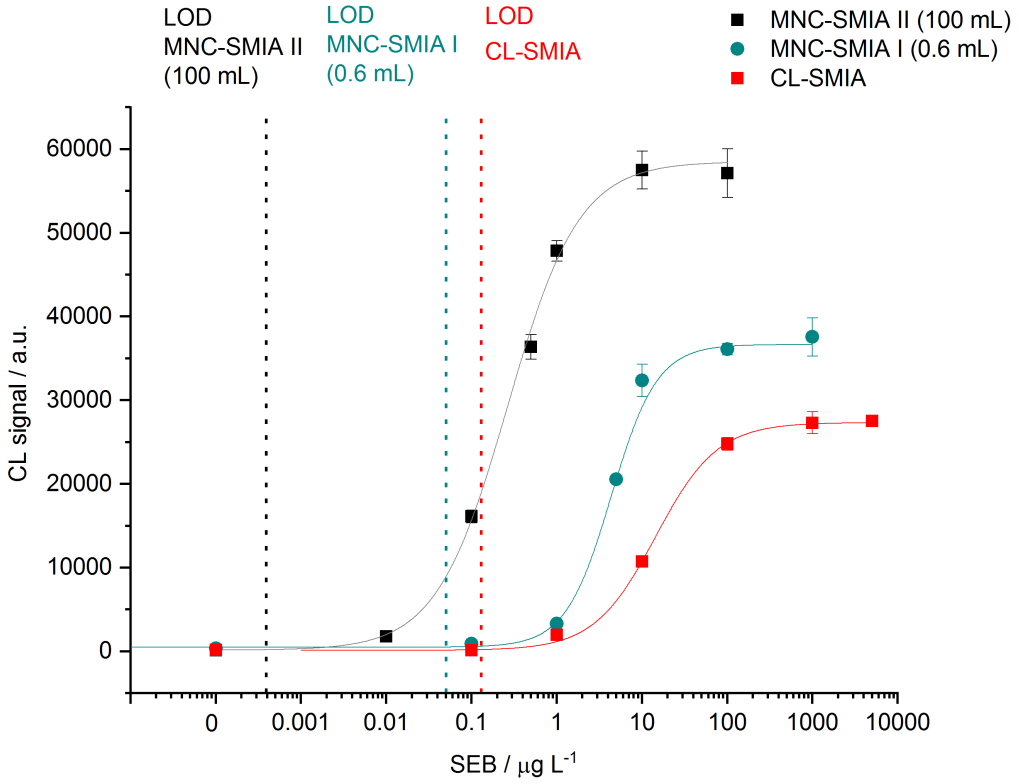

FIGURE 4.52: Comparison of calibration curves for the quantification of SEB in 100 mL milk analyzed by MNC-SMIA I (0.6 mL), MNC-SMIA II (100 mL) and CL-SMIA. Standard deviations (n = 3) are indicated as error bars.

TABLE 4.13: Comparison of MNC-SMIA I (0.6 mL), MNC-SMIA II (100 mL) and CL-SMIA.

Type of assay	**LOD /** $\mu g\,L^{-1}$	**EC50 /** $\mu g\,L^{-1}$	**WR /** $\mu g\,L^{-1}$	**Assay time**
CL-SMIA	0.13	14.5	4.6 - 45.8	18 min
MNC-SMIA I	0.05	4.4	1.9 - 10.3	4 h
MNC-SMIA II	3.9×10^{-4}	0.25	0.07 - 0.93	3 h

Chapter 5

Summary and Outlook

Since foodborne diseases have become one of the major threats to human health, food safety has increased public concern around the world. SEs are one of the most common causes of acute food contamination and poisoning, accounting for numerous foodborne-disease outbreaks all over the world. SEB is a heatstable enterotoxin produced by the ubiquitous appearing Gram-positive bacterium *S. aureus*, which is known as a major human pathogen. It is regarded as a potential biological warfare agent, which may be used for bioterrorism attacks on the food supply chain.
To ensure a fast surveillance and response to foodborne-disease outbreaks, a rapid analytical method is required which enables a sensitive quantification of SEB in large volumes of complex food matrices.
Current problems in the quantification and detection of SEB in food matrix is the lack of sensitivity, since the minimum level of toxin causing gastroenteritis in humans is only around 1 ng g^{-1} of food. Moreover, various analytical approaches such as biosensor technologies work well in buffer solutions, but fail when tested in complex matrices due to the interference of matrix components with binding reagents or techniqual equipment. Current analytical methods such as ELISA or MS-MS therefore require the prior enrichment and isolation of the target analyte from the complex food matrix, which is both time-consuming and rather labor-intensive.
Magnetic nanocomposites offer the major advantage of being easily separated from complex food matrices and are thus amenable to immunomagnetic enrichment procedures.
The aim of this thesis was the development of an immunoassay which couples the facile enrichment and isolation of SEB by IMS, based on superparamagnetic nanocomposites with specifically tailored magnetic and morphological characteristics, to the sensitive microarray analysis on the microarray platform MRC 3 SLT.

Firstly, a novel, simple and fast synthesis strategy based on a thermal decomposition approach was established to design highly and uniformly loaded iron oxide-shell silica-core nanocomposites. They are formed by maghemite nanoparticles (8.4 ± 1.0 nm) uniformly deposited on mesoporous silica nanoparticles (381 nm $\pm$ 111 nm). Their raspberry-shaped morphology can be confirmed by electron microscopy. Nanocomposites were extensively characterized with a variety of analytical methods.

Magnetic measurements were performed with a SQUID magnetometer, revealing the desirable superparamagnetic characteristics of the nanocomposites with a lack of any remanent magnetization at zero field. Overall, the obtained magnetic saturation value was found to be around 17 - 45 A m^2 kg^{-1}(γ-Fe_2O_3), depending on the reaction time.
After investigation of the influence of synthesis reaction time on composition, size and morphology as well as magnetic characteristics of the iron oxide-shell silica-core nanocomposites, an optimal synthesis reaction time of 30 minutes was applied for further experiments. Nanocomposites at this reaction time showed superparamagnetic properties with a high M_S value of 35.9 A m^2 kg^{-1}(γ-Fe_2O_3), without agglomeration tendencies.
The observed magnetic behavior can be utilized to rapidly attract nanocomposites in solution towards a permanent magnet (< 30 s) and to re-disperse them by gentle tapping after removal of the external magnetic field. The magnetization measurements confirmed that the designed iron oxide-shell silica core nanocomposites combine both highly advantageous magnetic features for applications in IMS - the easy manipulation by permanent magnets and superparamagnetism for easily switching on and off the magnetic response.
The iron oxidation state of the nanocomposites was analyzed by RM and compared to several synthesized reference nanoparticles. Three broad bands at around 350 cm^{-1}, 500 cm^{-1} and 700 cm^{-1} demonstrated a perfect match of the spectral signature of the nanocomposites and maghemite nanoparticles. These findings could be further verified by Mössbauer spectroscopy.
Additionally, excellent magnetic long-term stability over at least five months of the nanocomposites was verified by sequential SQUID magnetometry and RM measurements.

The bare iron oxide-shell silica-core nanocomposites were oleic acid-capped and therefore initially hydrophobic. For their final application in the IMS process of SEB in milk an appropriate hydrophilic functionalization approach was developed to broaden their use from nonpolar to aqueous systems. Furthermore, the functionalization improved their colloidal stability and provided an anchorage for the covalent binding of the anti-SEB antibodies. A fast hydrophilic ligand exchange approach by organosilane chemistry using ultrasonication was established. The presence of the organosilane coating on the nanoparticle surface was verified by TEM measurements. Zeta potential measurements of epoxysilane-functionalized nanocomposites revealed a high Zeta potential value of - 32.9 mV at neutral pH, which made this coating superior to the aminosilane functionalization.

Next, a rapid and sensitive detection and quantification method for SEB in complex food matrices such as milk should be developed.
As a first step, a flow-based CL-SMIA on the microarray platform MCR 3 SLT was developed in order to quantify SEB directly in the complex food matrix milk. Hereby, the sensitive antibody pair S1001/4/6 and S419/5/5-biotin, provided by the Robert-Koch Institute (Berlin, Germany), was used.

SEB spiked milk was injected into the microarray analysis platform MCR 3 SLT. The SEB in the milk is bound by the anti-SEB capture antibody immobilized on the microarray chip surface during the stop-flow incubation process. The sandwich is formed by using a biotin-labeled monoclonal detection antibody against SEB. For the CL detection first streptavidin poly-HRP and then the CL reagents (luminol and hydrogen peroxide) were pumped through the microarray channel. The CL signal was recorded by a CCD camera. Hereby, a LOD of 0.13 $\mu g\,L^{-1}$ and a broad WR from 4.6 $\mu g\,L^{-1}$ to 45.8 $\mu g\,L^{-1}$ was obtained.

For the first time, the novel iron oxide-shell silica-core nanocomposites were applied along with antibodies against SEB to establish a highly sensitive MNC-SMIA I on the microarray platform MCR 3 SLT. A selective enrichment and concentration step by IMS offers the possibility to increase the assay sensitivity and even enables the possibility to rapidly analyze larger amounts of food samples. To realize this immunoassay, iron oxide-shell silica-core nanocomposites functionalized with biotinylated anti-SEB detection antibodies were incubated in 0.6 mL milk spiked with SEB. The antibody-functionalized nanocomposites bind the SEB in the milk by an affinity reaction. For the selective enrichment of SEB, an IMS step was applied and the initial sample volume was reduced from 0.6 mL to 0.052 mL, equaling a volumetric concentration factor of 11.5. After direct injection of the sample in the microarray flow channel, SEB was quantified by CL-SMIA. The assay readout is performed by CL imaging. MNC-based SMIA I was step by step optimized resulting in an increase in the CL signal intensity and a decrease in the background signal of the microarray chip surface and therefore significantly improving the assay sensitivity. By implementation of a prior IMS step using superparamagnetic nanocomposites the LOD could be enhanced to 0.05 $\mu g\,L^{-1}$ compared to 0.13 $\mu g\,L^{-1}$ for the antibody-based CL-SMIA.

Since the major goal of this thesis was to establish a rapid, sensitive and cost-effective MNC-SMIA as a suitable analytical method for large-scale screening of food samples from the food supply chain, the sample volume was upscaled from 0.6 mL to 100 mL of milk. In order to guarantee a highly effective and rapid magnetic separation of the nanocomposites, the separation capability of iron oxide-shell silica-core nanocomposites in 100 mL milk was investigated in detail using both manual and automatic separation techniques (syringe and peristaltic pumps). ICP-measurements for determining the iron content before and after separation indicated that the manual separation by using only permanent magnets showed the highest recovery rate of 83.6 $\pm$ 3.0 %. Manual separation addtionally exhibited important features such as time-effectiveness (duration: 10 min) and practicability due to the simple technical setup.

Advancing the developed MNC-SMIA technology, the novel superparamagnetic nanocomposites proved suitable to large-scale enrichment procedures,

by further increasing sensitivity to a LOD of 0.39 ng L^{-1}, starting from a sample volume of 100 mL (volumetric concentration factor: 1923). The obtained assay sensitivity is comparable to the previously published multiplexed fluorescent magnetic suspension assay [3] but with a total assay time of around three hours proved to be less time-consuming and also cost-effective due to the in-house economic and large-scale production of iron oxide-shell silica-core nanocomposites.

During this thesis, an immunoassay which couples the facile enrichment and isolation of SEB by IMS, based on superparamagnetic nanocomposites, to the sensitive microarray analysis on the microarray platform MRC 3 SLT, was successfully developed. On the basis of our results, the application of the novel magnetic nanocomposites appeared to be a major improvement of the conventional CL-SMIA in food matrix.
First, enrichment procedures, even from large samples up to 100 mL, are now possible, resulting in a further improvement of sensitivity. Second, the analysis of colloidal or particulate samples is feasible, since the magnetic nanocomposite-immobilized target analyte can be easily and rapidly separated and isolated from the complex food matrix. Overall, the immunoassay seems to be a suitable tool for large-scale screening of samples from the food supply chain.

In this PhD thesis the detection and quantification of the proteoxin SEB in small and large volumes of the food matrix milk by MNC-SMIA on the MCR 3 SLT was developed. However, there is a huge variety of relevant proteotoxins. The immobilization of various different capture antibodies on the microarray chip surface along with functionalization of the nanocomposites with a set of distinct and specific antibodies, offers the great possibility for a future multiplex detection of a wider variety of proteotoxins such as ricin, abrin, botulinum neurotoxins type A and B and SEs (SEA - SEH). Even a simultaneous detection of both foodborne toxins and microorganisms might feasible. In this context, the food matrix could be simultaneously and rapidly screened for the presence of all relevant foodborne pathogens. Hence, in the near future, the antibody panel could easily be extended.
Additionally, since the magnetic nanocomposite-based SMIA is compatible with with analysis of complex food matrices such as milk, it might be a useful tool for the screening of further food samples in the food supply chain (e.g. yoghurt or baby food) or even other complex matrices in the diagnostical field such as patient samples (urine, blood).
An advancement in the automatic magnetic separation technology of the magnetic nanocomposites would offer the promising possibility to a more convenient and fully-automated inline-coupling of the IMS step with the sensitive microarray analysis.

Appendix A

MCR 3 SLT

A.1 Fluidic plan of the MCR 3 SLT

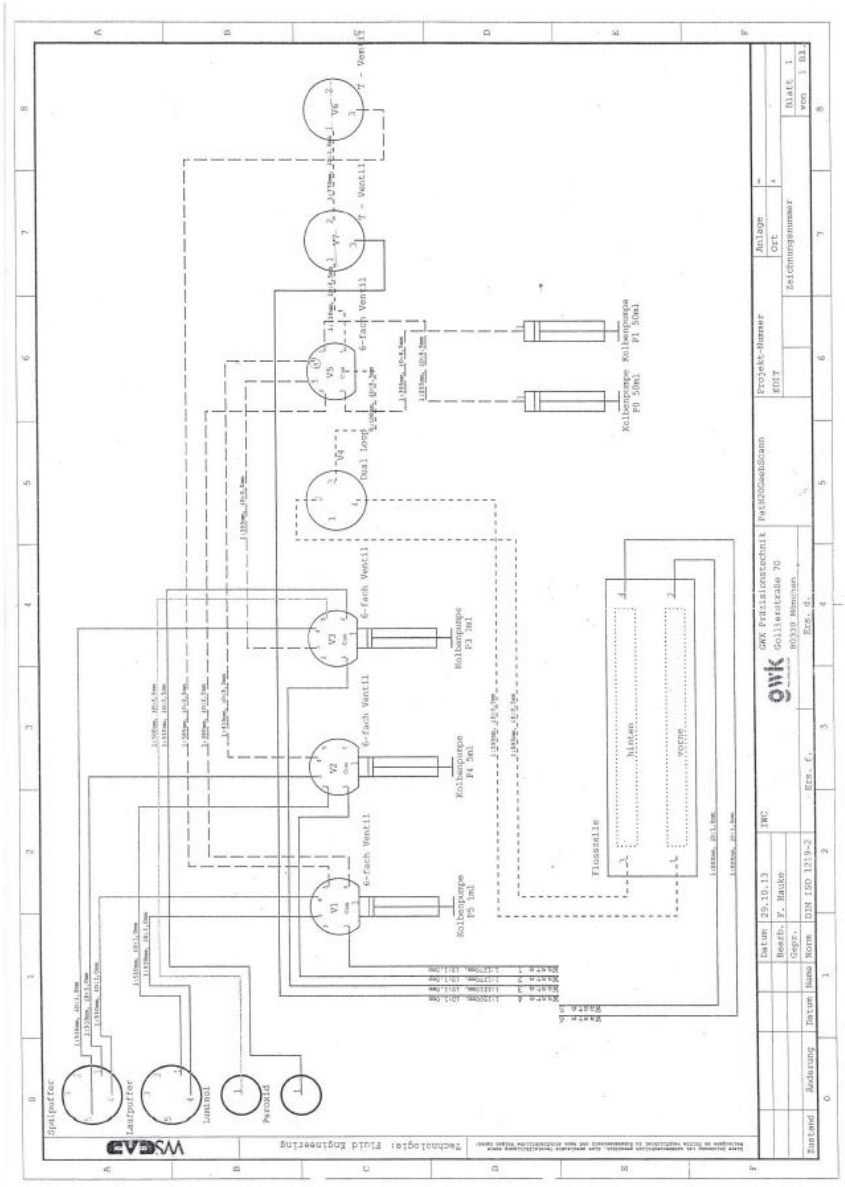

A.2 MCR 3 Program: MNC-SMIA (front channel)

Block start

- Pump 3 reference
- Pump 5 reference
- Valve 1 reference
- Valve 2 reference
- Valve 3 reference
- Valve 4 reference
- Valve 5 reference
- Valve 6 reference
- Valve 7 reference
- Block end

Block start

- Set temperature microarray chip to 37 °C
- Valve 6, pos. 1, direction unknown
- Valve 7, pos. 4, direction unknown
- Valve 5, pos. 6, direction right
- Message: Probe eingespritzt. Type Confirm
- Valve 4, pos. 2, direction unknown
- Wait 10 seconds
- Block end

Block start

- Set temperature microarray chip to 37 °C
- Valve 2, pos. 2, direction right
- Pump 4, direction intake, quantity, 1000 µL, flow 500 $\mu l\, s^{-1}$
- Valve 2, pos. 4, direction right
- Valve 5, pos. 4, direction right

- Pump 4, direction dispense, quantity 100 µL, flow 100 µl s^{-1}
- Block end, loops 3

Block start

- Set temperature microarray chip to 37 °C
- Valve 5, pos. 5, direction right
- Pump 0, direction dispense, quantity 150 µL, flow 50 µl s^{-1}
- Pump 0, direction dispense, quantity 600 µL, flow 2 µl s^{-1}
- Block end

Block start

- Set temperature microarray chip to 35 °C
- Valve 3, pos. 5, direction right
- Pump 3, direction intake, quantity 100 µL, flow 200µl s^{-1}
- Valve 3, pos. 6, direction right
- Pump 3, direction intake, quantity 100 µL, flow 200 µl s^{-1}
- Valve 3, pos. 5, direction right
- Pump 3, direction intake, quantity 100 µL, flow 200 µl s^{-1}
- Valve 3, pos. 6, direction right
- Valve 5, pos. 3, direction right
- Pump 3, direction dispense, quantity 400 µL, flow 20 µl s^{-1}
- Block end

Block start

- Camera on, exposure 50 seconds, front channel
- Buzzer, duration 2000
- Block end

Block start

- Valve 2, pos. 2, direction right
- Pump 4, direction intake, quantity 1500 µL, flow 500 µl s^{-1}
- Valve 2, pos. 4, direction right
- Valve 5, pos. 4, direction right
- Pump 4, direction dispense, quantity 150 µL, flow 500 µl s^{-1}
- Block end

Block start

- Valve 1, pos. 3, direction right
- Pump 5, direction intake, quantity 1000 µL, flow 68 µl s^{-1}
- Valve 1, pos. 5, direction right
- Valve 6, pos. 1, direction unknown
- Valve 7 pos. 4, direction unknown
- Valve 5, pos. 6, direction right
- Pump 5, direction dispense, quantity 1000 µL, flow 68 µl s^{-1}
- Block end, loops 3

Bibliography

[1] I. V. Pinchuk, E. J. Beswick, V. E. Reyes, *Toxins* **2010**, *2*, 2177–2197.

[2] WHO, World Health Day 2015: From farm to plate, make food safe, WHO, `http://www.who.int/mediacentre/news/releases/2015/food-safety/en/` (visited on 07/31/2018).

[3] D. Pauly, S. Kirchner, B. Stoermann, T. Schreiber, S. Kaulfuss, R. Schade, R. Zbinden, M.-A. Avondet, M. B. Dorner, B. G. Dorner, *Analyst* **2009**, *134*, 2028–2039.

[4] L. An-Hui, E. L. Salabas, F. Schüth, *Angewandte Chemie* **2007**, *119*, 1242–1266.

[5] W. Wu, Z. Wu, T. Yu, C. Jiang, W.-S. Kim, *Science and Technology of Advanced Materials* **2015**, *16*, 023501.

[6] R. E. Rosensweig, *Ferrohydrodynamics*, Dover Publications, New York, **1997**.

[7] C. Rümenapp, B. Gleich, A. Haase, *Pharmaceutical Research* **2012**, *29*, 1165–1179.

[8] B. Issa, M. I. Obaidat, A. B. Albiss, Y. Haik, *International Journal of Molecular Sciences* **2013**, *14*.

[9] C. Kittel, *Reviews of Modern Physics* **1949**, *21*, 541–583.

[10] C. Alexiou, R. Jurgons, R. Schmid, A. Hilpert, C. Bergemann, F. Parak, H. Iro, **2005**, *293*, 389–393.

[11] K. M. Krishnan, *IEEE transactions on magnetics* **2010**, *46*, 2523–2558.

[12] M. Opel, K. W. Nielsen, S. Bauer, S. Goennenwein, J. C. Cezar, D. Schmeißer, J. Simon, W. Mader, R. Gross, **2008**, *63*, 437–444.

[13] J. Park, K. An, Y. Hwang, J.-G. Park, H.-J. Noh, J.-Y. Kim, J.-H. Park, N.-M. Hwang, T. Hyeon, *Nature Materials* **2004**, *3*, 891.

[14] A. K. Gupta, M. Gupta, *Biomaterials* **2005**, *26*, 3995–4021.

[15] S. Majidi, F. Zeinali Sehrig, S. M. Farkhani, M. Soleymani Goloujeh, A. Akbarzadeh, *Artificial Cells Nanomedicine and Biotechnology* **2016**, *44*, 722–734.

[16] S. Behrens, I. Appel, *Current Opinion in Biotechnology* **2016**, *39*, 89–96.

[17] S. Behrens, *Nanoscale* **2011**, *3*, 877–892.

[18] J. K. Oh, J. M. Park, *Progress in Polymer Science* **2011**, *36*, 168–189.

[19] N. Griffete, J.-F. Dechezelles, F. Scheffold, *Chemical Communications* **2012**, *48*, 11364–11366.

[20] B. Julian-Lopez, C. Boissiere, C. Chaneac, D. Grosso, S. Vasseur, S. Miraux, E. Duguet, C. Sanchez, *Journal of Materials Chemistry* **2007**, *17*, 1563–1569.

[21] P. Tartaj, T. González-Carreño, C. Serna, *Advanced Materials* **2001**, *13*, 1620–1624.

[22] K. Jaeyun, K. Hoe Suk, L. Nohyun, L. Taeho, K. Hyoungsu, L. Taekyung, S. In Chan, M. W. Kyung, H. Taeghwan, *Angewandte Chemie* **2008**, *120*, 8566–8569.

[23] M. Cano, G. de la Cueva-Mendez, *Chemical Communications* **2015**, *51*, 3620–3622.

[24] D. Nagao, M. Yokoyama, N. Yamauchi, H. Matsumoto, Y. Kobayashi, M. Konno, *Langmuir* **2008**, *24*, 9804–9808.

[25] S. I. Stoeva, F. Huo, J.-S. Lee, C. A. Mirkin, *Journal of the American Chemical Society* **2005**, *127*, 15362–15363.

[26] A. B. Dávila-Ibáñez, M. A. López-Quintela, J. Rivas, V. Salgueirino, *The Journal of Physical Chemistry C* **2010**, *114*, 7743–7750.

[27] S. Ramesh, I. Felner, Y. Koltypin, A. Gedanken, *Journal of Materials Research* **2000**, *15*, 944–950.

[28] Y. Zhu, H. Da, X. Yang, Y. Hu, *Colloids and Surfaces A: Physicochemical and Engineering Aspects* **2003**, *231*, 123–129.

[29] F. Chen, R. Shi, Y. Xue, L. Chen, Q.-H. Wan, *Journal of Magnetism and Magnetic Materials* **2010**, *16*, 2439–2445.

[30] M. Ocaña, M. Andrés-Vergés, R. Pozas, C. J. Serna, *Journal of Colloid and Interface Science* **2006**, *294*, 355–361.

[31] L. Ren, C. Teng, L. Zhu, J. He, Y. Wang, X. Zuo, M. Hong, Y. Wang, B. Jiang, J. Zhao, *Nanoscale Research Letters* **2014**, *9*, 163.

[32] J. E. Lee, N. Lee, H. Kim, J. Kim, S. H. Choi, J. H. Kim, T. Kim, I. C. Song, S. P. Park, W. K. Moon, T. Hyeon, *Journal of the American Chemical Society* **2010**, *132*, 552–557.

[33] H. Qu, S. Tong, K. Song, H. Ma, G. Bao, S. Pincus, W. Zhou, C. O'Connor, *Langmuir* **2013**, *29*, 10573–10578.

[34] W. Wu, Q. He, C. Jiang, *Nanoscale Research Letters* **2008**, *3*, 397–415.

[35] M. Bloemen, W. Brullot, T. T. Luong, N. Geukens, A. Gils, T. Verbiest, *Journal of Nanoparticle Research* **2012**, *14*, 1100.

[36] R. De Palma, S. Peeters, M. J. Van Bael, H. Van den Rul, K. Bonroy, W. Laureyn, J. Mullens, G. Borghs, G. Maes, *Chemistry of Materials* **2007**, *19*, 1821–1831.

[37] E. K. U. Larsen, T. Nielsen, T. Wittenborn, H. Birkedal, T. Vorup-Jensen, M. H. Jakobsen, L. Østergaard, M. R. Horsman, F. Besenbacher, K. A. Howard, J. Kjems, *ACS Nano* **2009**, *3*, 1947–1951.

[38] H.-B. Xia, J. Yi, P.-S. Foo, B. Liu, *Chemistry of Materials* **2007**, *19*, 4087–4091.

[39] G. T. Hermanson in *Bioconjugate Techniques (Second Edition)*, Academic Press, New York, **2008**, pp. 783–823.

[40] J. Gallo, N. J. Long, E. O. Aboagye, *Chemical Society Reviews* **2013**, *42*, 7816–7833.

[41] J. Bart, R. Tiggelaar, M. Yang, S. Schlautmann, H. Zuilhof, H. Gardeniers, *Lab on a Chip* **2009**, *9*, 3481–3488.

[42] X. Zhang, Y. Zhang, *Molecules* **2013**, *18*.

[43] R. F. Egerton, *Physical Principles of Electron Microscopy*, Springer International Publishing, Alberta, Canada, **2016**, 203 pp.

[44] Transmission Electron Microscopy (TEM), `https://warwick.ac.uk/fac/sci/physics/current/postgraduate/regs/mpagswarwick/ex5/techniques/structural/tem/` (visited on 07/22/2018).

[45] J. Lim, S. P. Yeap, H. X. Che, S. C. Low, *Nanoscale Research Letters* **2013**, *8*, 381.

[46] Surface analysis, Encyclopedia Britannica, `https://www.britannica.com/science/surface-analysis` (visited on 07/22/2018).

[47] S. Bhatia in *Natural Polymer Drug Delivery Systems: Nanoparticles, Plants, and Algae*, (Ed.: S. Bhatia), Springer International Publishing, Cham, **2016**, pp. 33–93.

[48] A. K. Singh in *Engineered Nanoparticles*, (Ed.: A. K. Singh), Academic Press, Boston, **2016**, pp. 125–170.

[49] P. Biehl, M. von der Lühe, S. Dutz, H. F. Schacher, *Polymers* **2018**, *10*.

[50] P. A. Hassan, S. Rana, G. Verma, *Langmuir* **2015**, *31*, 3–12.

[51] C. Rümenapp, B. Gleich, H. G. Mannherz, A. Haase, *Journal of Magnetism and Magnetic Materials* **2015**, *380*, 271–275.

[52] C. Rümenapp, F. E. Wagner, B. Gleich, *Journal of Magnetism and Magnetic Materials* **2015**, *380*, 241–245.

[53] N. C. Bell, C. Minelli, J. Tompkins, M. M. Stevens, A. G. Shard, *Langmuir* **2012**, *28*, 10860–10872.

[54] H. Fissan, S. Ristig, H. Kaminski, C. Asbach, M. Epple, *Analytical Methods* **2014**, *6*, 7324–7334.

[55] Walther Meißner Institut - SQUID magnetometry, `https://www.wmi.badw.de/methods/squid.htm` (visited on 07/26/2018).

[56] A. G. Kolhatkar, A. C. Jamison, D. Litvinov, R. C. Willson, T. R. Lee, *International Journal of Molecular Sciences* **2013**, *14*, 15977–16009.

[57] A. Wiesheu, P. Anger, R. Weiss in *Praktikumsskript, Nebenfach Analytische Chemie-Organische Spurenanalytik*, Technische Universität München, Großhadern, **2017**.

[58] N. P. Ivleva, S. Huckele, B. Weinzierl, R. Niessner, C. Haisch, T. Baumann, *Analytical and Bioanalytical Chemistry* **2013**, *405*, 9071–9084.

[59] S. P. Schwaminger, D. Bauer, P. Fraga-Garcia, F. E. Wagner, S. Berensmeier, *CrystEngComm* **2017**, *19*, 246–255.

[60] Y.-S. Li, J. S. Church, A. L. Woodhead, *Journal of Magnetism and Magnetic Materials* **2012**, *324*, 1543–1550.

[61] D. L. A. de Faria, S. Silva Venâncio, M. de Oliveira, *Journal of Raman Spectroscopy* **1998**, *28*, 873–878.

[62] M. Hanesch, *Geophysical Journal International* **2009**, *177*, 941–948.

[63] F. J. Berry, S. Skinner, M. Thomas, *Journal of Physics: Condensed Matter* **1998**, *10*, 215.

[64] Introduction to Mossbauer Spectroscopy: Part I, `http://www.rsc.org/Membership/Networking/InterestGroups/MossbauerSpect/Intropart1.asp` (visited on 07/27/2018).

[65] J. Coates in *Encyclopedia of Analytical Chemistry*, American Cancer Society, **2006**.

[66] Y. Wang, J. K. Salazar, *Comprehensive Reviews in Food Science and Food Safety* **2015**, *15*, 183–205.

[67] T. Martinović, U. Andjelković, M. Š. Gajdošik, D. Rešetar, D. Josić, *Foodomics - Novel insights in food and nutrition domains* **2016**, *147*, 226–235.

[68] M. Á. Argudín, M. C. Mendoza, M. R. Rodicio, *Toxins* **2010**, *2*.

[69] R. J. Langley, Y. T. Ting, F. Clow, P. G. Young, F. J. Radcliff, J. M. Choi, R. P. Sequeira, S. Holtfreter, H. Baker, J. D. Fraser, *PLOS Pathogens* **2017**, *13*, e1006549.

[70] N. Benkerroum, *Critical Reviews in Food Science and Nutrition* **2017**, 1–28.

[71] J.-A. Hennekinne, M.-L. De Buyser, S. Dragacci, *FEMS Microbiology Reviews* **2012**, *36*, 815–836.

[72] F. J. Bone, D. Bogie, S. C. Morgan-Jones, *Epidemiology and Infection* **1989**, *103*, 449–458.

[73] M. L. Evenson, M. W. Hinds, R. S. Bernstein, M. S. Bergdoll, *International Journal of Food Microbiology* **1988**, *7*, 311–316.

[74] L. S. Do Carmo, C. Cummings, V. Roberto Linardi, R. Souza Dias, J. Maria De Souza, M. J. De Sena, D. Aparecida Dos Santos, J. W. Shupp, R. Karla Peres Pereira, M. Jett, *Foodborne Pathogens and Disease* **2004**, *1*, 241–246.

[75] T. Asao, Y. Kumeda, T. Kawai, T. Shibata, H. Oda, K. Haruki, H. Nakazawa, S. Kozaki, *Epidemiology and Infection* **2003**, *130*, 33–40.

[76] A. Ostyn, M. L. D. Buyser, F. Guillier, J. Groult, B. Félix, S. Salah, G. Delmas, J. A. Hennekinne, *Eurosurveillance* **2010**, *15*, 19528.

[77] B. Fries, A. Varshney, *Microbiology spectrum* **2013**, *1*.

[78] Z. Xu in *Significance, Prevention and Control of Food Related Diseases*, (Ed.: B. Peters), InTech, Rijeka, **2016**.

[79] T. Berger, A. Eisenkraft, E. Bar-Haim, M. Kassirer, A. A. Aran, I. Fogel, *Disaster and Military Medicine* **2016**, *2*, 7.

[80] K. A. Stevens, L.-A. Jaykus, *Critical Reviews in Microbiology* **2004**, *30*, 7–24.

[81] O. Olsvik, T. Popovic, E. Skjerve, K. S. Cudjoe, E. Hornes, J. Ugelstad, M. Uhlén, *Clinical Microbiology Reviews* **1994**, *7*, 43–54.

[82] B. Schmitz, A. Radbruch, T. Kümmel, C. Wickenhauser, H. Korb, M. L. Hansmann, J. Thiele, R. Fischer, *European Journal of Haematology* **1994**, *52*, 267–275.

[83] J. Austin, F. Pagotto in *Encyclopedia of Food Sciences and Nutrition (Second Edition)*, Academic Press, Oxford, **2003**, pp. 3886–3892.

[84] H. Fatima, K.-S. Kim, *Korean Journal of Chemical Engineering* **2017**, *34*, 589–599.

[85] S. S. Leong, S. P. Yeap, J. Lim, *Interface Focus* **2016**, *6*.

[86] J. R. Stephens, J. S. Beveridge, M. E. Williams, *Physical Chemistry Chemical Physics* **2012**, *14*, 3280–3289.

[87] G. Pappert, M. Rieger, R. Niessner, M. Seidel, *Microchimica Acta* **2010**, *168*, 1–8.

[88] I. Aprodu, G. Walcher, J. Schelin, I. Hein, B. Norling, P. Rådström, A. Nicolau, M. Wagner, *International Journal of Food Microbiology* **2011**, *145*, 61–65.

[89] D. O. Oluwayelu, A. I. Adebiyi, *African Health Sciences* **2016**, *16*, 640–645.

[90] S. Ott, R. Niessner, M. Seidel, *Journal of Separation Science* **2011**, *34*, 2181–2192.

[91] J. D. Brewster, *Journal of Microbiological Methods* **2003**, *55*, 287–293.

[92] J. Brunt, M. D. Webb, M. W. Peck, *Applied and Environmental Microbiology* **2010**, *76*, 4143–4150.

[93] C. Peskoller, R. Niessner, M. Seidel, *Journal of Chromatography A* **2009**, *1216*, 3794–3801.

[94] S. Wu, N. Duan, H. Gu, L. Hao, H. Ye, W. Gong, Z. Wang, *Toxins* **2016**, *8*, (Ed.: V. L. Tesh), 176.

[95] H. Igarashi, H. Fujikawa, M. Shingaki, M. S. Bergdoll, *Journal of Clinical Microbiology* **1986**, *23*, 509–512.

[96] S. A. Rose, P. Bankes, M. Stringer, *International Journal of Food Microbiology* **1989**, *8*, 65–72.

[97] M. Gholamzad, M. R. Khatami, S. Ghassemi, Z. Vaise Malekshahi, M. B. Shooshtari, *Jundishapur Journal of Microbiology* **2015**, *8*, e26793.

[98] I. G. Wilson, J. E. Cooper, A. Gilmour, *Applied and Environmental Microbiology* **1991**, *57*, 1793–1798.

[99] N. K. Sharma, C. E. D. Rees, C. E. R. Dodd, *Applied and Environmental Microbiology* **2000**, *66*, 1347–1353.

[100] C. E. Kientz, A. G. Hulst, E. R. Wils, *Journal of Chromatography A* **1997**, *757*, 51–64.

[101] J. H. Callahan, K. J. Shefcheck, T. L. Williams, S. M. Musser, *Analytical Chemistry* **2006**, *78*, 1789–1800.

[102] I. Sospedra, C. Soler, J. Mañes, J. M. Soriano, *Journal of Chromatography A* **2012**, *1238*, 54–59.

[103] Z. A. Muratovic, T. Hagström, J. Rosén, K. Granelli, K.-E. Hellenäs, *Toxins* **2015**, *7*, 3637–3656.

[104] G. C. Saunders, M. L. Bartlett, *Applied and Environmental Microbiology* **1977**, *34*, 518–522.

[105] A. A. Wieneke, R. J. Gilbert, *Journal of Hygiene* **1985**, *95*, 131–138.

[106] G. Stiffler-Rosenberg, H. Fey, *Journal of Clinical Microbiology* **1978**, *8*, 473–479.

[107] C. Morissette, J. Goulet, G. Lamoureux, *Applied and Environmental Microbiology* **1991**, *57*, 836–842.

[108] M. A. Poli, V. R. Rivera, D. Neal, *Toxicon* **2002**, *40*, 1723–1726.

[109] K. M. Koczula, A. Gallotta, *Essays in Biochemistry* **2016**, *60*, (Ed.: P. Estrela), 111–120.

[110] S. Rong-Hwa, T. Shiao-Shek, C. Der-Jiang, H. Yao-Wen, *Food Chemistry* **2010**, *118*, 462–466.

[111] P. Khan, D. Idrees, M. A. Moxley, J. A. Corbett, F. Ahmad, G. von Figura, W. S. Sly, A. Waheed, M. I. Hassan, *Applied Biochemistry and Biotechnology* **2014**, *173*, 333–355.

[112] M. Seidel, R. Niessner, *Analytical and Bioanalytical Chemistry* **2008**, *391*, 1521.

[113] A. Díaz, F. Sanchez, J. García, *Analytica Chimica Acta* **1996**, *327*, 161–165.

[114] S. Miller, U. Karaoz, E. Brodie, S. Dunbar in *Methods in Microbiology*, *Vol. 42*, (Eds.: A. Sails, Y.-W. Tang), Academic Press, **2015**, pp. 395–431.

[115] A. Szkola, E. M. Linares, S. Worbs, B. G. Dorner, R. Dietrich, E. Martlbauer, R. Niessner, M. Seidel, *Analyst* **2014**, *139*, 5885–5892.

[116] A. G. Gehring, D. M. Albin, A. K. Bhunia, S. A. Reed, S.-I. Tu, J. Uknalis, *Analytical Chemistry* **2006**, *78*, 6601–6607.

[117] B. Elsholz, R. Wörl, L. Blohm, J. Albers, H. Feucht, T. Grunwald, B. Jürgen, T. Schweder, R. Hintsche, *Analytical Chemistry* **2006**, *78*, 4794–4802.

[118] A. Sachdeva, A. K. Singh, S. K. Sharma, *Journal of the Science of Food and Agriculture* **2013**, *94*, 707–712.

[119] B. Swaminathan, P. Feng, *Annual Review of Microbiology* **1994**, *48*, 401–426.

[120] K. Narsaiah, S. N. Jha, R. Bhardwaj, R. Sharma, R. Kumar, *Journal of food science and technology* **2012**, *49*, 383–406.

[121] J. Wojciechowski, D. Danley, J. Cooper, N. Yazvenko, C. R. Taitt, *Sensors* **2010**, *10*.

[122] E. A. E. Garber, K. V. Venkateswaran, T. W. O'Brien, *Journal of Agricultural and Food Chemistry* **2010**, *58*, 6600–6607.

[123] J. Wang, Y. Yang, L. Zhou, J. Wang, Y. Jiang, K. Hu, X. Sun, Y. Hou, Z. Zhu, Z. Guo, Y. Ding, R. Yang, *Immunopharmacology and Immunotoxicology* **2009**, *31*, 417–427.

[124] W. Lian, D. Wu, D. V. Lim, S. Jin, *Analytical Biochemistry* **2010**, *401*, 271–279.

[125] G. Schlosser, P. Kačer, M. Kuzma, Z. Szilágyi, A. Sorrentino, C. Manzo, R. Pizzano, L. Malorni, G. Pocsfalvi, *Applied and Environmental Microbiology* **2007**, *73*, 6945–6952.

[126] T. Miyamoto, H. Kamikado, H. Kobayashi, K.-i. Honjoh, M. Iio, *Journal of Food Protection* **2003**, *66*, 1222–6.

[127] Y. M. Shlyapnikov, E. A. Shlyapnikova, M. A. Simonova, A. O. Shepelyakovskaya, F. A. Brovko, R. L. Komaleva, E. V. Grishin, V. N. Morozov, *Analytical Chemistry* **2012**, *84*, 5596–5603.

[128] H. Yu, J. Raymonda, T. McMahon, A. Campagnari, *Biosensors and Bioelectronics* **2000**, *14*, 829–840.

[129] C. E. Park, M. Akhtar, M. K. Rayman, *Applied and Environmental Microbiology* **1994**, *60*, 677–681.

[130] C. E. Park, M. Akhtar, M. K. Rayman, *Applied and Environmental Microbiology* **1992**, *58*, 2509–2512.

[131] C. Vernozy-Rozand, C. Mazuy-Cruchaudet, C. Bavai, Y. Richard, *Letters in Applied Microbiology* **2004**, *39*, 490–494.

[132] K. Petcharoen, A. Sirivat, *Materials Science and Engineering: B* **2012**, *177*, 421–427.

[133] R. M. Cornell, U. Schwertmann, *The Iron Oxides: Structure, Properties, Reactions, Occurrences and Uses*, 2nd ed., John Wiley & Sons, **2003**, 712 pp.

[134] A. Wolter, R. Niessner, M. Seidel, *Analytical Chemistry* **2007**, *79*, 4529–4537.

[135] S. C. Donhauser, R. Niessner, M. Seidel, *Analytical Sciences* **2009**, *25*, 669–674.

[136] K. Kloth, R. Niessner, M. Seidel, *Biosensors and Bioelectronics* **2009**, *24*, 2106–2112.

[137] S. Lengger, J. Otto, D. Elsässer, O. Schneider, A. Tiehm, J. Fleischer, R. Niessner, M. Seidel, *Analytical and Bioanalytical Chemistry* **2014**, *406*, 3323–3334.

[138] W. Baaziz, B. P. Pichon, S. Fleutot, Y. Liu, C. Lefevre, J.-M. Greneche, M. Toumi, T. Mhiri, S. Begin-Colin, *The Journal of Physical Chemistry C* **2014**, *118*, 3795–3810.

[139] K. Mandel, F. Hutter, C. Gellermann, G. Sextl, *ACS Applied Materials & Interfaces* **2012**, *4*, 5633–5642.

[140] S. Mørup, M. F. Hansen, C. Frandsen, *Beilstein Journal of Nanotechnology* **2010**, *1*, 182–190.

[141] J. Santoyo Salazar, L. Perez, O. de Abril, L. Truong Phuoc, D. Ihiawakrim, M. Vazquez, J.-M. Greneche, S. Begin-Colin, G. Pourroy, *Chemistry of Materials* **2011**, *23*, 1379–1386.

[142] S. Kamali-M., T. Ericsson, R. Wäppling, *Thin Solid Films* **2006**, *515*, 721–723.

[143] I. Dézsi, C. Fetzer, á. Gombkötő, I. Szűcs, J. Gubicza, T. Ungár, *Journal of Applied Physics* **2008**, *103*, 104312.

[144] L. Zhang, R. He, H.-C. Gu, *Applied Surface Science* **2006**, *253*, 2611–2617.

[145] I. de Berti, M. Cagnoli, G. Pecchi, J. Allessandrini, S. J. Stewart, J. F. Bengoa, Marchetti, *Nanotechnology* **2013**, *24*, 175601.

[146] G. Kandasamy, D. Maity, *International Journal of Pharmaceutics* **2015**, *496*, 191–218.

[147] Z. Lin, X. Wang, Z.-J. Li, S.-Q. Ren, G.-N. Chen, X.-T. Ying, J.-M. Lin, *Talanta* **2008**, *75*, 965–972.

[148] Granitzer P., Rumpf K., Poelt P., Reissner M., *Physica Status Solidi c* **2014**, *11*, 1004–1006.

[149] K. Rumpf, P. Granitzer, P. M. Morales, P. Poelt, M. Reissner, *Nanoscale Research Letters* **2012**, *7*, 445–445.

[150] B. Chertok, A. E. David, V. C. Yang, *Biomaterials* **2010**, *31*, 6317–6324.

[151] V. Silva, P. Andrade, M. Silva, A. Bustamante D., L. De Los Santos Valladares, J. Albino Aguiar, *Journal of Magnetism and Magnetic Materials* **2013**, *343*, 138–143.

[152] C. J. Serna, M. P. Morales in *Surface and Colloid Science*, (Eds.: E. Matijević, M. Borkovec), Springer US, Boston, MA, **2004**, pp. 27–81.

[153] A. Kunze, M. Dilcher, A. Abd El Wahed, F. T. Hufert, R. Niessner, M. Seidel, *Analytical Chemistry* **2015**, *88*, 898–905.

[154] S. S. Groves, M. J. Turell, C. L. Bailey, V. N. Morozov, *The American Journal of Tropical Medicine and Hygiene* **2008**, *78*, 63–69.

[155] M. Johnson, *Materials and Methods* **2012**, *2*, 2329–5139.

[156] Y. Xiao, S. N. Isaacs, *Journal of Immunological Methods* **2012**, *384*, 148–151.

[157] M. A. McClain, C. T. Culbertson, S. C. Jacobson, N. L. Allbritton, C. E. Sims, J. M. Ramsey, *Analytical Chemistry* **2003**, *75*, 5646–5655.

[158] B. Saha, T. H. Evers, M. W. J. Prins, *Analytical Chemistry* **2014**, *86*, 8158–8166.

[159] M. Yang, Y. Kostov, H. A. Bruck, A. Rasooly, *International Journal of Food Microbiology* **2009**, *133*, 265–271.